

**THE DEVELOPMENT OF A MULTICHANNEL ATOMIC MAGNETOMETER ARRAY
FOR FETAL MAGNETOCARDIOGRAPHY**

BY

ROBERT WYLLIE IV

A DISSERTATION SUBMITTED IN PARTIAL FULFILLMENT OF
THE REQUIREMENTS FOR THE DEGREE OF

DOCTOR OF PHILOSOPHY

(PHYSICS)

AT THE

UNIVERSITY OF WISCONSIN–MADISON

2012

ACKNOWLEDGMENTS

First, I would like to thank Thad Walker for making my experience along the road to this thesis a completely positive one. His boundless enthusiasm and curiosity for his work will always serve as an example for me, and he has been gracious with his praise and generous with credit for what we have done. When potential students ask me how I like working with him, it's a relief to be able to tell them how unreservedly great that experience has been. Any future success I have as a physicist, I owe in large part to him.

I should also mention my undergraduate institution, Denison University. In particular, the truly extraordinary commitment of the physics department to helping their students flourish. I remember several moments that still feel significant: Kim Coplin, with just a touch of exasperation, telling me she didn't know the answer to my question, before I asked it; Steve Doty telling me the two ways to get rid of moss are starving it of sunlight and scrubbing it vigorously (the latter is the only one that really works); Dan Homan imagining what Debye must have thought in the moment when he learned his theory led to such an accurate description of specific heat in conductors, and many others. I thank everyone there for helping prepare me for my experiences afterward.

Ron Wakai and his biomagnetism lab have been very helpful. They have greatly helped with both the practicalities of working with physicists who know precious little about the signal they are trying to detect, to more detailed technical assistance and guidance in the design and use of our device.

My peers have done a great deal give me the experience I've had here. In particular, I'd like to thank Nick Proite and Brian Lancor for many hours of discussion, helping me hone my thoughts

about physics and everything else. I would also like to thank Matt Kauer and Greg Smetana, who have contributed a great deal to the work in this thesis, as well as everyone else who has come through Thad's lab during my time here.

Finally, I owe an un-repayable debt of gratitude to my family. I thank Bill and Sarah Prueter for treating me always with kindness and generosity. To my parents, Robert and Elaine, I am grateful for unwavering love and support. Finally, I thank my loving wife and partner, Betsy. There's no telling where I would be without her influence, but surely not writing this. To her, I owe everything.

DISCARD THIS PAGE

TABLE OF CONTENTS

	Page
LIST OF TABLES	vi
LIST OF FIGURES	vii
ABSTRACT	xii
1 Introduction	1
1.1 Atomic magnetometer renaissance	3
2 SERF Theory	6
2.1 Historical optical magnetometry	7
2.1.1 Traditional atomic magnetometry	7
2.1.2 The SERF regime	8
2.2 SERF magnetometer	15
2.2.1 Optical pumping	15
2.2.2 Spin-relaxation from binary collisions and probe absorption	18
2.2.3 Diffusion	19
2.2.4 Larmor precession	21
2.2.5 Equation of motion and steady-state response	23
2.2.6 Response to dynamic fields	29
2.2.7 Sensitivity and Bandwidth	33
2.2.8 Probe Faraday rotation	35
2.3 Warts and imperfections	38
2.4 Spatial dependence of laser parameters	38
2.4.1 Transverse spatial dependence of a Gaussian beam	38
2.4.2 Longitudinal dependence of a weak probe	39

	Page
2.4.3 Longitudinal dependence of the pump	40
2.5 Light shift	44
3 Apparatus	47
3.1 Cell, heatsink, and heaters	49
3.2 Optics and mounts	53
3.3 Electronics	55
3.3.1 Heaters and thermistors	56
3.3.2 Coils and coil drivers	58
3.3.3 Data acquisition system	59
3.4 Magnetometer array	62
4 Data Collection and Analysis	67
4.1 Setting up magnetometers to operate in DC mode	67
4.2 Residual field nulling	69
4.3 Characterization procedure using DAQ program	70
4.3.1 Coil driving circuit calibration	70
4.3.2 Magnetometer calibration and initial noise measurement	71
4.3.3 Additional noise measurements (Probe and electronic)	72
4.3.4 Chirp response measurement	77
4.4 Optimization	78
4.5 Signal measurements	80
5 Noise analysis	83
5.1 Magnetic noise	85
5.1.1 Johnson noise from nearby conductors	85
5.1.2 Magnetic noise from nearby electronic circuits	86
5.1.3 Noise from sources outside the MSR	86
5.2 Fundamental quantum noise sources	87
5.2.1 Spin-projection noise	88
5.2.2 Photon shot noise (basic)	89
5.2.3 Experimental measurement of fundamental noise	90
5.2.4 Averaged parameters	92
5.2.5 Spatially dependent magnetometer response	92
5.3 Technical noise sources	99
5.3.1 Signal aliasing	99
5.3.2 Probe polarization rotation in optical fiber	100

Appendix

	Page
5.3.3 Probe frequency and intensity noise	102
5.3.4 Pump laser fluctuations	104
5.3.5 Laser Misalignment	105
6 Extensions and different operating modes	107
6.1 Non-parametric field modes	107
6.1.1 Diffusion mode pumping	108
6.1.2 Feedback mode	113
6.2 Parametric field modes	122
6.3 Z-Mode	123
6.4 Transverse pumping SERF magnetometer	129
7 Biomagnetism	138
7.1 MCG characteristics	138
7.2 Signal processing	142
7.2.1 Single-channel processing techniques	144
7.2.2 Multiple-channel processing techniques	145
7.2.3 Advanced nonlinear noise reduction	147
7.2.4 Comparison of SERF and SQUIDs for noise processing	149
7.3 MCG	150
7.4 Phantom measurements	154
7.5 Fetal MCG	156
8 Conclusions and future work	161
APPENDICES	
Appendix A: Dipole electric polarizability	172
Appendix B: Operating mode parameters	177
Appendix C: Cell characterizations	180
Appendix D: Materials	182
Appendix E: Electronics	184
Appendix F: Fetal MCG report	195
Appendix G: Magnetic field coils	199
Appendix H: Magnetometer parts list	206

DISCARD THIS PAGE

LIST OF TABLES

Table	Page
3.1 Design requirements	48
3.2 Pumping parameter space	64
4.1 Calibration frequencies	71
4.2 Noise types	79
5.1 Noise budget	84
7.1 Noise implications for signal processing	143
Appendix	
Table	
C.1 Nominal cell properties	180
D.1 Material properties	183
E.1 Heater controller parts list	189
E.2 Coil control box features	191
F.1 Fetal MCG report average measurements	195
G.1 Coil calibration: transversely pumped magnetometer	205
H.1 Magnetometer parts list	206
H.1 Magnetometer parts list	207

DISCARD THIS PAGE

LIST OF FIGURES

Figure	Page
2.1 M_x magnetometer setup	9
2.2 Spin-exchange collision	10
2.3 The SERF regime	12
2.4 Slowing down factor and the spin-temperature distribution	13
2.5 Relaxation rates from spin-exchange	14
2.6 Magnetometer pump/probe geometry	16
2.7 Optical pumping	17
2.8 Spin relaxation due to collisions with atoms and walls	22
2.9 Sensitivity and polarization vs. pumping rate	24
2.10 Magnetometer vector sensitivity-adjusting $\tilde{\Omega}_\perp$ and R	26
2.11 Magnetometer vector sensitivity- $\tilde{R}=1$	27
2.12 Magnetometer swept field response	28
2.13 Magnetometer frequency response	31
2.14 Vector response to AC fields	32
2.15 Frequency response with actual relaxation rates	34

Figure	Page
2.16 Probe Faraday rotation	36
2.17 Diffusion length	42
2.18 Spatial dependence of R and P_z	43
2.19 Pump laser light shift	45
3.1 Single magnetometer	49
3.2 Windows and mirrors	52
3.3 Optical elements and the optics tube	54
3.4 Electrical heaters	56
3.5 H-Bridge schematic	57
3.6 Data acquisition flow chart	61
3.7 Swept field fit and ambient MSR gradients	63
3.8 Magnetometer array schematic and photograph	65
4.1 Amplitude and phase calibration	73
4.2 Noise measurement	76
4.3 Chirp signal calibration	78
4.4 Effect of probe intensity noise	80
4.5 Artist's rendition of magnetometer position for a fMCG measurement	82
5.1 Field from distance objects outside MSR	87
5.2 Reference values for the photon shot noise given the magnetometer performance	91
5.3 Spatially dependent modeling of the magnetometer, without any bias fields	95
5.4 Spatially dependent magnetometer performance, including Ω_{LS}	96
5.5 Spatially dependent magnetometer performance, including Ω_{LS} and an offset field Ω_0	98

Appendix Figure	Page
5.6 Fiber polarization noise	101
5.7 Probe frequency and intensity noise	103
5.8 δR vs. frequency fluctuations and δP_x for δR	105
6.1 Diffusion pumping radial P_z and radial sensitivity	110
6.2 Diffusion pumping model through the cell	112
6.3 Diffusion pumping noise measurement	114
6.4 Feedback loop block diagram	116
6.5 Feedback coil for feedback gradiometer	118
6.6 Feedback noise measurement	119
6.7 Feedback performance for real time noise suppression of fMCG data	121
6.8 Bessel functions in Fourier expansion of z-mode sensitivity	126
6.9 z-mode noise performance	128
6.10 Pump-probe-large DC field geometry for the transversely pumped SERF magnetometer	131
6.11 The DC term of the response for P_x and P_y for the transversely pumped SERF magnetometer	132
6.12 Optimum pulse shape and a cartoon of the polarization dynamics for the transversely pumped SERF magnetometer	133
6.13 Simulation for non-ideal pulse area	135
6.14 Initial transversely pumped resonance measurements	137
7.1 Simulated MCG and fMCG signal and bandwidth	140
7.2 STFT of the simulated MCG signal	141
7.3 Nonlinear signal processing	148

Figure	Page
7.4 Adult MCG measurements	152
7.5 Removal of periodic interference from an MCG signal	153
7.6 Phantom MCG	155
7.7 Raw fMCG measurement	157
7.8 Calibrated fMCG measurement	158
7.9 Fetal MCG analyzed using PCA	160
Appendix	
Figure	
B.1 DC-mode optics	178
B.2 Diffusion pumped optics	179
C.1 He diffusion	181
C.2 Uncalibrated B_y sweep showing typical channel-to-channel variation	181
E.1 Heater H-bridge controller	188
E.2 Nominal thermistor calibration for magnetometer temperature measurement	190
E.3 Coil control box	192
E.4 Noise measurements for coil driving circuit settings	194
F.1 Average SERF fMCG measurement with relevant feature intervals	196
F.2 Average SERF fMCG measurement from another time segment	197
F.3 Average SQUID fMCG measurement	198
G.1 Calibration for the individual coils wrapped around each magnetometer and field uniformity simulations	200
G.2 Field uniformity for the large coil used in feedback mode	202

Figure	Page
G.3 Transversely pumped magnetometer coil calibration and simulation	204

ABSTRACT

Biomagnetic signals can provide important information about electrical processes in the human body. Because of the small signal sizes, magnetic detection is generally used where other detection methods are incomplete or insufficiently sensitive. One important example is fetal magnetocardiography (fMCG), where the detection of magnetic signals is currently the only available technique for certain clinical applications, such as the detection of cardiac arrhythmia. Until now, magnetometers based on superconducting quantum interference devices (SQUIDs), which can operate at sensitivities down to $1 \text{ fT}/\sqrt{\text{Hz}}$ have been the only option. The low T_c superconductors and associated cryogenics required for the most sensitive devices has led to interest in alternative technologies. In the last decade, atomic magnetometers operating in the spin-exchange relaxation-free (SERF) regime have demonstrated a higher sensitivity than SQUIDs while operating near room temperature. Though large SERF magnetometer arrays have not yet been built, smaller arrays should be sufficient for applications such as fMCG. In this thesis, we present the design and characterization of a portable four-channel SERF atomic magnetometer array with a $5\text{--}10 \text{ fT}/\sqrt{\text{Hz}}$ single channel baseline sensitivity. The magnetometer array has several design features intended to maximize its suitability for biomagnetic measurement, specifically fMCG, such as a compact modular design and large, flexible channel spacing from 5–15 cm. The modular design allows for easily adding units to the array and the independent positioning and orientation of each magnetometer, in principle allowing for non-planar array geometries. Using this array in a magnetically

shielded room, we acquire adult magnetocardiograms and, for the first time with a SERF magnetometer, fMCG. We also investigate the use of different operational modes of the magnetometer to extend its functionality, specifically modulation methods for additional directional sensitivity, the possibility of operation in large DC fields, feedback methods to help make a high suppression ratio hardware gradiometer, and using diffusion to perform the magnetometer measurement with atoms outside the influence and noise contribution of pumping lasers.

Chapter 1

Introduction

Human biomagnetism has been an important area of fundamental research and medicine since the first low noise measurements using superconducting quantum interference devices (SQUIDs) [Cohen et al., 1970]. Since that time, impressive improvements have been made in the design and engineering aspects of SQUID sensors for biomagnetic studies, and integrated commercial systems are now available with hundreds of individual SQUID channels designed to cover an entire human head [Wiksw, 1995]. These systems, operating with sensitivities near $1 \text{ fT}/\sqrt{\text{Hz}}$, have allowed an increasingly diverse set of novel measurements to be performed.

Magnetic signals can provide access to unique or complimentary information concerning underlying phenomena in the human body. For example, the distribution of electrical potentials at the surface of the skin is distorted by tissue and bone in the intervening conduction path [Wakai et al., 2000], which makes accurate reconstruction of the original source distribution difficult and can inhibit the electrical signals altogether. Magnetic signals from the same sources are unaffected by tissue and bone, simplifying the source localization [Wiksw, 1995]. For example, magnetoencephalography (MEG) can be used in pre-surgical studies or to image cognitive function, where knowledge of the position of the neurologic currents is important [Hämäläinen et al., 1993, Wiksw, 1995]. In another example, fetal magnetocardiography (fMCG) is currently the only

sufficiently sensitive technique for certain clinical applications, such as the detection of cardiac arrhythmia.

Until recently, magnetometers based on superconducting quantum interference devices (SQUIDs) provided the only option for biomagnetism applications demanding the highest possible sensitivity, usually operated in arrays of matched gradiometers with 30 or more channels. SQUIDs have achieved a noise limit of around $1 \text{ fT}/\sqrt{\text{Hz}}$ [Robbes, 2006], but they are expensive ($\sim \$10 \text{ k/channel}$) and require liquid ^4He for the low T_c systems needed for the demanding signal-to-noise ratio (SNR) in sensitive biomagnetic applications, like fMCG [Li et al., 2004].

Fetal MCG can be used to detect and diagnose dangerous arrhythmia *in utero*, such as supraventricular tachycardia or *torsades de pointes* [Cuneo et al., 2003, Wakai et al., 2003]. In this application, precise imaging of the fetal heart is not necessary, but electrical signals are attenuated by an insulating layer covering the fetus, so they cannot provide sufficient resolution for diagnosis [Wakai et al., 2000]. As a non-imaging application, fMCG demands fewer magnetometers, just enough for signal processing enhancement through spatial filtering.

The demands of fMCG sets several restrictions on magnetic sensors. First, the the largest feature in fMCG is the QRS peak, which has a magnitude of $\sim 1 \text{ pT}$ and a bandwidth of $\sim 100 \text{ Hz}$. Therefore, the fundamental noise of the detector must be $< 10 \text{ fT}/\sqrt{\text{Hz}}$ in a 100 Hz bandwidth starting near DC for a 10:1 SNR. Second, the background magnetic noise at the detector must be below this same limit. Passive magnetically shielded rooms (MSR) using hi-permeability materials like mu-metal are typically used, but practical limits are placed on the achievable attenuation of external signals due to the high cost of MSR materials. Cheaper eddy current shields are suitable at higher frequencies, but attenuated external fields in the $0\text{--}100 \text{ Hz}$ bandwidth are often well above the MSR noise limit in the frequency band of interest [Platzek et al., 1999]. Another way to increase the SNR is to detect the gradient of the magnetic field, rather than the magnetic field itself. This is the typical detection method for SQUID sensors, where detector spacing of a few cm is chosen to maximize the SNR from the fetus compared to gradients from signals outside the MSR or the pregnant adult's much larger heart signal [Wolters et al., 2003].

1.1 Atomic magnetometer renaissance

Atomic magnetometers have recently shown promise for use in biomagnetism. Atomic vapor magnetometers operating in the spin exchange relaxation free (SERF) regime [Allred et al., 2002] have recently surpassed the sensitivity of SQUID systems, achieving $160 \text{ aT Hz}^{-1/2}$ sensitivities [Dang et al., 2010]. Additionally, the application of microfabrication techniques to the manufacture of mm-scale alkali-metal vapor cells and integrated fiber-coupled optics [Shah et al., 2007] allows the possibility of large arrays of SERF magnetometers, similar to current commercial SQUID systems. Besides offering increased sensitivity, atomic magnetometers are operated at temperatures between 25–180 C [Budker and Romalis, 2007], replacing expensive cryogenics and maintenance of SQUID systems with simple resistive electrical heating and passive thermal insulation.

Proof-of-principle biomagnetic measurements have been made previously. Adult MEG has been measured using a similar sized fiber coupled atomic magnetometer operating as in this work, in a different detection mode [Johnson et al., 2010]. Single channel sensitivity was comparable to this work, but quadrant photodiode detection was used to construct gradiometer signals, rather than the use of multiple magnetometers. A similar technique using a photodiode array was used previously [Xia et al., 2006], but with a large non-portable setup. While using a single probe beam to make measurements in multiple parts of the cell is appealing for technical reasons, the effective separation between the atoms participating in the measurement is small compared the the signal source depth of an MCG measurement. The individual sensors will measure approximately the same signal from sources as deep as fMCG, and fMCG signals would be suppressed with the background noise by these implementations.

Adult MCG studies have also been performed. Bison et al. [2009] used an array of 25 room temperature Cs (non-SERF mode) magnetometers as a 19-channel set of 2nd order gradiometers to map adult MCG in an eddy-current shield. They were able to suppress the noise by a factor of 1000 using this technique, but were still limited to $300 \text{ fT}/\sqrt{\text{Hz}}$. Knappe et al. [2010] used a single channel microfabricated mm-scale alkali-metal vapor cell to measure adult MCG in an MSR. Their

signals compare well with SQUIDs simultaneously measuring the MCG, largely because they were able to get the detector much closer to the subject's chest. The measurements were performed with a sensitivity $100\text{-}200\text{ fT}/\sqrt{\text{Hz}}$ but in a much quieter shielded room [Bork et al., 2000]. Results from a single magnetometer were presented, as opposed to multiple channels, as we use here.

To summarize, these previous studies used either a single magnetometer, gradiometers with baseline $\sim 1\text{ cm}$, or magnetometers without high enough sensitivity for fMCG. In contrast, we have developed a four-channel portable atomic magnetometer array suitable for the demands of fMCG. The channel spacing in this work is flexible and can be adjusted between $5\text{-}15\text{ cm}$. Each magnetometer in the array features a $5\text{-}10\text{ fT}/\sqrt{\text{Hz}}$ noise floor from $10\text{-}100\text{ Hz}$ and has adjustable channel spacing and orientation. All channels are self-contained, including local tri-axial nulling coils, in principle allowing the channels to be placed in an arbitrarily oriented non-planar geometry. The SERF channel spacing is significantly larger than previous biomagnetic studies, suitable for optimizing background rejection.

Using this magnetometer in a magnetically shielded room (MSR), we have demonstrated the use of the array to successfully detect MCG from 17 adult subjects. Additionally, we have detected the first fMCG signal using an atomic magnetometer (to the best of our knowledge), a proof-of-principle experiment for an application well suited to the budding field of SERF biomagnetometers, where high sensitivity but modest channel counts are required.

In addition to successfully measuring fMCG signals, we have also worked on extension of the methods of SERF magnetometry to address shortcomings in the traditional method of operation presented in Allred et al. [2002]. For example, SQUIDs can be made as hardware gradiometers with excellent uniform background rejection. The most commonly used technique takes advantage of the ability to fabricate pickup coils with very uniform characteristics for two spatially separated turns. An equivalent technique for SERFs is important, but in many ways is a more difficult challenge. We demonstrate the use of feedback to suppress these background signals despite significant nonuniformities in the individual magnetometer response.

We increase the channel count using a previously developed modulation technique [Li et al., 2006] to simultaneously detect two magnetic field components from a single magnetometer without loss of sensitivity, demonstrating the technique is suitable for use without degradation in a closely packed array. We also make use of our relatively low buffer gas pressure cells to set up a situation in which the atoms that participate in the magnetometer measurement do so in a spatial region of the cell devoid of pump light, which has some practical advantages.

Finally, we describe and show the initial measurements of a method to spin-polarize alkali atoms transverse to a strong magnetic field through a transverse spin resonance. The resonance feature can be used to detect magnetic fields in the same way as the traditional SERF, and can be made to be spin-exchange relaxation free despite the presence of the large DC magnetic field in which it operates. In this transverse pumped magnetometer, the signal has the additional benefit of being a Larmor frequency, rather than a quasi-DC signal requiring calibration (as a traditional SERF does). This modulation method could allow SERF magnetometers to be operated in earth-sized background fields.

The structure of the thesis is as follows: Chapter 2 will outline the difference between traditional atomic magnetometers and SERF magnetometers and outline the wide parameter space in which the usual method of using a SERF can operate. Chapter 3 describes the details of the four magnetometer array built and tested as the bulk of the work for this thesis. Chapter 4 will outline the data collection procedure, including the procedures used to cancel background magnetic fields and calibrate the magnetometers. A noise budget is presented and discussed in detail in chapter 5. In chapter 6, we discuss four extensions to the traditional DC-mode SERF magnetometer pioneered at Princeton by Romalis' group, one of which may allow extension of SERF magnetometry to high DC magnetic fields. Specific requirements of biomagnetic signals, in particular fMCG, are dealt with in chapter 7, as well as the basic signal processing tools used to help determine magnetometer performance with real signals. At the end of chapter 7, we present the first SERF detected fMCG signal. We conclude with directions for future development.

Chapter 2

Theory of SERF magnetometry

This chapter provides a brief overview of how an atomic gas can be used as a magnetic sensing device. We provide a general description of a traditional atomic magnetometer and discuss its limitations, followed by an introduction to the SERF regime that allowed these limitations to be surpassed and led to the most sensitive magnetic sensing device currently developed [Dang et al., 2010]. We will also provide an outline of the SERF magnetometer and an overview of the theoretical description of its operation in its most sensitive and simplest mode, which we refer to as “DC-mode.” This overview is meant to aid the understanding of the design, operation, and characterization of the magnetometers developed as part of this thesis, and to lay the theoretical foundation for an analysis of the fine points in later chapters. We sketch or expand upon the derivations and useful results presented elsewhere, for example in articles developing specific implementations of SERFs [Allred et al., 2002, Kominis et al., 2003, Ledbetter et al., 2008], reviews on optical atomic magnetometers [Budker and Romalis, 2007], or several thorough thesis on the subject, in particular [Kornack, 2005, Li, 2006, Seltzer, 2008].

2.1 Historical optical magnetometry

Optical atomic magnetometers were first developed in the late 1950's in the Bell-Bloom or M_x style, which built an oscillator from an optically pumped Rb gas [Bell and Bloom, 1957, Dehmelt, 1957]. Further development led to the Hanle type magnetometer [Cohen-Tannoudji et al., 1969], which utilized a directly pumped ^3He gas intermixed with Rb gas used as a probe for the ^3He spins. Other types have been developed, such as those based on coherent population trapping [Scully and Fleischhauer, 1992] and nonlinear magneto-optical Faraday rotation [Budker et al., 2000]. These techniques fall under the category of optically pumped magnetometers, and have achieved sensitivities below $100 \text{ fT}/\sqrt{\text{Hz}}$ [Alexandrov and Bonch-Bruевич, 1992].

We focus on the Bell-Bloom type as a simple example of an optically pumped atomic magnetometer. We will discuss the relaxation mechanisms that limit the sensitivity of the Bell-Bloom magnetometer, as well as how the SERF magnetometer overcomes those restrictions.

2.1.1 Traditional atomic magnetometry

Any atom with a nonzero magnetic moment can be made to be a magnetometer. A magnetic field applied perpendicular to the magnetic moment will cause a torque on the atom, resulting in the Larmor precession of the atom about that magnetic field at angular frequency $\Omega = \gamma B/q$, where γ is the gyromagnetic ratio and B is the magnitude of the magnetic field. For atoms, $\gamma = g\mu_B/\hbar$, where g is the Landé g -factor for the level participating in the detection. The factor q is a quantity which accounts for the hyperfine interaction and the fact that at low magnetic fields, the nuclear spin acts to increase the inertia of the total atomic angular momentum. For a free atom, q is constant dependent upon the nuclear spin. Since γ is determined by fundamental constants and quantum numbers, a measurement of the Larmor frequency of a precessing atom is a direct measure of the magnetic field.

The trick then becomes increasing the sensitivity of the measurement. As a first approximation, the observation of precession of a collection of nV atoms with coherence time T_2 can be used to

measure a magnetic field with precision

$$\delta B \simeq \frac{1}{\gamma \sqrt{nV T_2 t}}, \quad (2.1)$$

where t is the measurement time and V is the measurement volume [Budker and Romalis, 2007, Ledbetter et al., 2008]. When the precession is continuously observed, (2.1) is optimized for the largest number of atoms precessing with the same phase for as long as possible. These requirements can contradict one another, for example when $T_2 \propto n^{-1}$. Indeed, changing the relationship between the spin coherence time and the atomic number density is the significance of the SERF regime, and the enabling discovery for ultra-high sensitivity atomic magnetometers [Allred et al., 2002].

Fundamentally, an atomic magnetometer requires alignment of an atomic vapor and subsequent detection of changes in atomic alignment. For alkali vapor magnetometers, it was realized that this could be accomplished through optical pumping and subsequent detection of the atomic precession through the modulation of the absorbed pump light [Bell and Bloom, 1957, Bloom, 1962, Dehmelt, 1957], as in figure 2.1. Modern atomic magnetometers designed to work in a broad range of magnetic background environments still make use of techniques developed by Bell and Bloom (for example, [Aleksandrov et al., 1995, Groeger et al., 2006, Schwindt et al., 2007]) with technical refinements to improve the magnetometer performance. In research conditions, sensitivities of a few $\text{fT}/\sqrt{\text{Hz}}$ can be achieved [Aleksandrov et al., 1995], though these increases are obtained by increasing the detector volume or operating at higher frequencies.

2.1.2 Spin exchange collisions and the SERF regime

For a fixed volume, the sensitivity of these traditional devices is often limited by spin-exchange (SE) collisions between alkali-atoms [Allred et al., 2002], such that $T_2 \sim T_{\text{se}} = (n\bar{v}\sigma_{\text{se}})^{-1}$, where \bar{v} is the thermal atomic velocity and σ_{se} is alkali-alkali SE cross section for the chosen atomic species, ($1.9 \times 10^{-14} \text{ cm}^{-2}$ for ^{87}Rb - ^{87}Rb , [Gibbs and Hull, 1967]). When this is the case, it is only fruitful to increase n as long as the signal-to-noise ratio (SNR) is not dominated by SE collisional decoherence.

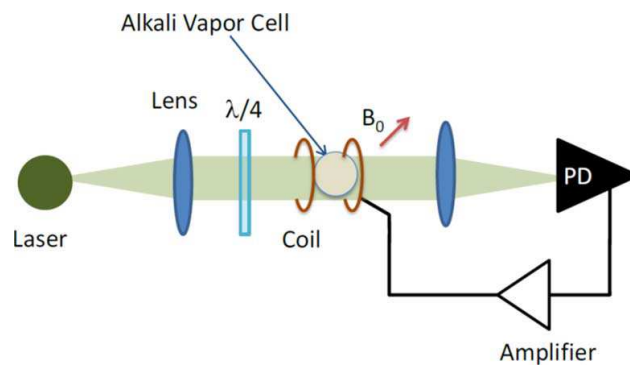


Figure 2.1: Illustration of operation of a feedback locked M_x mode magnetometer (reprinted from [Kitching et al., 2011] with the author's permission). A circularly polarized optical pumping beam creates an atomic polarization along the direction of its angular momentum. Without feedback, an oscillating field generated by the coils would drive the atoms to oscillate around B_0 when the driving field was resonant with the Larmor frequency of B_0 . The precession of atomic spins modifies the susceptibility of the vapor at the precession frequency, detected here by measuring the absorption of the pumping light. The system becomes self-oscillatory at Ω_0 when feedback is applied.

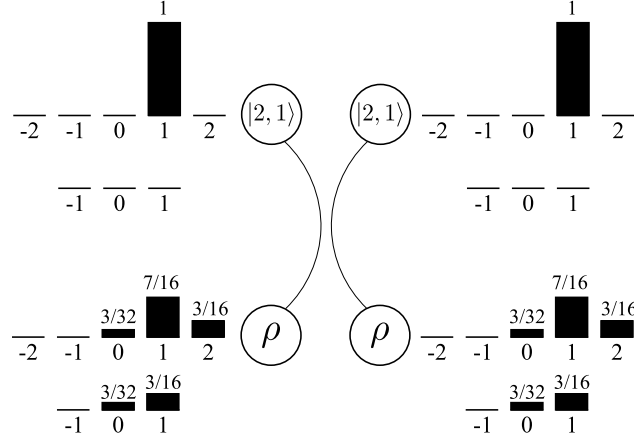


Figure 2.2: A Rb-Rb SE collision (adapted from [Walker and Happer, 1997]). These collisions preserve the angular momentum projection $m_{f_1} + m_{f_2}$, but redistribute population among the hyperfine sublevels consistent with angular momentum conservation. Between SE collisions, atoms in different hyperfine manifolds precess in opposite directions at nearly the same frequency. If they are allowed to precess for too long, this leads to rapid decoherence as a result of the SE level redistribution.

Figure 2.2 shows a diagram of an alkali-alkali SE collision. These collisions couple the electron spin of each colliding atom, leaving the nuclear spin of each atom, as well as the total angular momentum, conserved during the collision time. The result is distribution of angular momentum in a set of $|F, m_f\rangle$ states to a statistical distribution of final states consistent with the preservation of the total angular momentum projection $m_{f_1} + m_{f_2}$. Ignoring small corrections, the hyperfine Landé g -factor for the ground state F-levels is opposite in alkali-metal atoms,

$$\begin{aligned}
 g_F &\simeq g_s \frac{F(F+1) - I(I+1) + J(J+1)}{2F(F+1)} \\
 &= 1/2 && ({}^{87}\text{Rb } 5^2S_{1/2}, F = 2) \\
 &= -1/2 && ({}^{87}\text{Rb } 5^2S_{1/2}, F = 1)
 \end{aligned}$$

So while the total angular momentum projection is conserved during a SE collisions, the redistribution into different F-levels results in precession in opposite directions after such a collisions. An atom which begins with some orientation, undergoes a SE collision, precession for a significant portion of a Larmor period, and undergoes SE again does not end up with its orientation preserved. In other words, SE collisions lead to decoherence if the precession angle is on the order of a single rotation or larger ($\Omega T_{se} \geq 2\pi$).

Spin exchange relaxation constitutes a fundamental limit on the coherence of an atomic gas [Bouchiat and Brossel, 1966], and their use as magnetometers [Budker et al., 1998] for many cases. However, it has been understood for some time that magnetic resonance lines were narrowed when the SE rate was sufficiently high compared to the magnetic field induced Larmor frequency ($\Omega T_{\text{se}} \ll 2\pi$) [Happer and Tam, 1977, Happer and Tang, 1973]. Figure 2.3 shows the three relevant SE regimes, where traditional atomic magnetometers operate in the precession regime figure 2.3(a) and the SERF regime is shown in figure 2.3(c).

Rapid SE collisions lead to the spin-temperature distribution [Anderson et al., 1960, Baranga et al., 1998, Savukov and Romalis, 2005], a maximum entropy distribution consistent with angular momentum and energy conservation. In spin-temperature, the density matrix can be simply described in terms of a single spin temperature parameter β as $\rho \propto e^{-\beta F_z}$, where

$$\beta = \ln \left| \frac{1+P}{1-P} \right| \quad (2.2)$$

and $\mathbf{P} = \langle \mathbf{S} \rangle / S$ is the electron spin polarization. This distribution relates the average total angular momentum to the average electron angular momentum by the so-called slowing down factor $q(P)$ [Baranga et al., 1998, Savukov and Romalis, 2005],

$$\langle F_z \rangle = q(I, P) \langle S_z \rangle \quad (2.3)$$

$$q(3/2, P) = \frac{6 + 2P^2}{1 + P^2} \quad (2.4)$$

For $I = 3/2$, the slowing down factor varies smoothly from 6–4 (figure 2.4a). Figure 2.4b demonstrates how the spin-temperature distribution changes for varying polarization and the slowing down factor for each polarization.

Rapid SE leads to a new SE relaxation regime in which the relaxation rate decreases quadratically with field [Allred et al., 2002, Happer and Tam, 1977],

$$\Gamma_{\text{SE}} = \Omega^2 T_{\text{SE}} \left(\frac{1}{2} - \frac{(2I+1)^2}{2q^2} \right). \quad (2.5)$$

For ^{87}Rb at 150 C, the SE rate is $1/T_{\text{SE}} \approx 70 \times 10^3 \text{ s}^{-1}$. Using this temperature and a vapor pressure model of ^{87}Rb [Alcock et al., 1984], figure 2.5 shows the SE relaxation rate as a function of magnetic fields perpendicular to the pump direction.

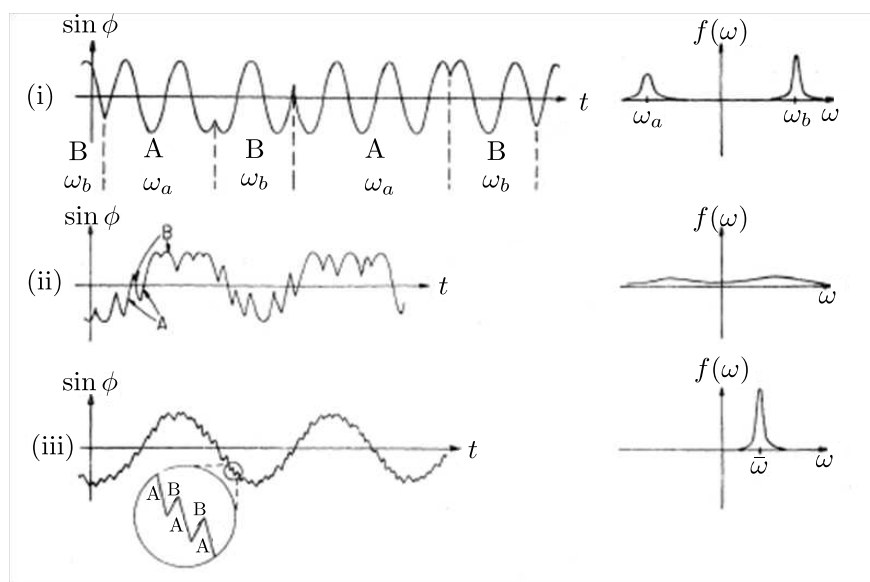


Figure 2.3: Spin exchange regimes in increasing ratios of T_{SE}/Ω , reprinted from [Happer and Tam, 1977] with author permission. Traditional atomic magnetometers operated at relatively low SE rates, as in (i). Increasing T_{SE}/Ω initially leads to faster decoherence (ii), but then narrows again (iii) when T_{SE} becomes the dominant rate and enforces that individual atoms, on average, precess as the entire density matrix would. Each atom rapidly changes hyperfine levels due to rapid SE, but the net result is statistically preferential precession at a lower frequency, for each atom and for the density matrix as a whole.

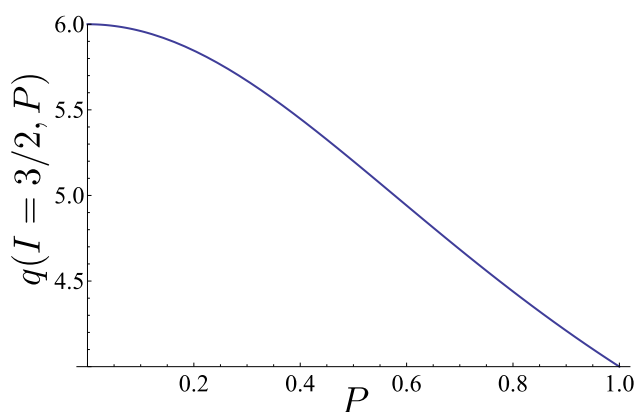
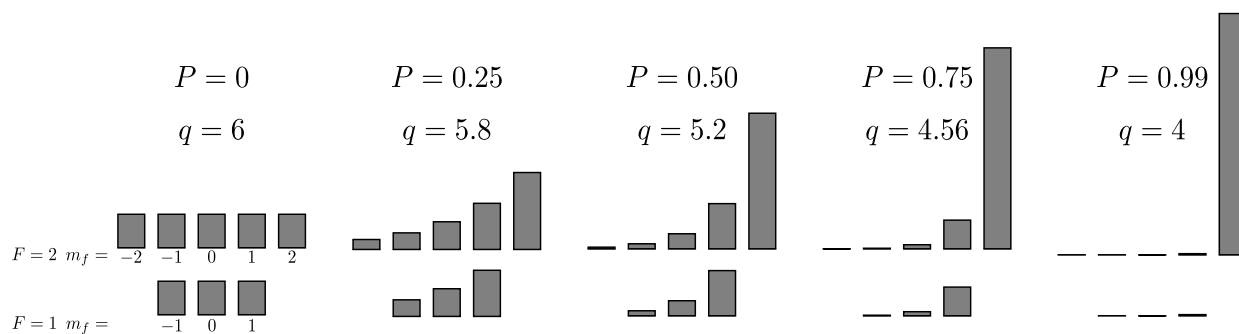
(a) Slowing down factor for $I = 3/2$ (b) Spin-temperature distribution at various P

Figure 2.4: (a) Slowing down factor $q(P)$ for $I = 3/2$ atoms. (b) Spin temperature distributions for a variety of average polarization values. Even for zero polarization, most of the atoms ($5/8$) are in the $F = 2$ manifold and rapid SE ensures the atoms maintain a weighted precession of the average spin.

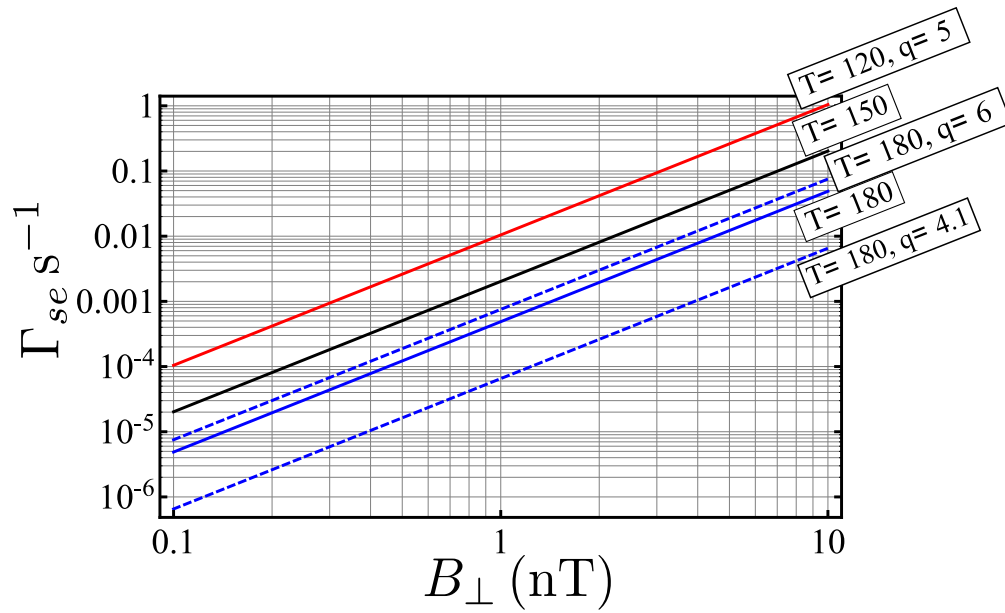


Figure 2.5: Γ_{SE} according to (2.5) with a range of model temperatures (120, 150, 180 C) at slowing down factor $q = 5$ for ^{87}Rb as well as comparisons at 180 C with $q = 4.1$ and $q = 6$.

2.2 SERF magnetometer

To be concrete, we will discuss the system of interest in this work, an isotopically pure ^{87}Rb atomic vapor in a buffer gas of combined He and N_2 . This chapter deals with the primary detection scheme used in this work, what we call DC-mode operation, first presented by Allred et al. [2002]. The general description of a magnetometer from the previous section still applies, but the atoms will now be interrogated by a linearly polarized probe perpendicular to the pump beam, as in figure 2.6 (this geometry and coordinate system will be used in the future equations of this work, unless otherwise specified).

We will describe the physics of this system in the SERF limit, where rapid SE causes the density matrix to assume a spin-temperature distribution. The ground state can be described by Bloch equations with only a few important terms [Ledbetter et al., 2008]: optical pumping, spin destruction, and Larmor precession. The spin destruction term will include any ground state spin destruction mechanism, in particular coupling spin and angular momentum during binary collisions, photon absorption by the probe beam, and diffusion to the cell walls.

Optical pumping creates a nonzero average electron spin along the propagation direction of the pumping laser. Orthogonal magnetic fields cause the population spin to precess at the slowed down Larmor frequency. Spin-relaxation collisions, the absorption of photons, and wall collisions interrupt the precession. The balance between optical pumping, spin relaxation, and Larmor precession determines the dynamics of the atomic polarization and the performance of the magnetometer.

2.2.1 Optical pumping

Optical pumping can be quite complicated in the full hyperfine picture [Happer and Wijngaarden, 1987]. We will use the simplifying assumption that the hyperfine levels are not well resolved due to pressure broadening. The 6.8 GHz ground state splitting for ^{87}Rb requires about half an amagat or more of buffer gas in order to reach this regime at $\sim 18 \text{ GHz/amg}$ [Romalis et al., 1997].

Figure 2.7 shows the a simplified energy level diagram for ^{87}Rb . Circularly polarized optical pumping light resonant with the D1 transition selectively pumps atoms out of a single hyperfine

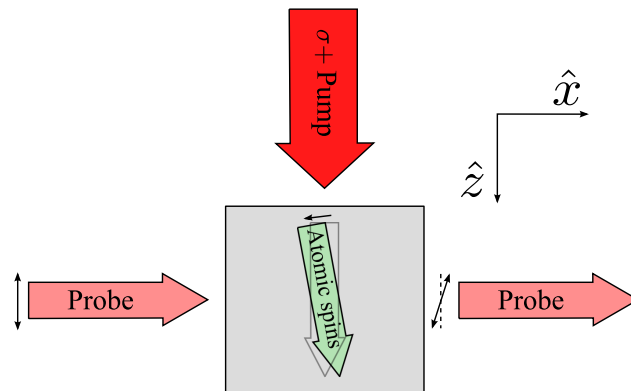


Figure 2.6: General magnetometer model with orthogonal pump and probe beams. The circularly polarized pump creates an atomic orientation, while the linearly polarized probe is sensitive to changes in that orientation. The same coordinate system is used throughout this work.

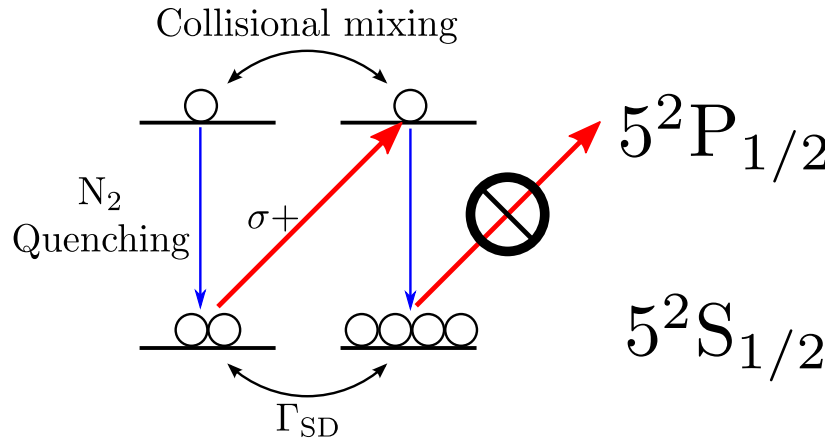


Figure 2.7: Simplified energy level diagram of ^{87}Rb . D1-line optical pumping works by utilizing angular momentum selection rules to selectively excite atoms from a single sublevel. In the excited state the atoms are quenched by collisions with N_2 , which randomize the spin and populate both ground states equally. Thus, for each pump photon absorbed, $1/2$ unit of angular momentum is deposited into the vapor.

level, due to angular momentum selection rules forbidding excitation from the $m_s = 1/2$ ground state by $\sigma+$ polarized light. Once excited, the atoms undergo spin-randomizing collisions with the buffer gas before they undergo non-radiative decay through collisions with N_2 . The process deposits $1/2$ unit of angular momentum on average from the absorption of a photon. Though the electron spin is randomized in the excited state, the nuclear spin is essentially conserved, hence the process tends to polarize the nuclear spin as well, and creates a spin temperature distribution.

A comprehensive understanding of angular momentum optical pumping in alkali buffer gas mixtures is still an active area of research [Happer et al., 2010, Lancor and Walker, 2010], but for the relatively low buffer gas pressures and polarizations in these cells, the above description is sufficiently accurate. Under these assumptions, optical pumping contributes to the evolution of the total angular momentum

$$\left. \frac{d\langle \mathbf{F} \rangle}{dt} \right|_{\text{OP}} = \frac{R}{2} (1 - \mathbf{s} \cdot \mathbf{P}), \quad (2.6)$$

where s is the photon spin and R is the optical pumping rate (the rate at which unpolarized atoms absorb linearly polarized light). R is the convolution of the pumping photon flux and the unpolarized atomic cross-section σ_0 ,

$$R = \int_{-\infty}^{\infty} \Phi(\nu' - \nu) \sigma_0(\nu' - \nu_0) d\nu' \quad (2.7)$$

$$R \approx \Phi_0 \sigma_0(\Delta\nu) \quad (2.8)$$

$$\Phi_0 = \frac{\mathcal{I}}{h\nu} \quad (2.9)$$

$$\sigma_0 = r_e f c \mathcal{L}(\Delta\nu) \quad (2.10)$$

$$\mathcal{L}(\Delta\nu) = \frac{\Delta\Gamma/2}{(\Delta\nu)^2 + (\Delta\Gamma/2)^2}, \quad (2.11)$$

where ν and ν_0 are the laser center frequencies and atomic absorption center frequencies, respectively, r_e is the classical electron radius, f is the oscillator strength, the laser intensity is \mathcal{I} , and $\Delta\nu = \nu - \nu_0$ is the laser detuning from the atomic transition. The approximation (2.8) holds when the linewidth of the atomic transition is much greater than the linewidth of the laser, and $\Phi(\nu' - \nu) \approx \Phi_0 \delta(\nu' - \nu)$. The lasers in this work are all single mode with linewidth < 10 MHz, and we use this approximation throughout the rest of this work.

2.2.2 Spin-relaxation from binary collisions and probe absorption

Under the assumptions for this simplified model, Rb-Rb and Rb-buffer gas binary spin-destruction collisions are a fundamental limit on the spin-coherence time of $\langle F \rangle$ [Baranga et al., 1998, Erickson et al., 2000, Kadlecik et al., 2001]. The spin-destruction rates for Rb-Rb and Rb-N₂ are taken from [Chen et al., 2007], while the rates for Rb-He are taken from [Allred et al., 2002]. They are all lumped into a single ground-state spin-destruction rate, Γ_{sd} :

$$\Gamma_{\text{Rb-Rb}} = \left(4.2 \times 10^{-13} \frac{\text{cm}^3}{\text{s}} \right) [\text{Rb}] \quad (2.12)$$

$$\Gamma_{\text{Rb-N}_2} = \left(1.3 \times 10^{-25} \frac{\text{cm}^3}{\text{s K}^3} \right) T^3 [\text{N}_2] \quad (2.13)$$

$$\Gamma_{\text{Rb-}^4\text{He}} = (9 \times 10^{-24} \text{ cm}^2) \bar{v} [^4\text{He}] \quad (2.14)$$

$$\Gamma_{sd} = \Gamma_{\text{Rb-Rb}} + \Gamma_{\text{Rb-N}_2} + \Gamma_{\text{Rb-}^4\text{He}}, \quad (2.15)$$

where the quantities in brackets represent the number density, in cm^{-3} .

An additional spin-destruction mechanism is through the absorption of probe photons. Assuming a weak, linearly polarized probe beam with a propagation direction perpendicular to the pump (as in figure 2.6), we treat the absorption of probe photons as a simple relaxation mechanism. The photon absorption rate can be written similarly to R in the limit of a narrow probe laser linewidth compared to the atomic transition [Ledbetter et al., 2008],

$$\Gamma_{\text{pr}} = \Phi_{0,\text{pr}}\sigma_{0,\text{pr}}, \quad (2.16)$$

where the probe photon flux Φ_{pr} has the same definition as (2.9). The atomic ensemble evolves under the influence of spin-destruction collisions and probe absorption as

$$\left. \frac{d\langle \mathbf{F} \rangle}{dt} \right|_{\text{collisions}} = -(\Gamma_{\text{sd}} + \Gamma_{\text{pr}})\mathbf{S}. \quad (2.17)$$

2.2.3 Diffusion

Diffusion carries angular momentum from where it is deposited by the pump to other places in the cell. Its effect on the evolution of the angular momentum is [Ledbetter et al., 2008]

$$\left. \frac{d\langle \mathbf{F} \rangle}{dt} \right|_{\text{diff.}} = D\nabla^2 \langle \mathbf{F} \rangle, \quad (2.18)$$

where D is the diffusion coefficient for alkali atoms under the cell conditions (buffer gas makeup, pressure, temperature). Interactions between polarized alkali atoms and the glass container walls tend to completely depolarize the atoms (both the electronic and nuclear spin) [Wagshul and Chupp, 1994, Walker and Happer, 1997], enforcing the boundary condition $\langle \mathbf{F} \rangle|_{\text{walls}} = 0$.

There are various methods of dealing with the diffusion contribution to the evolution of the angular momentum Ledbetter et al. [2008], Wagshul and Chupp [1994], Walker and Happer [1997]. For our purposes, the diffusion term has two important effects. 1) Broadly, it increases the rate at which angular momentum is lost from the vapor, reducing T_2 and increasing the number of pump photons required to obtain a given steady state polarization. 2) Diffusion changes the detailed spatial dependence of the polarization.

In what immediately follows, we only account for the first effect, treating diffusion purely as an extra relaxation rate Γ_D , which will be important for the estimation of the overall performance of the magnetometer. Later, we will address the spatial dependence of all the terms involved in the angular momentum dynamics, and include a more nuanced treatment of diffusion.

We rewrite (2.18) to describe the angular momentum loss to the walls as [Ghosh, 2009, Wagshul and Chupp, 1994]

$$\frac{d\langle \mathbf{F} \rangle}{dt} = -\Gamma_D \langle \mathbf{F} \rangle \quad (2.19)$$

$$\Gamma_D \approx D_0(T) \left(\frac{p_0}{p} \right) \times 3 \left(\frac{\pi}{l} \right)^2, \quad (2.20)$$

with the standard pressure to gas pressure ratio p_0/p , and the term $3 \times (\pi/l)^2$ coming from a normal mode expansion of the solutions of (2.18), and using the velocity of the atoms in the fundamental diffusion mode. For Rb in nitrogen and helium buffer gases, the fundamental diffusion coefficients are [Happer et al., 2010, p 193]

$$\begin{aligned} D_0(\text{Rb} - \text{N}_2) &= 0.159 \frac{\text{cm}^2}{\text{s}} & T_0 &= 60 \text{ C} \\ D_0(\text{Rb} - {}^4\text{He}) &= 0.35 \frac{\text{cm}^2}{\text{s}} & T_0 &= 80 \text{ C} \\ D_0(T) &= D_0|_{T_0} \left(\frac{T}{T_0} \right)^{3/2}, \end{aligned}$$

where the final equation describes how to obtain the fundamental mode diffusion coefficient at a temperature T when it has been measured at a different temperature T_0 . The measurements above were both performed at $p_0 = 1$ atm. We estimate $\Gamma_D = 420$ 1/s for our experiment using our cell side length $l = 1$ cm, He pressure 0.029 amg, and N_2 pressure 0.066 amg, at $T = 145$ C. This result was obtained by finding

$$\Gamma_D = q(P) \left(\frac{1}{\Gamma_{D,\text{N}_2}} + \frac{1}{\Gamma_{D,\text{He}}} \right)^{-1}.$$

In the spin-temperature limit we can express electron spin depolarization at the walls as occurring at a rate enhanced by $q(P)$, since both the electron and nuclear polarization are lost at the wall.

Then the effective relaxation rate due to wall collisions is $\dot{P}\Big|_{\text{diff.}} = -\frac{q(P)}{T_D} P$.

The diffusion loss rate Γ_D depends on the buffer gas makeup, pressure, and temperature, but in a different way than the ground-state spin destruction rate due to binary collisions Γ_{sd} . Figure 2.8 shows plots of the total relaxation rate $\Gamma = \Gamma_D + \Gamma_{sd}$ as a function of initial helium pressure, nitrogen pressure, and cell operating temperature. As the figures make clear, diffusion is an important contribution to the angular momentum relaxation under our typical operating conditions, (50 Torr N₂, 22 Torr He, and 145 C cell temperature). Cells optimized for maximum sensitivity would utilize higher buffer gas pressure to limit diffusive losses.

2.2.4 Larmor precession

Between spin-destruction collisions with atoms, walls, or probe photons, the atomic ensemble precesses due to the influence of a small external magnetic field,

$$\left. \frac{d\langle \mathbf{F} \rangle}{dt} \right|_{\text{Larmor}} = \boldsymbol{\Omega} \times \langle \mathbf{S} \rangle. \quad (2.21)$$

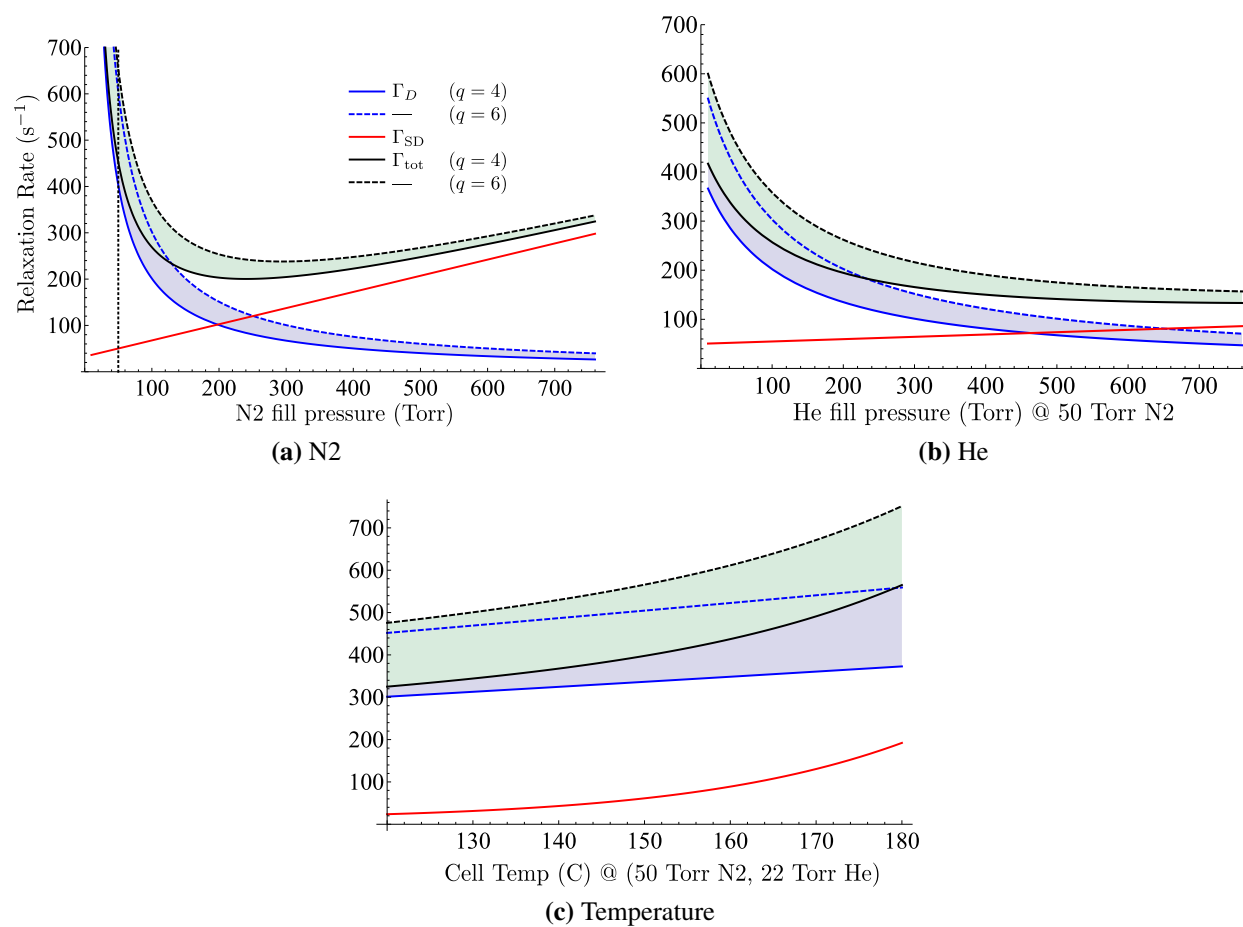


Figure 2.8: Total relaxation rate, including diffusion losses, for a square cell of 1 cm side length. Subfigures (a) and (b) show the total relaxation loss as a function of initial buffer gas pressures for N₂ and He, respectively, at 145 C cell temperature. Since the relaxation rates due to diffusion and binary collisional relaxation depend differently on pressure, a minimum exists for each buffer gas mixture. The vertical dotted line in (a) corresponds to the buffer gas pressure in most of the cells used for magnetometry in this work. Subfigure (c) shows the binary collisions depend more strongly on cell temperature.

2.2.5 Equation of motion and steady-state response

Under the influence of the processes listed above, and assuming optical pumping and SE collisions enforce a spin-temperature distribution, then the electron polarization is governed by the following differential equation [Allred et al., 2002, Ledbetter et al., 2008],

$$q(P) \frac{d\mathbf{P}}{dt} = q(P) D \nabla^2 \mathbf{P} + \boldsymbol{\Omega} \times \mathbf{P} + R \mathbf{s} - \Gamma' \mathbf{P}, \quad (2.22)$$

where we have assumed that the slowing down factor $q(P)$ is constant in time. If we fold in the effect of diffusion using an effective total relaxation rate $\Gamma = \Gamma_D + \Gamma_{sd} + \Gamma_{pr}$ (section 2.2.3), the steady state solution to (2.22), assuming perfect pump circular polarization $\mathbf{s} = \hat{z}$, is

$$\mathbf{P} = \frac{R}{\Gamma' (\Gamma'^2 + \Omega^2)} \begin{pmatrix} \Gamma' \Omega_y + \Omega_x \Omega_z \\ -\Gamma' \Omega_x + \Omega_y \Omega_z \\ \Gamma'^2 + \Omega_z^2 \end{pmatrix}, \quad (2.23)$$

where $\Gamma' = R + \Gamma$. Equation (2.23) can also be expressed in terms of P_z ,

$$P_x = P_z \left(\frac{\Gamma' \Omega_y + \Omega_x \Omega_z}{\Gamma'^2 + \Omega_z^2} \right) \approx P_z \frac{\Omega_y}{\Gamma'} \quad (2.24)$$

$$P_z = \frac{R}{\Gamma'} \left(\frac{\Gamma'^2 + \Omega_z^2}{\Gamma'^2 + \Omega^2} \right) \approx \frac{R}{\Gamma'}, \quad (2.25)$$

where the approximations are valid when $\Gamma' \gg \Omega$. For typical $\Gamma' \sim 1000 \text{ s}^{-1}$, this is true for magnetic fields below $B \sim 1 \text{ nT}$. In the configuration diagrammed in figure 2.6, the probe beam will be sensitive to P_x .

To obtain a sense of the parameter space topology of a DC-mode magnetometer, it is helpful to normalize all parameters to the total spin-destruction rate. Ignoring Γ_{pr} , which can be made arbitrarily small, this choice of normalization is convenient because $\Gamma_{sd} + \Gamma_D$ for a single atomic species depends on the permanent properties of the cell (e.g. buffer gas composition, cell geometry) as well as the cell temperature, and only weakly on the cell polarization through Γ_D . Per unit atom participating in the measurement, the smaller Γ the better. Henceforth we indicate a normalized

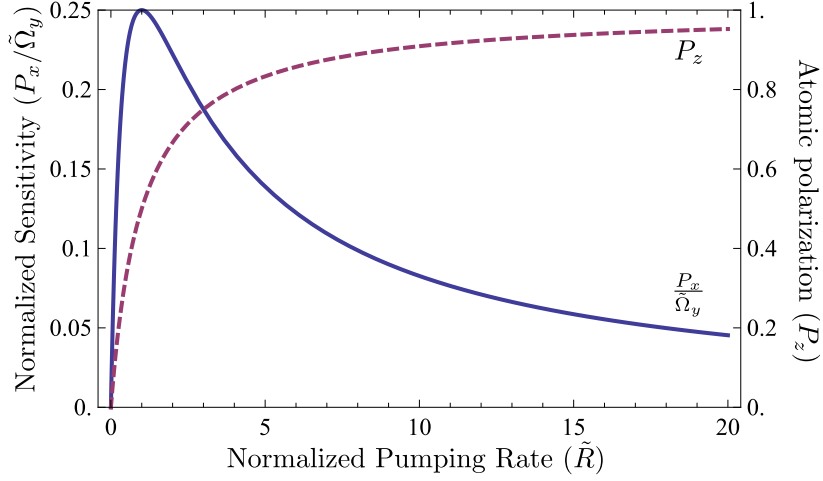


Figure 2.9: Normalized sensitivity (blue) and polarization (purple-dashed) vs \tilde{R} . This graph indicates that for a given relaxation rate, the maximum sensitivity is at $P_z = 1/2$ and the sensitivity is maximized for any pumping rate for smaller Γ .

quantity as

$$\tilde{R} = R/\Gamma$$

$$\tilde{\Omega} = \Omega/\Gamma,$$

and, (2.24) is

$$P_x = \frac{\tilde{R}}{\tilde{R} + 1} \left(\frac{(\tilde{R} + 1)\tilde{\Omega}_y + \tilde{\Omega}_x\tilde{\Omega}_z}{(\tilde{R} + 1)^2 + \tilde{\Omega}^2} \right). \quad (2.26)$$

First we examine the DC-sensitivity P_x/Ω_y . Assuming finite ground-state spin-relaxation, the sensitivity is maximized for comparatively small probe absorption ($\Gamma_{\text{pr}} \ll \Gamma_{\text{sd}} + \Gamma_D$) and $\tilde{R} = 1$ ($P_z = 1/2$). Optical pumping is necessary to achieve any signal, but $R \gg \Gamma$ simply pins the atoms to the pump axis through rapid absorption of pump photons, decreasing P_x and the sensitivity. Even so, figure 2.9 shows the sensitivity falls off more slowly for overly high pumping rates than overly low pumping rates. Coupled with strong absorption from an optically thick atomic vapor, this means beginning with $\tilde{R} \gg 1$ and optimizing \tilde{R} using an applied signal is a good method for finding the best pumping parameters.

So far, we have described the operation sensitivity of the SERF magnetometer to a single vector projection of Ω , and the sensitivity in figure 2.9 indicates the sensitivity to an applied field in

this direction. This is true for $\Gamma' \gg \Omega_z$. When $\Gamma' \ll \Omega_z$, the polarization is proportional to an orthogonal field $P_x \propto \Omega_x$, though with diminished sensitivity. In the intermediate regime, we can write the response to a general field perpendicular to the pump direction as (from (2.26))

$$\frac{\partial P_x}{\partial \Omega_\perp} = \frac{\partial P_x}{\partial \Omega_x} \frac{\partial \Omega_x}{\partial \Omega_\perp} + \frac{\partial P_x}{\partial \Omega_y} \frac{\partial \Omega_y}{\partial \Omega_\perp} \quad (2.27)$$

$$\approx \frac{R}{\Gamma' (\Gamma'^2 + \Omega_z^2)} \frac{\Gamma' + \Omega_z \Omega_\star}{\sqrt{1 + \Omega_\star^2}}, \quad (2.28)$$

where $\Omega_\star = \Omega_x/\Omega_y$ and $\Omega_\perp^2 = \Omega_x^2 + \Omega_y^2$. The approximation in (2.28) is $\Omega_\perp^2 \ll \Omega_z^2 + \Gamma'^2$. Figure 2.10 shows how (2.28) (normalized to Γ) varies with Ω_\star and \tilde{R} .

A slice of figure 2.10(B), where $\Omega_x = \Omega_y$ and approximately ideal pumping $\tilde{R} = 1$, reveals the dependence of the maximum perpendicular sensitivity on $\tilde{\Omega}_z$, as well as the mixing angle of the measured scalar response ϕ_{xy} ,

$$\phi_{xy} = \frac{(\partial P_x / \partial \Omega_x)}{(\partial P_x / \partial \Omega_y)} = \frac{\Omega_z}{\Gamma'}. \quad (2.29)$$

These quantities are shown in Figure 2.11. The importance of ϕ_{xy} will be seen later when we investigate signal processing techniques and gradiometer performance using multiple independent magnetometers (chapter 4 and chapter 6).

Another interesting feature of the DC-mode magnetometer is its response to an adiabatically (compared to Γ) swept Ω_y field. When the other fields are well nulled, (2.24) has a dispersive-like shape,

$$P_x = \frac{R\Omega_y}{\Gamma'^2 + \Omega_y^2}. \quad (2.30)$$

The shape of this feature varies interestingly as non-zero bias fields $\Omega_{x,z}$ are introduced, and some examples are shown in figure 2.12a.

Ideally, the curves in figure 2.12 could be used to characterize the pumping rate and transverse field magnitudes of the magnetometer. In reality, this can be complicated. The spatial dependence on the pump laser becomes important, as $R \rightarrow R(x, y, z)$. The pump exits a single mode fiber before going through the cell (see chapter 3) and so has a Gaussian profile. If the waist is known, the transverse dependence on $R(x, y)$ is straightforward, at least at the front of the cell. The longitudinal dependence $R(z)$ is more complicated and depends on P_z . Even in the case of zero transverse

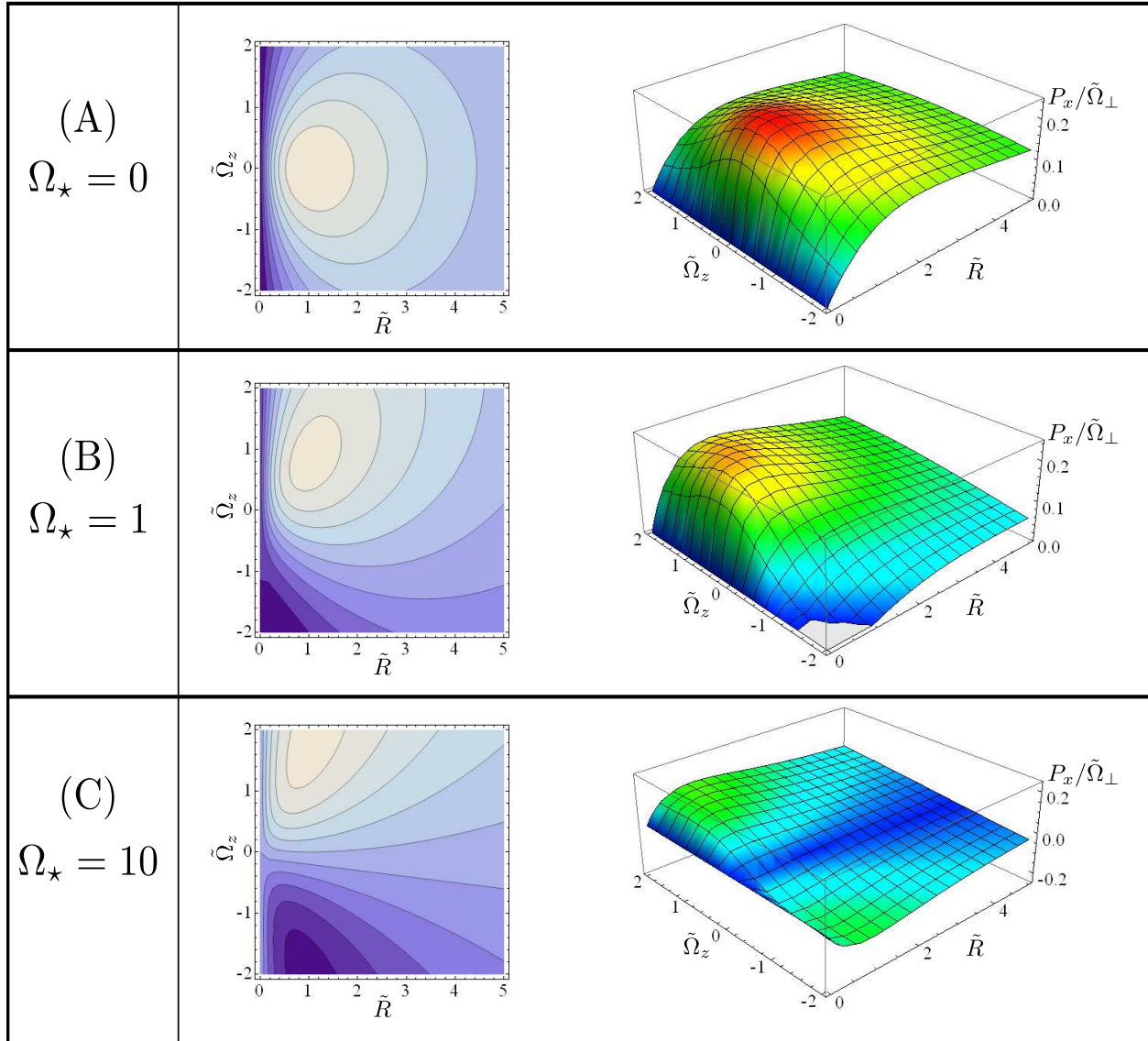


Figure 2.10: DC sensitivity to fields perpendicular to the pump, Ω_{\perp} . The most sensitive operation point is with $\Omega_z = 0$ and $\Omega_{\perp} = \Omega_y$ (A). However, residual light shifts can impart nonzero Ω_z , which increases the relative sensitivity to Ω_x , while decreasing the overall maximum sensitivity, as in (B) and (C).

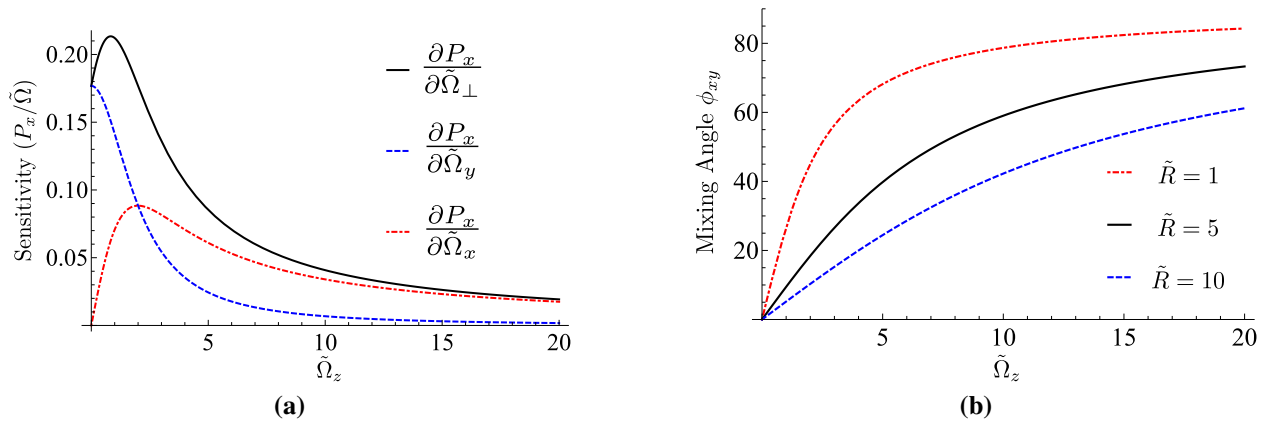


Figure 2.11: (a) Transverse sensitivity at $\tilde{R} = 1$ and $\Omega_x = \Omega_y$ (black) and the individual component sensitivity to Ω_x (red dash-dot) and Ω_y (blue, dashed)). (b) Mixing angle, describing how much response is from each transverse magnetic field component. $\phi_{xy} = 0$ corresponds to response from Ω_y alone. The mixing angle is somewhat suppressed at higher pumping rates.

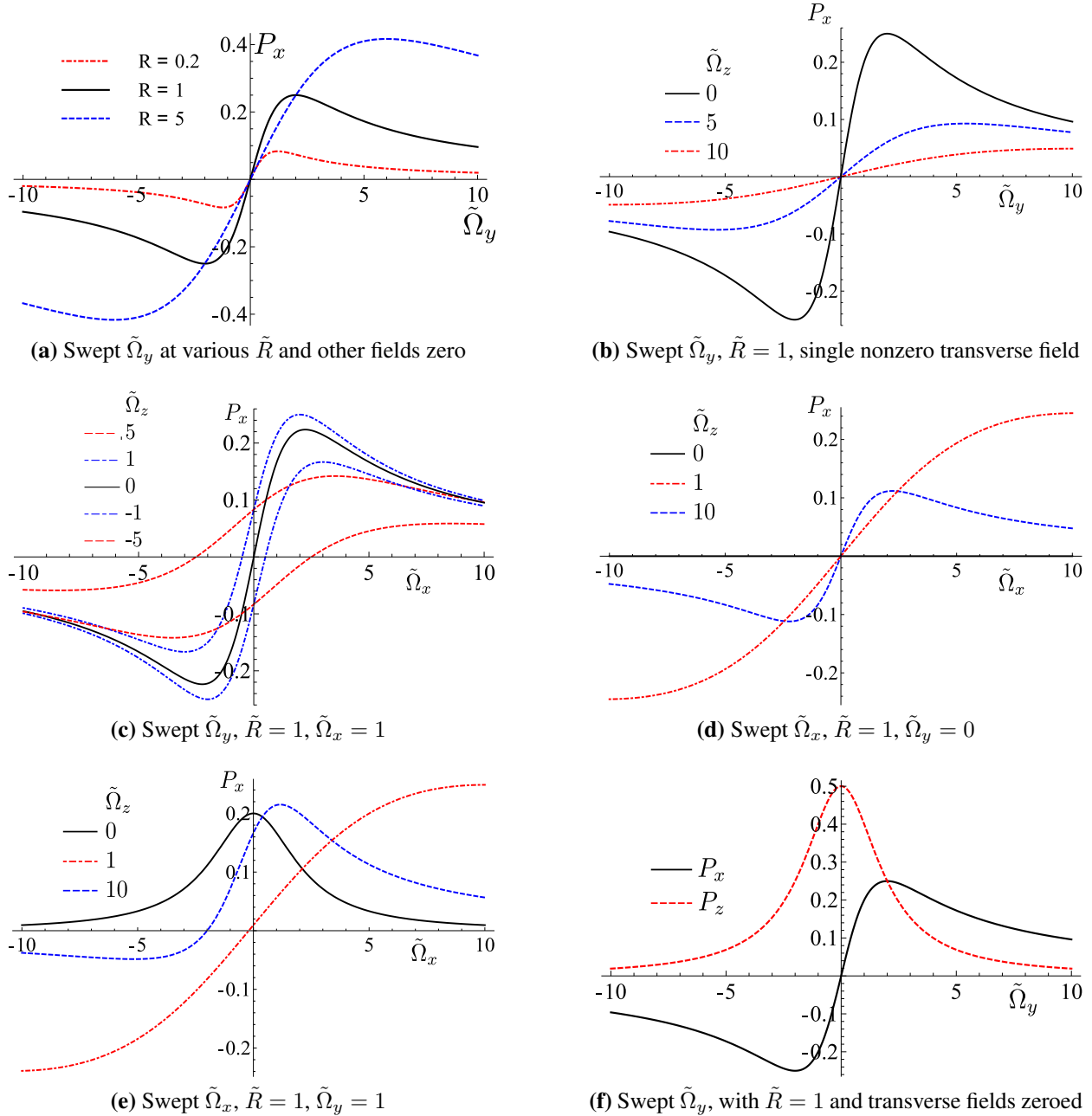


Figure 2.12: Plots of the atomic response to an adiabatically swept magnetic field under various conditions. Plots (a)–(c) show swept $\tilde{\Omega}_y$, while (d) and (e) show the response to swept $\tilde{\Omega}_x$. When the transverse fields are swept, the P_z is changed significantly (f). Practically, this alters the propagation of the pump beam through the cell, making characterization by swept field a more complicated problem.

fields and no light shifts, (2.30) is now spatially dependent and the resulting experimental measurement is an average over the pump and probe intersection volume. We do not account for these effects in presenting these curves.

For these reasons, experimentally obtained data corresponding to figure 2.12 is easiest to interpret when a small section of the central feature is used, where the applied field is small and $\partial P_z / \partial \Omega_y \approx 0$. In this central regime (which is, after all, the DC-SERF operating regime), the slope of the experimental signal is a figure of merit, provided probe beam parameters are constant. That is, a magnetometer with a sharper slope will have a higher fundamental sensitivity (per unit atom). We will deal more with the spatial dependence of the pump laser in section 2.4.

2.2.6 Response to dynamic fields

We now consider the response of (2.22) to dynamic magnetic fields. Imagine both DC and AC fields are present, $\boldsymbol{\Omega} = \boldsymbol{\Omega}_0 + \boldsymbol{\Omega}_1 e^{i\omega t}$, where $\Omega_1 \ll \Omega_0$. Then the AC fields do not much change the steady-state solution, and \mathbf{P}_0 is still (2.23). If $\mathbf{P}(t) = \mathbf{P}_0 + \mathbf{P}_1(t)$, then (2.22) gives

$$q(P)\dot{\mathbf{P}}_1(t) = \boldsymbol{\Omega}_1 \times \mathbf{P}_0 e^{i\omega t} + \boldsymbol{\Omega}_0 \times \mathbf{P}_1(t) + \boldsymbol{\Omega}_1 \times \mathbf{P}_1(t) e^{i\omega t} - \Gamma' \mathbf{P}_1(t) \quad (2.31)$$

$$+ \underbrace{\boldsymbol{\Omega}_0 \times \mathbf{P}_0 + R\mathbf{s} - \Gamma' \mathbf{P}_0}_0, \quad (2.32)$$

where the last terms sum to zero because \mathbf{P}_0 is the steady-state solution. The first order linear response at the applied frequency is then

$$-i\bar{\omega}\mathbf{P}_1 = \boldsymbol{\Omega}_1 \times \mathbf{P}_0 + \boldsymbol{\Omega}_0 \times \mathbf{P}_1 - \Gamma' \mathbf{P}_1, \quad (2.33)$$

where $\bar{\omega} = q(P)\omega$. Solutions to (2.33) can be found by transforming into the rotating basis, e.g. $P_{\pm} = P_x \pm iP_y$, but are complicated. An important simplification is when $\boldsymbol{\Omega}_0 = \Omega_{0z}\hat{z}$ and $\boldsymbol{\Omega}_1 = \Omega_{1x}\hat{x} + \Omega_{1y}\hat{y}$. Then

$$P_{1x} = P_{0z} \frac{(\Gamma' - i\bar{\omega})\Omega_{1y} + \Omega_{1x}\Omega_{z0}}{(\Gamma' - i\bar{\omega})^2 + \Omega_{0z}^2} \quad (2.34)$$

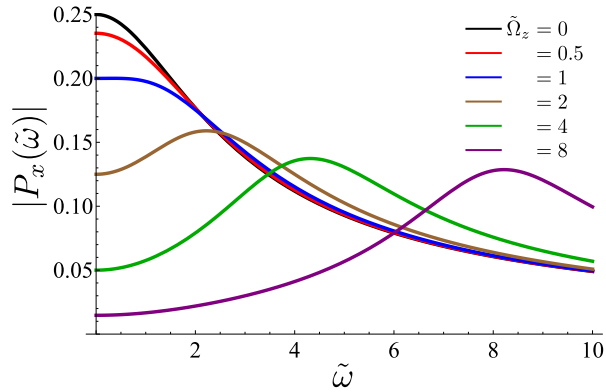
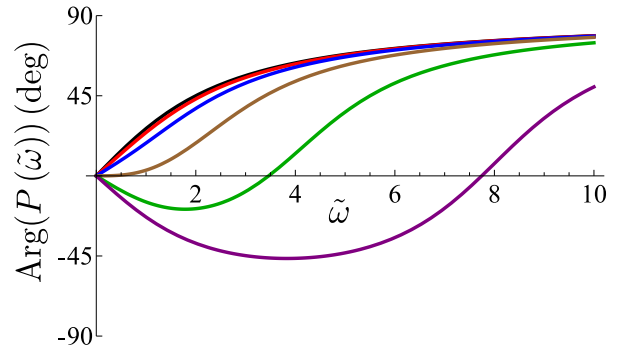
$$|P_{1x}| = P_{0z} \sqrt{\frac{(\Gamma'^2 + \bar{\omega}^2)\Omega_{1y}^2 + \Omega_{0z}^2\Omega_{1x}^2}{(\Gamma'^2 + \Omega_{0z}^2)^2 + \bar{\omega}^2(\bar{\omega}^2 - (\Omega_{0z}^2 - \Gamma'^2))}}. \quad (2.35)$$

A final useful simplification is when $\Omega_0 = 0$, in which case (2.35) gives the frequency response for the zero field magnetometer

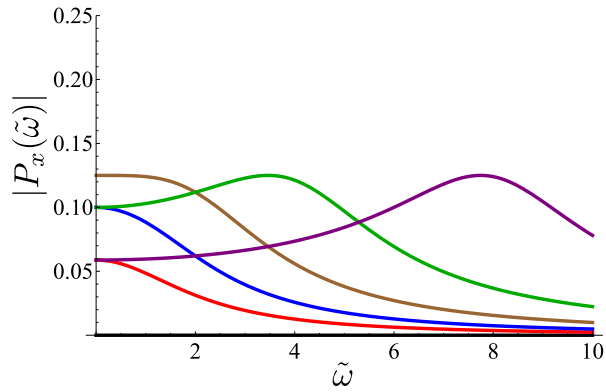
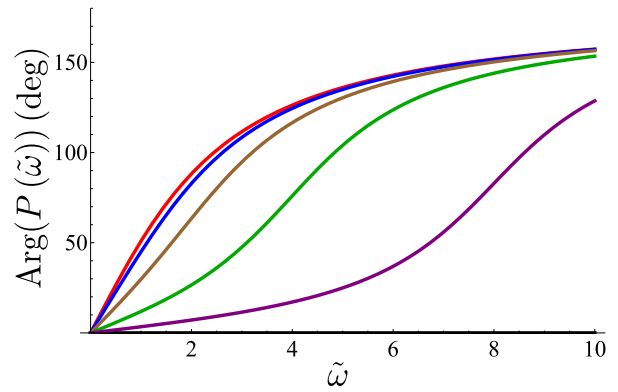
$$|P_{1x}| = P_{0z} \frac{\Omega_{1y}}{\sqrt{\Gamma'^2 + \bar{\omega}^2}}. \quad (2.36)$$

In the zero bias field regime, the SERF magnetometer acts as a first order low pass filter centered at zero frequency, and is sensitive only to the y -component of the oscillating field. The bandwidth would seem to be $\Gamma'/q(P)$, but the amplitude of P_{0z} depends upon similar factors, and is a subtlety that will be addressed shortly (section 2.2.7).

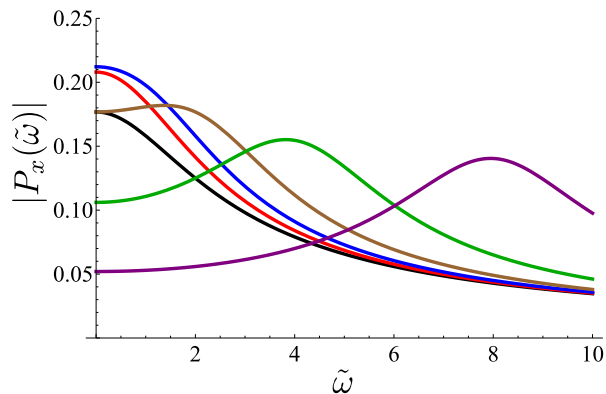
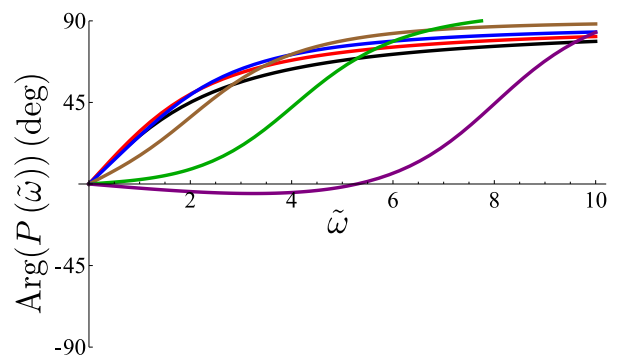
Figure 2.13 shows the amplitude and phase response for various scenarios of operating parameters. The two cases described explicitly in (2.35) and (2.36) are the most important for normal DC-mode operation.

(a) Response to $\tilde{\Omega}_{1y}$ when $\tilde{\Omega}_{1x} = 0, \tilde{\Omega}_z = 0 - 8$ 

(b) Phase response for (a)

(c) Response to $\tilde{\Omega}_{1x}$ when $\tilde{\Omega}_{1y} = 0, \tilde{\Omega}_z = 0 - 8$ 

(d) Phase response for (c)

(e) Response to $\tilde{\Omega}_{1x} = \tilde{\Omega}_{1y} = 1/\sqrt{2}, \tilde{\Omega}_z = 0 - 8$ 

(f) Phase response for (e)

Figure 2.13: Amplitude (a,c,e) and phase (b,d,f) response of the magnetometer for differing projections of an AC field onto the x-y plane, and for different DC fields applied along the pump direction. The various curves all correspond to the same set of $\tilde{\Omega}_z$, as in (a).

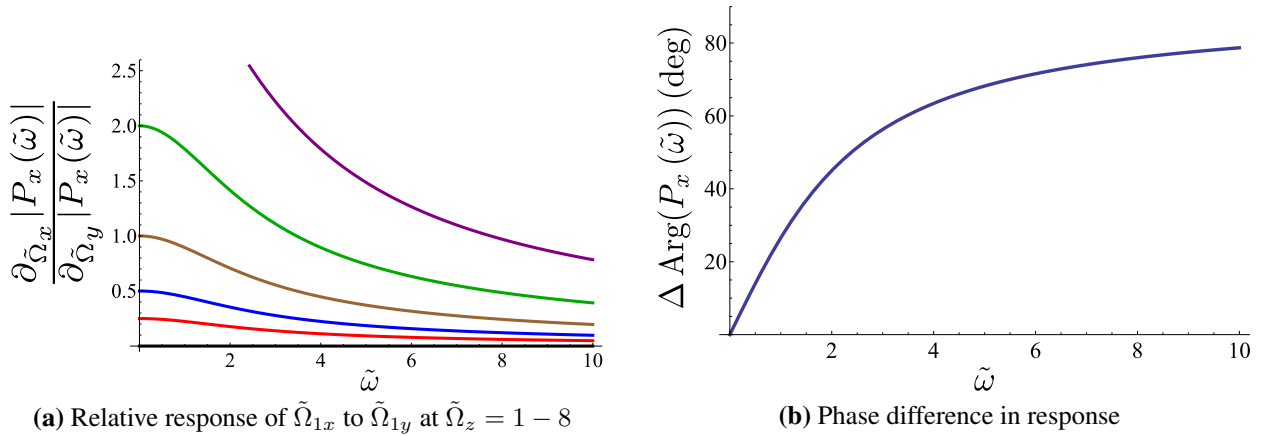


Figure 2.14: (a) The relative amplitude of the magnetometer sensitivity to $\tilde{\Omega}_{1x}$ and $\tilde{\Omega}_{1y}$ depends upon the applied $\tilde{\Omega}_z$, with increasing relative (though not absolute) sensitivity to $\tilde{\Omega}_{1x}$ increasing from zero. (b) The phase difference between the response to orthogonal magnetic fields.

2.2.7 Sensitivity and Bandwidth

The normalization used in the previous sections is useful for visualizing the behavior of a SERF magnetometer in DC-mode as experimental quantities are varied. However, normalization by Γ obscures some important considerations for applied use, such as how the magnetometer frequency response overlaps with the signals we wish to detect, e.g. MCG. It is clear from (2.35) that the effective bandwidth depends upon the three parameters R , Ω_z , and Γ . Yet how these parameters should be varied in order to obtain the greatest SNR for a MCG is unclear.

Using (2.35), we can obtain

$$\left. \frac{\partial |P_{1x}|}{\partial \Omega_{1y}} \right|_{\Omega_{1x}=0} = \frac{P_{0z}}{\Gamma} \sqrt{\frac{(\tilde{R} + 1)^2 + \tilde{\omega}^2}{((\tilde{R} + 1)^2 + \tilde{\Omega}_{0z}^2) + \tilde{\omega}^2(\tilde{\omega}^2 - \tilde{\Omega}_{0z}^2 + (\tilde{R} + 1)^2)}}, \quad (2.37)$$

which unambiguously decreases with Γ , though we should note again this is a per atom quantity and does not take into account changes in total sensitivity due to atomic number density.

The dependence of the magnetometer response to R and Ω_{0z} is more complicated. To provide a concrete description of the frequency response of a magnetometer, we model a ^{87}Rb vapor cell at 145 C with 50 Torr N_2 and 22 Torr He (the estimated parameters for our cells, see chapter 3). Evaluation of (2.12) and (2.20) for these conditions gives $\Gamma_{\text{sd}} = 2\pi \times 8.1$ Hz and $\Gamma_D = 2\pi q(P) \times 13.1$ Hz. Using the sum of these two terms as the base relaxation rate Γ_0 , we model the magnetometer under $\Gamma = \Gamma_0$ and $\Gamma = \Gamma_0/2$. Figure 2.15 shows the relative response under several conditions, normalized to (2.35) evaluated at $\Gamma = \Gamma_0$, $R = \Gamma_0$, and $\Omega_z = 0$,

$$P_{1x}|_{\text{ref.}} = \frac{\Omega_{1y}}{\sqrt{2}\sqrt{4 + q(1/2)^2\omega^2}}.$$

Relative response above unity implies better sensitivity than $P_{1x}|_{\text{ref.}}$ (again, per unit atom). In chapter 7 we will investigate the optimum operating conditions for the magnetometer given what is known about the frequency content of an MCG and fMCG signal. A brief inspection of figure 2.15 seems to indicate that the high frequency response can be obtained at the smallest expense of low frequency response by increasing the pumping rate.

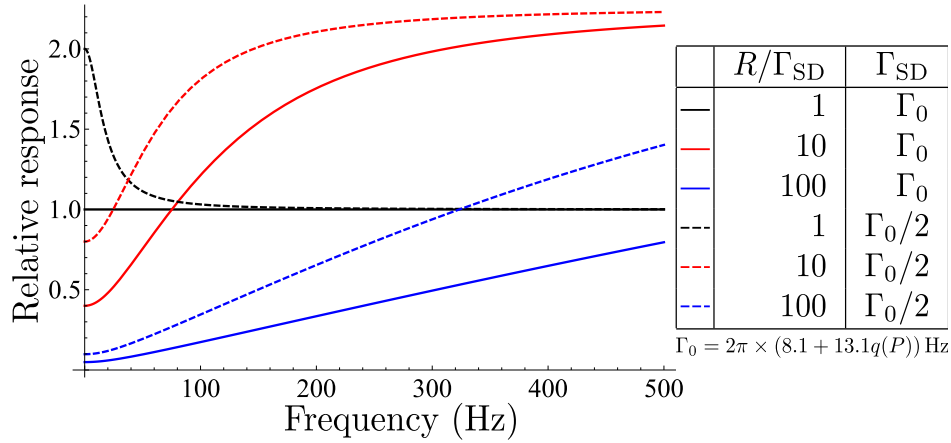
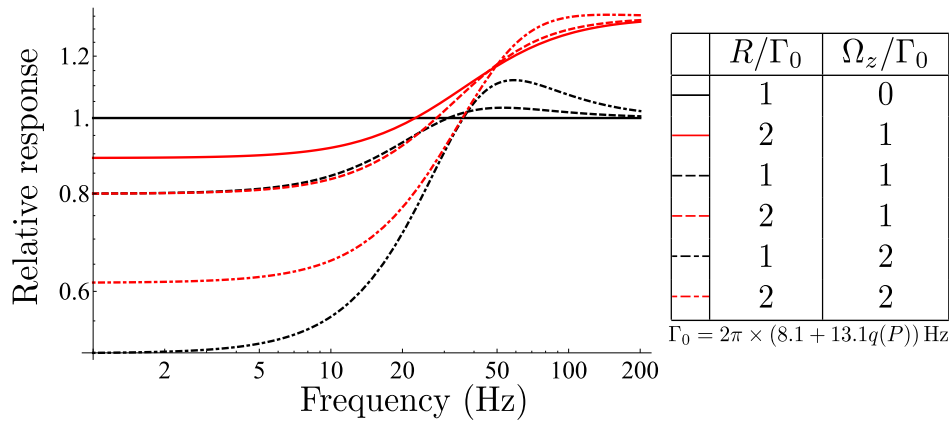
(a) Response to Ω_{1y} , normalized to the response when $\Omega_z = 0$, $R = \Gamma_0$ (b) Response to Ω_{1y} , normalized to the response when $\Omega_z = 0$, $R = \Gamma_0$

Figure 2.15: Both graphs show the magnetometer response, normalized to the case when $R = \Gamma_0$ and there are no applied DC fields. Subfigure (a) emphasizes that decreasing Γ globally increases the sensitivity at every frequency for the same relative pumping rate. Subfigure (b) demonstrates the interesting trade-off between sensitivity at different frequencies. Black (red) lines represent $\tilde{R} = 1(2)$, and solid (dashed) {dot-dashed} lines represent $\tilde{\Omega}_z = 0(1)\{2\}$. The high-frequency relative response is determined by the pumping rate. The relative low-frequency limit, as well as the details of the transition between low-frequency and high frequency relative response depend upon $\tilde{\Omega}_z$. In these plots, the dependence of $q(P)$ on R is accounted for.

2.2.8 Probe Faraday rotation

The previous sections have described how the pump laser and the magnetic fields in figure 2.6 interact with a Rb vapor cell to produce a sample polarization sensitive to magnetic fields. The detection of these magnetic fields can be accomplished using any probe sensitive to changes in \mathbf{P} . A simple and very sensitive method utilizes the fact that \mathbf{P} alters the atomic polarizability, which can be measured through the detection of a suitable parameter of a laser propagating through the vapor. This interaction is characterized by the dipole electric polarizability $\vec{\alpha}$. Expressions for the dipole electric polarizability are derived following [Bonin and Kresin, 1997] in appendix A. We use the results here.

For the D2 transition using the assumptions made in appendix A, the Faraday rotation is

$$\phi = -\frac{1}{4}[\text{Rb}]l r_e f_{D2} c \mathcal{D}(\Delta\nu) P_x. \quad (2.38)$$

Absorption of the probe beam has two effects. Higher absorption rates decrease sensitivity through Γ_{pr} (2.16). Absorption also decreases the number of photons used to measure the rotation angle, decreasing the signal size and increasing the effective photon shot noise limit of the magnetometer. While (2.38) is maximized at $\mathcal{D}(\Delta\nu)|_{\text{max}} \rightarrow \mathcal{D}(\Delta\Gamma/2) = 1/2$, the optimum probe detuning is actually $\Delta\nu > \Delta\Gamma/2$ due to these two effects. Ignoring for a moment Γ_{pr} , the signal size $\mathcal{S} \propto I_0 \phi$. Assuming exponential absorption and $P_x \ll 1$, this can be written

$$\mathcal{S} = \frac{\mathcal{P}_2}{2} x \text{OD}(x) e^{-\text{OD}(x)} \frac{B_y}{B_0} \quad (2.39)$$

where $x = \Delta\nu/(\Delta\Gamma/2)$ is the normalized detuning, $\text{OD}(x) = nl\sigma_{02}$ is the optical depth, and

$$B_0 = \left(\frac{R\gamma}{\Gamma'^2 + \Omega^2} \right)^{-1} \quad (2.40)$$

is a characteristic effective field, which is determined by $P_x = B_y/B_0$ for small Ω_x . Figure 2.16 shows how absorption modifies the maximum signal size.

In DC-mode, ϕ is directly proportional to the applied magnetic field through the frequency dependent P_x (2.35), and a direct measurement proportional to this angle can easily be achieved for small angles using a balanced polarimeter. For reference, using our experimental parameters

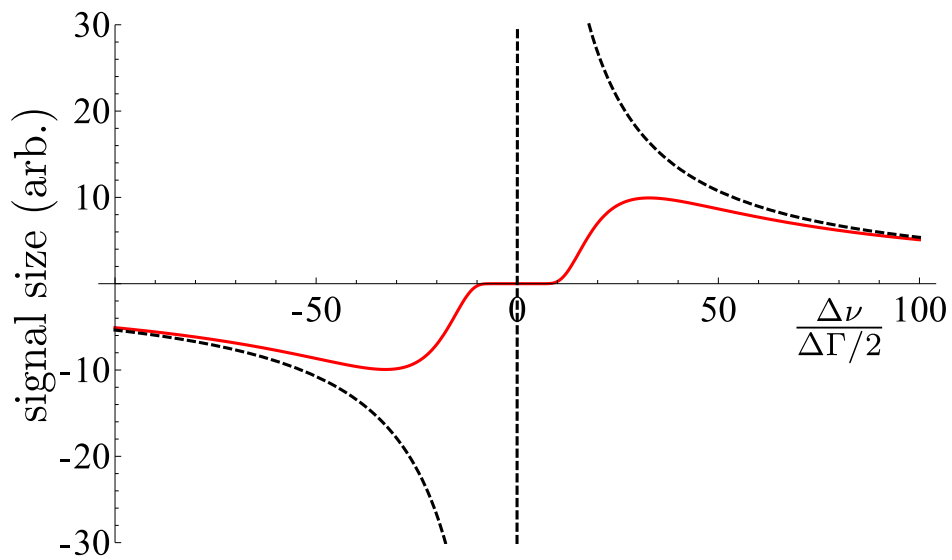


Figure 2.16: Signal size versus detuning from the D2 transition, normalized to the transition linewidth. The dashed line is the purely dispersive shape in the rotation angle, while the solid red line takes into account absorption from the D2 line as well. The model uses the standard cell parameters from appendix B.

(see appendix B), (2.38) evaluates to $\phi/B_y \approx 0.1 \mu\text{Rad/fT}$. For perspective, the differential photocurrent is $\Delta I = 2P_0\epsilon\phi$, with probe laser power $P_0 = 1 \text{ mW}$ and a photodiode power to current conversion $\epsilon \approx 0.6 \text{ A/W}$, is around 250 pA/fT .

2.3 Warts and imperfections

The discussion of section 2.2 is meant to provide a feel for the primary operating regime of the magnetometer (DC-mode) as well a basis for understanding the experimental setup and trade-offs made to build an array of magnetometers. The SERF magnetometer model discussed above ignores many important aspects of magnetometer performance. Some of these were mentioned explicitly, such as ignoring the effects of diffusion, the spatial dependence of the laser profiles, and the light shift from the pump lasers (which causes an effective magnetic field). We discuss these additional complications in the final part of this chapter. The light shift especially will have important bearing on the use of the magnetometers in an array. We will generally ignore the hyperfine splitting in this work. It mainly affects tunable parameters like the pumping rate for a certain absolute laser frequency, and ignoring it makes most of our calculations approximate, especially in the frequency region between the hyperfine levels. The simulations and experimental work are mostly performed with both lasers many linewidths off resonant where the fine-structure description should be sufficient.

2.4 Spatial dependence of laser parameters

The spatial dependence of the pump and probe lasers is important in understanding and optimizing the magnetometer design. The transverse intensity profiles of both lasers are well described by Gaussian profiles at the front of the cell. As they propagate through the atomic vapor, absorption complicates the dependence on the longitudinal coordinate.

2.4.1 Transverse spatial dependence of a Gaussian beam

Since both lasers exit a polarization-maintaining fiber before interacting with the atoms (see chapter 3), both lasers are Gaussian. The intensity of a general Gaussian beam propagating in the \hat{z} direction with minimum waist w_0 can be written as a function of position,

$$I(r, z) = I_0 \left(\frac{w_0}{w(z)} \right)^2 \exp \left(\frac{-2r^2}{w^2(z)} \right), \quad (2.41)$$

where the intensity at the center of the beam is

$$I_0 = \frac{2\mathcal{P}_0}{\pi w_0^2}, \quad (2.42)$$

\mathcal{P}_0 is the total laser power and w_0 is the beam waist. The parameter $w(z)$ describes how the transverse profile of the beam changes as a function of propagation distance. It can be expressed in terms of the Rayleigh range z_R

$$w(z) = w_0 \sqrt{1 + \left(\frac{z}{z_R}\right)^2} \quad (2.43)$$

$$z_R = \frac{\pi w_0^2}{\lambda}. \quad (2.44)$$

Various w_0 have been used during this work, but all are larger than 500 μm . In other words, for all lens configurations used, the collimated beam $z_R > 1$ m. The optical path length here is on the order of 10 cm, so $w(z) \approx w_0$. Then we can write the intensity at the front of the cell for each laser (using the coordinate system in figure 2.6)

$$I_1(x, y, z = 0) = I_{10} \exp\left(-2\frac{x^2 + y^2}{w_1^2}\right) \quad \text{D1 Pump} \quad (2.45)$$

$$I_2(x = 0, y, z) = I_{20} \exp\left(-2\frac{y^2 + z^2}{w_2^2}\right) \quad \text{D2 probe,} \quad (2.46)$$

where we have assumed the center of the lasers are centered on the cell, and the center of the cell has coordinates $(x, y, z) = 1/2 \times (l, l, l)$, where the cell is a cube of side length l . Note the naming convention, where $\{A\}_i$ parameters denote pump (probe) values for $i = 1(2)$, respectively.

2.4.2 Longitudinal dependence of a weak probe

Beer's law describes the attenuation of light as it passes through an absorbing medium. For intensity I and propagation direction \hat{x} , the absorption is

$$\frac{dI}{dx} = -n\sigma I. \quad (2.47)$$

For a relatively weak probe beam ($\Gamma_{\text{pr}} \ll R$), the polarization is independent of the probe beam. Assuming $P_x \ll 1$, $\sigma \approx \sigma_{02}(\Delta\nu)$, and the solution to (2.47) can be written by inspection,

$$I_2(x) = I_{02} e^{-n\sigma_{02}x} \quad \text{Probe absorption.} \quad (2.48)$$

The total probe intensity profile is the combination of (2.48) and (2.46),

$$I_2(x, y, z) = I_{02} e^{-n\sigma_{02}x} \exp\left(-2\frac{y^2 + z^2}{w_2^2}\right) \quad \text{Probe intensity profile.} \quad (2.49)$$

2.4.3 Longitudinal dependence of the pump

By design, the pump beam optically pumps the atoms, which makes the absorption power dependent (nonlinear). Further, collisions with the wall depolarize the atoms, imposing a boundary condition for the polarization equation. Finally, as discussed in section 2.2.3, diffusion alters the spatial dependence within the cell of the pump beam.

The differential absorption equation is the same as for the probe case, only for the pump the cross section depends upon the polarization. For the pump beam propagating in the \hat{z} direction with circular polarization, the differential absorption is

$$\frac{dI_1}{dz} = -n\sigma_{0D1}(1 - P_z)I_1. \quad (2.50)$$

When the laser linewidth is small compared to the absorption linewidth, the frequency profile of the laser is not shifted as it is absorbed (no spectral hole-burning) [Lancor et al., 2010], and $R(z) \propto I_1(z)$, so

$$\frac{dR}{dz} = -n\sigma_{0D1}(1 - P_z)R. \quad (2.51)$$

Taking full measure of these effects requires the simultaneous solution of (2.51) and the steady-state of (2.22), with the boundary conditions $P(\mathbf{r})|_{\mathbf{r} \rightarrow \text{walls}} = 0$ and initial condition $R(x, y, 0) = R_0(x, y)$, where R_0 is described by the intensity profile of the Gaussian beam, as discussed above. A full treatment requires numerical solution to the equations. However, much of the physics can be captured using various simplifications and approximations.

To start with, we will use a simple model to account for diffusion in the single dimension longitudinal to the pump [Walker and Happer, 1997]. The boundary condition for the pumping rate is $R(z \rightarrow 0) = R_0$, and we enforce the diffusion depolarization boundary condition by the

approximate solution

$$P(z) \approx P_0(z) (1 - e^{-z/z_D}) (1 - e^{-(l-z)/z_D}) \quad (2.52)$$

$$P_0(z) = \frac{R(z)}{R(z) + \Gamma}. \quad (2.53)$$

Care must be taken in treating the diffusion relaxation rate. If we want to get reliable estimates for particular cell configurations, our model must account for all the angular momentum loss due to diffusion. The angular momentum loss in the longitudinal direction should fall out of the solution to the problem, but the loss in the transverse plane must be explicitly included. We do this phenomenologically by setting the $\Gamma = \Gamma_{\text{sd}} + \Gamma_D|_{2\text{D}}$, where the 2D loss rate is simply $\Gamma_D|_{2\text{D}} = \frac{2}{3}\Gamma_D$.

The parameter z_D is a characterization of the longitudinal distance travelled by the angular momentum through diffusion in time $T_D \propto 1/(R + \Gamma)$,

$$z_D = 2\pi \sqrt{q(P) \frac{D}{R + \Gamma}}, \quad (2.54)$$

where D is the diffusion coefficient discussed in section 2.2.3, and Γ includes transverse diffusion, as described above. Then (2.51) can be dealt with iteratively in small steps, beginning at the front of the cell, ensuring modest changes in pumping rate at each step. Figure 2.17 shows the diffusion length as a function of pumping rate ($\tilde{R} = R/(\Gamma_{\text{sd}} + \Gamma_D)$) and the expected longitudinal pump profile and polarization profile for various pumping rates, with the cell parameters otherwise similar to those described above. We use an approximate effective pumping rate,

$$R_{\text{eff}} = \frac{R_{\text{front}} + R_{\text{back}}}{2}$$

$$\tilde{R}_{\text{eff}} = \begin{cases} \tilde{R}_0 - \frac{1}{2} & \tilde{R}_0 \geq \frac{1}{2} \\ 0 & \tilde{R}_0 < \frac{1}{2} \end{cases}$$

to calculate an average slowing down factor and transverse diffusion relaxation rate.

Figure figure 2.18 shows solutions for many different combinations of initial normalized pumping rate \tilde{R} and pump detuning. These plots are modelled at the same cell parameters discussed above. The pump power was set to 4 mW, a value approximately consistent with the maximum value delivered to four cells simultaneously. A laser waist was chosen (to vary the intensity) as

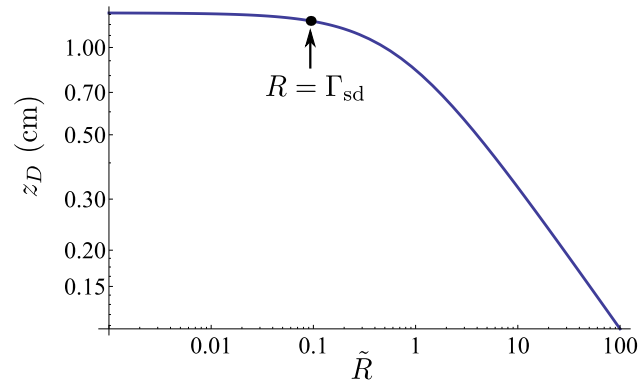
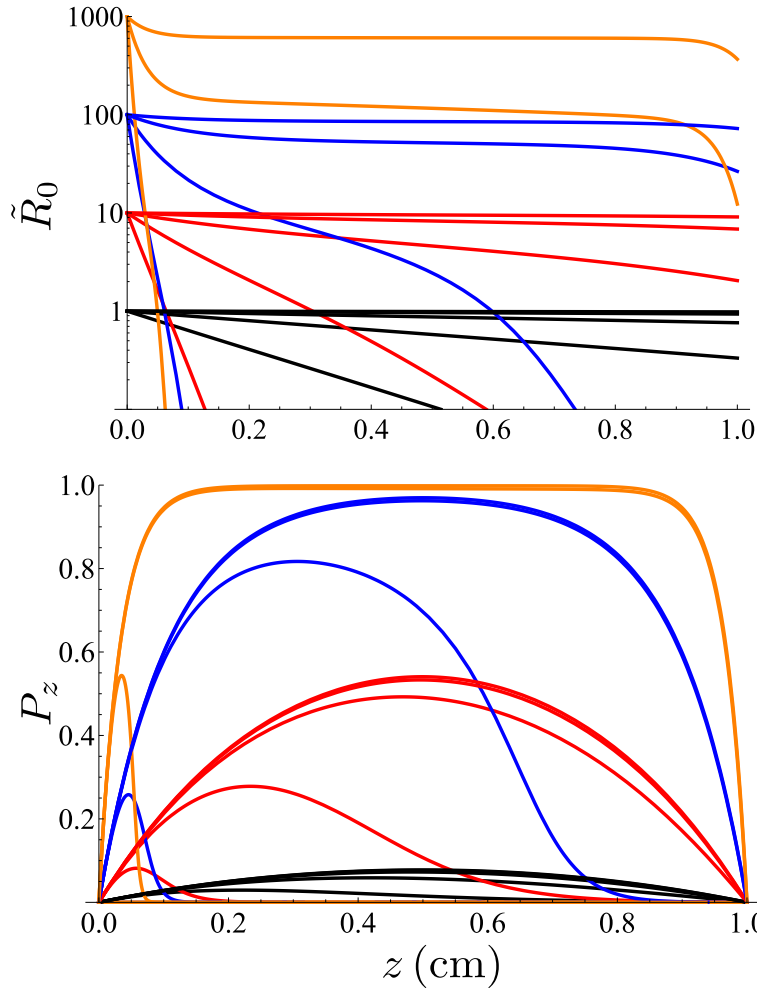


Figure 2.17: The diffusion length z_D from the simple model of \tilde{R}_{eff} and the operating parameters used throughout this chapter. The length is characteristic of how far angular momentum is carried from its origin in a time characterized by the rate $R + \Gamma_{\text{sd}} + 2/3 \times \Gamma_D$, where the diffusion term is reduced to account for relaxation in the transverse direction. The labelled point is at an initial pumping rate equal to the collisional spin-destruction rate.

well as an initial pumping rate \tilde{R} . Then the detuning was chosen to make these values consistent. Clusters of curves of the same color in figure 2.18 correspond to the same initial pumping rate but different intensity and detuning. The table provides a list of the particular parameters used, where the detuning is expressed in terms of number of linewidths. For some of the lower intensities, high pumping rates are nonphysical for the pump power. We will expand on this simple 1-D model in chapter 6, where we will discuss operation of the magnetometer in a regime where the pump waist is much smaller than a diffusion length.



$2w_0$ (mm)	\tilde{R}				$\frac{\Delta\nu}{\Delta\Gamma/2}$			
	Black	Red	Blue	Orange				
10	1	10	100	1000	7.5	2.4		
5		—			15.2	5.2	1.4	
2.5		—			30.4	10.5	3.2	0.4
1.25		—			60.7	21.0	6.7	1.9
0.625		—			121.5	42.0	13.5	4.2

Figure 2.18: Solutions to the coupled pump 1-D pump propagation and polarization equations for various pumping parameters. Clusters of the same colored curves in the pumping plot correspond to the same initial \tilde{R} but at different combinations of intensity and detuning. The resulting polarization as a function of longitudinal coordinate is shown below. The laser power was set to 4 mW, and a waist and initial pumping rate chosen. Then the detuning consistent with those parameters was calculated. The table lists the parameters used in the calculation.

2.5 Light shift

The atomic polarizability has a vector component that gives rise to an effective magnetic field [Appelt et al., 1999, Bonin and Kresin, 1997, Happer and Mathur, 1967]. In appendix A we present a derivation that follows [Bonin and Kresin, 1997] for finding the vector light shift. The result from a circularly polarized pump beam near the D1 resonance, as it pertains to atomic magnetometry, can be found in the literature [Shah and Romalis, 2009b],

$$\Omega_{\text{LS}} = r_e f c \Phi_0 \mathcal{D}(\nu) \hat{z} \quad (2.55)$$

$$= R \frac{\Delta\nu}{\Delta\Gamma/2} \hat{z}, \quad (2.56)$$

where (2.56) is obtained for the narrow laser linewidth limit, using (2.8). This field acts as any real Ω_z in how it affects the response of the magnetometer, though $\Omega_{\text{LS}} \rightarrow \Omega_{\text{LS}}(x, y, z)$ through the complicated Gaussian and propagation determined spatial dependence of the pump beam as it is attenuated by the atoms.

Figure 2.19 shows a plot of the light shift in field units $\Omega_{\text{LS}}/\gamma$, normalized to $w_0 = 1$ cm and $\mathcal{P}_0 = 1$ mW. Since $\Omega_{\text{LS}} \propto \mathcal{P}_0/w_0^2$, figure 2.19 can be used to quickly estimate the Ω_{LS} for any input pump beam parameters. With $\gamma \approx 2\pi \times 28$ GHz/T, the resulting effective field is larger than the spin relaxation mechanisms in the sensitivity equation (2.35). This would cause a noticeable decrease in sensitivity and change in frequency response if the background magnetic fields were cancelled but the light shift remained. In reality, the procedure used to cancel the background magnetic fields cannot distinguish between light shifts and real magnetic fields, and the signal weighted average light shift is cancelled. Gradients in the light shift will remain, mainly decreasing the magnetometer sensitivity by decreasing the sensitivity at the spatial locations in the cell where the pump intensity is high enough to cause the local light shift to be much different than the average light shift.

Finally, the light shift has important bearing on using more than one magnetometer. If the magnetometers and pump polarization are not aligned so the light shifts are pointed in the same direction in the room reference frame, there can be effective magnetic field differences of the order of the light shifts at the two magnetometer positions. This fact makes the use of a single set of

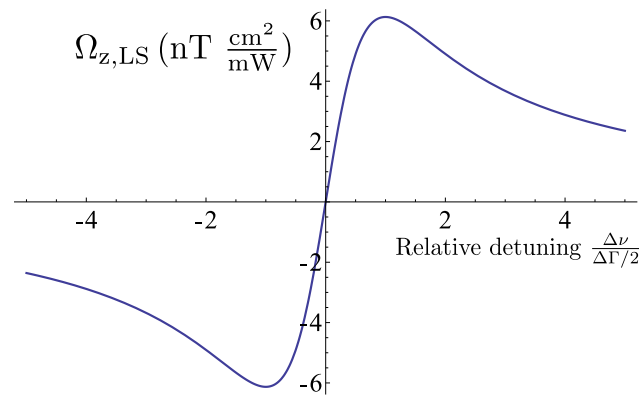


Figure 2.19: The light shift from the cell with buffer gas contents described throughout this work, normalized for unit power (mW) and laser waist (cm). Comparing this figure to figure 2.18, it is clear that for many situations, the light shift can cause sizable magnetic fields. For example, with a reasonable $w_0 = 0.25$ cm, the peak light shift is 100 nT for a 1 mW beam. A 0.25 cm waist essentially ensures that the gradient of the light shift will be the entire light shift, since the transverse intensity profile varies widely over the cell area.

cancellation coils to cancel the ambient fields difficult, since one set will not be able to cancel the light shift at both magnetometers.

Chapter 3

Apparatus

One of the main goals of this work was the design and implementation of a device for measuring actual magnetic fields from human hearts which could be set up quickly and temporarily in a magnetically shielded room (MSR). This loosely puts two competing sets of design constraints on the magnetometers. For the optimum measurement capabilities, those constraints come down to maximizing the SNR from a heart. As for the magnetometer as a practical device to be used with human subjects, the limitations have to do with flexibility in positioning the magnetometer, human comfort, and other practical matters. Table 3.1 summarizes these requirements, as well as the way they are addressed in our design. The rest of this chapter will expand upon the details of the design, the challenges faced and the ways in which these challenges were overcome.

Table 3.1: Summary of the design requirements for an array of multiple SERF magnetometers for measurement of biomagnetic signals. Requirement type refers to either requirements relating to maximizing the SNR of a biomagnetic measurement or the practical necessities of operating with human subjects, with part time access to an MSR, and with the understanding that the magnetometers are still being prototyped and must retain some flexibility in configuration.

Req. type	Requirement	Design solution
SNR	Minimize working cell to skin distance	Good thermal insulation (6 mm skin to cell).
	Minimize metal near cell	Use non-magnetic ceramics and plastics for structural parts, ensure metals are copper or aluminum, if possible.
	For array, make unit spacing ~ 5 cm for fMCG (baseline similar to source distance)	Multiple cells, enforces single magnetometer size limitation.
Practical	Array must be portable	<p>Completely modular design:</p> <ul style="list-style-type: none"> • Pump and probe single lasers fiber coupled to all magnetometers. • Individual cubic tri-axial coils for each magnetometer for local field adjustment. • Electrical heating. <p>Optics and electronics fit on a wheeled cart, can be installed in minutes.</p>
	Array must be re-positionable with respect to stationary subject laying on a bed	Complete modularity, and mount to commercial SQUID, which has ceiling gantry.
	Flexibility to make on-the-fly changes	Magnetometer optics are reconfigurable.

3.1 Cell, heatsink, and heaters

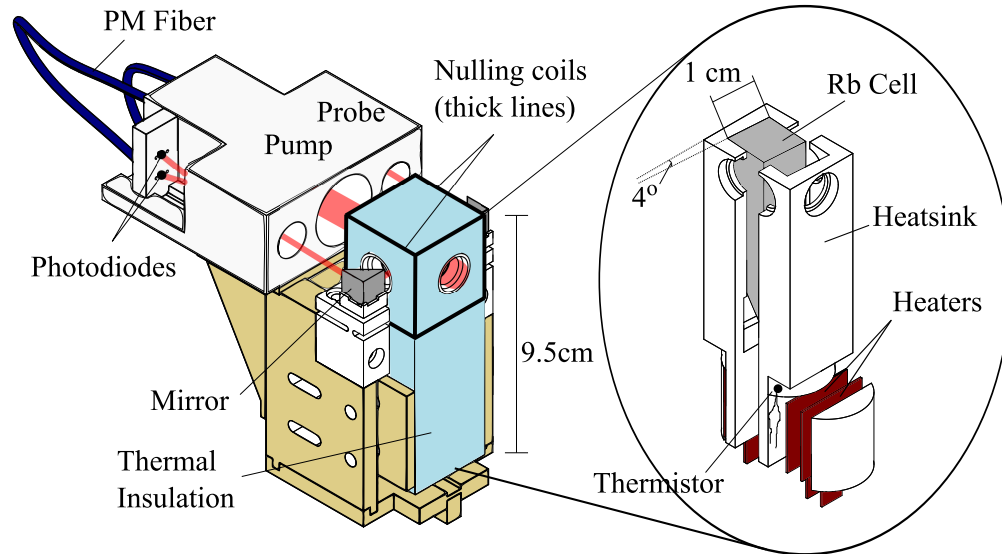


Figure 3.1: Single magnetometer unit (left) with view inside the thermal insulation (right). Cubic tri-axial nulling coils are wrapped around the insulation. The optics are removable and completely reconfigurable. We have found the 4° angle greatly reduces probe noise, we presume by reducing etalon effects.

Figure 3.1 shows a single magnetometer unit. The inset displays a Pyrex ^{87}Rb vapor cell press-fit inside a boron-nitride heatsink thermally contacted to resistive-film heaters and a high temperature thermistor, all surrounded by thermal insulation. The vapor cell is $1 \times 1 \times 5 \text{ cm}^3$ rectangular container with isotopically pure ^{87}Rb . For this work, four different cells were used, three from Triad Technologies (nominally channels 1, 2, and 4) and the other from Ophos Instruments (channel 3; we use “channels” and “magnetometers” interchangeably throughout this work). The Ophos cell was filled with 100 Torr N_2 buffer gas, while other cells contained 50 Torr N_2 and 760 Torr He at the time of manufacture. The N_2 prevents radiation trapping [Happer, 1972], while the He was included to limit diffusion to the walls.

Subsequent absorption linewidth measurements of the Triad Technologies cells showed slow loss of buffer gas pressure indicating He loss consistent with diffusion through the Pyrex cell walls [Walters, 1970]. While unanticipated, this is a well known problem of borosilicate glasses (such as Pyrex), and its prevention requires the use of aluminosilicate glass (GE-180, for example) commonly found in high pressure SE optical pumping experiments. The pressure in the cells can

be estimated as a function of time by [Walters, 1970]

$$p = p_0 e^{-\frac{A}{Vl}Pt}, \quad (3.1)$$

where p_0 is the original cell pressure and A and V are the cell area and volume, $l = 1.25$ mm is the cell wall thickness, and $P = 1.75 \times 10^{-9}$ cm²/s is the diffusion coefficient for Helium through Pyrex. This results in a time constant of around 170 days for our cell parameters. For reference, the three cells containing Helium were received in mid-March 2010. Finally, it bears mentioning that although cells 1,2, and 4 are nominally the same, they seem to exhibit different characteristics from one another, and obviously from cell 3. More information about the cells can be found in appendix C.

The cell is mounted in a thermally conductive ceramic heatsink. The clamping mechanism holds the heat-sink approximately square to the pump and probe laser beam paths. If the heat-sink also held the cell square to its sides, this would maximize etalon effects from the surfaces of the Pyrex cell. While in theory this design should be insensitive to these kinds of effects, we have found a substantial difference in the differential noise of a transmitted probe through an empty cell when the probe is sent through perpendicular to the cell faces versus at a small angle. Thus, the heat-sink is machined to hold the cell at a 4° angle to the laser paths.

Aside from holding the cell, the main purpose of the heatsink is to thermally contact the cell with the electric heaters, yet maintain separation between them to limit the size of the heater magnetic fields produced at the cell detection volume. The ceramic should have the highest thermal conductivity possible in order to minimize the power needed by the heaters and the insulation thickness. We have used two machinable ceramics with success: Shapal-M (thermal conductivity of 90 W/m K) and Boron-Nitride (30-60 W/m K, see appendix D). The heatsinks for all four magnetometers used here are Boron-Nitride, though Shapal-M is preferred for its higher thermal conductivity and because Boron-Nitride is self-lubricating and tends to leave a thin film on contact surfaces. Additionally, Boron-Nitride heat conduction is anisotropic, so a rod may conduct heat radially more than axially, depending on the orientation of the ceramic molecular axis.

The maximum use temperature for a SERF Rb magnetometer is $\sim 180^\circ\text{C}$, requiring special care in material selection. Many materials were considered for the insulation, but the current insulation

is Aerogel, a silica based carbon-fiber reinforced fabric, with an ultra-low thermal conductivity of 0.021 W/m K (for reference, the thermal conductivity of still air is 0.024 W/m K). Using three layers of 2 mm thick sheets to surround the heat sink, with holes cut for optical access, allows maintaining the cells at 140–180 C with about 4 W of heater power and warm but not uncomfortable outer surface temperature. Assuming this system obeys Newton’s law of cooling, we can estimate the effective thermal conductivity of the Aerogel insulation system including loss from the openings necessary for the laser beam path. In steady-state, the heat loss from the ceramic to the environment should go as

$$h_{\text{eff}}A(\Delta T) = P_{\text{h}}, \quad (3.2)$$

where h_{eff} is the effective heat transfer coefficient from the ceramic heatsink to its surroundings, A is the ceramic surface area, ΔT is the temperature difference between the ceramic and the surroundings, and P_{h} is the heater power required to maintain ΔT . Evaluating using the ceramic surface area as if it were solid, $h_{\text{eff}} = 4.6 \text{ W}/(\text{m}^2 \text{ K})$. We can use a lumped capacitance model of the heat transfer to write an effective thermal resistance R_{eff} and compare it with the thermal resistance we would expect from heat diffusion through the thermal insulation R_{t} ,

$$R_{\text{eff}} = \frac{1}{h_{\text{eff}}A}$$

$$R_{\text{t}} = \frac{L_{\text{t}}}{k_{\text{t}}A}$$

where L_{t} and k_{t} are the thermal insulation thickness and conductivity. The enlightening ratio $R_{\text{t}}/R_{\text{eff}} = 1.3$ indicates the actual power loss is enhanced by about a factor of 1/3 from the windows over what it would be where the entire magnetometer wrapped in thermal insulation.

The time-constant for the system of density ρ , specific heat C_p and volume V to come into thermal equilibrium is

$$\tau = \frac{\rho C_p V}{h_{\text{eff}}A} = \frac{\rho C_p V \Delta T}{P_{\text{h}}}, \quad (3.3)$$

where the second equality uses (3.2). This is around 40 minutes for our Boron-Nitride heat sink.

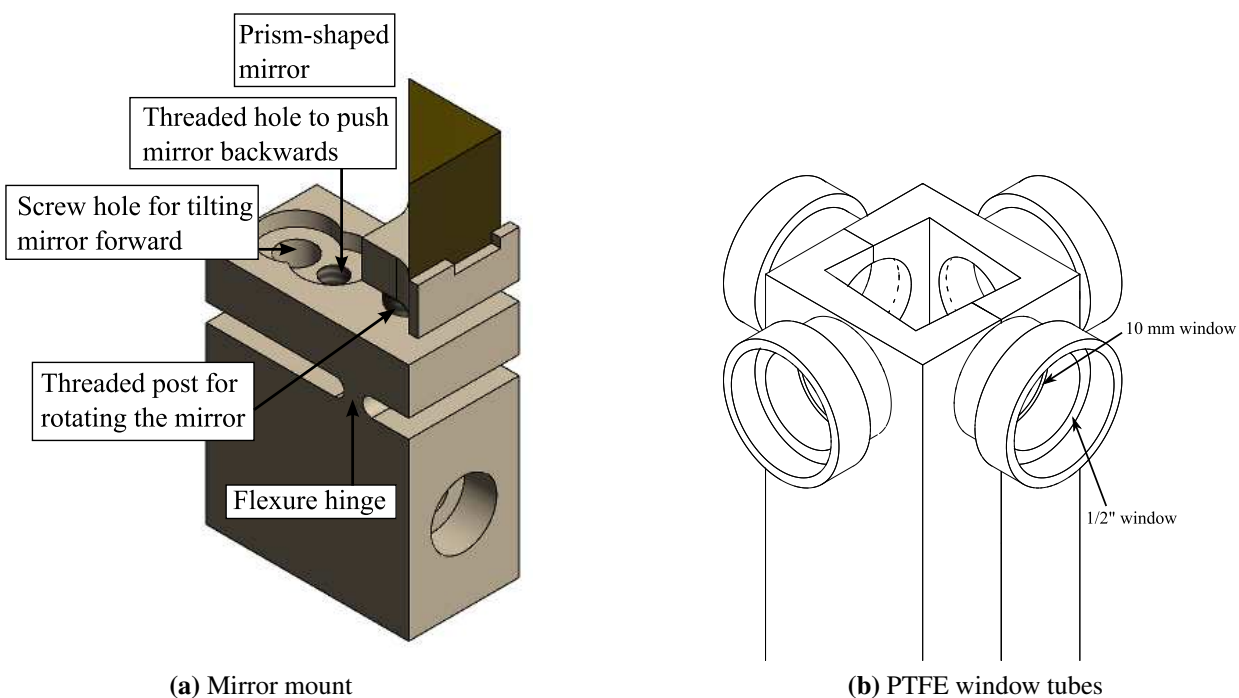


Figure 3.2: (a) Mirror mount for steering the probe beam. A single screw can be set in either the through hole (with a threaded hole in the block beneath) to pull the flexure hinge and tilt the mirror downwards, or in the threaded hole to push against the block below and tilt the flexure hinge and mirror upwards. The mirror sits on a mount attached to the flexure hinge with a threaded rod so it can be rotated about its axis. (b) A diagram of four window tubes. There are staggered insets for two different diameter windows (10 mm and 1/2 in). The windows have a tendency to fall out, but can be kept in using FEP tape stuck along their outer rim to provide pressure between the tubes and the window edges.

3.2 Optics and mounts

Cuts must be made in the thermal insulation to allow optical access. Heat loss through these cuts is limited by Teflon tubes that are loosely fitted against the heat sink in the insulation, and which hold two AR-coated windows separated by a thin air gap, as shown in figure 3.2(a). In addition to providing better thermal insulation, these tubes provide a clear optical path maintained free of debris from the stringy/powdery Aerogel cloth. We have noticed occasional (building up over months) deposits on the windows of a white, dusty substance. The source of this material is probably white PTFE thread-tape that we have used to clamp the heatsink pieces together, and which we have found to bleach over time. Further investigation revealed PTFE tapes have varying maximum use temperatures and not all are suitable for the SERF oven. The optics tubes were designed to be removable for cleaning as a result of this buildup. However, we have some initial indication that the magnetometers perform just as well without the optics tubes, and it would be interesting to see if they are truly necessary in the future.

Figure 3.2(b) shows the plastic mirror mounts which enable steering the probe beam through the cell and detection optics. Rotation is accomplished by turning the mounts on a threaded rod, while standard screws tilt the mirror by pulling/pushing the plate holding the mirrors to/from the mirror mount base. The base and mirror plate are attached through a flexure hinge. Mounting is eased by the use of rectangular prism shaped dielectric mirrors.

Figure 3.3(a) shows a schematic of the optical elements used to operate the magnetometer. The pump beam is collimated by a single lens or lens system to achieve the desired pump diameter (collimated beam waists from 0.5–2.4 mm were used in this work), then sent through a Glan-Taylor polarizer aligned with the output of the polarization maintaining fiber to maximize the transmitted light. Finally, a 0-order quarter waveplate is used to circularly polarize the output beam. Figure 3.3(b) shows a CAD image of all the optics in the schematics of figure 3.3(a). Both lasers are fiber-coupled from sources outside the MSR. The pump beam path goes through the central 1” bore (tapped with Thorlabs’ 1.035”-40 threads).

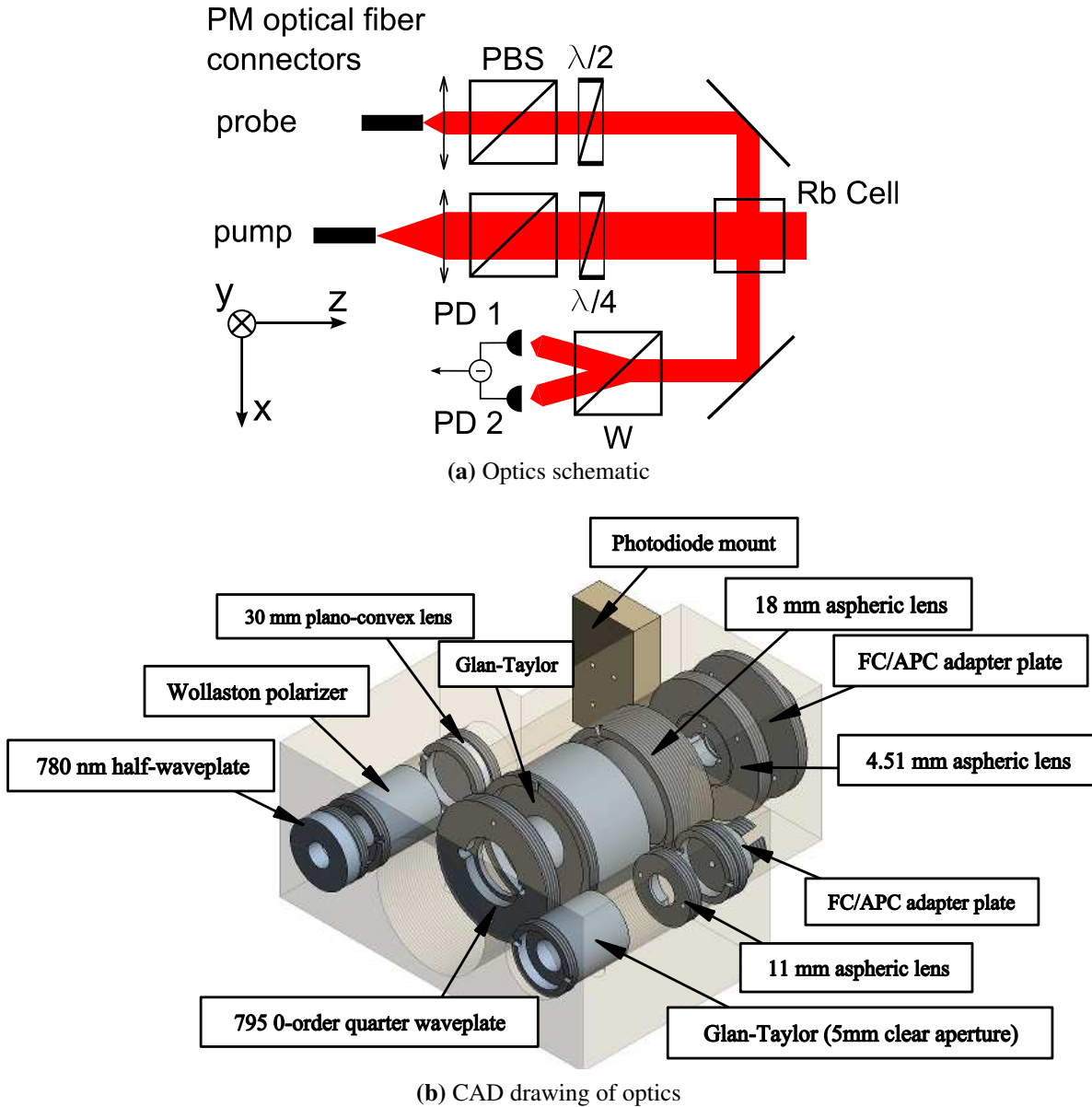


Figure 3.3: (a) Schematic of the optics necessary for operation of the magnetometer, including creating a circularly polarized pump and a linearly polarized probe with balanced polarimetry on the probe. (b) CAD image of the optics tubes, which is transparent to show the optics mounted inside. Tubes are meant to be compatible with Thorlabs parts, using Thorlabs threading (either 0.535-40" or 1.035-40"). All parts are either mounted in externally threaded adapters, or are held in place by retaining rings. The optics configuration shown here produces $w_{0,pu} = 2.5$ mm, $w_{0,pr} = 1.1$ mm

There are two 0.5” collimation tubes (tapped with Thorlabs’ 0.535”-40 threads). The output of the probe polarization-maintaining fiber is collimated by a single lens or lens system (collimated beam waists of 1.2–2.35 mm were used in this work) and sent through a linear polarizer. After being reflected through the cell by the two mirrors in figure 3.2(b), there is a 0-order half-waveplate, a Wollaston polarizing beam splitter, a focusing lens, and the photodiodes wired to produce a difference signal.

The fibers are single-mode polarization maintaining (PM, terminated in FC-APC connections). We have found these connections can become magnetized, and periodic demagnetization has significantly decreased the residual magnetic fields at the cell sensor volume. Additionally, the polarization of the lasers gets rotated in the fibers by 1/100-1/1000. This would look like a signal if not for the polarizer in the probe path on the output of the probe fiber. We fully discuss this effect in chapter 5.

3.3 Electronics

A single atomic magnetometer operating in DC-mode has four separate electronic subsystems: cell heaters and thermistor, nulling/calibration coils and coil driving circuitry, and the photodiodes with transimpedance amplifiers, and an analog to digital converter (ADC) acquisition system.

The electronics requirements for an atomic magnetometer operated in a MSR present a unique set of design challenges. At typical calibrations, $1 \text{ fT}/\sqrt{\text{Hz}}$ level sensitivity requires detection of $\text{pA}/\sqrt{\text{Hz}}$ level electrical currents, sometimes near DC. This task is complicated by the requirement that detection electronics not generate excess large gradient DC fields or excess magnetic field noise. Additionally, the magnetometer must be portable (to get it out of the way when the MSR needs to be used for SQUID measurements) and actual biomagnetism measurements require it to be flexibly positioned.

The easiest way to satisfy most of the requirements is to use long flexible electrical cables and to put the electronics outside the MSR. This is the tact we have taken in this work, yet it is at odds with generally accepted low noise analog electronics techniques, which preference shorter cable

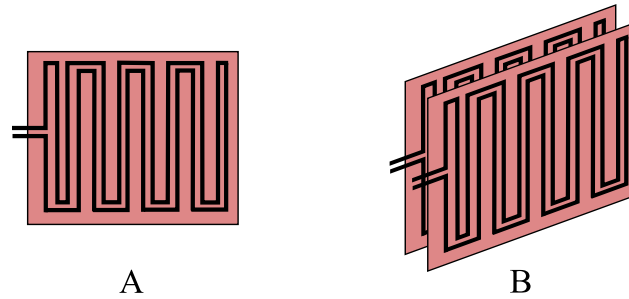


Figure 3.4: (a) Illustration of the current path in the cell heaters. (b) Putting two heaters back to back and wiring them in anti-series helps suppress the magnetic field produced by heater currents. Each cell uses two sets of these heater pairings, wired in series to reduce the magnetic field further.

lengths, especially for photodiode leads. The electronics components described here indicate a balance of these competing objectives.

3.3.1 Heaters and thermistors

We begin with the heaters and thermistor. The cells were operated at a temperature of 140–180 °C. Each magnetometer requires 4 W of heater power in thermal equilibrium at 145 °C, corresponding to electrical currents near 0.5 A, large enough to produce potentially disruptive magnetic fields and gradients.

The heaters are Minco thermofoil (model #HR5578R4.6L12A), covered in a silicone coating. Each heater has a resistance of 4.6Ω and is a $19.05 \times 19.05 \text{ mm}^2$ square, with a small protrusion for the heater leads. The heater foil is patterned in a 2D plane (see figure 3.4). This allows matching two pairs of heaters so that currents in the heaters go through the same path but opposite direction, suppressing the amplitude of the fields produced by the pair. The magnetometers used in this work have two sets of pairs all wired in series, which are oriented to suppress the residual fields even further. When only a single magnetometer is used, the dipolar field pattern expected from the heater sets ensures $B_H \sim \text{pT}$ and are easily cancelled by the application of suitable bias fields. In this case, DC currents can be used without any change in noise level, although there are noticeable shifts in the magnetometer offset.

When the magnetometers are placed in an array, the field $B_{H,ij}$ produced at magnetometer i by magnetometer heater j for each heater is different and depends upon the details of the spatial

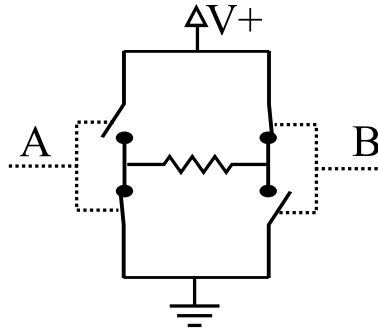


Figure 3.5: H-bridge schematic diagram. The switches are controlled synchronously by digital signals A and B to switch the connection polarity across the load.

configuration of the system. Additionally, dipolar patterned fields from the heaters may make the fields $B_{H,y,ij}$ larger for $i \neq j$. Cancellation of these fields by a single tri-axial set of nulling coils is impossible. This problem is solved either by adding coils to individually adjust the magnetic fields in each cell, or by operating the heaters at AC frequencies fast compared with the Larmor frequency associated with the heater fields, i.e. $\omega_H \gg \Omega_H$. For the AC case, the atoms respond to the time-averaged field, which of course is zero. Using the standard H-bridge circuit (see figure 3.5, and described in detail in appendix E), we can use a single DC source and reverse the current through the heaters at rates of 100 kHz or more. This frequency allows the weak requirement that the heater fields be $B_H \ll 25 \mu\text{T}$ at the magnetometers to prevent heater-related response from the magnetometer. When using the heaters at AC, we have noticed that the silicone encapsulating the resistive heating element tends to disintegrate and leave behind its fiberglass mesh substructure. This substructure is insulating as well, and we have not had any problem with the heaters shorting. Chopping the current direction through the heaters introduces a noticeable amount of electronic noise at high frequencies, which gets attenuated and aliased into the frequency band of our noise measurement. Since the noise looks like it comes from 10 MHz ring-down of some transmission line, this may be fixed by using purely sinusoidal heater drivers.

As described in section 3.1, the time constant for reaching thermal equilibrium for the magnetometer is around 40 min. This makes heating at constant output power inconveniently slow, even when the steady-state power is known in advance. A software feedback loop is used to control the heaters to optimally reach their set-point, using the thermistor read by a NI PXI-4065 DMM to

measure the temperature. When more than one magnetometer is operated at once, a digital circuit switches which thermistor is connected to the DMM, and the software PID state is stored for the next iteration. This feedback loop must be disabled while the FPGA is acquiring data, mainly because the data acquisition program and heater control program compete for resources and the currents used by the DMM to measure the resistance of the thermistors produces a magnetic field noticeable to the magnetometers. A future design of the magnetometer should consider using thermocouples to measure the temperature. Many thermocouple types utilize magnetic materials, such as chromium or iron, but type-T thermocouples (Copper-Constantan) should be acceptable.

We have found some thermistors contain magnetic components, typically in the leads. The thermistors used here are nonmagnetic, Honeywell 112-103FAJ-B01, 10 k NTC type. Details about the thermistor can be found in appendix E.

3.3.2 Coils and coil drivers

Each magnetometer has a set of tri-axial square coils centered around the cell detection volume. These coils are used for nulling the external fields to reach the most sensitive magnetometer regime, for the application of calibration fields to characterize the magnetometers, for the application of large magnetic fields necessary for z-mode modulation, and for feedback operation (see chapter 6). Noise in the circuitry used to drive these coils results in self-inflicted magnetic field noise at the magnetometer, causing a corresponding decrease in SNR. Even worse, the noise at each magnetometer is uncorrelated, eliminating suppression by difference detection. A coil driving circuit was designed as part of this work is described in detail in appendix E. Its main purpose is coupling an adjustable DC offset to an arbitrary applied field with the lowest possible resulting current noise. It has a potentiometer to control the DC offset and a BNC front-panel connector to couple any other signals onto each axis. On the lowest (experimentally usable) noise setting, it currently has a floor of about $3 \text{ fT}/\sqrt{\text{Hz}}$.

The final electrical component is the photodiode amplifier. We use SRS 570 current to voltage converters. These devices have widely configurable gain and filtering options. Anti-aliasing filtering is performed with the configurable front-panel filter options of these detectors. We typically use 12 dB 300–1000 Hz low pass filtering for DC mode operation and sampling at 20 kHz.

In our effort to keep electronics outside the shielded room, the photodiode leads are quite long (10 m). This is generally inadvisable [Hobbs, 2000]. We have found that in order to minimize electronic pickup noise, some attention must be paid to the wiring itself. For low noise shielded design with easily purchased modular components, we have selected Cat. 6 shielded twisted pair Ethernet cable. This cable contains four pairs of twisted pair conductors, each with a different turns ratio to minimize cross-talk and the entire cable is shielded with copper foil (some cheap cables come with steel shielding, so each cable should be tested with a magnet). The signals on each cable are selected to have relatively uniform range to further limit cross-coupling. For example, the heaters are all on a single Cat. 6 cable, the photodiodes on a different one, and then one cable each for the three sets of nulling coils and the thermistor of a single magnetometer. The cable shields are all grounded on one side, outside the shielded room.

We have also notice 60 Hz and harmonic pickup is limited by replacing the standard AC outlet equipment cables with shielded ones.

3.3.3 Data acquisition system

One significant part of this work was streamlining the data acquisition (DAQ) process to alleviate the difficulties in optimizing the system and to make the device more amenable for use with human subjects.

The signal from a SERF magnetometer depends on many particular parameters of the experiment, and hence must be calibrated with a known magnetic field in order to have an absolute measurement of the background field amplitude, which is most important for characterizing the noise floor of the magnetometer. The magnetometer response (2.38) changes when just about any experimental parameter is changed. It is sensitive to all parameters of the pump and probe lasers (intensity, frequency, and waist), the temperature of the vapor cell, and the ambient magnetic fields

when the measurement is performed. Further, it can be difficult to determine using a real-time measurement whether the SNR is being improved or degraded when changes are made to the experimental parameters. One common problem is adjusting the probe power, where the photodiode signal size increases with probe power, but the noise can either decrease or increase depending on the probe frequency and other system parameters (see chapter 6 for a detailed analysis of this and other noise issues).

Quick calibration mitigates these problems. The original DAQ program was written and developed as part of this work to work on LabView DAQmx devices, specifically the PCMCIA DAQcard-6024E, and to calibrate and analyze information from a single magnetometer. This structure has been expanded to four channels and improved by Matt Kauer to operate on an FPGA-based DAQ device (NI PXI-7851R). A block diagram of the program is shown in figure 3.6, consisting of four main phases:

- Calibrate the frequency response of the output circuitry that drive the calibration coils
- calibrate the magnetometer frequency response, accounting for the output circuitry and frequency response in the coils themselves (if any)
- take a recording without any applied signal to measure the noise power spectral density (PSD)
- Have the option of reusing the same calibration to take other noise measurements

These separate steps are discussed in detail in chapter 4.

Typical sampling parameters for the measurement period are 20 kHz sampling frequency (to avoid aliasing, we down-sample to 1 kHz during analysis) and 5-300 s sampling period. The signal is typically only conditioned with output filters on the transimpedance amplifiers described previously.

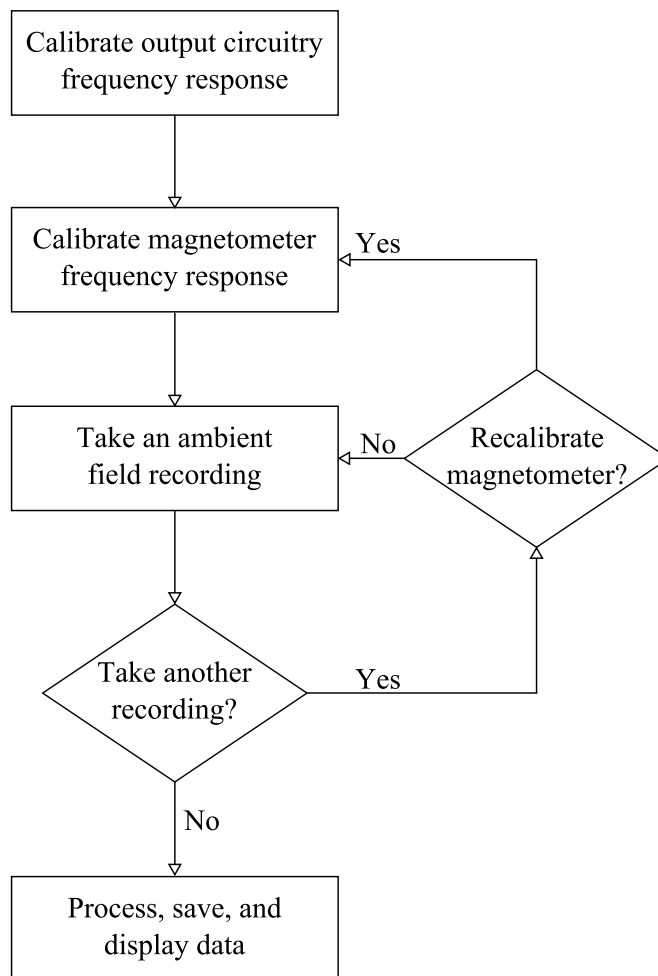


Figure 3.6: Flow chart of the magnetometer characterization program. The magnetometer does not need to be recalibrated before every noise run. Generally, if nothing has been intentionally changed, the same calibration can be reused until the DC fields have significantly changed.

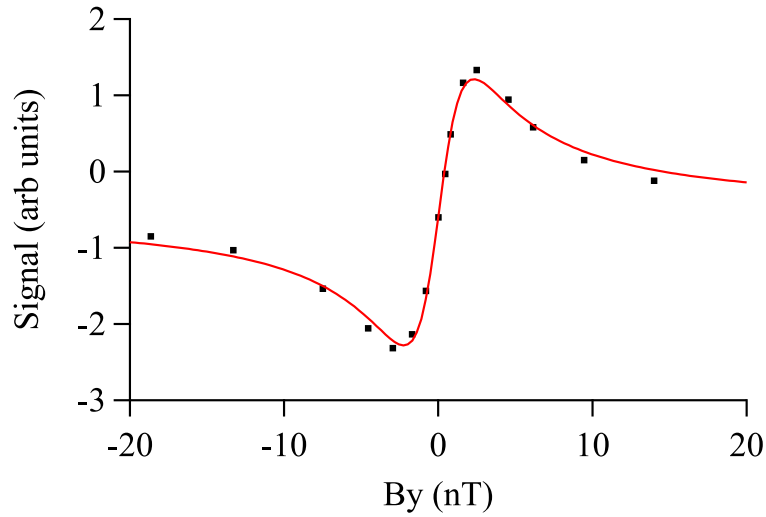
3.4 Magnetometer array

The magnetometer described above is a complete unit, encapsulating all the necessary parts to operate in the SERF regime. As a result, individual magnetometer channels are unconstrained with respect to one another, due to local fiber coupled optics and individual magnetic field control at each cell. Making an array of such units is as easy as constructing them and ensuring the operation of one does not interfere with another. In the work described here, we have operated with an array of four such magnetometers, and the only limits on expanding the system are in acquiring additional auxiliary equipment needed to run the magnetometer (power supplies, data acquisition devices, etc).

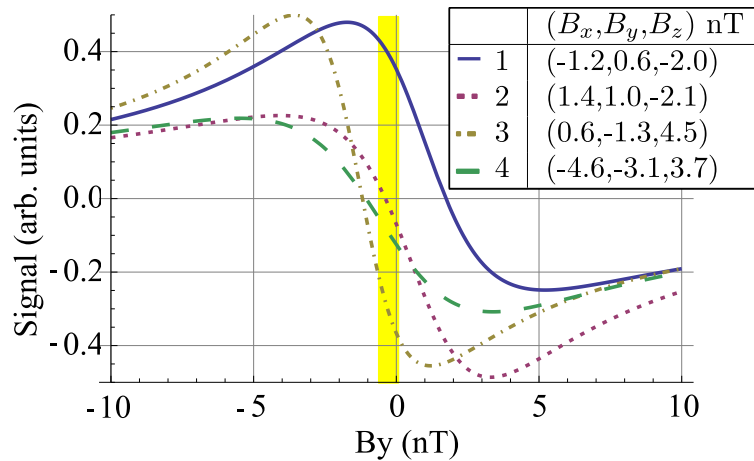
DC fields in the MSR, 10–50 nT, decrease the fundamental sensitivity according to (2.24) and require nulling. Figure 3.7(a) shows a sweep of B_y and a fit with $R = 400 \approx \Gamma$ to (2.24) with $\Omega_x, \Omega_z = 0$. For this R , B_y must be nulled to better than $|B_y| \leq 2$ nT to remain in the sensitive linear region of the response. If the MSR magnetic fields were sufficiently uniform, we could use a single set of tri-axial coils with side length a and array channel baseline spacing d such that $a \gg d$ to simultaneously cancel the magnetic fields at all magnetometers. Having tried this, we have found two problems with this approach that resulted in the choice of small individual cancellation coils for each magnetometer.

First, residual MSR magnetic field gradients are too large on the scale of the spacing of our magnetometers to allow a uniform nulling field to be used. Figure 3.7(b) shows the response predicted by (2.24) for four magnetometers in the presence of measured MSR magnetic field gradients and R from the fit in figure 3.7(a). B_x , B_y , and B_z are the differences from the measured zero values at each magnetometer channel. As shown in figure 3.7(b), these gradients cause a decrease in both the single channel sensitivity and the effective multichannel B_y operating range (highlighted in yellow), which has been decreased by a factor of 4 to $|B_y| \leq 0.5$ nT.

Second, and most importantly, are the effective fields caused by the pump laser, described in section 2.5. At high optical depths corresponding to high temperatures, the pump beam is absorbed before polarizing the entire cell length unless it is detuned $\Delta\nu_1 > 1$ from resonance, resulting



(a) Swept field response (points) and fit (line)



(b) Simulation, using the width in (a)

Figure 3.7: (a) Magnetometer signal as a function of applied field (dots) and a fit to an amplitude scaled version of (2.24). (b) A simulation of P_x for multiple magnetometers in the presence of the measured magnetic field gradients from the zero values at each channel. With only a single set of tri-axial coils, these are the minimum gradients in the shielded room, and represent the best-case operating point for the four magnetometers. In this case, a compromise value for B_y must be chosen, reducing the usable operating range. This illustrates the need for local control over the magnetic fields at each cell.

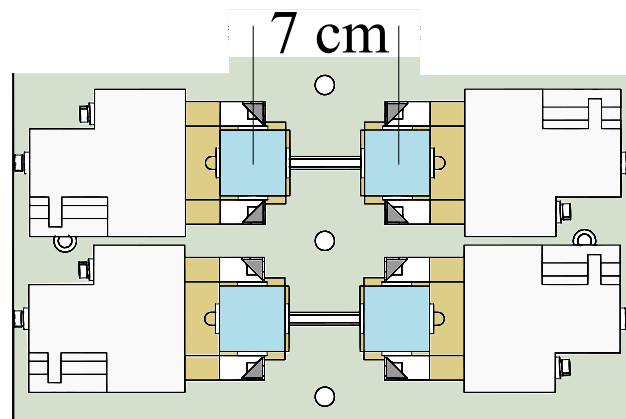
Table 3.2: A summary of the various options on where to set pump parameters to operate the magnetometer. Qualitatively, for high optical depth cells and uniform pump transverse profile, it is difficult to simultaneously satisfy the three desired optimum conditions: $R = \Gamma$, $\Omega_{LS} = 0$, and pumping the entire cell.

R_0/Γ	$\Delta\nu/(\Delta\Gamma/2)$	Polarization	light shift	total sensitivity
1	Low	Low	Low	Low since atoms not polarized
High	Low	High	Low	Low since $\frac{R}{(R+\Gamma)^2} \ll 1$
1	High	$\frac{\Omega_{LS}}{R} = \Delta\nu/(\Delta\Gamma/2)$		Low since high light shift
High	High			

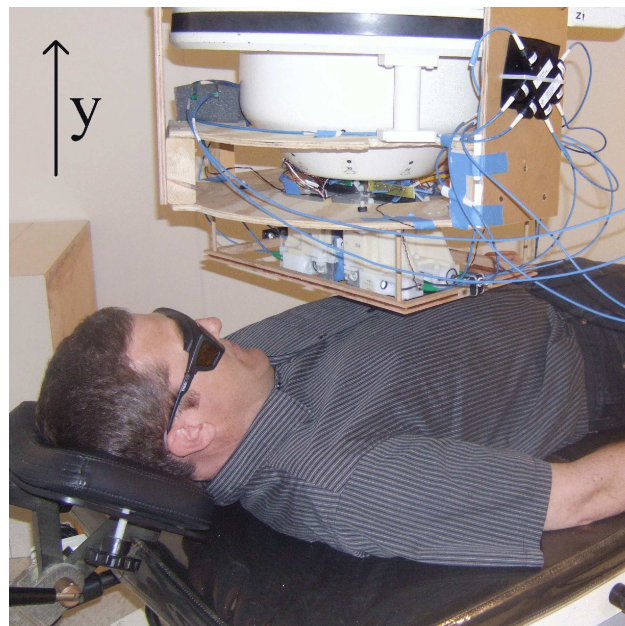
in a nonzero Ω_{LS} . In other words, looking at pump propagation through the cell (figure 2.18), considering the equation governing the magnetometer sensitivity ((2.35)) and the light shift as a function of detuning (figure 2.19), there are essentially three operating regimes, outlined in table 3.2. For high optical depth cells, there is no way to simultaneously optimize $R = \Gamma$, $\Omega_{LS} = 0$, and maintaining pump light throughout the cell.

The magnitude $|\Omega_{LS}|$ is roughly the same from cell to cell, but the direction with respect to the nulling coils depends on the orientation of the magnetometer and the direction of \hat{s} . For our laser parameters, we expect the pump light to cause effective fields of magnitude ~ 50 nT. Orienting all the magnetometers to have the same light shift with respect to the external coils mitigates the problem, though the nonuniform light shift within each cell due to the spatial intensity profile of the laser results in a broadening of the magnetometer linewidth [Appelt et al., 1999]. The light shift still presents a problem for the prospects of differing individual channel orientation and tilt, or nonplanar arrays. There are also practical problems associated with large coils, such as limited magnetometer adjustment and complications with calibration fields when the magnetometers are not aligned with the coil axis. These problems are all solved by using individual sets of coils for each magnetometer.

The magnetometers were mounted on a plastic mounting plate which allows the adjustment of the magnetometer baseline spacing figure 3.8. This baseplate is mounted to an existing SQUID gantry in the MSR, which allows 6-axis adjustment of the magnetometer position. Figure 3.8(bottom) shows a photograph of the array mounted to the gantry in the MSR. Human subjects lie on a bed



(a) Array schematic, from above



(b) Photo of array mounted to gantry above subject

Figure 3.8: (a) Four channel magnetometer array, with 7 cm channel spacing. This array is mounted on an existing SQUID gantry top-down, as in the photo (b). In adult subject trials, the subject lays on a bed and the array is centered over the subject's heart by equalizing the signal in all four channels in real time. For fMCG studies, the array is angled and positioned below the naval. The \hat{x} , \hat{y} , and \hat{z} axes in the text refer to magnetometer body axes. Here, all \hat{y} are aligned and correspond to the sensitive direction for all magnetometers.

under the array, which can be translated, rotated, and tilted using the gantry controls. For convenience in these initial tests, our measurements were made with planar square array and channel spacing of 7 cm. Physical limitations permit a 4.5 cm minimum planar array spacing for all four elements. More magnetometers can be added, with 7 cm spacing in the vertical direction of figure 3.8(a), while the optics tubes require the spacing in the horizontal direction to be >10 cm. In our setup, the four elements operate independently and could be tilted or translated with respect to one another by adjusting their mounting to the plate. It should be straightforward to implement non-planar geometries.

Using three layers of 2 mm thick thermal insulation and including the distance from the front of the cell to the position of the center of the intersection of the pump and probe beams, the minimum physical distance to the skin for each magnetometer in this design is about 1 cm. When using the magnetometers, we typically avoided putting them in direct contact with the skin, as normal breathing motion tended to cause the subject to bump the device and produce vibration noise. The safety margin was on the order of an additional 1 cm spacing from the skin (2 cm total), somewhat larger than Knappe et al. [2010], where where the reported distance was 5 mm from the skin. Better engineering would allow the 1 cm minimum distance to be used in measurements.

Chapter 4

Data Collection and Analysis

This chapter describes the characterization and operation of the magnetometer, as well as commonly used signal processing techniques for the application of biomagnetism. After the previous chapters on the basic theory and apparatus design, this chapter serves as something of a manual for the actual use and characterization of the magnetometer.

The initial setup of the magnetometers includes alignment of the laser paths, initial balancing of the polarimeter, and residual DC field nulling. After this procedure, the magnetometers should be as close as possible to the zero field regime, and at their most sensitive given other experimental parameters. Then each channel's response, both amplitude and phase, are calibrated against known applied magnetic fields.

After the calibration phase, the magnetometers are ready to measure fields of interest. For characterization of magnetometer performance, these are the background fields in the MSR, while for biomagnetism these will be MCG or fMCG.

4.1 Setting up magnetometers to operate in DC mode

For biomagnetism studies, the array is mounted on the SQUID gantry. Each magnetometer is aligned separately. The only flexibility in the pump beam path is in the relative orientation of

the optics tube to the cell holder, so the first step is aligning the pump beam with the cell. We have found it sufficient to align the pump beam to travel through the center of the front and back windows.

The probe beam alignment is performed using the mirrors (see figure 3.1 and figure 3.2) with the orientation of the optics tube fixed. As described in section 3.2, the mirror mounts allow mirrors to be rotated about their center and, using one of two screw holes, tilted back and forth. One of the tilt screws should be used for each mirror mount, even if it is not necessary, to minimize vibrations that would occur in the otherwise unconstrained flexure hinge assembly.

Once the beam paths are aligned, the polarimeter needs to be balanced. This is done by blocking the pump beam (to ensure $P_x = 0$), and measuring the output of the transimpedance amplifier. The half-waveplate in figure 3.3 is used to zero the output signal (balance the intensities on the differential photodiodes). Sometimes this probe-only signal will be unstable, with larger than normal low-frequency noise in the signal. This indicates either a gross misalignment of the polarization maintaining fiber such that the output polarization drift is large (see section 3.2), or more likely an increased sensitivity to the alignment of the probe beam, which varies slowly with stray air currents and temperature fluctuations of the system.

In the latter case, the increased sensitivity can often be removed by more careful probe beam alignment, ensuring the beam path traverses through the center of the optics rather than too near their edges, and that the light incident upon the photodiodes is centered on the photodiodes and does not overfill them. The same symptoms occur when the probe intensity is too high at the photodiodes, presumably causing non-common mode nonlinear response in the photodiodes themselves. This can be simply tested by decreasing the probe intensity and rechecking the noise spectrum. Finally, we have been able to decrease this low frequency type noise by measuring photodiode response vs. intensity curves and choosing uniform pairs to make the balanced polarimeter. This process is labor intensive and provides marginally better than random matching. In the future, photodiode pairs constructed on a single chip should be considered to minimize differences due to manufacturing processes.

4.2 Residual field nulling

The nulling process is similar to previous DC mode SERF magnetometers [Li, 2006, Seltzer and Romalis, 2004] and makes use of terms proportional to orthogonal fields in the steady-state response (2.24), which we reprint here for convenience,

$$P_x = P_z \left(\frac{\Gamma' \Omega_y + \Omega_x \Omega_z}{\Gamma'^2 + \Omega_z^2} \right) \approx P_z \frac{\Omega_y}{\Gamma'}$$

From the equation above it is obvious that the magnetometer will respond with the application of a field Ω_x only if $\Omega_z \neq 0$, and vice-versa. We find the DC null fields for a single magnetometer as follows:

- sweep B_y and set the operating point in the center of the dispersive curve (figure 2.12a), where the magnetometer is most sensitive.
- apply a ~ 50 pT oscillating field $B_0 \sin(\omega t) \hat{x}$ at 10–30 Hz and adjust B_z until there is no response to B_0 , ensuring B_y remains at its most sensitive operating point. If the response is difficult to find at first, a larger field may be used.
- apply $B_0 \sin(\omega t) \hat{z}$ and adjust B_x to null the response, again ensuring B_y is adjusted to maintain maximum sensitivity.
- repeat until residual response to B_x and B_z is minimized.

For the modular four-magnetometer array, we repeat this procedure for each individual unit. Iterating the procedure two times eliminates any offsets of the local field at the first magnetometer caused by adjusting the fields in the later ones to below the adjustment procedure sensitivity. The easy extension of the single magnetometer nulling procedure to all four magnetometers is one important feature of the modular array.

There is no cross-talk between our four channels because the magnetometers are fundamentally passive devices. Non-uniform light shifts from the Gaussian pump laser intensity profile cause non-uniform effective magnetic fields as in (2.56). Due to the residual Ω_z term in (2.24), each magnetometer retains some sensitivity to B_x . This is typically a correction of $\leq 10\%$ and its effect is ignored when characterizing the magnetometers.

As discussed in section 3.4, the magnetometers must be within approximately 1 nT of their null point in order to maintain uncompromised sensitivity. Background field variations in the shielded room are typically smaller by an order of magnitude or more on the timescales of a 30 s MCG measurement. Long-term variations can take the magnetometers outside of the optimal measurement range, but are easily compensated between measurements. Very occasionally, the DC offset of the fields in the MSR will shift a large amount on an inconvenient timescale (i.e once per few minutes), which essentially prohibits the use of the magnetometer. The source of these fields is probably the construction of a building physically near the MSR, including slow moving cranes, large trucks, and industrial elevators. If the changes are only in the detection direction, they can also be compensated by negative feedback of the magnetometer signal to the magnetic coils, which we will discuss in detail in section 6.1.2.

4.3 Characterization procedure using DAQ program

Once the DC null fields have been set, each magnetometer is simultaneously characterized using the DAQ program. The normal characterization and data acquisition stages described below all use sampling frequency $f_s = 20$ kHz, with a two-pole low-pass filter set between 300–1000Hz, using a 16-bit FPGA digitizer.

4.3.1 Coil driving circuit calibration

Digital to analog converter (DAC) outputs on the FPGA board allow the DAQ program to send signals to the magnetometers. However, these signals need to be conditioned and converted into properly sized current sources to drive the magnetic coils. The coil control electronics box (see appendix E) has a control input for this purpose. The input voltage is scaled, added to a DC offset set by a front-panel potentiometer, and applied to a voltage to current converter subcircuit, which produces a constant voltage across an output resistor R_o . If we take the input voltage to the coil control box produced by the DAQ system as V_i and the output voltage across the output resistor as V_o , then the complex gain of the output circuit

Table 4.1: A list of frequencies, in Hz, used to calibrate the magnetometer frequency response. 8 cycles of each frequency are applied to the device under test and the response detected.

2.57	5.45	18.7	29.3	37.5	37.5	53.2	69.7	75.1	83.3
91.9	101.3	113.7	129.1	134	153.7	167.7	189.3	197.5	

$$A(\omega) = \frac{V_o(\omega)}{V_i} \quad (4.1)$$

is characterized by applying a known, constant amplitude sinusoidal signal $V_i(t) = V_i \sin(\omega t)$ at frequencies across the 200 Hz bandwidth of interest and recording $V_o(\omega)$. V_i is applied for a length of time $T \geq 8 \times \frac{2\pi}{\omega}$, and then the resulting signal fitted to a sinusoid to extract the response amplitude and phase $V_o(\omega)$. Knowing the output resistance across which we measured the voltage and the magnetic field coil calibration $\chi(\omega)$ allow us to back out what magnetic field B_0 is applied to the magnetometer by using the output of the DAQ system and the coil control box,

$$B_0(\omega) = A(\omega)\chi(\omega)\frac{V_i}{R_0} = \eta(\omega)V_i. \quad (4.2)$$

Table 4.1 shows a table of all the frequencies used to characterize the magnetometer. The coil driving circuitry needs to be calibrated whenever the gain of the box is changed. In the absence of any changes, the DAQ program will calibrate the driving box once per day to account for slow circuit changes due to temperature and aging, and as a consistency check. Note that $\chi(\omega)$ is constant for the small coils wrapped around the magnetometers because their small size and spatial separation from any mu-metal ensures their inductive reactance is low compared to the coil-driving circuit output impedance at the frequencies of interest.

4.3.2 Magnetometer calibration and initial noise measurement

After $A(\omega)$ is determined, the magnetometers themselves need to be calibrated. The DAQ output remains connected to the coil control box (as above) but the DAQ input now reads the output voltage from the transimpedance amplifier (V_m). This frequency response is taken in the same way as described above to characterize the magnetometer response to an applied field,

$$\xi(\omega) = \frac{V_m(\omega)}{B_0}, \quad (4.3)$$

which can be rewritten using (4.2) as

$$\xi(\omega) = \frac{V_m(\omega)}{\eta(\omega)V_i}. \quad (4.4)$$

The technique described above determines $\xi(\omega_i)$ using (4.4) at the frequency points listed in table 4.1. Then $\xi(\omega)$ is extrapolated by fitting this function to an empirically modified version of the theoretically expected low field magnetometer frequency response (2.36),

$$|\xi(\omega)| = a \frac{\sqrt{\Gamma'/2}}{\sqrt{(\omega - \omega_0)^2 + (\Gamma'/2)^2}} \times (1 + b\omega + c\omega^2) \quad (4.5)$$

$$\arg(\xi(\omega)) = \frac{180}{\pi} \tan^{-1} \left(\frac{\omega - \omega_0}{\Gamma'} \right) \quad (4.6)$$

where the last term in parenthesis has small b and c coefficients to account for phenomenological differences between (2.36) and the actual measured curve, likely resulting from nonuniformities in the cell polarization and pump intensities.

The results of one such calibration are presented in figure 4.1(inset). At this point, the DAQ program measures the output of the magnetometer without any applied signal for several seconds, and uses (4.3) to deconvolve the unknown applied magnetic field which produces the measurement, V_m . The field spectral density ($\sqrt{\text{PSD}}$) is characterized to display the noise floor and identify any noise peaks using

$$\frac{\delta B}{\sqrt{\text{Hz}}} = \frac{\sqrt{\text{PSD}(V_m)}}{|\xi(\omega)|}. \quad (4.7)$$

Figure 4.1 is an example of the result of the calibration procedure described above. The points correspond to data taken at the various frequencies, and fits with 95% confidence intervals are shown overlaid on top, which allows for a 10% variation in the fit amplitude and uncertainty in the precise form of the frequency response, a problem for producing high quality difference signals. These measurements are normalized to the maximum in each measurement, but the overall response amplitude is different for each magnetometer.

4.3.3 Additional noise measurements (Probe and electronic)

The calibration procedure described in section 4.3.2 provides a measure of the *total* signal from the output of a magnetometer and treats it as if it were all generated by magnetic field. A perfect

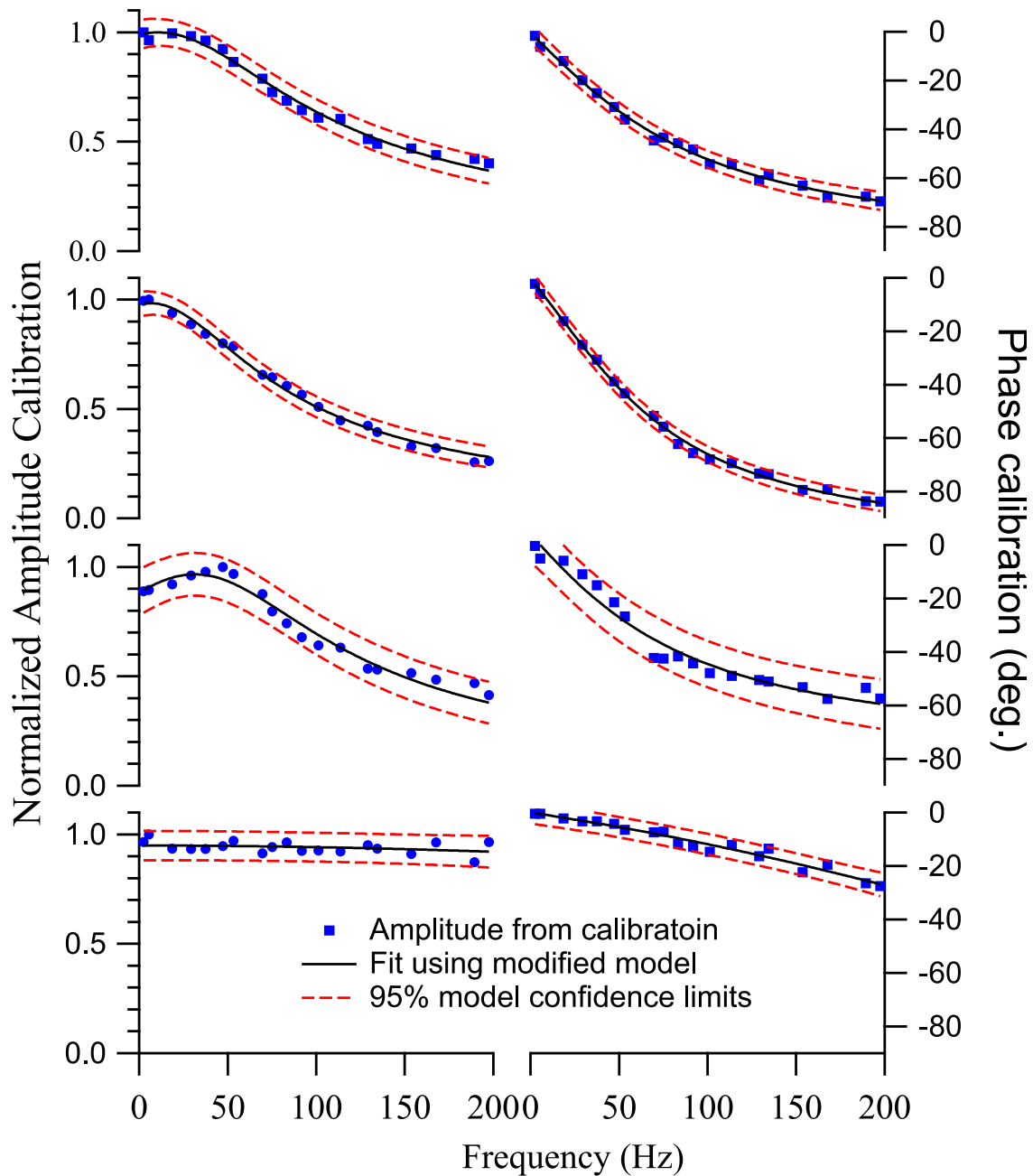


Figure 4.1: An example of the results of the amplitude and phase calibration. The blue points are the results of measurements of responses to the system at different frequencies (normalized). The solid black lines are fits to a modified theoretical model, and the red dashed lines indicate the 95% confidence interval for the fit model. The amplitude and phase fit parameters are not required to be consistent. The shapes of the curves for each channel are typical (e.g. channel 4 is always broad, channel 3 often has a nonzero central frequency). We are still unclear what is different in each cell to cause these discrepancies.

SERF magnetometer would be limited by quantum noise, and it is useful to estimate the noise from non-magnetic sources.

According to (2.24), blocking the pump beam and measuring the noise leaves the magnetometer insensitive to magnetic fields in any direction ($P_z = 0$), and the magnetometer signal is a combination of fundamental quantum noise (spin-projection and photon shot noise) as well as technical noise associated with electrical pickup and probe fluctuations kind. Treating this signal as an effective magnetic field (scaling it by $\xi(\omega)$) gives an estimate of the total non-magnetic noise in our system.

The argument above disregards two subtle signal sources that are sometimes important. First, noise induced by the pump beam will clearly not be detected when the pump beam is blocked. Several individual avenues are available for the pump beam to cause a change in signal: direct detection of scattered pump light by the photodiodes, changes in pump intensity or frequency causing changes in $\langle P_z \rangle$ averaged over the probe beam path, and changes in the pump intensity and frequency changing the effective field induced by the light shift (2.56), which couples time varying fields in the probe direction to P_x with time varying strength.

The purely electrical component of the noise of a magnetometer can be measured by blocking the pump and probe beams. We do not see any difference in the noise spectrum (although there is a small offset shift) between blocking and unblocking the pump, suggesting stray pump light itself is not an important factor. We will address two issues relating to changes in pump laser parameters in detail (chapter 5), but they can be large because of nonlinear absorption effects in the optically thick vapor cell. This type of noise manifests itself in differences between the magnetic noise floor of two channels, when not limited by probe noise. Thus, blocking the pump beam can underestimate the technical noise of the magnetometer in the case where the technical noise is induced by the pump itself.

The second subtle signal source is residual pumping by the probe beam itself. This can be caused by some remaining elliptical polarization in the probe beam. Considering the extinction ratio of the polarizers used for the probe ($> 10,000 : 1$), the most likely source of elliptic polarization is birefringence in the cell glass, perhaps induced through stress by physically clamping the

cells in the Boron-Nitride. Here, the atoms are weakly pumped to a polarization P_x determined in part by the fluctuating ambient field amplitudes. This effect causes the probe noise to over-estimate the non-magnetic noise level, since it adds back in magnetic noise. This effect is non-negligible, especially in channel 3, where the magnetometer retains obvious sensitivity to fields perpendicular to the normal direction DC-mode direction. This may be due to the higher pressure-broadened linewidth leading to higher probe absorption rates in this cell.

With these two caveats, we take the probe noise as a measure of the total non-magnetic noise of our system. Figure 4.2 shows the result of the calibration process, with both normal magnetic and probe noise. For the low-frequency components of the cell, the probe noise dominates, while the noise floor is dominated by other sources. The noise floor is constant over time, but residual sinusoidal magnetic fields often dominate the signal. Figure 4.2 shows a measurement with a relatively quiet background, displaying only a few such peaks near at 6.7, 50.5, 60, 101, and 120 Hz. The 6.7 Hz peak in particular is the largest background signal in the room, is well-characterized by a sinusoid, and is circularly polarized. We have verified that it emanates from a large HVAC fan located almost directly above the MSR on the next floor, perhaps 5–10 m from the center of the MSR. Though this makes real time analysis of the magnetometer signals difficult, large sinusoidal signals tend not to interfere with MCG measurement because they are narrowband and easily identified. Standard signal processing techniques can easily remove them (see section 7.2).

An important and often overlooked feature of figure 4.2 and figure 4.1 pertains to bandwidth. Looking at figure 4.1, one is tempted to conclude that the bandwidth of the magnetometers may be a problem for biomagnetic signals that require measurement of frequency content up to 100 Hz or more. If the signals were limited by the noise performance of the magnetometer alone, then this would be true. Inspection of figure 4.2 does not show a decrease in performance at the knee frequency of the calibration. The reason is because the magnetometers are dominated by magnetic noise, which is white. A more meaningful characterization of “bandwidth” would be the frequency at which the non-magnetic noise level of the magnetometer is equal to the magnetic noise level as the sensitivity of the magnetometer decreases. We can reasonably conclude from a measurement

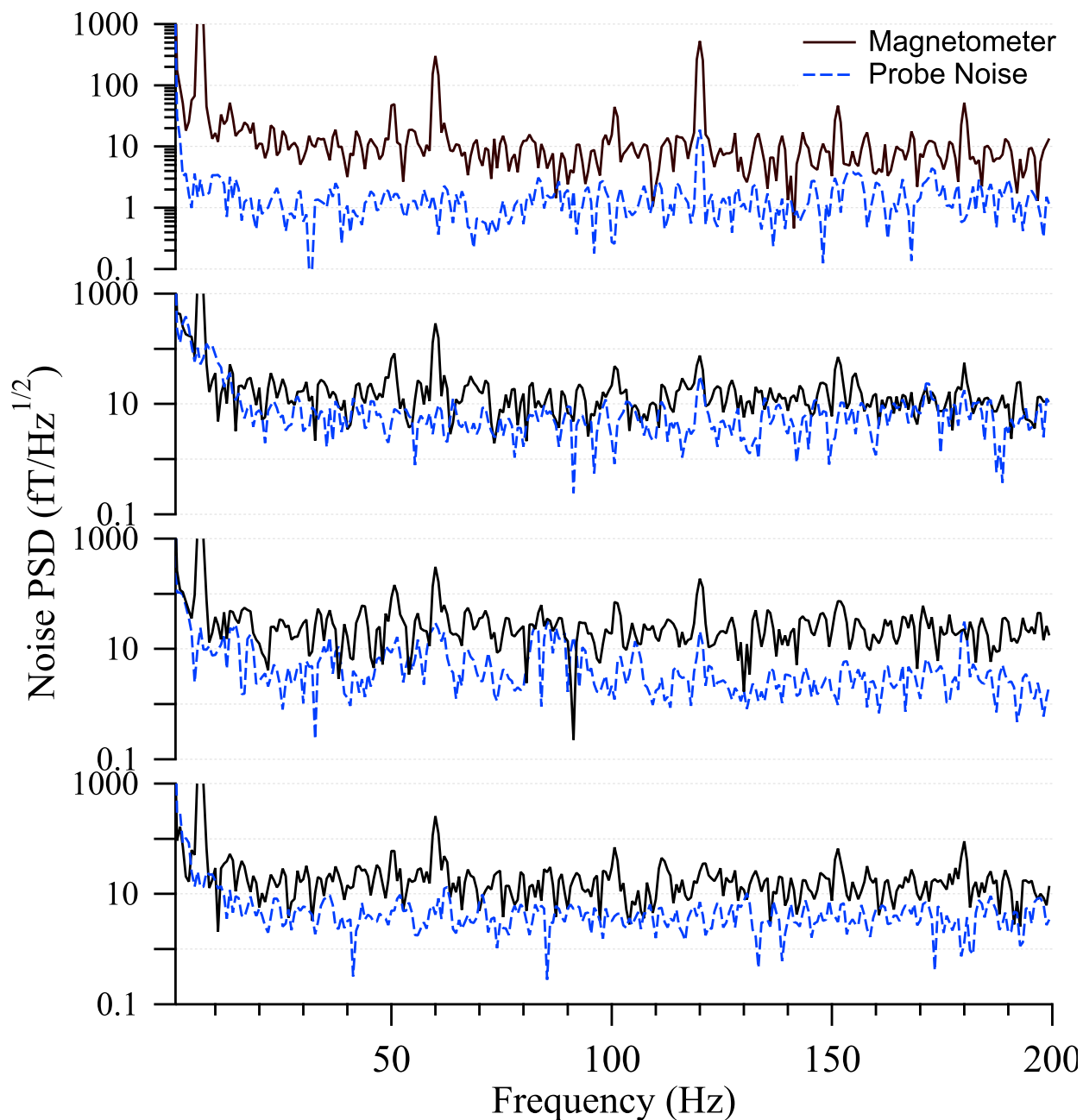


Figure 4.2: Calibrated noise measurements for the four channels (ch1 on top to ch4 on bottom), on a relatively quiet day. The 6.7 Hz peak from an HVAC fan is easily identifiable as the biggest signal in the MSR. This plot illustrates the typical relationship between magnetic noise and probe noise for each magnetometer (e.g. the probe noise in channel two is typically a larger fraction of the total noise than the other channels).

like figure 4.2 that the usable bandwidth of our atomic magnetometer in this particular MSR environment is over 200 Hz. Said differently, judging by the noise floor, one of our channels will perform as well as any other magnetic detector in the same shielded room to frequencies past 200 Hz, even if the other sensor is a SQUID magnetometer with a much higher bandwidth.

4.3.4 Chirp response measurement

Finally, the frequency calibration described above can be generalized to any swept-frequency measurement. For example, if we generalize the input amplitude for every sinusoidal frequency to a time-varying function, the response to that function, $V_i \rightarrow V_i(\omega(t))$ in (4.1) and (4.2), then the response to that function can be characterized by deconvolution (which is a generalization of matching amplitudes and phases of discrete sinusoidal signals).

We have recently switched to this process, using a frequency chirp signal applied to the magnetometers, and measuring the magnetometer response this way. The benefits to this technique are a faster calibration with better resolution between frequency points. Chirps measuring the same response take only a fraction of the time, mainly because the sinusoidal technique requires 8 cycles, which can take seconds for the lowest calibration frequencies. The disadvantages are that highly spectrally peaked noise components are more likely to interfere with this technique, since a chirp response continuously measures a signal.

The chirp response function used for the calibration is

$$V_i(t) = V_i \sin(Ate^{Bt}), \quad (4.8)$$

where A sets the base frequency scale and B sets the sweep velocity. A Labview VI (Frequency Response Function.vi) takes the applied chirp signal B_i and the response signal V_m and measures the frequency response function

$$\xi(\omega) = \frac{S_{im}(\omega)}{S_{ii}(\omega)} \quad (4.9)$$

where S_{im} is the cross spectral density of the stimulus signal with the appropriate conversion from output voltage to magnetic field given by (4.2) and the response, and S_{ii} =PSD of the stimulus signal. To help reject noise sources, four of these data sets are averaged for each magnetometer

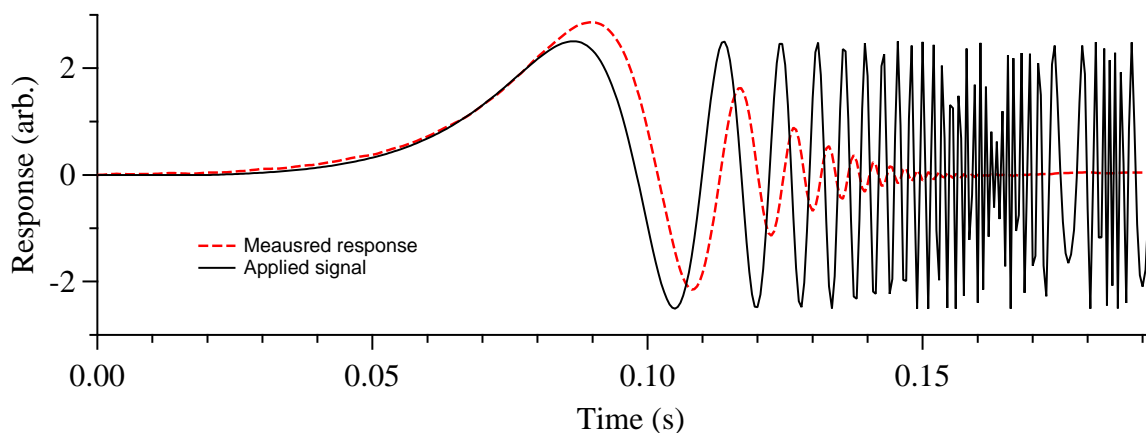


Figure 4.3: An example of the chirp calibration signal applied (black) to the magnetometers and the response (red). Using the chirp signal allows the magnetometers to be characterized more quickly.

to calculate the frequency response function. Figure 4.3 shows an example of the time series calibration signal represented by (4.8), and the magnetometer response from such a calibration.

4.4 Optimization

After characterizing the pump, probe, and electronic noise levels, we have a picture of how the magnetometers are performing. Table 4.2 gives a summary of the different types of measurements we make to characterize the limits the magnetometer noise level. We are satisfied when the magnetometer noise level is consistent with the expected background magnetic noise level of the MSR, which is around $4 \text{ fT}/\sqrt{\text{Hz}}$ including the noise from our current controllers (see chapter 5). This also requires the probe noise level to be significant below the magnetic noise level, important for accurate single channel measurements, but even more so for multichannel measurements where the noise suppression will depend upon the degree of correlation between the noise levels at each magnetometer, as will be discussed in more detail in chapter 7.

Often, these conditions are only partially met. For example, the probe noise might dominate the spectrum in the $1/f$ region of the spectrum, and then magnetic noise dominates, like in figure 4.2. Alternatively, it may appear the probe noise is limiting the performance when the electronic noise

Table 4.2: Different types of noise measurements used to characterize magnetometers. This characterization provides a feel for how the magnetometers are performing, and what is limiting them.

Measurement	Method	Noise level interpretation
Magnetic Noise	Nothing blocked	Same as probe: limited by probe noise Higher than probe: If channels are same, magnetic noise If channels are different, may be pump noise
Probe Noise	Block pump beam	Quantum noise plus non-pump technical noise and electric noise
Electronic noise	Pump and probe blocked	Noise purely from electronics (mostly pickup)

is too high. We briefly discuss the process of laser optimization in order to achieve the best noise performance, given information about the relative amplitudes of the three noise measurements.

First, if the noise level is dominated by electric noise, that means either the electronic noise level is too high, or conversion factor from field to output current by the magnetometer is too low. Sometimes the electric noise is too high because of a poor choice of settings on the I-V converters, such as forgetting to apply the anti-aliasing filters or using gain that is too low (500 nA/V is typical). Otherwise, we have worked pretty hard to eliminate electronic noise, so the easiest thing is typically to find a way to increase the magnetometer response, in terms of absolute signal.

Considering the difference in the performance of the magnetometers, it is best to optimize all channels simultaneously. A small oscillating magnetic field B_y , about the size of a normal calibration field and near 10 Hz, is applied to all magnetometers through a large coil. The amplitude of the response is marked, and then the pump laser frequency and intensity is tuned to increase or decrease the response. Once a maximum is found, the fields (especially B_z) must be re-tuned, and the process can be repeated. Watching all signals simultaneously ensures that, due to nonuniform temperature and relaxation in each cell, all cells respond adequately. This seems to be especially important for channel 2, where the response is always low compared with the others to begin with. If adjustment of the pump beam alone does not fix the problem, the probe beam can be adjusted as well. When electronic noise is most important, increasing the signal size is paramount.

If the probe noise is the largest noise source, the problem can be more subtle. For example, if the probe noise has mostly $1/f$ character, this might be the result of photodiode nonlinear response, coupled with slow variations in the exact position of the probe incident upon the photodetectors.

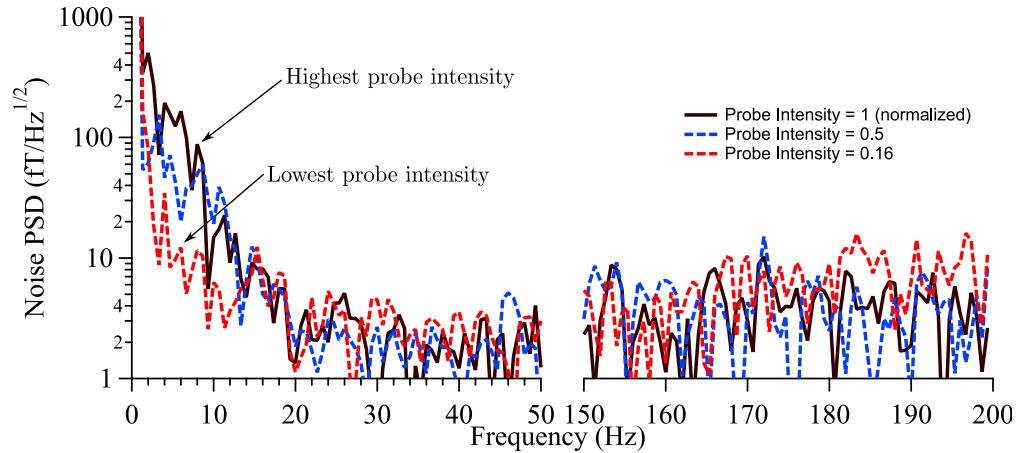


Figure 4.4: A plot of the probe noise for three different probe intensities. The highest was taken without any attenuation. In the other two, ND=0.3 and ND=0.3+0.5 filters were used to attenuate the probe light before the fiber splitter. Though the overall signal decreases when the light is attenuated, the $1/f$ amplitude also decreases. In the higher frequency ranges, electronic noise begins to be important where the bandwidth of the magnetometer decreases the response below the electronic noise threshold.

In this instance, *decreasing* the probe intensity (and so the response to a uniform applied field) can decrease the noise. As an example, figure 4.4 shows three different measurements for the probe noise under identical circumstance, except for probe intensity. The lowest intensity probe shows better $1/f$ noise performance but pays a price in the higher frequency noise level. The high frequency performance is compromised because the electronic noise overwhelms the probe signal at lower frequency for the same bandwidth, as we discussed in section 4.3.3.

4.5 Signal measurements

Adult signal measurements are performed similarly to noise measurements. After the magnetometer characterization has been performed, recordings of the ambient magnetic field can be taken with arbitrary length for 20 kHz sampling frequency. For biomagnetic signals, the longest continuous stretch required is 300 s (for fMCG measurements).

There are a couple of techniques we use when acquiring biomagnetic signals to minimize the time a subject must spend in the MSR. First, before the subjects arrives, the magnetometers are mounted on the SQUID gantry and put into position above the subject bed. Magnetic gradients in the MSR will cause the nulling fields to change as the magnetometers are physically repositioned,

especially for rotations which change the projection of the magnetometer plane onto the MSR floor/ceiling plane. The magnetometers are positioned near their anticipated operating point to minimize the required adjustments. Second, the pneumatic bed is lowered so that the subject can slide comfortably underneath the magnetometers and into position. Then the bed can be raised to the correct position, and finally the magnetometer can be moved into precise position by an operator who sits inside the MSR.

For fetal MCG measurements, an ultrasound is performed to identify the position of the fetal heart. In the initial measurements presented in this thesis, a commercial SQUID device was used to measure the fMCG signal after the ultrasound to cross-validate SERF measurements and to help identify an initial orientation for the SERF array. Finally, the SERF array is placed as close as possible to the subject's skin without the subject bumping the magnetometer during normal respiration. The channel position for the fMCG signals in this work is shown in figure 4.5.

Background signals and the mother's MCG can swamp the fMCG signal in real time. While signal processing techniques do a very good job, it is important to position the magnetometer to optimize the fMCG signal, requiring a real time or quasi-real time measurement in which the fMCG is at least visible. We mentioned previously one large source of interference the background spectrum, the 6.7 Hz signal from an HVAC fan. The fan can be turned off for short periods of time (~ 1 Hr) and the few fMCG measurements performed here had the fan turned off for a large part of the measurement period.

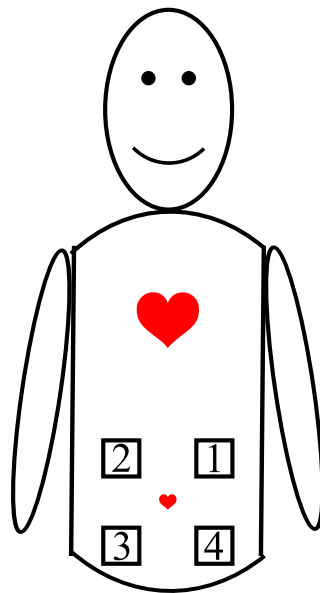


Figure 4.5: An artist's rendition of the channel positions of the magnetometers for the fMCG measurements. The relative position of the fetus is unknown, but the relative channel positions to the mother's heart are qualitatively correct. From this figure, we expect the mother's MCG signal to be largest in channels 1,2, and smaller in channels 3,4, and for those pairs to have approximately equal amplitudes. All channels should have similar phase.

Chapter 5

Noise analysis

This chapter presents a careful noise analysis, both of the atomic magnetometer itself and its environment. This noise analysis informs choices about extensions to DC-mode of operation (chapter 6), as well as our discussion of biomagnetism and which signal processing techniques promise to enhance the SNR of fMCG (chapter 7).

We can lump the noise sources into three categories: Magnetic, fundamental quantum, and technical noise. Since we are interested in the application where a single magnetic source is the signal of interest, magnetic noise includes any other magnetic source. Fundamental quantum noise essentially limits the sensitivity of the SERF detector itself, and comes from random projection noise in the measurement of the atomic spin and the measurement of the probe polarization rotation. Technical noise is anything else that could result in spurious signal, including but not limited to electronic pickup noise on the photodiode leads, slow rotations in the output polarization from the laser fiber optics, and movement of the probe laser on the photodiode surface area coupled to position-dependent photodiode response.

Table 5.1 lists the various sources of noise for each of the three types we consider for the DC-mode magnetometer discussed so far, as well as an estimate for the noise magnitude. The rest of this chapter will deal with each noise source individually.

Table 5.1: Magnetometer Noise Budget. Two results are quoted for the photon shot noise. The basic model is (5.18) where P_z , Γ_{pr} , and Γ are all averages over the laser interaction volume. The detailed models are refinements, where these quantities are made position dependent and effects such as light shifts are incorporated. Where the source is not expected to produce a white frequency profile, we note the expected frequency profile, though in most cases these are qualitative descriptions. When the noise source can be quantitatively estimated, a value or range of values is quoted. When upper limits are placed based on our measurements, these limits are quoted.

Type	Source	Level (fT/ $\sqrt{\text{Hz}}$)	Spectrum
Magnetic	MSR Johnson noise	1.1	
	Electrical current noise in nulling coils	3.9	
	^{87}Rb Johnson noise	0.9	
	Copper in nulling coils	0.1	
	Subtotal magnetic white noise	4.2	
	Fields from outside MSR (HVAC fan)	(10×10^3)	sinusoidal
	Fields from outside MSR(Construction)	$(1 - 100 \times 10^3)$	offset
	Noise from DC cell heaters	$(\ll 5)$	
Quantum	Spin-projection noise	0.8	
	Spin-projection noise (min)	0.5	
	Photon shot noise (averaged model)	0.1	
	Photon shot noise (3D model, no Ω_{LS})	0.2	
	Photon shot noise (3D model)	0.7	
	Photon shot noise (3D model, $\bar{\Omega}_{LS} = 0$)	1.1	
	Photon shot noise (measured)	1.5	
	Quantum subtotal (spn and exp. psn)	1.7	
Technical	Electronic	0.5	
	Signal aliasing	suppressed -30 dB-6 dB/Octave	
	Fiber polarization rotation	$\delta B/B < 1/500$	$(1/f)$
	Probe frequency noise	$\delta B/B < 1/100$	$(1/f)$
	Pump frequency noise	$\delta B/B < \delta \nu_2 (10^4 \text{ MHz})^{-1}$	
	Pump intensity noise	$\delta B/B = \delta \mathcal{P}_2/\mathcal{P}_2$	
	Laser angular misalignment (\mathcal{P} dependence)	$\delta \theta \frac{\delta \mathcal{P}_1}{\mathcal{P}_1} \left(\frac{50 \text{ pT}}{\text{degree}} \right)$	
Laser angular misalignment ($\delta \nu$ dependence)	$\delta \theta \delta \nu_1 \times \left(\frac{1 \text{ fT}}{\text{MHz degree}} \right)$		
Total	(no current noise in nulling coils)	2.4	
Total	(white noise level)	4.6	

5.1 Magnetic noise

Magnetic noise generally includes any magnetic source that falls within the frequency band of interest and limits the achievable SNR of the desired signal. Clear examples can be seen in figure 4.2(a). An important contribution to the single channel magnetometer noise floor in figure 4.1(b) and figure 4.2 is Johnson noise in nearby electrical conductors. These conductors carry thermal currents which generate roughly white-noise profile magnetic fields. The most important noise sources in our case are likely the mu-metal walls of the MSR and ^{87}Rb thin-film remaining on the Pyrex cell walls. Noise calculations for useful conductor geometries are available, and we use the results of [Lee and Romalis, 2008] in our Johnson noise estimates provided below.

5.1.1 Johnson noise from nearby conductors

We characterize the MSR as a set of 6 high-permeability infinite planes of distance $a = 1$ m away from the detector. The noise spectral density $\delta\tilde{B}$ from one of these planes is

$$\delta\tilde{B} = \frac{1}{\sqrt{6\pi}} \frac{\mu_0 \sqrt{k_B T \sigma d}}{a}, \quad (5.1)$$

in the direction of the plane area, where T is the temperature of the wall, d is its thickness, and σ is the electrical conductivity. The noise in each direction is then the quadrature-added sum of two planes, $\delta\tilde{B}_{\text{MSR}} = 1.1 \text{ fT}/\sqrt{\text{Hz}}$.

There is also a film of ^{87}Rb coating the cell. Modeling this film as a thin circular disk of thickness $d = 10$ nm, radius $r = 1$ cm, and $a = 0.5$ cm from the measurement volume, the noise contribution from this film is approximately [Griffith et al., 2010, Lee and Romalis, 2008]

$$\delta\tilde{B}_{\text{Rb}} = \frac{1}{\sqrt{8\pi}} \frac{\mu_0 \sqrt{k_B T \sigma_{\text{Rb}} d}}{a} \frac{1}{1 + a^2/r^2}, \quad (5.2)$$

and the noise from the rubidium is approximately $0.9 \text{ fT}/\sqrt{\text{Hz}}$.

The next closest conductors are the nulling coils wrapped around the magnetometers, seen in figure 3.1. The equation for the Johnson noise field far away from a conducting wire is [Lee and Romalis, 2008]

$$\delta\tilde{B}_{\text{wire}} = \sqrt{\frac{3}{128}} \mu_0 \sqrt{k_B T \sigma_{\text{cu}} y_0^2} a^{-5/2} \quad (5.3)$$

where $a = 2.5$ cm is the distance from the wire to the measurement volume and $y_0 = 160$ μm is the radius of the 28-gauge wire used for the coils. Our coils consist of 2-sets of four such physical wires for each axis, or 32 total wires. Up to factors of order unity having to do with the vector nature of the fields and whether they are correlated for wires that are connected, adding the fields in quadrature yields a modest $\delta\tilde{B}_{\text{coils}} = 0.14$ fT/ $\sqrt{\text{Hz}}$.

5.1.2 Magnetic noise from nearby electronic circuits

There are four electrical signals that carry currents near our sensor volume as a result of the heaters, thermistor measurement, photodiodes, and the magnetic nulling coils themselves. The heaters operate at around 0.5 A current which would be problematic, but is alleviated by the techniques described in section 3.3 and appendix E. Noise measurements of the type in figure 4.2 do not show any difference between the heaters on or off, giving an upper bound for the noise due to heater currents. The photodiode currents are very small (~ 1 μA), and the thermistor measurement current is not applied during magnetic field measurement.

That just leaves excess current noise in the circuit which drives the nulling coils. We measured the electrical current noise in the circuitry used to drive our nulling coils using a transimpedance amplifier. This contributes ~ 4 fT/ $\sqrt{\text{Hz}}$ to the magnetic noise level, depending on the coil current controller settings (see appendix E).

5.1.3 Noise from sources outside the MSR

Figure 4.2 shows that attenuated sources outside the MSR can still be seen in the magnetic noise level. This is especially true for low frequency noise sources, since the overall MSR shielding factor decreases as the eddy-current shielding factor decreases. One large source, mentioned previously, is the HVAC fan, which has a consistent ~ 10 pT amplitude signal.

As a guess of the magnitude of the problem, we take a dipole model of an automobile, from Vrba [2002, fig. 2]. This figure can be used to find (very roughly) the field from a car as a function of distance, shown in figure 5.1. Due to the construction, trucks, cranes, and construction elevators are all located ~ 50 m from the MSR. If these fields have a similar or larger field than a car, this

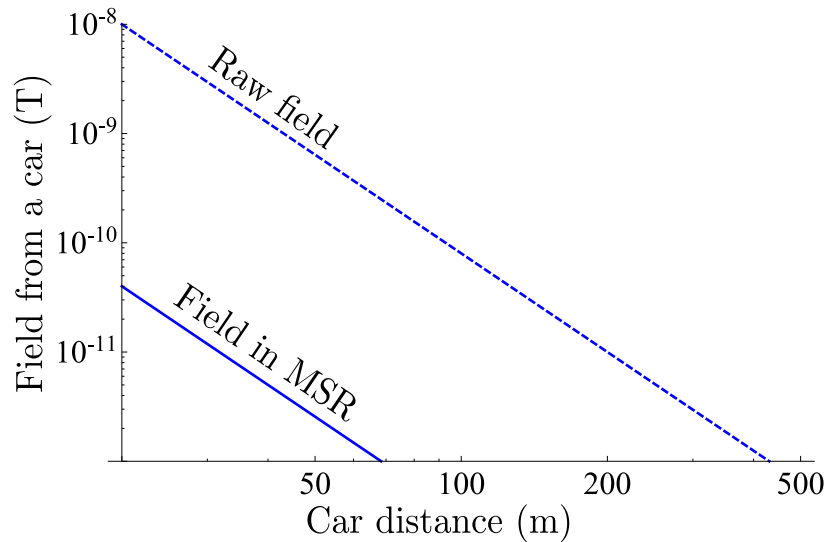


Figure 5.1: Field from a dipole model of a car [Vrba, 2002]. The dashed line is the actual field, the solid line is the field attenuated by a factor of 250, the approximate DC attenuation of the MSR. It seems reasonable to suspect fields from larger objects like trucks, cranes, and elevators to have similar or even larger fields. The proximity of heavy construction near the MSR during the measurement period of the data represented here causes potentially large fields compared to the background noise level.

could cause real problems in recording measurements (since there are large changes in the field amplitudes). It helps that the characteristic frequency is very low ($\ll 1$ Hz).

5.2 Fundamental quantum noise sources

Though single channel SERF magnetometers are often limited by environmental magnetic noise, noise sources below this level are still important for signal processing applications, and fundamental noise limits impose a hard lower bound on these capabilities. There are two fundamental quantum noise sources which limit the maximum theoretical magnetic field resolution: spin-projection noise and photon shot noise. These parameters depend on the details of the laser parameters, ambient magnetic fields, cell properties, magnetic field gradients, etc.

A brief summary of the relevant calculations is presented in the appendix of Ledbetter et al. [2008], for the basic case of uniform laser parameters across the cell measurement volume, and no light shifts. We introduce those results here, before expanding upon this basic theory, adding

additional refinements to obtain a more realistic picture of these noise sources in our system and how they might be optimized.

5.2.1 Spin-projection noise

Spin-projection noise comes from using the probe beam to measure the polarization P_x perpendicular to the quantization axis, defined by the pump laser. The uncertainty in the angular momentum F_x per atom is

$$\Delta F_x = \sqrt{\langle F_x^2 \rangle - \langle F_x \rangle^2} \quad (5.4)$$

Assuming no magnetic fields and no ellipticity to the probe polarization, $\langle F_x \rangle = 0$ by symmetry. The remaining term $\langle F_x^2 \rangle = \text{Tr}(\rho F_x^2)$, can be evaluated in spin temperature as $\text{Tr}(\rho F_x^2) = q(P)/4$, for normalized $\text{Tr}(\rho) = 1$ [Ledbetter et al., 2008]. Averaging the measurement from a set of N uncorrelated atoms, the uncertainty in the total angular momentum vector decreases according to Poisson statistics,

$$\delta F_x(P) = \sqrt{\frac{q(P)}{4N}}. \quad (5.5)$$

For a continuous measurement and the measurement time long compared to the spin-decoherence time [Kornack, 2005, Ledbetter et al., 2008],

$$\langle \delta F_x \rangle = \delta F_x \sqrt{\frac{2T_2}{t}}, \quad (5.6)$$

where the angular momentum coherence time is $T_2 = q(P)/\Gamma'$ (chapter 2). Finally, assuming the spin-temperature distribution allows us to relate the total angular momentum and electron spin through the slowing down factor, $\langle F_x \rangle = q(P) \langle S_x \rangle$. With $P_x = 2 \langle S_x \rangle$ as usual, we can use (5.6), (5.5) to find

$$\delta P_x = \sqrt{\frac{2}{N\Gamma't}}. \quad (5.7)$$

In our geometry, δP_x mimics a magnetic field, and can be expressed as an effective noise field using (2.24) and (2.25) as

$$\delta \tilde{B}_y = B_0 \sqrt{\frac{2}{N\Gamma'}} \quad (5.8)$$

$$\delta \tilde{B}_y \approx \frac{\Gamma'}{R\gamma} \sqrt{\frac{2\Gamma'}{N}} \quad (5.9)$$

where the approximation holds for small fields, and B_0 relates to the prefactor of (2.24),

$$P_x = \frac{B_y}{B_0} \quad (5.10)$$

$$B_0 = \left(P_z \frac{\gamma \Gamma'}{\Gamma'^2 + \Omega_z^2} \right)^{-1} \quad (5.11)$$

$$P_z = \frac{R}{\Gamma'} \quad (5.12)$$

Note B_0 has units of magnetic field, and is minimized for the normal optimal magnetometer scaling response, i.e. for low fields and $R = \Gamma$. We have assumed $\Omega_x^2 + \Omega_y^2 \ll \Omega_z^2$ in the expression for B_y . Equation (5.11) may look strange, since it could be further simplified if the expression for P_z in terms of R and Γ is used. However, the form of (5.11) will be useful shortly, when diffusion becomes important. When calculating P_z , we will handle Γ' differently than in the other terms in B_0 .

For small fields, spin-projection noise can be minimized for $R = 2\Gamma$, which is a larger pumping rate than the condition for optimizing the signal size (2.26) (where $R = \Gamma$). The minimum spin-projection noise is [Ledbetter et al., 2008]

$$\delta B_{\min} = \frac{3}{\gamma} \sqrt{\frac{3\Gamma}{2N}}. \quad (5.13)$$

Assuming the number of atomic participating in the measurement are $N = nV$, and the effective volume $V = \pi w_2^2 \times 2w_1$ is the intersection of the pump and probe beams, and using the experimental parameters in appendix B, we estimate the spin-projection noise to be $0.8 \text{ fT}/\sqrt{\text{Hz}}$. The minimum relaxation rate at our densities and accounting for relaxation due to diffusion is $0.5 \text{ fT}/\sqrt{\text{Hz}}$.

5.2.2 Photon shot noise (basic)

Photon shot noise occurs because the polarization of the probe laser is determined by counting the difference in the number of photons arriving at the two different photodiodes in figure 3.3. Counting uncorrelated photons results in uncertainty per unit frequency in the polarization of the

probe beam as $\delta\tilde{\phi}_{\text{psn}} \propto \dot{N}_{\text{ph}}^{-1/2}$. The number flux of photons that participate in the measurement is

$$\delta\tilde{\phi}_{\text{psn}} = \frac{1}{2\sqrt{\dot{N}_{\text{ph}}}} \quad (5.14)$$

$$\dot{N}_{\text{ph}} = \frac{\mathcal{P}_2}{h\nu_2} e^{-nl\sigma_{02}(\Delta\nu_2)}, \quad (5.15)$$

where \dot{N} is the photon detection rate for the probe power \mathcal{P}_2 , which is measured at the front of the cell. The exponential term accounts for probe absorption by the atomic vapor.

Since our signal is a polarization rotation, shot noise in this signal mimics a magnetic field, and once again (2.24), (2.25) and now (2.38) can be used to relate the uncertainty in the rotation to an uncertainty per root frequency in magnetic field (neglecting hyperfine structure) [Ledbetter et al., 2008]. To make extensions to this description easier in the following sections, we express relation between the effective magnetic field noise and photon shot noise through a calibration factor, the polarization rotation per unit field,

$$\delta\tilde{\phi} = \frac{\phi}{B_y} \tilde{B}_y \quad (5.16)$$

$$\frac{\phi}{B_y} = \frac{1}{4} r_e f c n l \mathcal{D}(\Delta\nu_2) \frac{1}{B_0}. \quad (5.17)$$

We have assumed uniform response from all the atoms in the probe beam area and along its propagation length through the atomic medium.

The full expression for the photon shot noise is then

$$\delta\tilde{B}_y = B_0 \frac{2}{\sqrt{\Gamma_{\text{pr}} \text{OD}_{02} n l A \Delta\nu_2 \mathcal{D}(\Delta\nu_2)}}, \quad (5.18)$$

with $\text{OD}_{02} = nl\sigma_{02}(0)$ the D2 optical depth on resonance. We recover Ledbetter et al. [2008, eq. A10] in the limit $\Delta\nu \gg \Delta\Gamma/2$, and assuming the probe beam area is spread uniformly across the square cell. Using the spatially averaged laser intensity for the parameters in appendix B to evaluate (5.18) suggests a photon shot noise level of $0.1 \text{ fT}/\sqrt{\text{Hz}}$.

5.2.3 Experimental measurement of fundamental noise

Comparison with the probe noise measurement described in section 4.3.3 is not as straightforward as one would like, because it includes electronic and other technical noise sources. We

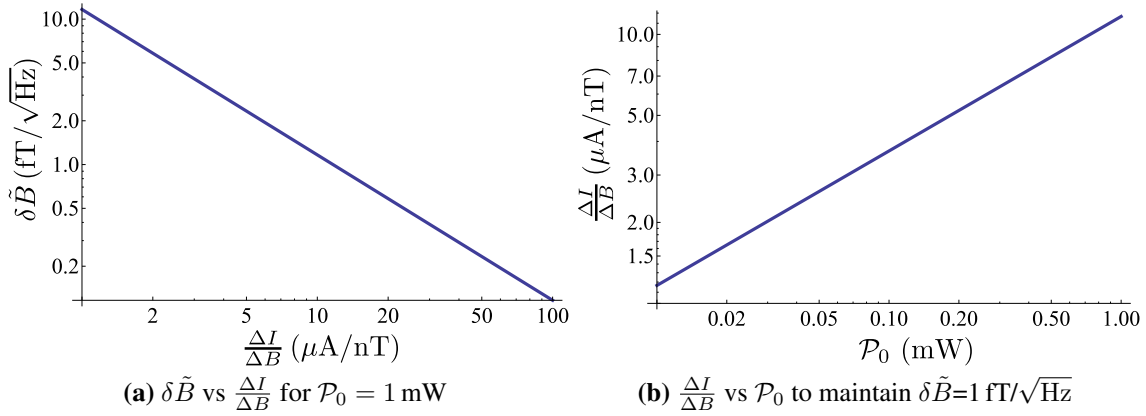


Figure 5.2: Plots of the electrical measure of photon shot noise as various experimental parameters are varied. \mathcal{P}_0 is not independent of the photon shot noise, so while (b) appears to suggest lower power is better, there is a hidden linear dependence on \mathcal{P}_0 since $\Delta I/\Delta B \propto \mathcal{P}_0$. The quantities are plotted this way because they are easily accessible experimentally.

can still measure the photon shot noise level experimentally by independently measuring the total (summed) power incident upon the photodiodes, \mathcal{P}_0 . Because photo-electrons are produced directly through absorption of photons, using the wavelength-dependent conversion efficiency of the photodiodes (similar for all silicone photodiodes), $g \approx 0.6$ A/W at 780 nm, the independent current from each photodiode is $I_p = g\mathcal{P}_0/2$, and the noise in the differential photocurrent $\delta I_p = \sqrt{2}I_p$ the electrical current will display the same quantized noise,

$$\frac{\delta I_p}{\sqrt{\Delta f}} = \sqrt{2e\delta I_p} \quad (5.19)$$

$$= (2)^{1/4} \sqrt{eg\mathcal{P}_0} \quad (5.20)$$

The experimentally obtained differential photocurrent per unit field $\Delta I_p/\Delta B$, either measured through the normal calibration process or using the central slope of dispersion sweeps like figure 2.12a, can then be used to find the expected photon shot noise

$$\frac{\delta B}{\sqrt{\text{Hz}}} = \left(\frac{\Delta I_p}{\Delta B}\right)^{-1} \frac{\delta I_p}{\sqrt{\text{Hz}}} \quad (5.21)$$

For a typical measured $\Delta I_p/\Delta B = 10\mu\text{A/nT}$ and total probe power of 1 mW, (5.21) evaluates to $\delta B/\sqrt{\text{Hz}} = 1.5$ fT/ $\sqrt{\text{Hz}}$.

5.2.4 Averaged parameters

When compared to the derived experimental measurement of the photon shot noise, we have found evaluating (5.18) with averaged laser parameters from the front of the cell gives unrealistically low results (compare $0.1 \text{ fT}/\sqrt{\text{Hz}}$ to the experimental result, $1.5 \text{ fT}/\sqrt{\text{Hz}}$). The reason is the spatial dependence of the sensitivity due to the spatial dependence of the pump and probe laser intensities, both transverse and longitudinal.

The photon shot noise, expressed as $\delta\tilde{\phi}$, can be calculated knowing just the probe light intensity incident upon the photodiodes. It would be present without a vapor cell, and is only dependent upon the cell through the attenuation of the probe light. The conversion to effective magnetic field in (5.18) utilizes a factor calculated for the magnetometer, the rotation per unit field ϕ/B_y , which is really a function of position.

5.2.5 Spatially dependent magnetometer response

A more detailed method of modeling the magnetometer uses a differential expression for the probe polarization per unit length and integrates this through the cell, weighting the result by the amount of probe light at each point. A differential and position dependent version of the rotation per unit field is calculated below. From (2.38) and (5.11)

$$\frac{\partial(\phi/B_y)}{\partial x} = \frac{1}{4}nr_e f_2 c \mathcal{D}(\Delta\nu_2)/B_0(x, y, z) \quad (5.22)$$

$$= \frac{1}{4}n\sigma(\Delta\nu_2) \left(\frac{\Delta\nu_2}{\Delta\Gamma/2} \right) \frac{1}{B_0(x, y, z)} \quad (5.23)$$

$$= \frac{\mathcal{C}(\Delta\nu_2)}{B_0(x, y, z)} \quad (5.24)$$

$$\mathcal{C}(\Delta\nu_2) = \frac{1}{4}n\sigma(\Delta\nu_2) \left(\frac{\Delta\nu_2}{\Delta\Gamma/2} \right). \quad (5.25)$$

$B_0(x, y, z)$ depends upon the complicated propagation effects, and to calculate it requires the solution to the steady state equation (2.23). As discussed in Section 2.4, numerical techniques are necessary to address (5.23), such as relaxation methods [Wagshul and Chupp, 1994], [Press et al., 2007, sec. 18.2].

The total rotation per unit field is

$$\frac{\phi}{B_y} = \frac{\mathcal{C}(\Delta\nu_2)}{\mathcal{P}_2} \int_{-l/2}^{l/2} dz \int_{-l/2}^{l/2} dy \int_{-l/2}^{l/2} \frac{\mathcal{I}_2(x, y, z)}{B_0(x, y, z)} dx, \quad (5.26)$$

where the probe incident power (\mathcal{P}_2) and intensity (\mathcal{I}_2) are normalized such that

$$1 = \frac{1}{\mathcal{P}_2} \iint_{y,z} \mathcal{I}_2(0, y, z) dy dz. \quad (5.27)$$

The spatial dependence of the probe can be written in advance as (2.49). We make use of the results developed in section 2.4 to model the pump propagation and Gaussian transverse spatial dependence. Then, (5.26) can be integrated numerically. Finally, the field term in $B_0(\mathbf{r})$ will depend on the spatial properties of the pump laser through the light shift, as (2.56).

To model the polarization, we use the same technique used in section 2.4. The polarization is calculated as it would be under diffusion-free conditions, and then an exponential decay to the walls with characteristic decay length z_d from (2.54) is enforced, only this time in all directions. We make a 3D grid, and setup an initial 2D grid to represent the pump laser intensity profile incident upon the cell in the $\hat{x} - \hat{y}$ plane. Next, each point on this 2D grid is propagated forward one unit in the \hat{z} direction, similarly to the 1D case in section 2.4. This process is repeated until discretized versions of the polarization and pumping rate are obtained for the entire length of the cell. These functions are interpolated and used to calculate the other parameters of interest. The fundamental parameter is the figure of merit (FOM), which in our calculations is related to the integrand of (5.26) by the gyromagnetic ratio scaling,

$$\text{FOM} = \frac{\mathcal{I}_2(\mathbf{r})}{\gamma B_0(\mathbf{r})} \quad (5.28)$$

$$= \mathcal{I}_2(\mathbf{r}) P_z(\mathbf{r}) \frac{\Gamma'(\mathbf{r})}{\Gamma'(\mathbf{r})^2 + \Omega(\mathbf{r})^2}. \quad (5.29)$$

In our calculations, the decrease in polarization due to diffusion should be accounted for through the diffusion length, and so the polarization was calculated without any explicit relaxation term from diffusion, like in section 2.4. However, in calculating the FOM, the correct Γ' must account for the total spin-relaxation rate, $\Gamma' = R + \Gamma_{\text{pr}} + \Gamma_{\text{sd}} + \Gamma_{\text{D}}$, since it describes how quickly a polarized atom relaxes. Once the FOM is calculated, the integral in (5.26) is performed numerically.

The rotation measurement noise is calculated through (5.14), and combined with ϕ/B_y yields the photon shot noise.

The model parameters used are shown in appendix B. The laser parameters are close to the optimum used in our experiments. The pump laser is detuned many linewidths from resonance, which ensures uniform optical pumping but results in a large light shift. Figure 5.3 shows R , Ω_{LS} , and P_z for the simple model described above. Our diffusion model was designed to be used in high pressure buffer gas cells [Walker and Happer, 1997], where the diffusion length is very small. It captures the gross position dependence of the polarization, but none of the polarization smearing that would occur if a full numerical solution to (2.23) was used. For example, the dimple in P_z in the center of figure 5.3(b) is due to Γ_{pr} , evident by comparing to figure 5.3(d). There is extra relaxation there, but for our diffusion lengths this would probably be smoothed over.

To illustrate the importance of the light shift for the magnetometer sensitivity, we perform two sets of simulations, one with this term and the other without. The difference is in the FOM, and can be seen in figure 5.4(a,c) ($\Omega_{LS} = 0$) and figure 5.4(b,d). The FOM is obviously lower when including the light shift, leading to a higher photon shot noise ($0.8 \text{ fT}/\sqrt{\text{Hz}}$ vs $0.2 \text{ fT}/\sqrt{\text{Hz}}$). These quantities are shown in figure 5.4. The description and simulations presented above are meant to capture the behavior of the magnetometer, but the roughness of the diffusion model for our low pressure cells means we expect only order of magnitude agreement between photon shot noise calculated in this way and the measured value.

Finally, in actual operation, Ω_{LS} is partially cancelled by the application of an opposing real magnetic field from the procedure in section 4.2. The average gradient Ω_{LS} can be estimated from figure 5.3(c), and is $\pm\Delta\Omega_{LS}/w_{01}$ on either side of the pump center. We will examine what nulling field we predict, and how the nulling procedure affects the FOM.

During the nulling procedure, the sensitivity to Ω_x is measured and minimized. Considering the size of the light shift, this sensitivity comes almost entirely from the laser, and the integrated signal is used. At each position in the cell, we obtain the integrated sensitivity from (2.24) and an

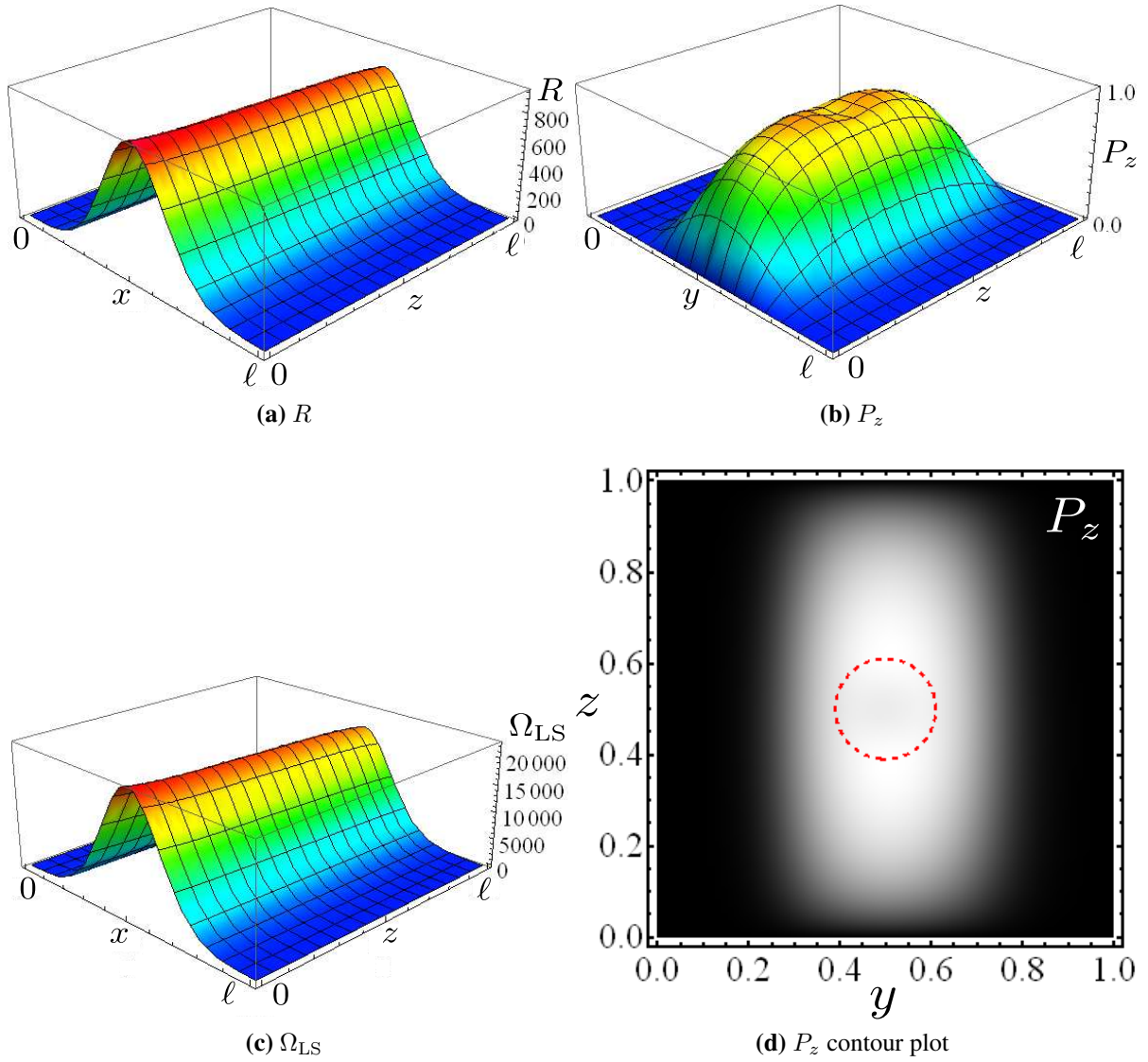


Figure 5.3: (a) the pumping rate, (c) the light shift, and (b,d) the polarization as a function of position in the cell. A simple model is used to account for diffusion and the results integrated numerically. In (d), the dashed red line corresponds to the position of the probe waist. Probe relaxation is seen in the slight P_z decrease in (b).

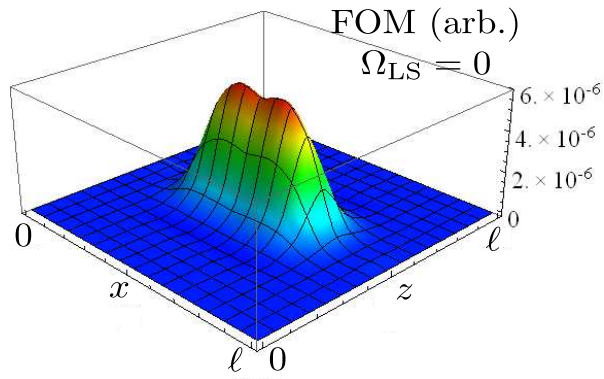
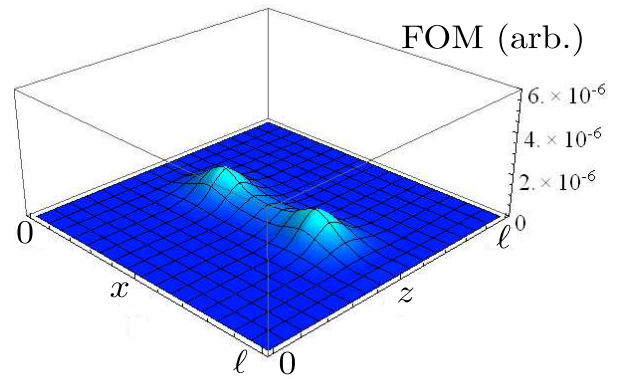
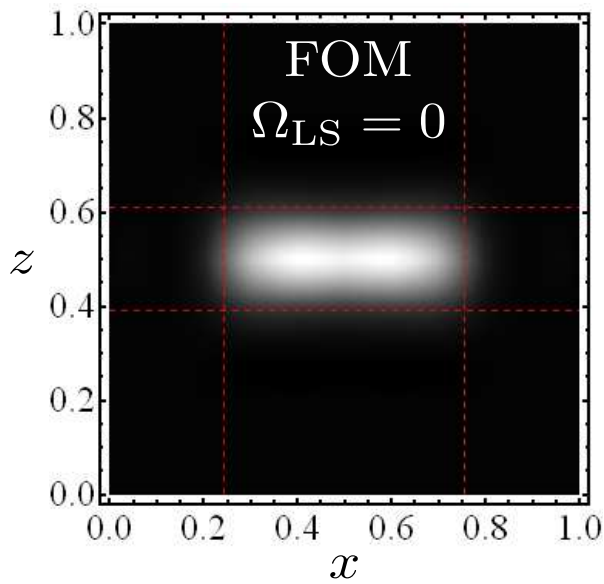
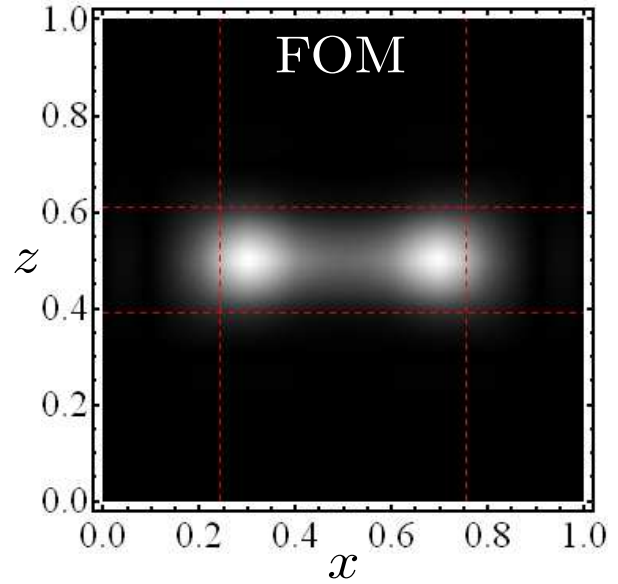
(a) FOM ($\Omega_{LS} = 0$)(b) Ω_{LS} (c) FOM ($\Omega_{LS} = 0$)(d) FOM with Ω_{LS}

Figure 5.4: 3D simulations of magnetometer parameters. Comparison of (e,g) and (f,h) shows difference in performance with and without light-shift. The red dashed lines in the density plots show the pump (\hat{z}) and probe (\hat{x}) waist profiles.

expression similar to (5.26)

$$\left\langle \frac{\partial P_x}{\partial \Omega_x} \right\rangle = \left\langle P_z(\mathbf{r}) \frac{\Omega_z(\mathbf{r})}{\Gamma'(\mathbf{r})^2 + \Omega_z(\mathbf{r})^2} \frac{2\mathcal{I}_2(\mathbf{r})}{\pi w_{02}^2 \mathcal{P}_2} \right\rangle. \quad (5.30)$$

Where $\Omega_z(\mathbf{r}) = \Omega_{\text{LS}}(\mathbf{r}) - \Omega_0$, and Ω_0 is the constant nulling field applied during the nulling procedure. We adjust Ω_0 to minimize (5.30) when using the magnetometer. For our simulations, after the polarization and pumping rate are found for all points in the cell, we calculate the averaged response $\left\langle \frac{\partial P_x}{\partial \Omega_x} \right\rangle \rightarrow f(\Omega_0)$ and then numerically find Ω_0 that minimizes this function. Then the total field $\Omega_z(\mathbf{r})$ is used in the FOM integration.

The results for the FOM with the cancellation field applied are shown in figure 5.5. The cancellation field was found to be $\Omega_0 = 0.95\Omega_{\text{LS}}$, which means the sensitivity to Ω_x is minimized approximately when the center of the pump shifts the ambient field nearly to zero. The noise level was $1.1 \text{ fT}/\sqrt{\text{Hz}}$, higher than the estimated value without Ω_{LS} , so the nulling procedure does not necessarily lead to the lowest noise when the the pump is far detuned.

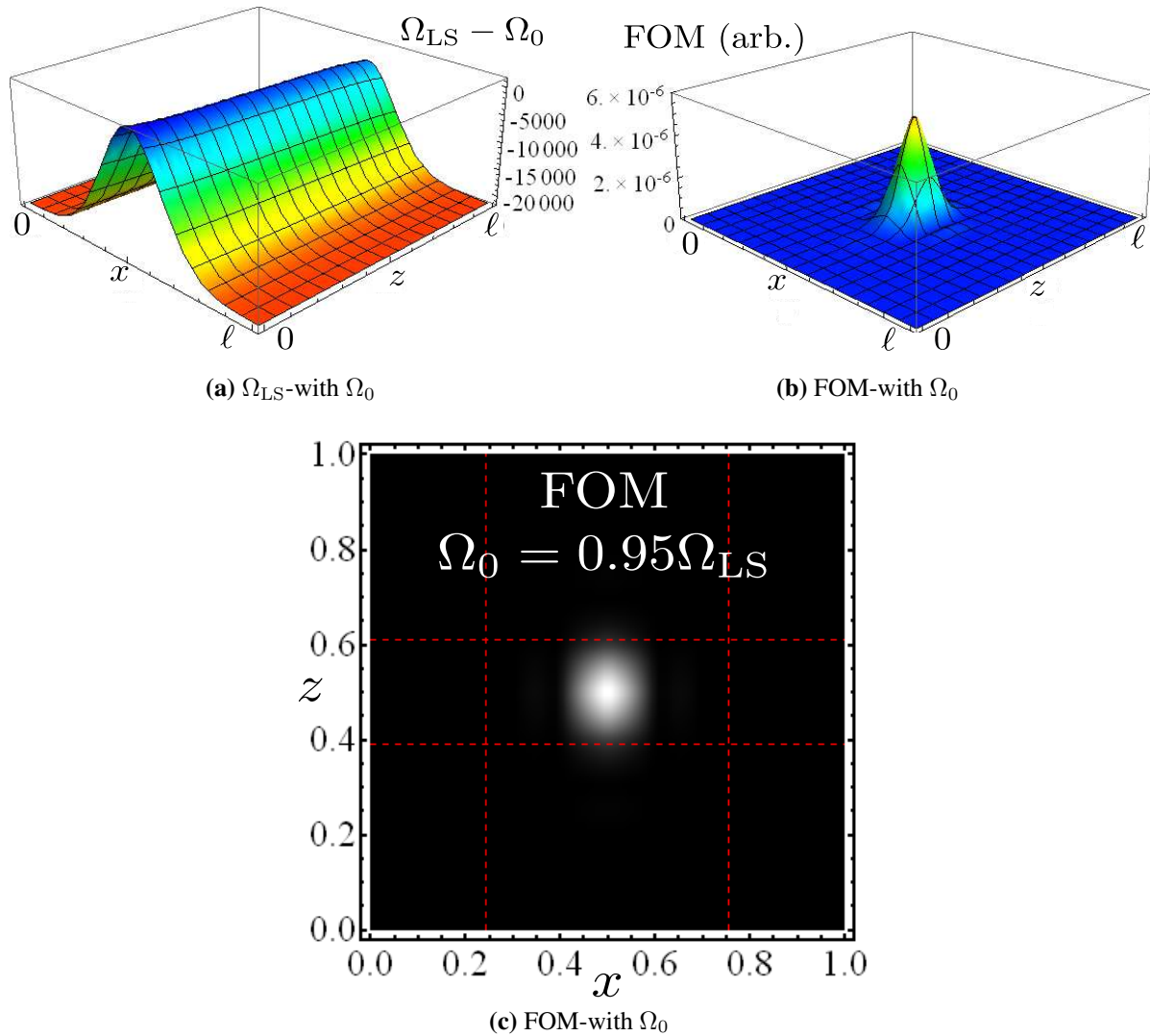


Figure 5.5: Similar to figure 5.4, except in addition to Ω_{LS} , we have added Ω_0 . The result favors atoms in the center of the pump beam, increasing the overall photon shot noise. (a) shows the total Ω_z , and indicates the offset is essentially the entire light shifted field. (b,c) show the FOM.

5.3 Technical noise sources

As indicated in table 5.1, our sensitivity is limited by fundamental detector noise and real magnetic fields. This restricts enhancement of MCG SNR through signal processing, because the techniques usually depend on combining magnetometer channels and reducing correlated signal corresponding to true but unwanted magnetic field. These techniques fail when the noise is primarily uncorrelated, as in the case of photon shot noise.

Noise reduction methods also benefit from having more channels of information. Parametric modulation [Li et al., 2006] can provide an extra channel per magnetometer, but at the cost of reduced sensitivity per channel because of an effective increase in photon shot noise. If the magnetometer is dominated by fundamental quantum noise, then this operation mode can decrease the sensitivity (see section 5.2). However, if the magnetometer is dominated by technical (non-magnetic non-quantum) noise, this mode of operation can greatly improve the sensitivity, especially at low frequencies.

The typical noise level of the probe measurement is $\delta I_{\text{pr}} \sim 10 \text{ pA}/\sqrt{\text{Hz}}$, or at typical I-V gain of 500 nA/V , $\delta V_{\text{pr}} \sim 5 \text{ nV}/\sqrt{\text{Hz}}$. If we are to remain dominated by the actual measurement, electronic noise must be much smaller than this level.

5.3.1 Signal aliasing

Aliasing is a phenomenon that occurs in any time-dependent system sampled at discrete time points. If we imagine a system sampled at sampling frequency f_s , the maximum frequency that can be uniquely represented is given by the Nyquist theorem is $f_{\text{max}} = f_s/2$. Signals with frequency components above f_{max} will be “aliased” into the baseband frequency range, a processes that maps any frequency $f_2 > f_s/2$ into the set of frequencies $0-f_s$.

Using our typical $f_s = 20 \text{ kHz}$, the Nyquist frequency is 10 kHz , and any spectral content above this frequency can get mapped back into the $0-200 \text{ Hz}$ range where we normally examine the noise floor. To alleviate this problem, we apply filtering on the photodiode amplifiers, but must

be careful not to attenuate signals we desire to measure. A compromise of a 2-pole low-pass filter at 300 Hz is chosen to accomplish these goals.

A second-order low-pass filter above its cutoff point decreases the power by 12-dB/octave. Since we characterize the noise floor by the amplitude spectral density, the noise contribution to the noise floor is 6-dB/octave above 300 Hz. This should attenuate any signals above 10 kHz by a factor of -30 dB (amplitude) or more. The aliased signal is uncorrelated with the baseband signal to which it gets aliased, and the two powers add in quadrature.

We notice significant electronic noise improvement with the application of these low pass filters, but some noise is pickup between the photodiode amplifiers and the FPGA system, a line which is not low-passed. For a quiet environment (no chopped heaters, thermistor measurement off), using low-noise wiring techniques and ferrite beads on the FPGA inputs wires, the electronic noise level is $2 \text{ pA}/\sqrt{\text{Hz}}$.

5.3.2 Probe polarization rotation in optical fiber

Polarization maintaining fibers require well-defined linear input polarization along one of two principle fiber axes. When used properly, the output polarization is stable to the extinction ratio, typically 20-30 dB. Residual rotation in the fiber leads to a fictitious magnetic field, since magnetic fields cause the same effect. This can limit SNR at low frequencies where the fiber polarization changes mostly occur (due to temperature or pressure fluctuations along the length of the fiber). The difference signal ΔI between a beam of incident intensity I_0 at an angle $\phi - \pi/4$ to the polarization axis of a polarizing beam splitter is

$$\Delta I = -I_0 \sin(2\phi) \approx 2I_0\phi. \quad (5.31)$$

Rotations in the fiber will lead directly to a difference signal which will drift over time. If the extinction ratio is a full 30 dB, the polarization angle will still drift from the fiber output $\phi = 1/1000$, we expect the *minimum* drift of the signal from a 1 mW probe to be $\delta I = 2 \mu\text{W}$. A typical magnetometer response around $\Delta I/\Delta B = 10 \text{ pW/fT}$ differential signal would correspond to an error of about 200 pT from polarization rotation in the PM fiber. This is much larger than the anticipated

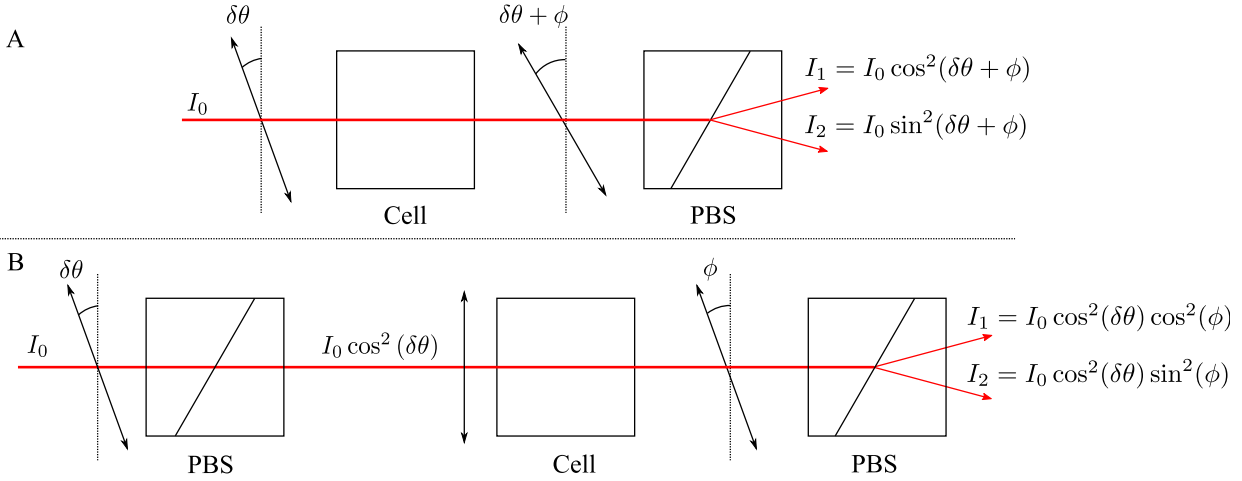


Figure 5.6: (A) Polarization rotation $\Delta\theta$ from the PM fiber results in a signal indistinguishable from magnetic field induced rotations $\delta\phi$. (B) This effect is largely eliminated by placing an output polarizer after the fiber, converting polarization fluctuations into intensity modulation.

fMCG signal of interest, with a maximum amplitude of 1 pT and frequency components near DC. We have taken measures to passively mitigate this problem, such as isolating the temperature variation in the optical fiber by enclosing it in protective tubing. At the cost of optical simplicity, another method is placing a polarizer at the output of the probe fiber, a technique utilized in our magnetometers. The polarization noise from the fiber is converted to intensity noise by the polarizer, to which the differential detection is much less sensitive. Specifically, the intensity noise after the Glan-Taylor is $\delta I = I_0 \delta\theta^2$, which gives rise to a measured signal from the differential photodetector only if there is already a misalignment between the probe polarization axis and the polarizer ϕ , for example as might be caused by an actual Faraday signal from a magnetic field. The difference signal generated (for small angles) is

$$\delta I = I_0 \sin(2\phi) \delta\theta^2, \quad (5.32)$$

which is equivalent to a fractional fictitious magnetic field

$$\frac{\delta B}{B} = 2I_0 \left(\frac{\Delta B}{\Delta I} \frac{\Delta \phi}{\Delta B} \right) \delta\theta^2, \quad (5.33)$$

where the fractions on the right hand side of (5.33) depend on the calibration of the magnetometer. With typical $\Delta\phi/\Delta B = 100 \text{ nRad/fT}$, the worst case scenario for a correctly coupled PM fiber

(extinction ratio of 1/100) correspond to $\Delta B/B = 1/500$. The actual magnetic field error depends on the real magnetic field in the case of a well aligned optical system ($\delta\phi = 0$ if $B = 0$), so at zero field there is no signal change. Finite fields $B < 0.5$ nT limit the fictitious field to $\Delta B < 1$ pT. This requirement on the size of the finite field is near the requirement to remain in the sensitive regime of the magnetometer and does not in reality impose any additional experimental limitation.

5.3.3 Probe frequency and intensity noise

We begin by characterizing the noise from changes in the probe laser intensity and frequency. Taking the form of the total signal \mathcal{S} given in section 2.2.8,

$$\mathcal{S} = \frac{\mathcal{P}_2}{2} x \text{OD}(x) e^{-\text{OD}(x)} \frac{B_y}{B_0}, \quad (2.39)$$

where x is the usual detuning normalized to the optical HWHM. For what follows, we assume the probe absorption rate is a negligible component of the total relaxation rate, $\Gamma_{\text{pr}} \ll \Gamma$, so the equilibrium polarization is unaffected by small changes in the probe laser.

Changes in the pump and probe parameters can be expressed by partial derivatives of this quantity. For example, we may calculate the effective field noise due to intensity fluctuations as

$$\delta B_y|_{\mathcal{P}_2} = \frac{\partial \mathcal{S}}{\partial \mathcal{P}_2} \left(\frac{\mathcal{S}}{B} \right)^{-1} \delta \mathcal{P}_2 \quad (5.34)$$

$$= \frac{\delta \mathcal{P}_2}{\mathcal{P}_2} B_y. \quad (5.35)$$

This equation assumes the photodiodes are precisely balanced in the presence of no external fields or pump light. We have not carefully measured the probe laser intensity noise, but we expect it to be dominated in the frequency region in which we are interested by fiber rotations rather than actual laser intensity noise, due to the effects described in the previous section.

The probe frequency dependence is

$$\delta B_y|_{\Delta\nu_2} = \frac{\partial \mathcal{S}}{\partial x} \left(\frac{\mathcal{S}}{B_y} \right)^{-1} \delta x \quad (5.36)$$

$$= \left(\frac{1}{x} - \frac{2}{1+x^2} + \frac{2x}{1+x^2} \text{OD}(x) \right) \delta x, \quad (5.37)$$

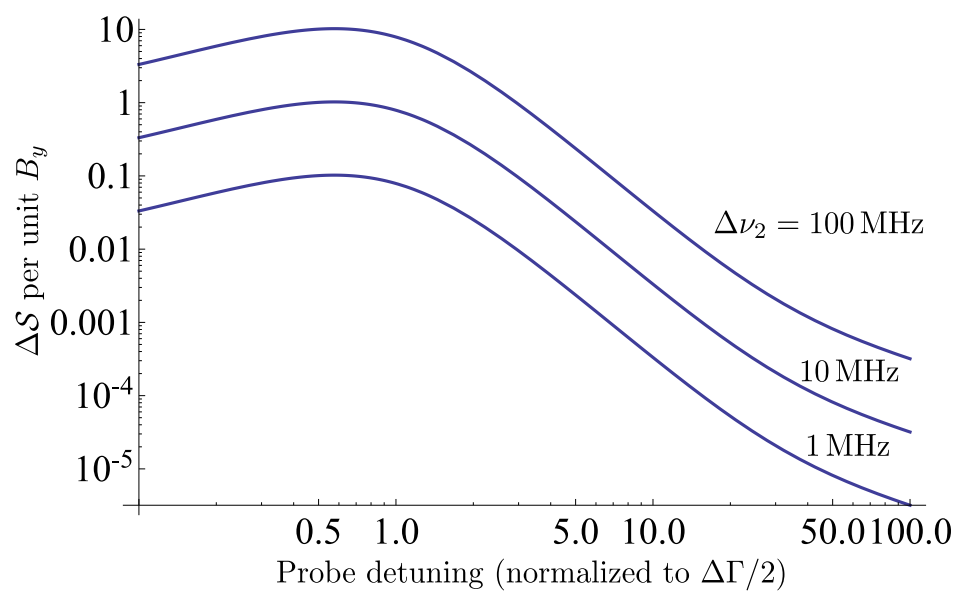


Figure 5.7: Relative frequency noise of the probe for unit B_y . At typical probe detuning $x \gg 1$, the noise is a small fraction of the detected signal for linewidths < 10 MHz. Larger very low frequency drift may occur, in which case stabilizing the laser to an external reference may be necessary.

which reflects both changes in absorption and rotation. A plot of (5.37) for $\Delta\nu = (1, 10, 100)$ MHz and unit B_y is shown in figure 5.7. For reasonable probe linewidths (< 10 MHz) and normal operating detuning ($x > 10$), the relative noise is suppressed by a factor of 100 or more.

5.3.4 Pump laser fluctuations

There is an angle characteristic of the magnetometer, $P_x = P_z\theta_x$, where θ_x describes the deviation angle from P_z for an applied field Ω_y with the familiar factor

$$\theta_x = \frac{\Gamma'\Omega_y}{\Gamma'^2 + \Omega^2}. \quad (5.38)$$

This expression separates the magnitude and tilt contributions to P_x . For maximum sensitivity and assuming no light shift, $\Gamma' = 2\Gamma$, and $\theta_x \approx 0.2$ rad/nT. Then $\theta_x \lesssim 1^\circ$ for $B_y \lesssim 100$ pT, quite a large field on our scale.

If laser fluctuations are not to add noise to the measurement, the field induced signal must be larger than the laser fluctuation induced signal. The pump laser only interacts with the measurement through P_x , so we just address this term. Using θ_x , the fluctuations in P_x to be compared are

$$\begin{aligned} \delta P_x|_{\Omega_y} &= \frac{\partial P_x}{\partial \Omega_y} \delta \Omega_y \\ &= \theta_x P_z \frac{\delta \Omega_y}{\Omega_y} \\ \delta P_x|_R &= \frac{\partial P_x}{\partial R} \delta R \\ &= \left(\frac{\partial \theta_x}{\partial R} P_z + \theta_x \frac{\partial P_z}{\partial R} \right) \delta R. \end{aligned}$$

In order for pump fluctuations not to limit the magnetometer signal, we want to satisfy the condition $\delta P_x|_{\Omega_y} \gg \delta P_x|_R$. After some algebra, this expression is

$$\frac{\delta \Omega_y}{\Omega_y} \gg \frac{R}{\Gamma'} \left(\frac{\Omega^2 - \Gamma'(\Gamma' + 2x\Omega)}{\Gamma'^2 + \Omega^2} + \frac{\Gamma}{R} \right) \left(\frac{\delta R}{R} \right). \quad (5.39)$$

The physical parameters that vary are the pump laser intensity and frequency, and (5.39) is a complicated function of these parameters. For $R = \Gamma$ and $\Omega = 0$, the sensitivity follows the curve

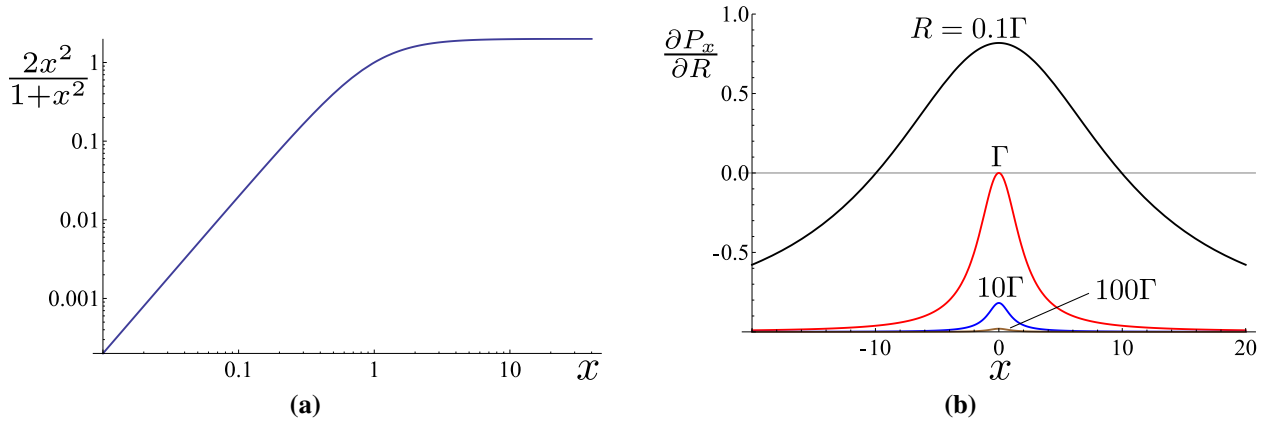


Figure 5.8: (a) A useful plot for calculating the δR from the physical parameter, δx . The asymptote at $R \rightarrow 2$ for $x \rightarrow \infty$. (b) δP_x due to fluctuations in R . This plot must be bounded between 1 and -1 since that covers the range of P_x .

in figure 2.9, and it should be evident that at $P_z = 1/2$, the sensitivity is insensitive to changes in pumping rate, which agrees with (5.39).

Given the discussion in section 5.2, it is unreasonable to ignore light shifts. The test in (5.39) requires relating δR to the physical parameters $\delta \mathcal{P}_1$ and δx ,

$$\delta R^2 = \left(\frac{\partial R}{\partial \mathcal{P}_1} \delta \mathcal{P}_1 \right)^2 + \left(\frac{\partial R}{\partial x} \delta x \right)^2 \quad (5.40)$$

$$\left(\frac{\delta R}{R} \right)^2 = \left(\frac{\delta \mathcal{P}_1}{\mathcal{P}_1} \right)^2 + \left(\frac{2x^2}{1+x^2} \frac{\delta x}{x} \right)^2. \quad (5.41)$$

Hence $\delta R/R$ is linear in relative power fluctuations and ranges from a factor of 0–2 $\delta x/x$. At our model detuning, $x \approx 20$, the relative noise level is $\delta B_y/B_y = \delta \nu_2 (\text{MHz})/10^4$ from frequency noise and $\delta \mathcal{P}_1/\mathcal{P}_1$ for intensity noise.

5.3.5 Laser Misalignment

We examine what happens if the probe laser is no longer orthogonal to the pump and picks up some sensitivity to P_z . If the probe beam propagates through the atomic vapor at a small angle θ above the $\hat{x} - \hat{y}$ plane, the longitudinal polarization component is now $P_x + \theta P_z$. We expect $\theta \sim 1^\circ$, which means $\theta \gg \theta_x$ in typical low-field conditions. This is a problem if there is extra noise coupled onto the signal for nonzero θ .

Noise analysis proceeds in much the same way as the previous section. Assuming a constant (non-drifting) angular misalignment, the noise is coupled onto the signal through noise in P_z ,

$$\delta P_x|_\theta = \theta \frac{\partial P_z}{\partial R} \delta R \quad (5.42)$$

$$= \theta \frac{\Gamma}{\Gamma'^2} \delta R. \quad (5.43)$$

The field noise can be computed from (5.11),

$$\delta B_y = \frac{\theta}{\theta_x} \frac{\Gamma}{\Gamma'} \frac{\delta R}{R} \quad (5.44)$$

$$= \theta \frac{\Gamma}{\gamma} \left(1 + \frac{\Omega^2}{\Gamma'^2} \right) \frac{\delta R}{R}. \quad (5.45)$$

The factor $\theta\Gamma/\gamma \approx 50$ pT for our parameters. Disregarding the light shift, this means we need $\delta R/R \ll 1/(5 \cdot 10^4)$. This is a difficult limit. For example, it means the noise limits due to angular misalignment coupled to pump noise are

$$\delta B_y|_{\theta+\delta\nu} \approx \theta \delta\nu_1 \times \left(\frac{1 \text{ fT}}{\text{MHz degree}} \right) \quad (5.46)$$

$$\delta B_y|_{\theta+\delta\mathcal{P}_1} \approx \theta \frac{\delta\mathcal{P}_1}{\mathcal{P}_1} \left(\frac{50 \text{ pT}}{\text{degree}} \right). \quad (5.47)$$

This calculation ignores the light shift, which for far detuned beams would increase the noise level significantly for the same misalignment angle. Note that the situation is not the same in nonlinear magneto-optic effect magnetometers, where the light shift imposes a fundamental limit on the sensitivity [Fleischhauer et al., 2000, Novikova et al., 2001]. The linewidth of the pump DFB is expected to be around 5 MHz, but the $1/f$ fluctuations are likely larger. Moreover, noise from the pump beam is difficult to diagnose by our characterization methods, since the sensitivity to background fields is blocked mainly by blocking the pump to test technical noise levels.

To test this, one could measure changes in the signal as the pump frequency or power is dithered slowly compared to Γ . Then the fluctuations in these parameters could be measured.

Chapter 6

Extensions and different operating modes

In this chapter, we discuss extensions to the DC-mode technique pioneered by Allred et al. [2002] and used in the measurements and discussions presented up until this point. These changes fall into two general categories: operation modes that do not require the application of large oscillating fields and modes that do.

6.1 Non-parametric field modes

By non-parametric, we mean to indicate methods which do not require the introduction of modulating fields large compared to the zero field dispersion linewidth in figure 2.12a. We have used two non-parametric field extensions to the DC-mode operation method. One, which we call diffusion-mode, uses diffusion to move angular momentum away from the pump beam, where T_2 is larger because there is no pumping light and some of the technical noise problems in the previous chapter are solved. The second method is feedback mode, in which we use our magnetometer array as feedback devices with the application of a feedback magnetic field.

6.1.1 Diffusion mode pumping

As we discussed in section 3.1 and section 2.2.3, the cells used in this work were originally filled with an amagat of He, which subsequently diffused through the Pyrex and left us with low pressure cells. The diffusion length, characterized by (2.54), is around 1.3 cm for our cells (in the absence of pump light). We expect angular momentum loss to the cell walls to be significant if the pumping laser is uniformly distributed throughout the cell.

To reiterate the concerns raised in table 3.2, there are three choices to operate a pump with a waist on the order of the cell size: high pumping rate near resonance (small light shift, high P_z throughout cell but low sensitivity), pumping rate to get $P_z = 1/2$ near resonance (small light shift, but for optically thick cells, the light is quickly attenuated), and pumping off resonance to get $P_z = 1/2$ (atoms pumped all through cell, but high light shifts).

The last regime would be the optimum were the pump intensity is uniform, since uniform light shifts can be cancelled by the application of a real magnetic field. For significant transverse dependence of the light shift, only the average can be cancelled with a pair of magnetic coils, and the difference between maximum (center of the pump beam) and the minimum (edge of the pump beam) approaches the full value of the light shift, which can be quite large and decreases the sensitivity (discussed in detail in section 5.2.5).

Three approaches can be used to address the problem. First, the pump beam could be made more uniform, either through expanding its waist or using a spatial filter to make a top-hat beam. Beam expansion is difficult due to design requirements that favor a compact array. Diffractive beam shapers may work for this purpose, although they typically create their uniform spatial distribution only in the working plane of the optic, producing a diverging beam.

Second, the probe beam could be limited so that it only samples the central portion of the pump laser. However, shrinking the probe beam has the side-effect of decreasing the number of atoms participating in the measurement, increasing the quantum noise and effective noise from technical noise sources.

For cells in which the diffusion length can be made large compared to the pump beam, a third option is to shrink the pump beam and expand the probe beam until the beam waist is approximately

equal to the diffusion length, $w_{02} \approx z_D$. We call this method diffusion-mode pumping, and discuss the relevant physics and results obtained with this mode.

We maintain the same power but shrink the pump waist, so the intensity and pumping rate become large, but only for a small central portion of the cell. In this central region, the polarization and light shift may be high, but with low sensitivity to magnetic fields. Atoms diffuse from the central, strongly polarized region to the regions outside the pump beam, remaining polarized until they undergo a spin-destruction collision.

Using the optics described in appendix B, the pump beam waist was reduced to $w_{01} = 0.51$ mm, and the probe beam waist was increased to $w_{02} = 2.75$ mm. The pumping rate becomes huge for such a small pump beam. At the center of the beam for cylindrical coordinate ρ , R_0 increases with area if the power is maintained constant,

$$R(\rho) = R_0 e^{-2\frac{\rho^2}{w_{01}^2}} \quad (6.1)$$

$$R_0 = \frac{2\Phi_{01}}{\pi w_{01}^2} \sigma_{01}(\Delta\nu_1). \quad (6.2)$$

Figure 6.1(top) shows simulations of $P_z(\rho)$ for various R_0 , but with x modified to make R consistent with our experimental w_0 and \mathcal{P}_1 described by the parameters in appendix B. The normalized pump profile is also shown. With a narrow waist, the atoms in a region up to the point at which $R(\rho) \approx \Gamma_{sd}$ are pumped to high polarization. This occurs at the critical radius,

$$\rho_c = \frac{w_{01}}{\sqrt{2}} \left(\ln \left(\frac{R_0}{\Gamma_{sd}} \right) \right)^{1/2}.$$

It can be seen that increasing the pumping rate extends the radius of highly pumped atoms very slowly. In the limit of $P(\rho < \rho_c) \approx 1$, the pump is linearly rather than exponentially attenuated. The dots on the normalized pump profile in figure 6.1 show where $\rho = \rho_c$ for each initial pumping rate. We calculate P_z by numerical solution to the 2D radial diffusion model in steady-state, modified from (2.23),

$$0 = q(P)D \frac{1}{\rho} \frac{\partial}{\partial \rho} \left(\rho \frac{\partial P(\rho)}{\partial \rho} \right) + R(\rho)(1 - P(\rho)) - \Gamma_{sd}P(\rho), \quad (6.3)$$

and we assume a cylindrical (rather than square) cell, with its axis of symmetry along the pump the boundary condition $P(l/2) = 0$. We compare the radial $1/B_0$ (section 5.2.5) to the theoretical

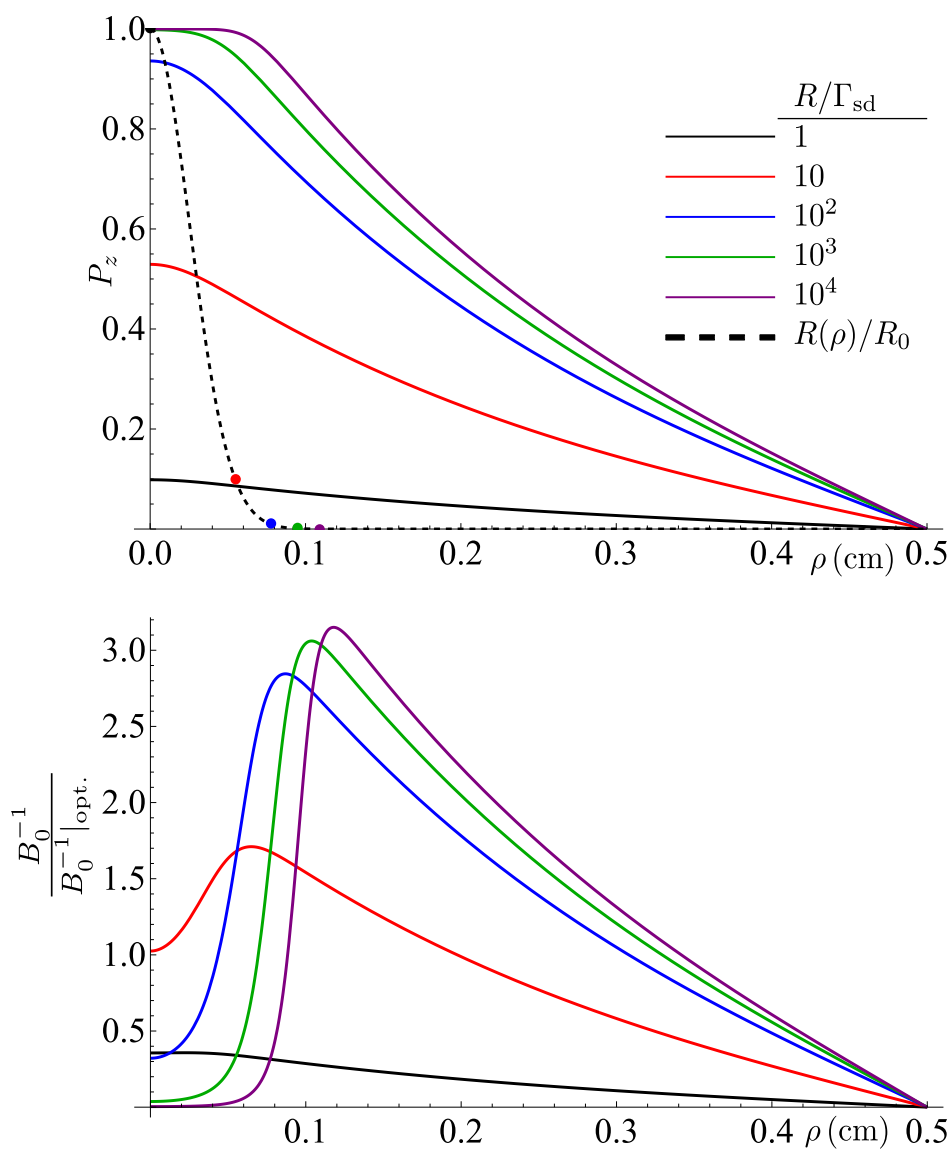


Figure 6.1: (a) Shows the solution to the radial diffusion problem for various starting pumping rates. (b) A plot of $B^{-1}(\rho)/B_{0,opt}^{-1}$, comparing the sensitivity per unit radius at each point in the cell compared with a uniformly pumped cell when $R = \Gamma$.

optimum if $P_z = 1/2$ everywhere. While the numerical solution gives the steady-state P_z , we must still account for diffusion losses in the relaxation rate of P_z when calculating the radial $1/B_0$, and use the effective decay rate Γ_D introduced in section 2.2.3. Figure 6.1(bottom) shows the normalized $B_{0,\text{opt.}}/B_0$, neglecting light shifts (these are only in the central portion of the cell, where $1/B_0$ is already small). At $\rho > \rho_c$, the polarization is large but the pumping rate is low, so $1/B_0$ is actually higher than the uniform pumped case for some cell positions. What will matter for noise purposes, however, is the FOM from section 5.2.5.

The previous simulations of pump propagation, shown in figure 6.1, are informative here. While the attenuation will be greater at the front and rear cell walls (all the atoms are sinking angular momentum, only a few see a high pumping rate), the high pumping rates ensure relatively uniform polarization through the cell and shorten the effective diffusion length inside the pump light cylinder. Very high pumping rates allow us to ignore diffusion in the z -direction and the polarization will be uniform along the \hat{z} -direction. For this simple model, we set $P_z(\rho > l/2) = 0$, and use the polarization profile $P(\mathbf{r}) = P_z(\sqrt{x^2 + y^2})$ for all z values in the cell. The FOM is found, and the results for different R_0 are displayed in figure 6.2.

The integrated FOM comes out significantly higher than the uniform case for $P_z \rightarrow 1/2$. At our operating parameters,

$$\iiint \frac{\text{FOM}}{\text{FOM}|_{P_z \rightarrow 1/2}} dV \approx 11$$

and the expected photon shot noise, calculated as in section 5.2.5, is $\delta B_{\text{psn}} = 70 \text{ aT}/\sqrt{\text{Hz}}$. The main advantage is apparent when comparing figure 6.2 to figure 5.5. Confining the pump light without confining the polarization moderates the light shift and pump absorption issues that make achieving $R = \Gamma$ difficult in the entire cell volume. The portion of the cell with good sensitivity to magnetic fields has increased.

The noise estimate is probably unrealistically low, and certainly lower than we have actually achieved. The spin-decay rate Γ_D we have used is known to be the exponential contribution to spin-relaxation with both exponential and non-exponential terms, and the effective relaxation rate should be higher Wagshul and Chupp [1994].

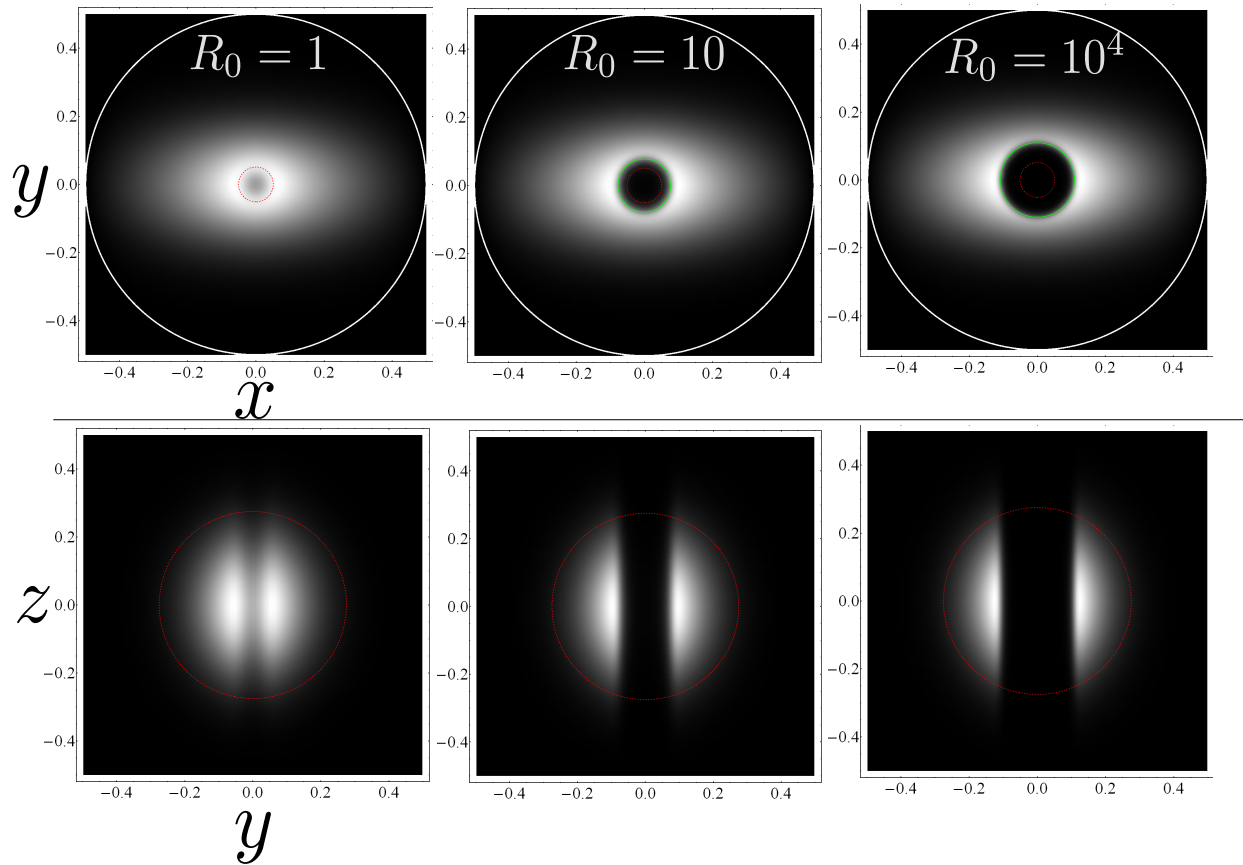


Figure 6.2: Models of diffusion mode pumping FOM for a variety of initial pumping rates. For the data in this thesis, the pumping rate was closest to $R = 10^4 \times \Gamma_{\text{sd}}$. The green circles have radius ρ_c , the red-dashed circles in the x-y plane have radius w_{01} and in the y-z plane have radius w_{02} .

A more careful analysis could be made by solving (2.23) using a diffusion mode expansion. Γ_D used in this analysis corresponds to the fundamental diffusion mode, but higher modes have faster decay rates. The solution to P_{z_i} can be characterized for each mode (i), with its own relaxation rate Γ_{D_i} , and the contribution to the sensitivity from each mode summed, $\sum_i P_{z_i}/\Gamma_{D_i}$. Such an analysis is being investigated at the time of this work.

Diffusion mode pumping requires $z_d = \sqrt{qD/\Gamma_{sd}} > w_{01}$. For cells of our size, this leads to relatively large wall relaxation Γ_D . It may be that high pressure cells compensate the difficulty of pumping a cell uniformly without large light shifts by their lower Γ .

In our experiment, diffusion mode pumping did seem to outperform a larger pump beam. Our best results were obtained using this method, and are shown in figure 6.3. Low frequency contributions to the noise profile are especially suppressed, and the usual 6.7 Hz peak can be seen with its harmonics.

Finally, because the pump light is hardly attenuated through the cell, there is significant pump power that must be dumped somewhere at the back of the cell. We have lined up two magnetometers and pumped them with a single beam, with similar noise performance, and it appeared we could have pumped up to four magnetometers with one beam. This might be a significant advantage in constructing a large magnetometer array, reducing significantly the optics necessary for the pump beam.

6.1.2 Feedback mode

Magnetic field feedback is a natural extension to the DC-mode magnetometer. For one thing, the DC-mode magnetometer signal can be used directly (by negation) as an error signal for B_y . Feedback is as easy as plugging the output of the I-V converter into a set of feedback coils, at least for that direction.

Magnetic field feedback has been used in previous experiments. The original M_x -mode magnetometers used feedback [Bell and Bloom, 1957] to measure the magnetic field. Bison et al. [2009] used a complicated feedback scheme to operate a 25-channel array of atomic magnetometers in

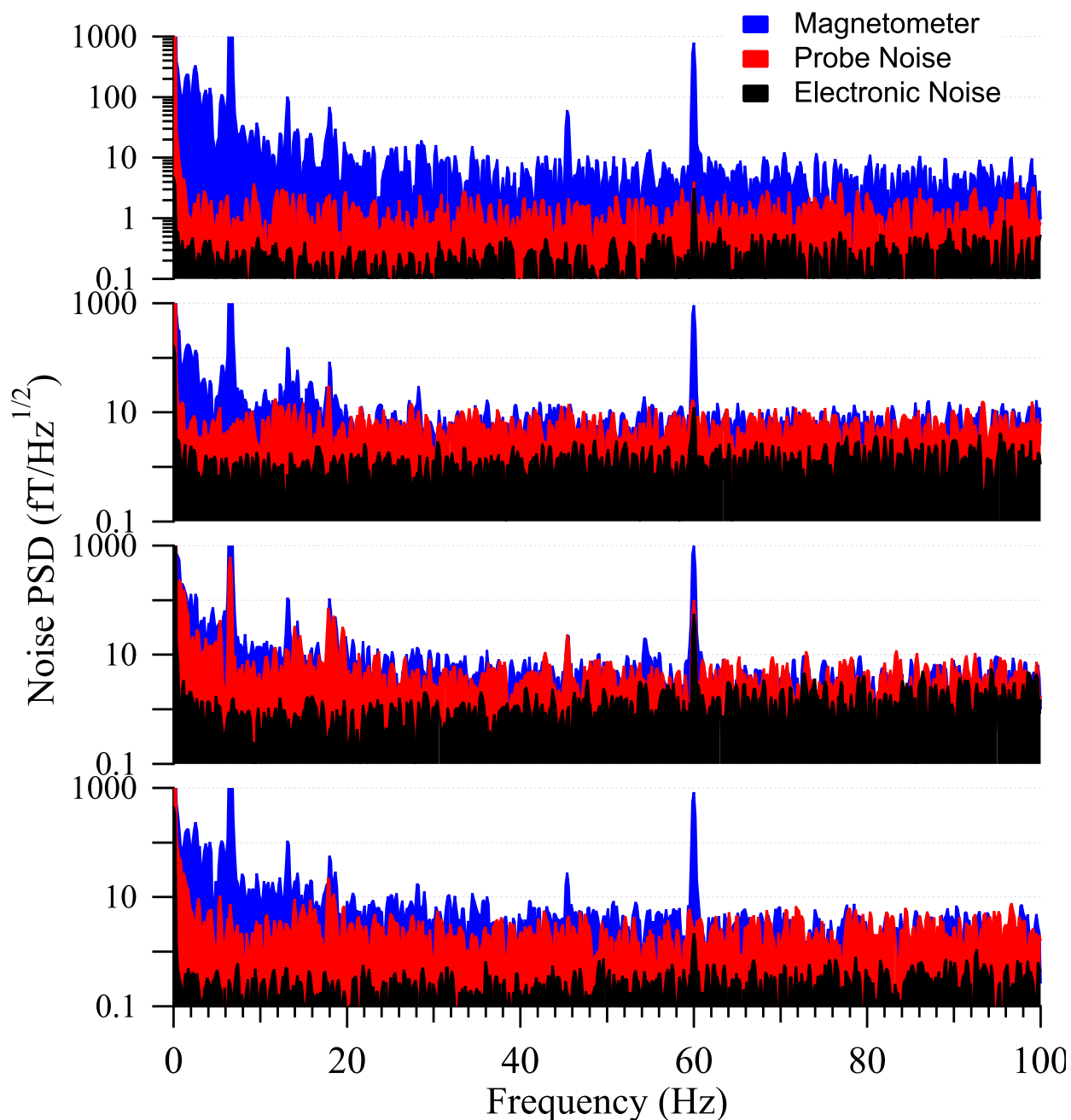


Figure 6.3: Noise characterization for the magnetometers operating in the diffusion pumped mode. The magnetic noise (black), probe noise (blue), and electronic noise (red) are overlaid to give a better indication of which are dominant. The probe noise level on channel 3 is deceptive, since it remains sensitive to fields even with the pump blocked.

the M_x mode and make them an effective 19-channel gradiometric array. Their objective was suppression of ambient noise in an eddy-current shield, and their second order gradiometer achieved a suppression ratio of 1:1000. Seltzer and Romalis [2004] built an unshielded magnetometer that operated in the SERF regime through 3-axis feedback, using a single DC-mode magnetometer to measure all three fields simultaneously. The process is equivalent to the one we use to null the fields in the first place (section 4.2). The signal is proportional to Ω_y , and if small modulating fields are added $\Omega(x) = \Omega_1 \sin(\omega_x t)$ and $\Omega(z) = \Omega_1 \sin(\omega_z t)$, then using lockin detection on ω_x (ω_z) measures B_z (B_x). These were all feedback to large Helmholtz coils surrounding the cells used in the experiment, and an unshielded noise level of around $1 \text{ pT}/\sqrt{\text{Hz}}$ in the difference signal was obtained. Similarly to Bison et al. [2009], Seltzer and Romalis [2004] described and implemented feedback primarily as a background field noise-reduction technique, and to our knowledge, SERF feedback has not been investigated in a MSR-type environment. However, it has many potential benefits for biomagnetism applications.

First, many of the technical noise sources described in section 5.3 are proportional to the overall signal. As one example, the noise from intensity fluctuations is proportional to the difference signal of the photodiodes. Feedback can be used to maintain zero difference signal in the presence of fluctuating magnetic fields, suppressing this noise source.

Second, the primary goal of fMCG is the accurate measurement of $B(t)$, which allows the extraction of medically relevant information. Since the fMCG signal has frequency elements that extend through the changing magnetometer frequency response, fMCG measurements (and any measurement where accurate $B(t)$ reconstruction is important) must be deconvolved with this response. Figure 4.1 shows a typical example of such a calibration and the fits used to characterize the response, and clearly these fits are not accurate to 1%. Averaging more response measurements would help if the response was stationary, but offset fields change frequently enough that this is impractical.

Furthermore, many signal processing techniques used in fMCG rely on measurements across multiple magnetometer channels. For example, simple gradiometry in the DC-mode setup would mean measuring an fMCG signal at multiple channels, deconvolving each measurement with the

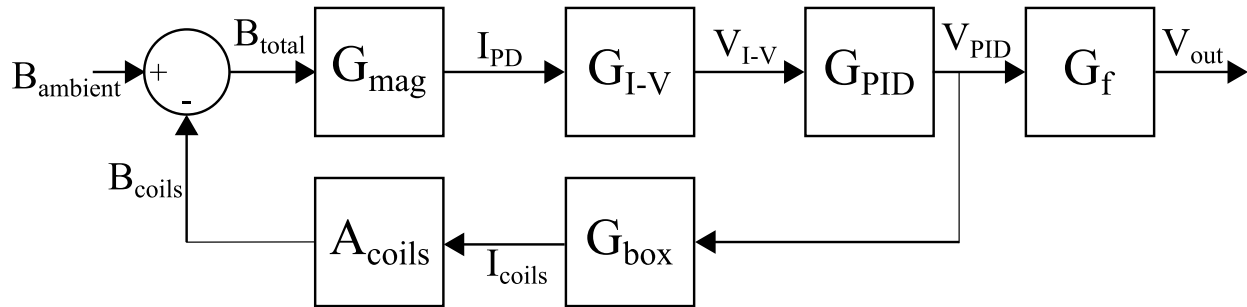


Figure 6.4: Block diagram of the feedback loop used to cancel B_y for each magnetometer. When the large feedback coil is used, the control box is replaced by a resistor, but otherwise the loop is the same.

response from each channel, and subtracting the result. For perfect measurements, a uniform field at two channels would give zero difference after this procedure. With a 10% error in the calibration, the suppression factor will depend on frequency and we wouldn't expect better than $\sim 85\%$ suppression at any frequency. More advanced techniques like PCA would work well on unknown calibrations but primarily if they are spectrally flat. In feedback mode, the signal measured becomes the current applied through the feedback coils to maintain zero field at the sensor. The feedback field is a linear function of current, so measuring the current gives a flat frequency response, and only an absolute calibration to relate the measurement to the ambient field.

Finally, if we need to detect anything in real time, the background magnetic fields in the MSR are quite large and can make this difficult. The 6.7 Hz peak alone has an amplitude between 5 – 20 pT, dwarfing the smaller fMCG features, and the mother's MCG will have a similar amplitude at the array position. Both sources are far from the array relative to the fetus, and so their fields are comparatively uniform across all channels. This calls for real-time gradiometry, but that is complicated by the requirement of real-time deconvolution.

We have used two methods of feedback. In the individual feedback mode, the magnetometer signal is conditioned through a PID loop and sent to the coil control box for each magnetometer, which uses the individual calibration coils for each magnetometer to maintain zero field. Figure 6.4 shows a block diagram of this technique. The output voltage V_o is a conditioned measurement control voltage for the voltage controlled current source output. As self-zeroing magnetometers,

the feedback lowers technical noise and flattens the frequency response, making real time measurement easier. However, the current electronics seem to increase the noise level significantly, and we have yet to obtain good results with this method.

A more useful improvement is using a single large feedback coil, as in figure 6.5, which we refer to as gradiometer feedback. The magnetometers are placed symmetrically about the center of the coil so that the magnitude of a field applied by these large coils is the same. One reference magnetometer, channel i , provides the error signal to this coil. Assuming the nulling process initially sets the field at each magnetometer to zero, feedback maintains the field at each channel

$$B_j(t) = \begin{cases} 0 & j = i \\ B_{0j}(t) - B_i(t) & j \neq i \end{cases}$$

for local ambient field B_{0j} and total field with feedback B_j . Typically there are different offsets for each channel applied locally to the calibration coils, adding a different DC term for each channel.

The great benefit is time-changing uniform magnetic fields get cancelled at each magnetometer, enhancing the SNR from nonuniform fields between the reference and other channels. Examining the noise budget table 5.1, the dominating magnetic noise is from circuit noise in the nulling coils, which will be uncorrelated, as is most technical and all quantum noise. When utilizing feedback mode, we expect the noise floor to modestly increase due to this uncorrelated noise, but to get a large decrease in correlated magnetic noise in the non-reference channels. This behavior is seen in figure 6.6, where the low frequency noise is mostly well cancelled, especially the uniform 6.7 Hz.

The advantages in real-time measurement are most easily seen when there is a signal of interest that we wish to isolate from background fluctuations. Fetal MCG was taken with this technique, and we present a portion of it in figure 6.7. This data corresponds to a 5 min continuous fMCG measurement, taken using the gradiometer feedback method with channel 4 (bottom green) as the feedback reference. The objective for real-time detection is signal optimization, and so we apply a 1-30 Hz 2-pole bandpass filter to help isolate the fMCG QRS signal from background. This filter was applied to the data during post processing, but the same filter can be applied in real-time using the I-V converter front-panel controls. During the initial part of the measurement (left), the

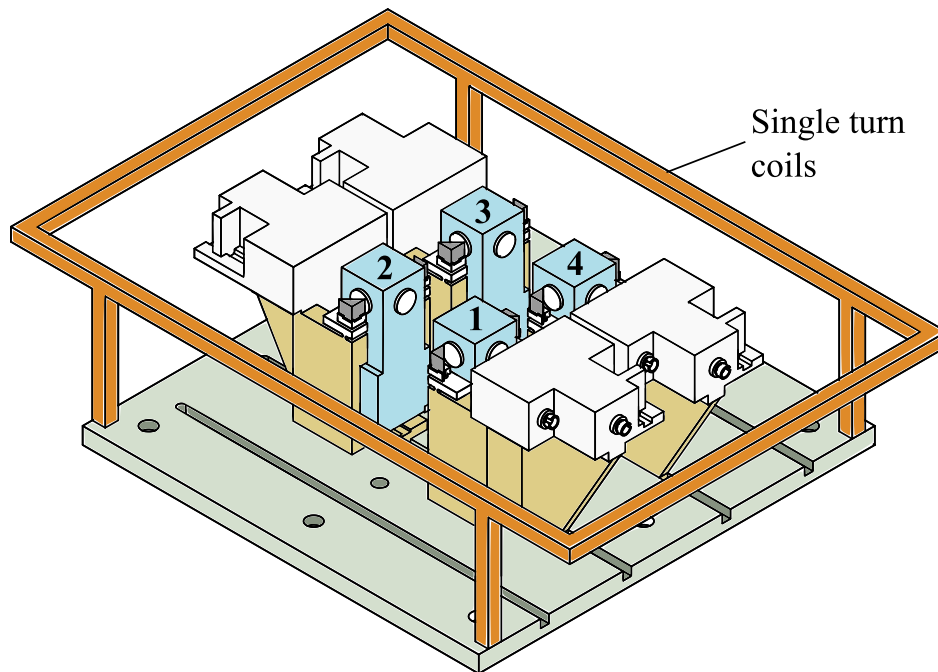


Figure 6.5: The magnetometer array, with the single rectangular coil. The magnetometers are placed symmetrically around the center of the coils, and the coil symmetry ensures the field seen by each magnetometer is the same. One magnetometer, i , provides the error signal, and feedback maintains $B_i = \text{const}$. The fields seen at the other magnetometers is $B_{j \neq i} = c_i + (B - B_i)$, where c_i is the constant offset applied locally to each magnetometer through its cancellation coils. If the fields are initially nulled, $c_i = 0$.

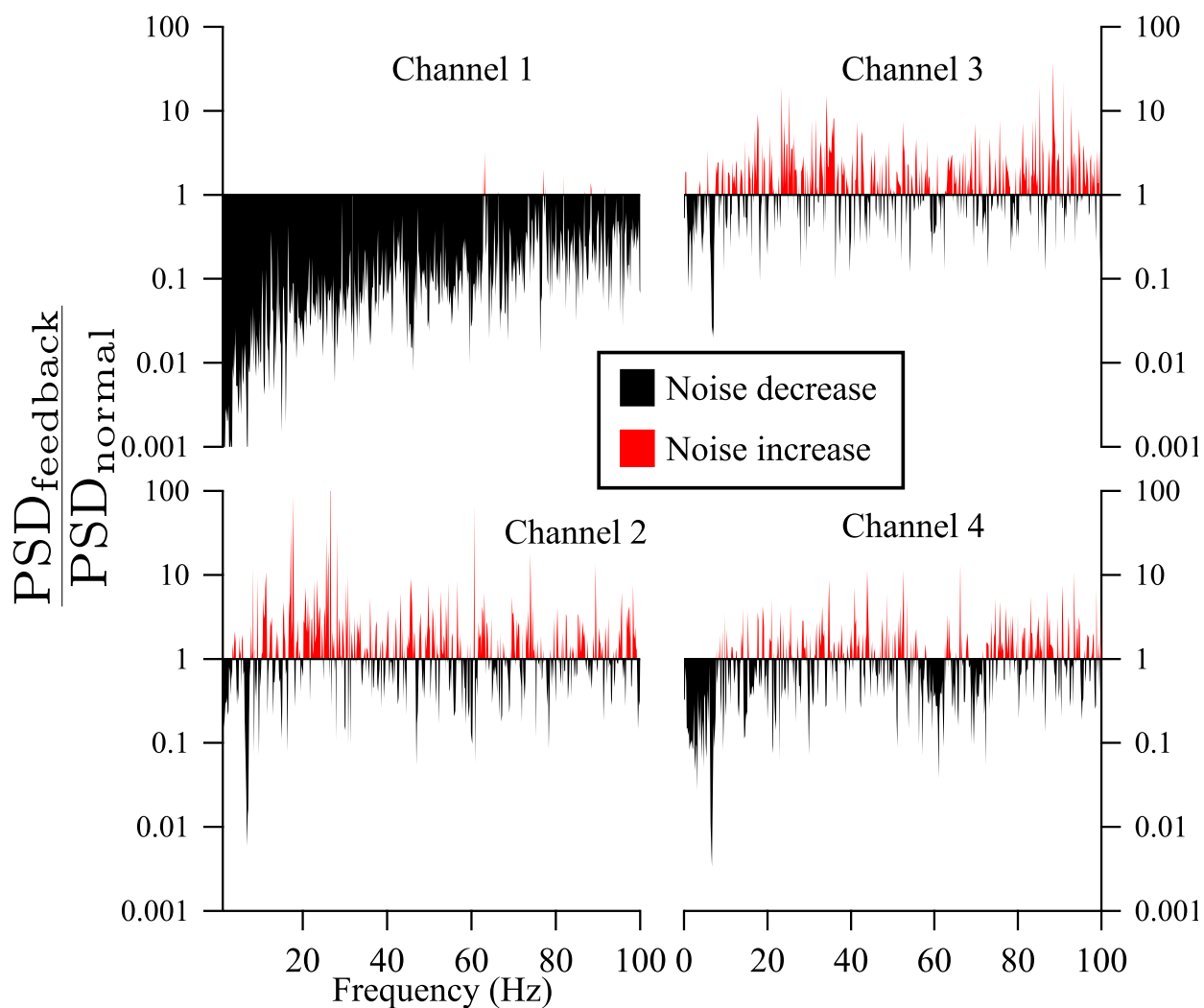


Figure 6.6: A plot of the ratio of spectral noise amplitudes between feedback off and feedback on. Numbers on this scale below 1 correspond to decreased noise, numbers above zero are increased noise. Channel 1 is not a field measurement, but rather monitoring the error signal, and is the performance of the feedback scheme.

HVAC fan was turned off, and the fMCG QRS complex is easily identified in all four channels. The mother's MCG signal is better cancelled in channel 3 than in channels 1 and 2. This is a result of the orientation of the array during the measurement, where channels 1,2 were closest to the mother's heart and 3,4 farthest (see figure 4.5).

Later in the measurement (right), the fan is turned on, and channel-4 responds to keep the field zeroed. In the feedback signal, the originally clear mother's QRS complex is barely discernible, and there is no sign of the fMCG QRS complex. In the other three channels, the fetal QRS complex is still seen.

Operation of the feedback loop is relatively straightforward, since the error signal is exactly the magnetometer signal. We follow the following procedure for using a magnetometer in feedback:

- Set up magnetometers with nulled DC fields
- Connect the desired reference magnetometer to the PID circuitry and connect the PID circuitry to the feedback coils

Large coils: The feedback signal is applied across the coils and a suitable series resistor.

Individual coils: Feedback voltage is applied to the input of the coil control box.

- The polarity of the feedback path can be adjusted by the “invert” output of the I-V converter— if the magnetometer output drops to zero or oscillates, the output is connected with the correct polarity.
- Set the I-V converter gain and frequency cutoff, using only a one-pole filter for the cutoff. Decrease the P-gain until the system no longer oscillates.
- With P-gain set, increase I-gain until the system oscillates, then decrease it back below this point. We generally do not use D gain.

Finally, we provide a general analysis of the feedback elements to understand the limits of the system, how they linearize the magnetometer response, and what issues we will have to overcome to generalize feedback in z-mode. The magnetic field will be suppressed by the closed loop gain as

$$b_{\text{tot}}(\omega) = \frac{b_a(\omega)}{1 + G_{\text{cl}}(\omega)}, \quad (6.4)$$

where $G_{\text{cl}} = G_{\text{mag}}(\omega)G_{\text{I-V}}(\omega)G_{\text{PI}}(\omega)G_{\text{box}}A_{\text{coils}}$ is the closed loop transfer function. When $G_{\text{cl}}(\omega) \gg 1$, the feedback field is equal to the ambient field, with any frequency dependence suppressed. For

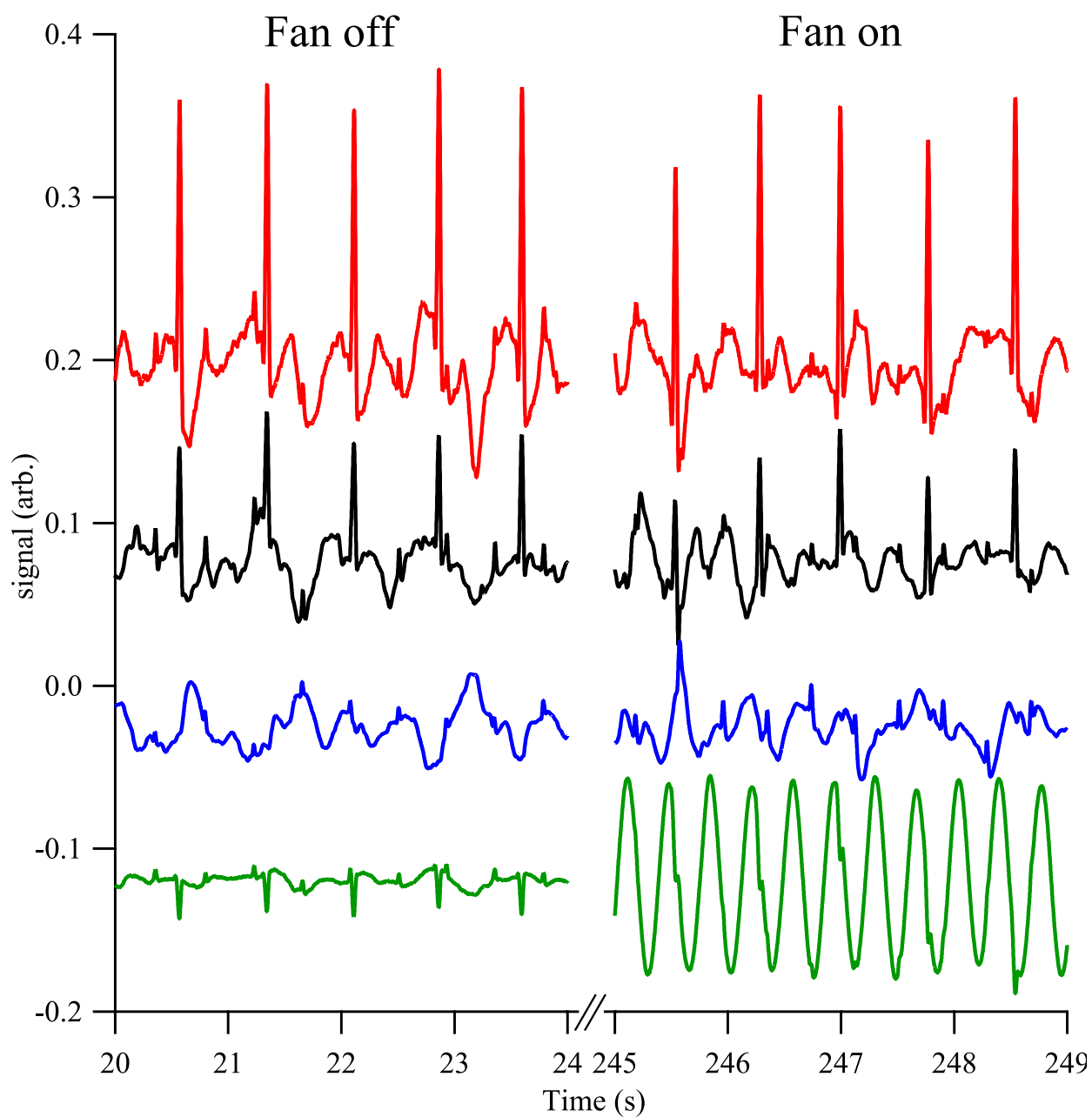


Figure 6.7: Data is from a continuous 5 min fMCG dataset in which the HVAC fan was turned on during the measurement. The bottom channel is the gradiometer feedback reference. The other three channels are largely unaffected by the fan turn on, and both the mother's and fetal MCG QRS complexes are clearly visible in real time both before and after the fan is turned on. The signals have been processed with a bandpass filter from 1-30 Hz, easily implemented in real time using the I-V front panel controls.

the large coils, $A_c = 3 \times 10^9$ fT/A and is used with a resistor, $G_{\text{box}} = R$. A typical calibration from the magnetometer is $G_{\text{mag}} \approx (5 \text{ pA/fT})f_m(\omega)$, where $f_m(\omega)$ is the normalized frequency response of the magnetometer, characterized in figure 4.1. Both $G_{\text{PID}}(\omega)$ and $G_{\text{I-V}}(\omega)$ are adjustable. For noise reasons, we prefer maximizing the amplitude of $G_{\text{I-V}}(\omega) \rightarrow G_{\text{I-V}}f_{iv}(\omega)$, and adjusting $f_{iv}(\omega)$ to maintain loop stability using a single pole low-pass filter with controllable settings via the I-V converter front-panel.

Near DC, the suppression of the large fan noise is important. To reduce the fan noise to $\sim 1 \text{ fT}/\sqrt{\text{Hz}}$, we need $G_{\text{ol}}(6 \text{ Hz}) \approx 10^5$. As with any negative feedback loop, the gain must be rolled off so that $G_{\omega_c} < 1$ at the frequency ω_c where the feedback loop components induce a 180° phase shift [Moore, J. H. and Davies, C. C. and Coplan, 2003, p 481]. In DC-mode, $f_m(\omega)$ has a 3 dB frequency around 50 Hz. If $f_m(\omega)$ is constant until high frequencies, the magnetometer roll-off is usually enough to suppress oscillations until the gain is turned up so much that the fundamental I-V converter bandwidth is important. However, if we want to use z-mode, we must ensure the feedback does not cancel the response from the z-mode modulation frequency, or else the sensitivity to the fundamental component of the signal will be suppressed. If the frequency must be rolled off by a linear filter $f_m(\omega)$, the maximum roll off from the combined $f_m(\omega)f_{iv}(\omega)$ filter is -20 dB/decade (amplitude). This would make the maximum gain at 10 Hz $G_{\text{ol}}(10 \text{ Hz}) = 10^4$, and would practically need to be less to maintain nonzero phase margin and to perturb the response at 1 kHz less. Lower ambient field suppression or nonlinear filtering might still allow z-mode feedback.

Measurement by the reference channel in feedback mode is made by monitoring the output voltage from the PID circuit, V_{PID} . Because flexibility is lost in the choice of antialiasing filters, the detection circuit has a low-pass antialiasing filter at 1 kHz, as well as 10x gain to minimize electronic measurement noise.

6.2 Parametric field modes

This entire thesis, to this point, has focused on the DC operation of the magnetometer, which is characterized by the steady-state response (2.24) and low frequency perturbations from oscillatory

fields, where P_x follows $\Omega_y(\omega)$, but with diminished amplitude and larger phase lag at higher frequencies.

Modulation methods utilize relatively large oscillating magnetic fields to modulate the atomic polarization, where these fields are no longer a perturbation on (2.24), and in fact dominate the response, which is best characterized in terms of the modulation frequency. We discuss two such modes in this work: z-mode and transverse pumping mode.

Z-mode pays a small price in sensitivity for simultaneous measurement of two field directions and higher frequency modulation [Li et al., 2006]. If the magnetometer is dominated by technical (non-magnetic and non-quantum) noise, this mode of operation can greatly improve the sensitivity, especially at low frequencies. Each measured field direction is counted as a measurement channel for signal processing purposes, and doubling the number of channels without increasing the number of cells is a potentially important boon for multichannel signal processing techniques.

A second modulation mode utilizes pumping transverse to a large magnetic field. Large amplitude but short time period 2π pulses are added along the transverse field direction, imposing a resonance on the transverse spin when the 2π pulse cycle frequency matches the transverse field. This magnetometer, which we call a transverse pumping magnetometer, can still operate in the SERF regime. Combined pump/pulse modulation can be used to control the precession frequency of the atoms even in the presence of large DC fields.

6.3 Z-Mode

In z-mode, the additional parametric field is a large oscillating field along the pump direction, $\mathbf{\Omega} = \Omega_x \hat{x} + \Omega_y \hat{y} + (\Omega_1 + \Omega_0 \cos(\omega_z t)) \hat{z}$ and the applied field Ω_0 is large, $\Omega_0 \gg \Omega_x, \Omega_y$. The details of this technique were first presented in Li [2006], Li et al. [2006], but we present a similar derivation here because the methods used in the analysis of the transverse pumping magnetometer are identical.

We assume spin temperature still holds and neglect hyperfine structure and diffusion, and assume the same magnetometer geometry as in figure 2.6. We will also ignore the dependence of the slowing down factor on P . The steady state equation (2.23) can be rewritten in terms of rotating

polarization ($P_{\pm} = P_x \pm iP_y$) and fields ($\Omega_{\pm} = \Omega_x \pm i\Omega_y$), e.g.

$$q\dot{P}_+ = -\Gamma'P_+ - i\Omega_+P_z + i\Omega_z(t)P_+ \quad (6.5)$$

$$q\dot{P}_z = \frac{1}{2i}(P_+\Omega_-P_-\Omega_+) - \Gamma'P_z + R \quad (6.6)$$

with $\Omega_z(t) = \Omega_z + \Omega_0 \cos 2\omega_z t$. If the transverse fields are small, then $P_z = R/\Gamma$ is a steady state solution, as before. Equation (6.5) can be solved with the ansatz $P_+ = A_+ e^{i\phi(t)}$. Plugging this into (6.5) gives

$$\dot{A}_+ = -\left(\frac{\Gamma'}{q} + i\left(\dot{\phi} - \frac{\Omega_z(t)}{q}\right)\right) A_+ - i\frac{\Omega_+P_z}{q} e^{-i\phi(t)} \quad (6.7)$$

which suggest the choice $\dot{\phi} = (\Omega_z(t) + i\Gamma')/q$, which can then be integrated using the explicit form of $\Omega_z(t)$ to get

$$\phi = \frac{1}{q} \left((\Omega_z + i\Gamma')t + \frac{\Omega_0}{\omega_z} \sin \omega_z t \right). \quad (6.8)$$

Assuming $\Omega_+ \ll \dot{\phi}$, it is approximately constant and (6.7) can be directly integrated,

$$A_+ = -i\frac{\Omega_+P_z}{q} \int dt' e^{-i\phi(t')} \quad (6.9)$$

$$= -i\frac{\Omega_+P_z}{q} \int dt' e^{(\Gamma' - i\Omega_z)t'/q - iu \sin \omega_z t'} \quad (6.10)$$

$$= i\Omega_+P_z \sum_{m=-\infty}^{\infty} \frac{\Gamma' + i(\Omega_z + mq\omega_z)}{\Gamma'^2 + mq\omega_z} J_m(u) e^{(\Gamma' - i\Omega_z)t/q - im\omega_z t} \quad (6.11)$$

where $u = \Omega_0/(q\omega_z)$ and the last line makes use of the Jacobi-Anger expansion,

$$e^{iu \sin \omega_z t} = \sum_{m=-\infty}^{\infty} J_m(u) e^{im\omega_z t}. \quad (6.12)$$

The expression for P_+ is given by our original ansatz,

$$P_+ = i\Omega_+ \frac{P_z}{\Gamma'} \sum_{m,m'} F_m J_m(u) J_{m'}(u) e^{-i(m-m')\omega_z t} \quad (6.13)$$

$$F_m = \frac{1 + i(\Omega_z + mq\omega_z)/\Gamma'}{1 + (\Omega_z + mq\omega_z)^2/\Gamma'^2}. \quad (6.14)$$

If $\Omega_z = 0$, the term F_m has a 2nd order bandpass filter response with cutoff frequency $|m|\omega_z = |\Gamma' - \Omega_z|/q$, which is centered at $m = 0$ and rolls off the importance of higher $|m|$ terms.

It is enlightening to Fourier expand the oscillator components of (6.13). The DC term is found by requiring $m' = m$ in the sum of (6.13), and terms oscillating at $n\omega_z$ are found by adding $\delta_{m,n\pm m'} e^{i\pm n\omega_z t}$ to the sum. After expanding the complex exponentials, the response is

$$P_+(\text{DC}) = i\Omega_+ \frac{P_z}{\Gamma'} \sum_m F_m J_m^2(u) \quad (6.15)$$

$$P_+(n\omega_z) = \Omega_+ \frac{P_z}{\Gamma'} \sum_m F_m J_m ((J_{m-n} - J_{m+n}) \sin \omega_z t + i(J_{m+n} + J_{m-n}) \cos \omega_z t) \quad (6.16)$$

(the argument u for the Bessel functions has been suppressed for compactness, $J_i \equiv J_i(u)$). Finally, our probe beam is sensitive to $P_x = \text{Re}(P_+)$. Qualitatively, the DC response will be sensitive to Ω_y , unless a static Ω_z mixes in sensitivity to Ω_x , the same behavior in DC-mode. For the AC cases, (6.16) indicates

$$\begin{aligned} P_x(n\omega_z) = & \sum_m \frac{P_z}{\Gamma'^2 + (\Omega_z + mq\omega_z)^2} J_m \times \\ & [\Omega_x (\Gamma' (J_{m-n} - J_{m+n}) \sin n\omega_z t - (\Omega_z + mq\omega_z) (J_{m+n} + J_{m-n}) \cos n\omega_z t) + \\ & \Omega_y (- (\Omega_z + mq\omega_z) (J_{m-n} - J_{m+n}) \sin n\omega_z t + \Gamma' (J_{m+n} + J_{m-n}) \cos n\omega_z t)]. \end{aligned} \quad (6.17)$$

Limits to these equations were previously discussed when the modulation frequency was large, $\omega_z \gg \Gamma'$ and the DC fields small ($\Omega_z \ll \Gamma'$) [Li et al., 2006]. Then only the $m = 0$ term is important because of the fast fall off of A_m for higher m . Making use of the identity $J_{-m}(u) = (-1)^m J_m$,

$$P_x(\text{DC}) \underset{\omega_z \gg \Gamma'}{\approx} -\frac{P_z}{\Gamma'} \Omega_y J_0(u)^2 \quad (6.18)$$

$$P_x(n\omega_z) \underset{\omega_z \gg \Gamma'}{\approx} -\frac{P_z}{\Gamma'} 2J_0(u) J_n(u) \begin{cases} -\Omega_x \sin n\omega_z t & n \in \text{odd} \\ \Omega_y \cos n\omega_z t & n \in \text{even} \end{cases} \quad (6.19)$$

Experimentally, the response of $P_x(\text{DC})$ can be obtained by low-pass filtering the modulated signal, while the Fourier components $n\omega_z$ can be detected by standard demodulation methods (e.g. using a lock-in amplifier). Under the high frequency, low DC field assumption for (6.18) and (6.19), then the DC and $n = 1$ terms can be used to simultaneously and independently measure

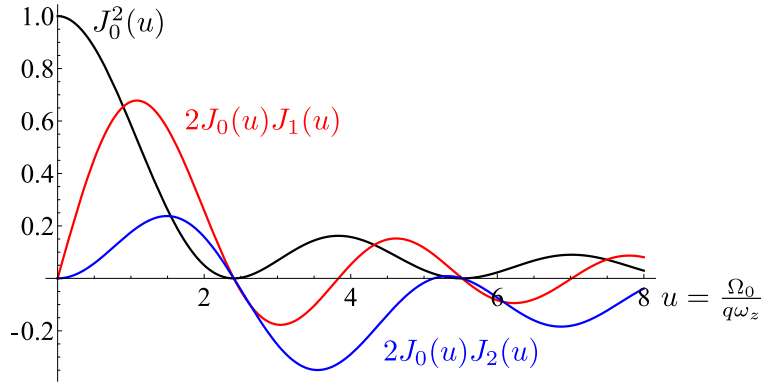


Figure 6.8: Amplitude of the first three Fourier terms which modify the DC sensitivity when $\omega_z \gg \Gamma'$. When using the DC and ω_z terms to detect Ω_y and Ω_x , the optimum is where two Bessel products cross, at $u = 0.9$. The sensitivity for each channel is 80% of the DC-mode sensitivity.

two components of the magnetic field, with a sensitivity modified from the original DC-mode by the Bessel function pre-factors $J_0(u)^2$ for Ω_y and $2J_0(u)J_1(u)$ for Ω_x , which can be seen by comparing (6.18) and (6.19) with (2.24). As discussed in Li et al. [2006], the $n = 2$ term could also be used for Ω_y detection, allowing lock-in detection of both signals, but $J_0(u)J_1(u)$ and $J_0(u)J_2(u)$ have a much lower common optimum. Figure 6.8 shows these first three terms, and the best dual-channel operation is where the DC and $n = 1$ Bessel product terms cross. The sensitivity here is still 80% of the original DC-sensitivity.

One complication is that, with our high Γ , $\Gamma' \approx 10^3 \text{ s}^{-1}$. Since the optimum response is where $u \sim 1$, the amplitude of the modulating field should be $\Omega_0 \sim q\omega_z$, however Ω_0 should be kept low enough to maintain SERF operation. This limits $\omega_z \ll 2\pi \cdot 10 \text{ kHz}$ for $T = 145^\circ\text{C}$. We typically operate at 1 kHz to compromise between the desire for higher frequency and increased relaxation rates due to higher SE relaxation. These frequencies are sufficient so that the $F_{i \geq 1} \ll F_0$.

Experimentally, Z-mode requires a slightly different nulling procedure. We begin with each magnetometer zeroed by the DC nulling process described in section 4.2. Imperfect initial photodiode balance and elliptical probe polarization can affect the DC offset, which does not affect our DC-mode operation but is important to ensure response at each frequency component aligns with the coil axes. For example, when the initially set DC values are used in z-mode, the response to the fundamental frequency ω_z typically includes B_y at the 10% level of B_x . While the different

frequency components are still orthogonal to one another, this indicates bias fields are still present, and the procedure below can be used to cancel them.

Ensuring the anti-aliasing filters have been increased to 3 kHz cutoff frequency, the z-mode field is applied at the same frequency $\omega_z \approx 2\pi \times 1 \text{ kHz}$ to each magnetometer individually. Currently, we use a set of FPGA outputs connected to the z-axis coil control box input, and change the control box gain to obtain suitable signal sizes. Two small test fields are used alternately, $\Omega_x = a \sin(\omega_1 t)$ and $\Omega_y = a \sin(\omega_1 t)$, of similar size to the calibration fields used in previous sections, and adjustments to the DC offset fields B_{0x}, B_{0y}, B_{0z} are made as follows:

- Assuming we will use the low-passed signal to measure B_y , adjust Ω_0 to maximize the response to Ω_x .
- Adjust B_{0x} to eliminate any $\sin^2(\omega_1)$ behavior in the fundamental response. Adjust B_{0z} to minimize the low-pass response while maximizing the fundamental response.
- Now watching the fundamental response, adjust B_{0y} to eliminate any $\sin^2(\omega_1)$ behavior. Readjust B_{0z} to minimize the low-pass response while maximizing the fundamental response.
- Readjust Ω_0 to ensure the fundamental response to B_x is maximized.
- If large changes in the offset fields were made during any step, this process should be repeated.

After the nulling procedure described above, the low-pass and fundamental response are sensitive to the “wrong” field to $< 5\%$. The two different magnetometer axes each require independent calibration. Calibration steps are the same as described in section 4.3.2, but occur in two separate steps, for each direction.

Figure 6.9 shows z-mode noise spectra. The probe noise (not shown) dominates the noise floor in these modes, mostly because the I-V converter gain must be turned down or else the large modulation field saturates them, and because the anti-aliasing filter frequency must be increased. Still, the noise floor from all channels is $< 20 \text{ fT}/\sqrt{\text{Hz}}$.

Expanding feedback to this mode requires some care, since the independent field components are separated in frequency space. Separation of the two signals B_x and B_y by electronic filtering

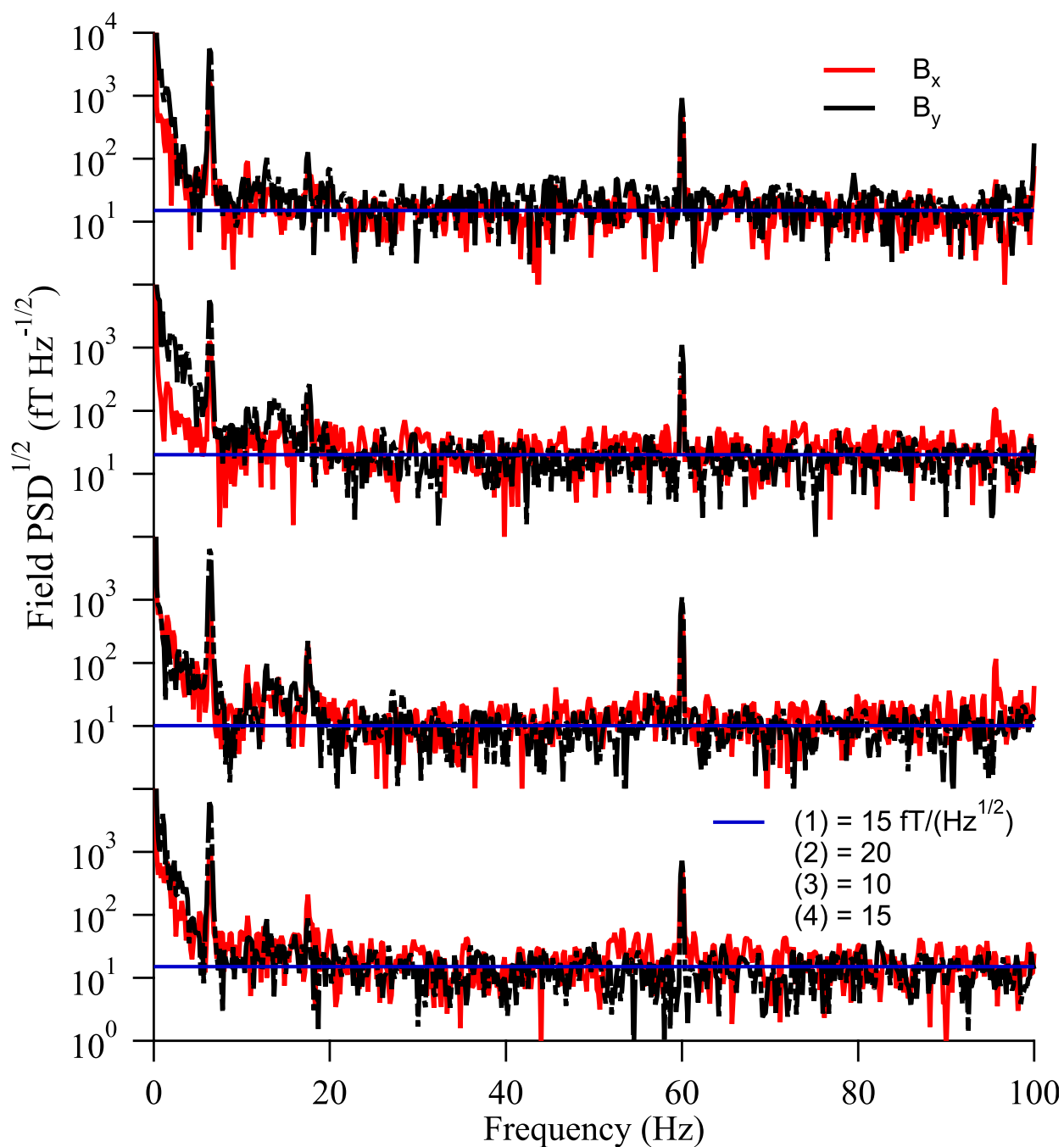


Figure 6.9: Noise spectra obtained using z-mode, using the DC and $n = 1$ components to measure B_y and B_x . The red and black dashed channels correspond to measurements of B_x and B_y respectively. The horizontal blue lines are references to guide the eye. Their values, reading from top to bottom (channel 1 to channel 4), are 10–20 fT/ $\sqrt{\text{Hz}}$.

would require a filter with a cutoff steep enough to isolate 100 Hz from 900 Hz, and with a gentle-enough phase response that the loop was stable, and with gain high enough to usefully suppress the background fields. This is a challenging filter, and we have not found a suitable implementation of it. Using the demodulated or low-passed signal introduces phase lags in the feedback path, requiring reduction of the signal gain in order to maintain stability. While a solution might exist that allows feedback to maintain both B_x and B_y at zero, a workaround is to use three magnetometers in z-mode, and use the fourth as an error signal to the big coils in feedback mode. This compromise allows the benefits from feedback in B_y while only decreasing the channel count from 8 to 7.

6.4 Transverse pumping SERF magnetometer

This section outlines a new method of SERF magnetometry, which takes advantage of spin-resonance in transverse pumping for high magnetic fields. While we describe the transverse pumping magnetometer in the context of SERF magnetometry, the basic technique is useful in any situation where one wants to polarize an alkali vapor perpendicular to a very large magnetic field, and can be extended to situations where one wants to control the alkali precession frequency, say to match the precession frequency of another precessing atom intermixed with the alkali. Previous studies have investigated this phenomenon at low transverse field amplitudes [Cohen-Tannoudji et al., 1969, Slocum and Marton, 1973]. To our knowledge, none have investigated it in the context of SERF magnetometry.

Before describing the transverse pumping magnetometer, we point out two limitations to any of the SERF techniques described above that this new method overcomes. First, practical vapor cell issues limit the maximum attainable Rb density to $n < 10^{15} \text{ cm}^{-3}$ at 200 °C. As we discussed in section 2.1.2, this limitation imposes an upper bound in the ambient field magnitude in which SE relaxation is suppressed. For a ^{87}Rb cell at 200 °C, the SERF condition is $|B| \ll 4\mu\text{T}$, which would prohibit SERF magnetometry in Earth's field environments. Feedback could be used to lower the ambient field into the SERF regime [Seltzer and Romalis, 2004], but this would be unsuitable for situations where the DC field is required, such as NMR applications where the DC field helps

increase spin-coherence times of the NMR sample. The transverse pumping magnetometer enables SERF operation in the presence of high DC fields. In particular, SERF operation in Earth-sized fields is feasible, and would open the possibility of extending SERF magnetometers to a host of new applications.

A second practical limitation is the need for calibration. Section 4.3.2 describes the calibration procedure, which enables a field measurement to be obtained from continuously monitoring alkali spins. This procedure is, for the most part, sufficient when absolute accuracy is unimportant (though see caveats in section 4.3.2 and section 7.2). This is the case in most biomagnetism applications, where the desired information is in the timing of signals rather than their overall amplitude. Magnetometers that detect an actual atomic precession frequency, such as those utilizing the M_x -technique, measure a frequency related through fundamental constants to the magnetic field, no external calibration necessary. Again, for SERFs, feedback can help (see section 6.1.2), but still requires accurate calibration of a set of magnetic coils. The transversely pumped SERF magnetometer can be used in closed loop mode as a resonator, with its resonance frequency determined by a Larmor frequency.

The geometry is in figure 6.10(a), where the pump and probe beams are still orthogonal, but there is a very large field orthogonal to both. Since this field is the largest interaction with the atoms, it defines the \hat{z} axis, and for this section we use a different set of coordinates, marked in figure 6.10(a).

The experimental scheme is now the fields in the transverse direction should be zero, but there is an applied large Ω_z and a periodic $\Omega_1(t)$ with period ω_1 , $\mathbf{\Omega} = (\Omega_z + \Omega_1(t))\hat{z}$. The pump is in the \hat{x} -direction. The Bloch equations, assuming spin-temperature and our new geometry, are the same as (6.5), except with the addition of a pumping term. For a CW pump laser,

$$q\dot{P}_+ = -i(\Omega_z + \Omega_1(t))P_+ - \Gamma'P_+ - i\Omega_+P_z + R \quad (6.20)$$

where P_+ and Ω_+ have the same definition as in the previous section. If the transverse fields are zero, $\Omega_+ = 0$ and $P_z = 0$. The choice of the form of $\Omega_1(t)$ is important. The optimum, for the case where we want to operate the magnetometer in the SERF regime, will not be sinusoidal

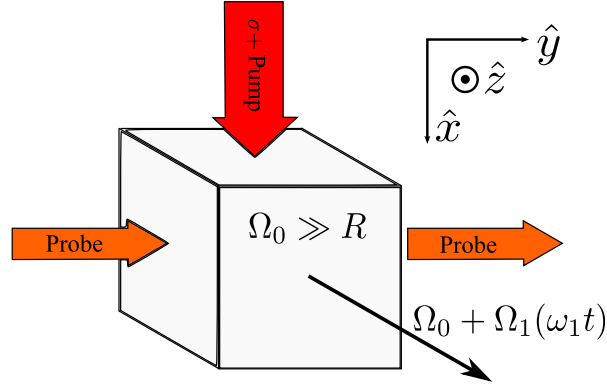


Figure 6.10: Diagram of the transverse pumping setup described in this section. Transverse pumping allows $P_x \approx 1$, despite $R \ll \Omega_z$.

modulation. However, to start with we will use $\Omega_1(t) = \Omega_1 \cos \omega_1 t$. Then the equation of motion for P_+ is

$$q\dot{P}_+ = -i(\Omega_z + \Omega_1 \cos \omega_1 t)P_+ - \Gamma'P_+ + R. \quad (6.21)$$

This equation can be solved in exactly the same manner as (6.5), with the substitution from that solution $-i\Omega_+P_z \rightarrow R$,

$$P_+ = \frac{R}{\Gamma'} \sum_{m,m'} F_m J_m(u) J_{m'}(u) e^{-i(m-m')\omega_1 t} \quad (6.22)$$

$$F_m = \frac{1 + i(\Omega_z + mq\omega_1)/\Gamma'}{1 + (\Omega_z + mq\omega_1)^2/\Gamma'^2}. \quad (6.23)$$

with $u = \Omega_0/(q\omega_1)$. The DC part for both spin components is once again found when $m' = m$,

$$P_x = \frac{R}{\Gamma'} \sum_{m=-\infty}^{\infty} \frac{J_m^2(u)}{1 + (\Omega_z + mq\omega_1)^2/\Gamma'^2} = \frac{R}{\Gamma'} \sum_m \frac{J_m^2(u)}{1 + \Delta\Omega_m^2/\Gamma'^2} \quad (6.24)$$

$$P_y = \frac{R}{\Gamma'} \sum_{m=-\infty}^{\infty} \frac{J_m^2(u)(\Omega_z + mq\omega_1)/\Gamma'}{1 + (\Omega_z + mq\omega_1)^2/\Gamma'^2} = \frac{R}{\Gamma'} \sum_m \frac{J_m^2(u)\Delta\Omega_m/\Gamma'}{1 + \Delta\Omega_m^2/\Gamma'^2}, \quad (6.25)$$

where in the right hand side we have made the substitution $\Delta\Omega_m = \Omega_z + mq\omega_z$, intended to make the resonance nature of the equation clear. Most of the physics of the transverse oscillator is in the above two equations, and they are plotted in figure 6.11 for $\Gamma' = 0.1\Omega_z$. First, if we imagine using the DC term as a magnetometer, the only field in the problem is Ω_z . If we look at the behavior of P_x , we see that there is a resonance for every m value, $\omega_1 = \Omega_z/(mq)$. At this resonance, P_x is

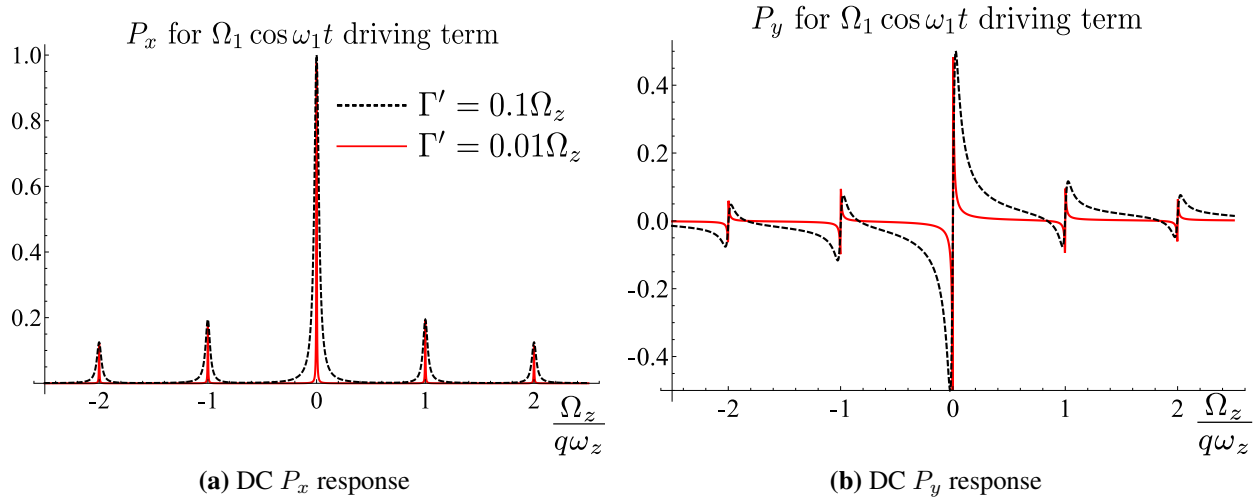


Figure 6.11: (a) The response along the pump beam, for good pumping $R \approx \Gamma'$ and two different fields, $\Omega_z = 10, 100\Gamma'$. (b) P_y for the same situations.

maximized for a single $J_m(u)$ term. The resonance at zero frequency is still the largest, but others show up at integer m . When not on resonance, the small pumping rate cannot pump the atoms. When on resonance, the motion of the atoms is complicated, but the sum of the modulation and DC fields conspires to allow the atoms to precess more slowly when oriented along \hat{x} than $-\hat{x}$.

P_y has a similar dispersive-like curve as the DC case, but again modified to have many resonances rather than a single one at zero frequency. The sharp central feature is a function of the relationship between Ω_z and ω_1 , and if we use a constant modulating frequency, small changes in Ω_z will be proportional to the difference from resonance. In fact, each term in the sum (6.25) is exactly the same equation as (2.24) if $\Omega_y \rightarrow \Delta_m$, except for the $J_m^2(u)$, which just modify the amplitude. All of the results developed in chapter 2 can be adapted to the behavior here in the transverse pumping case.

The structure of the modulating field becomes important here. If we wish to maximize the time spent aligned along the pump axis, then a repetitive pulse with the shape in figure 6.12a(b) is the best to use. The shape is approximately a periodic 2π pulse, with repetition frequency $\omega_1 = \Omega_z/q$, and here $q = (2I + 1)$, where I is the nuclear spin. We will discuss why q is independent of the polarization shortly. It is important to remember though that the actual precession rate of polarized

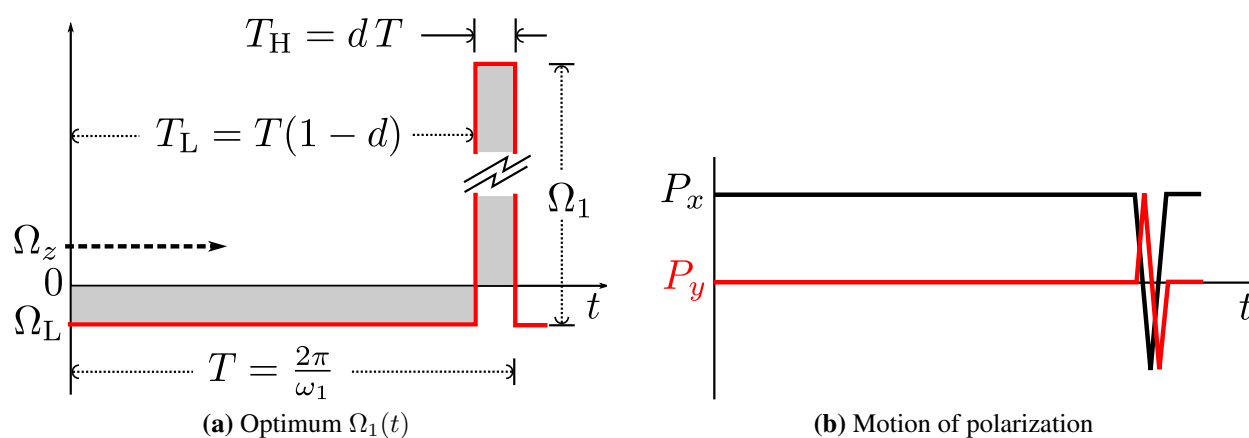


Figure 6.12: (a) Optimum shape for $\Omega_1(t)$. The AC-coupled pulse (in red) consists of two parts. Initially, the amplitude of the pulse is Ω_L for most of the periodic waveform. Then a large amplitude Ω_0 is applied for a time $\Omega_0 dT = 2\pi$. When the pulse frequency is $2\pi\Omega_z/q$, then $\Omega_L = -\Omega_z$, and these fields cancel out during the low portion of the pulse, and the SERF regime is maintained. For very short pulses, spin relaxation is suppressed because $dT \ll T_{se}$ (few collisions occur during the high field). The SERF regime is maintained during the entire pulse, despite the field averaged over a single pulse remaining large ($\Omega_z \gg R$). (b) Motion of the polarization components, under the assumptions described above. The shorter d , the higher the maximum P_x .

atoms for a physical field B is $\Omega = \gamma B/q$. The pulse is AC-coupled, thus over a single cycle the pulse area is enforced to be zero, and the averaged DC field is Ω_z , as it is without any pulse. This implies the motion of Rb atoms over one pulse cycle is always $T\Omega_z/q$.

In terms of the low (high) amplitudes $\Omega_{L(H)}$ and the low (high) time periods $T_{L(H)}$, and the total period $T = T_L + T_H = 2\pi/\omega_1$, there are three governing relations for the waveform in figure 6.12a:

$$\frac{\Omega_L}{q}T_L + \frac{\Omega_H}{q}T_H = 0 \quad (\text{AC coupled}) \quad (6.26)$$

$$d\frac{\Omega_1}{q}T = 2\pi x \quad (\text{Pulse area } 2\pi x) \quad (6.27)$$

$$T = \frac{2\pi q}{\Omega_z} \quad (\text{Resonant pulse frequency}). \quad (6.28)$$

These equations allow a solution for the low field under the conditions prescribed above (AC coupling and at resonance frequency),

$$\Omega_L = -\frac{x}{1-2d}\Omega_z. \quad (6.29)$$

For the limiting case of an infinitely short pulse with 2π area, $\Omega_L = -\Omega_z$.

This is a remarkably useful result: by making a short AC coupled 2π , and repeating that pulse at the resonance frequency, the total field T_L ($\Omega_z + \Omega_L$) is zero. For an infinitely short pulse, $\Omega = 0$, except during the pulse itself. The best pulse shape will delay the precession during the cycle until the pulse at the very end, during which the precession occurs rapidly. When $d \ll 1$ but finite, there is a pulse area $2\pi(1-2d)$ for which $\Omega_L = 0$ still. Hence, SE relaxation can always be suppressed during the long part of the cycle.

During the high part of the pulse, SE collisions can still lead to relaxation. This problem is mitigated by two effects. First, if the atoms are highly polarized, SE relaxation is suppressed since the atoms are pumped into the stretched hyperfine state [Savukov and Romalis, 2005]. Secondly, on resonance, $T = q2\pi/\Omega_z$, so the ‘‘on-time’’ for the high field is $T_H = 2\pi qd/\Omega_z$. If the pulse width is much shorter than the SE period ($T_H \ll T_{se}$), then few atoms undergo a SE collision during the time when such a collision could lead to relaxation. For $T = 145^\circ\text{C}$, $T_{SE} \approx 20\ \mu\text{s}$, requiring a minimum pulse amplitude $B_1 \gg d \times 1\ \mu\text{T}$. This is not a particularly stringent requirement on the pulse height, though the optimum performance is achieved for pulses approaching a delta-function.

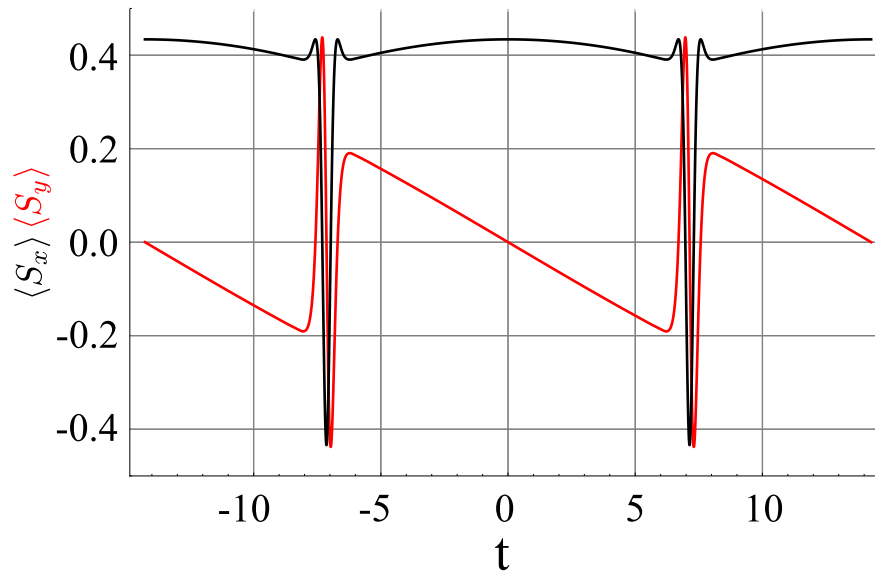


Figure 6.13: Simulation of the polarization components for $\Omega_1 T = 2\pi q \times 1.25$. The primary feature is $\Omega_z \neq 0$ during the long part of the pulse cycle, so the polarization continues to precess. The resonances are still prominent.

Hence SE relaxation is suppressed during the entire pulse cycle, despite the average magnetic field Ω_z over one cycle being arbitrarily large. While the transverse polarization is very sensitive to the resonance condition, the pulse area is not as critical. As long as the pulse height satisfies the description of the previous paragraph, SE relaxation is suppressed during the high part of the pulse. For the low part, the choosing a $\sim 2\pi$ pulse ensures the cancellation of the the ambient Ω_z by the AC coupled field for resonant pulse frequency. SERF is achieved in low ambient fields under the same conditions described in section 2.1.2, so the prescription to maintain SERF sensitivity is $T_{SE}\Omega_z(1-x) \ll 2\pi$. Figure 6.13 shows a plot of the motion of the two components of the polarization, when the pulse-width is not optimal. The most noticeable effect is that during the time between pulses, the atoms continue to slowly precess, due to the imperfectly cancelled ambient field. The resonances are still clearly visible, implying that optimization can be done experimentally on the pulse height.

We have obtained some initial results for the transverse pumping, shown in figure 6.14. The measured signal is the low-passed Faraday rotation measurement, which is proportional to P_y . For technical reasons, the plots were taken by setting ω_z and $\Omega_1 \approx 2\pi/T_H$, and then scanning Ω_z to find

the resonances. The bottom (blue) curve was taken by optimizing the pulse amplitude to minimize all but the first resonance in the signal. The bottom and top units are related through $\Omega = \gamma B/q$. For this measurement $\omega_z = 2\pi \times 35$ kHz.

One indication that no SE relaxation occurs during the peak of the pulse is whether the precession occurs at a rate governed by $q = 2I + 1$. During the large part of the pulse, atoms in different hyperfine manifolds precess in opposite directions at nearly the same frequency. If no spin exchange collisions occur, precession in each hyperfine level occurs independently at the rate given for $q = 4$, the free atom precession frequency. If SE collisions occur during precession, the precession rate is slowed, as atoms spend some in each hyperfine level during precession. This initial measurement suggests $q = 3.5$, which is probably off due to imperfect magnetic field coil calibration.

To use the system as a magnetometer, one may apply a large field Ω_z and feedback ω_1 to maintain resonance in the presence of an ambient field adding to Ω_z . An experimental challenge in this initial measurement was ensuring the pulse field and z-fields were uniform across all the atoms in the cell. If they are not, then the resonance frequency varies across the cell, and broadens the linewidth. A special set of coils was used for the pulse coils to help with this condition, described in chapter G.

In addition to magnetometry, transverse pumping may be used in a novel form of spin-exchange optical pumping (SEOP). Noble gas atoms may be polarized perpendicular to a magnetic field, with similar physics to the description above, only with the alkali spin as the pumping term. The noble gas precession frequency is set by the nuclear gyromagnetic ratio, and is around 1000 times less than the rubidium gyromagnetic ratio. For successful SEOP, we require the alkali spins to be aligned with the helium spins, and so we must be able to control the alkali precession.

The transverse pumping method described above allows alignment along the pump direction that is static compared to the timescale of noble gas precession. If the alkali pumping rate is modulate $R \rightarrow R e^{i\theta}$, where θ is the slow noble gas precession phase, then we have satisfied the necessary requirements. Such a configuration could be useful in the construction of noble gas gyros.

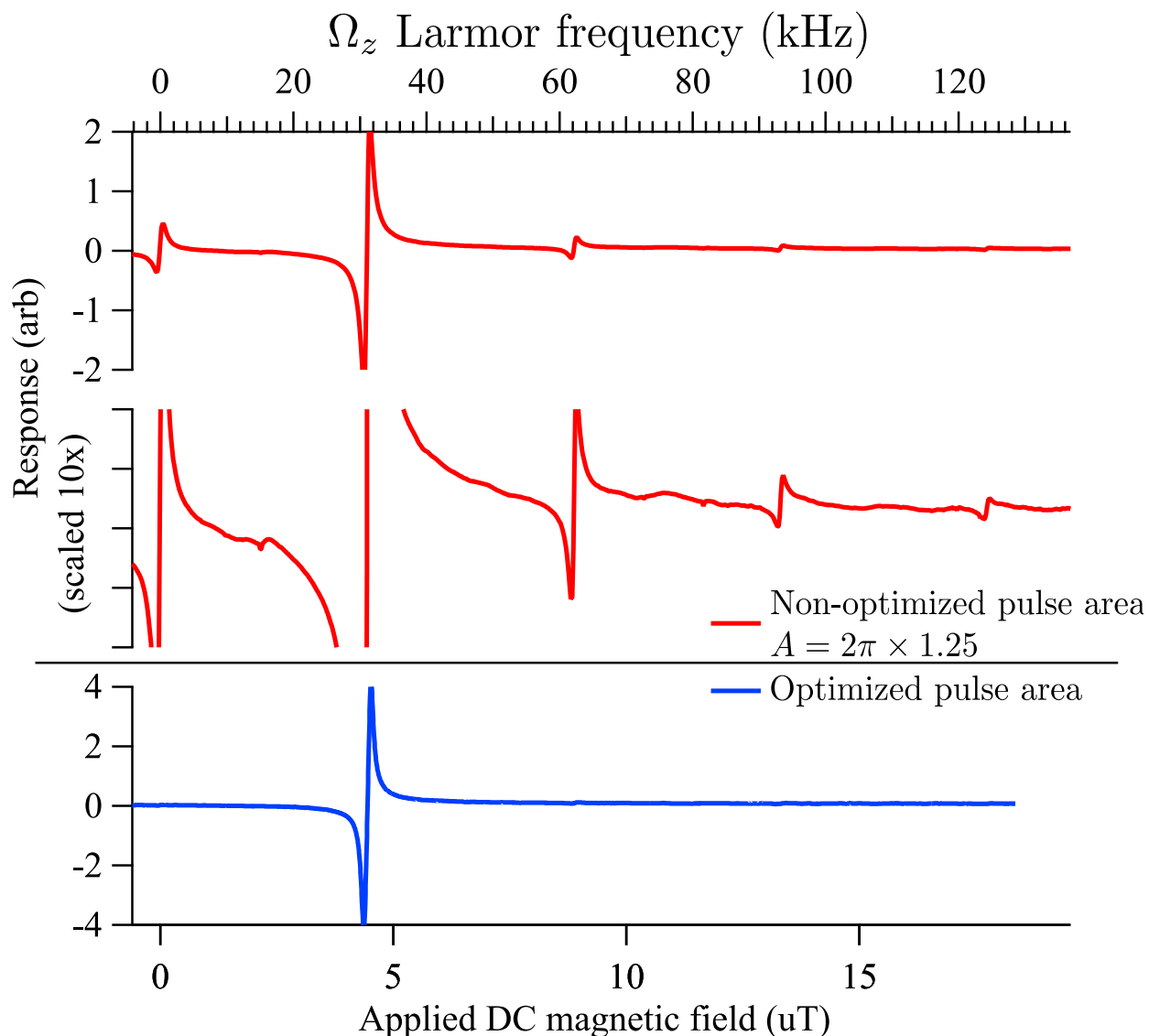


Figure 6.14: Low-passed response of the transverse pumped SERF magnetometer, as the large DC-field Ω_0 is swept. The data shows the relative insensitivity to the 2π -pulsewidth compared to the resonance linewidth. The main effect from incorrect pulse area is the appearance of extra resonance features (red curves). The blue curve shows the result for optimizing the pulsewidth by minimizing the DC resonance peak. The extra resonances largely disappear.

Chapter 7

Biomagnetism

In this chapter, we focus on the particulars of the signals for which we are developing the SERF magnetometer array: biomagnetic fetal MCG. We will talk about the general features of the biomagnetic signals for which we intend our array to be suitable. We will demonstrate the signal quality achievable by our array in real MCG applications, such as MCG and fMCG. Finally, we will broach the general issue of biomagnetic signal processing. We do not pretend to provide an exhaustive overview of this vast topic, aspiring merely to paint a picture of the applicable techniques and limitations, and especially to discuss how they inform design and operation decisions for our device.

7.1 MCG characteristics

We begin by examining the features of typical MCG signals. Databases of electrocardiogram (ECG) signals exist in downloadable form for testing signal processing algorithms, such as the PhysioBank ATM [Goldberger et al., 2000]. We use the ECGSYN, a resource from the PhysioNet Toolkit, which uses a mathematical algorithm to generate realistic ECG waveforms [McSharry et al., 2003]. The generator produces a digital waveform, which can be applied through the FPGA

output to a small coil or phantom head to test the magnetometer. The generator allows user selection of parameters such as heart rate and variation, QRS morphology and various other aspects of the MCG signal, as well as additive noise.

The standard features of an MCG signal are in the lower-left inset of figure 7.1. During fMCG arrhythmia detection, the desired information is related to the beat-to-beat timing interval of MCG features, such as the QT or PR intervals. Tables for healthy fetal populations of different gestational ages have been compiled, e.g. [Golbach et al., 2000], and deviations from these values can indicate specific abnormalities.

For an adult MCG, we use a model of default ECGSYN parameters but minimized variation and noise, at 60 bpm. We model a fetus with the same parameters, but at 130 bpm [Leeuwen et al., 2004]. Figure 7.1 shows an example of the waveforms (inset), as well as the amplitude spectral density for those waveforms. It is apparent that the region below 70 Hz is most important for fMCG.

Another useful way of characterizing a typical MCG spectrum is with a joint time-frequency transform. The Fourier spectrum of the MCG is itself periodic in time. Take a finite segment of MCG data, such as the sample data in figure 7.1. We break this into i segments of length $T \leq T_{\text{beat}}$, where T_{beat} is the beat period (RR interval). The Fourier transform of each segment is the same only when $T = T_{\text{beat}}$.

There are many joint time-frequency techniques to examine this behavior. The short term Fourier transform (STFT) is one such technique, which uses a windowed FFT, where the window is time shifted to obtain the FFT as a function of time. Figure 7.2 shows an example of the STFT applied to the sample MCG in figure 7.1, where the color scale is a log scale. The important features of this figure are the widely varying FFT with time. Additionally, the P and T features of the signal have low bandwidth, and to accurately identify where they begin for timing purposes will require high sensitivity from 1-10 Hz for MCG, and at slightly higher frequencies for fMCG.

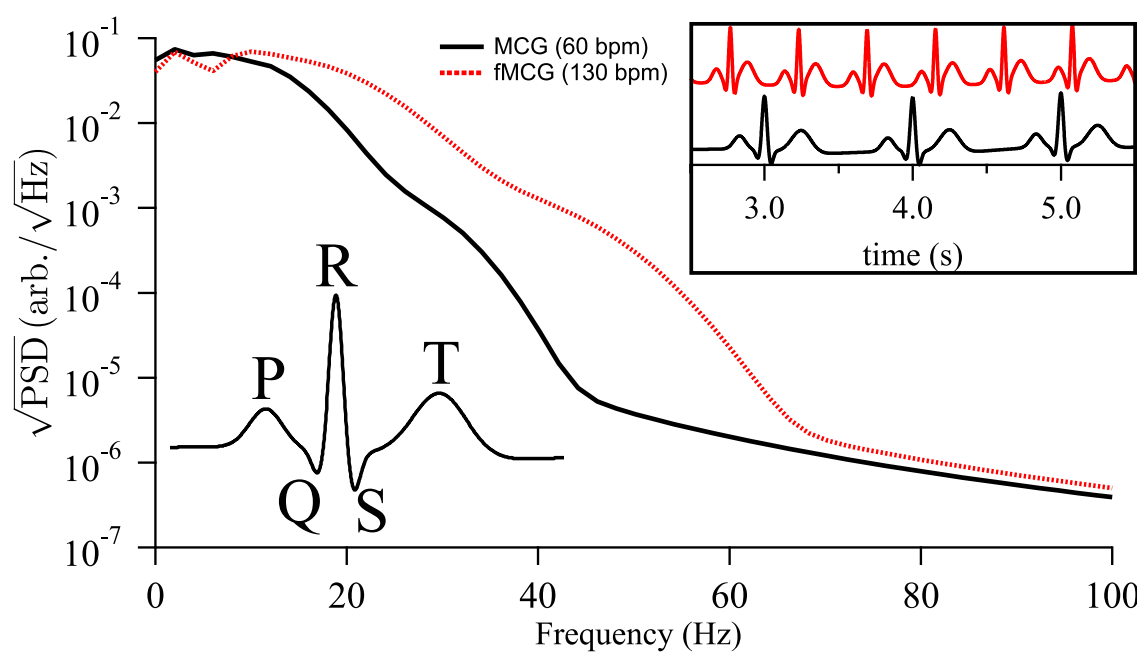


Figure 7.1: Simulated example MCG (black) and fMCG (red), from a mathematical model [McSharry et al., 2003] and generated by the online PhysioNet Toolkit ECGSYN waveform generator. The only difference in the simulated parameters are the average heart rate, 60 bpm for the MCG and 130 bpm for fMCG. The amplitude for both signals is arbitrary. The upper right inset is a portion of the time series generated by the ECGSYN generator. The lower left inset has the standard labelling for the features of an MCG

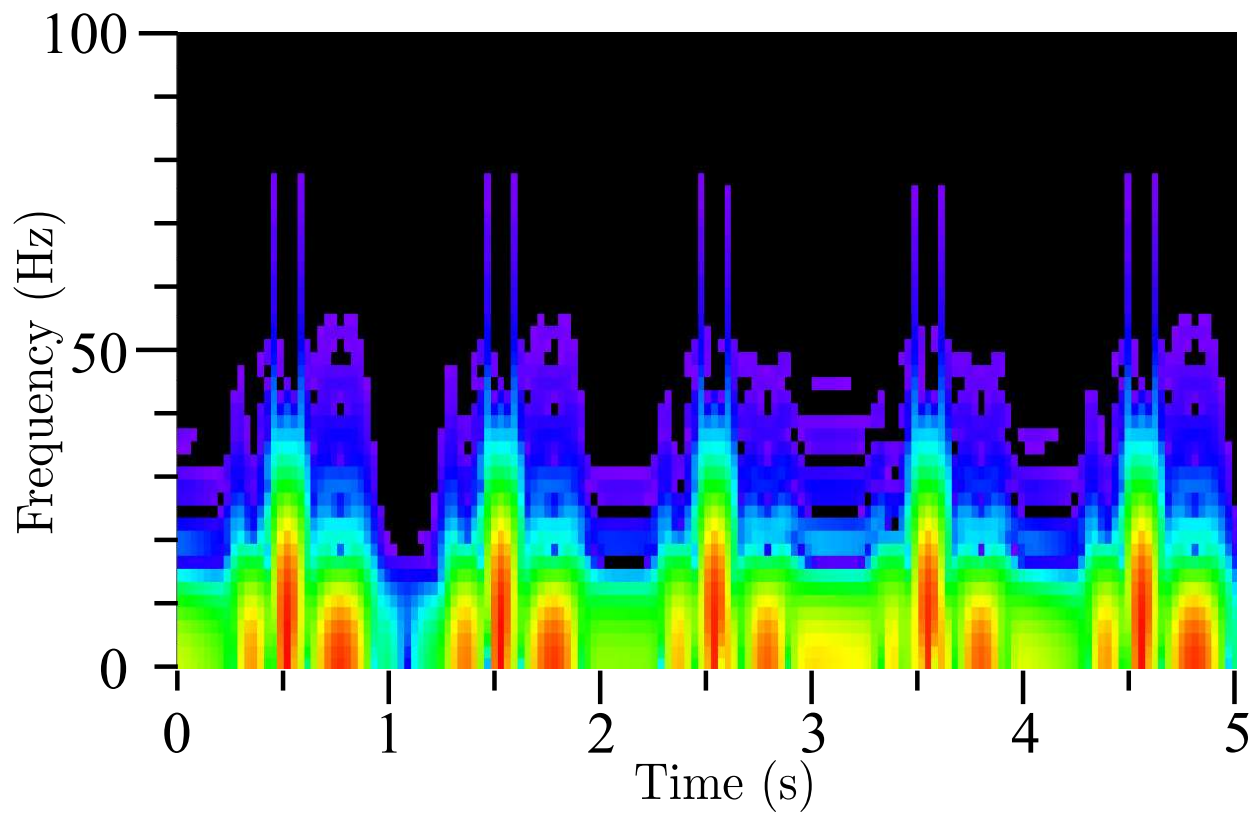


Figure 7.2: STFT of the sample MCG signal presented in figure 7.1. The STFT essentially uses a sliding window across the time domain to compute an FFT as a function of time. The color scale is logarithmic in signal size. The P, QRS-complex, and T waves are all visible. One important point of this figure is that to resolve the P and T waves, the frequency performance of the magnetometer below 10 Hz is important.

7.2 Signal processing

After the calibration and acquisition procedure (section 4.3), magnetometer recordings are corrected by deconvolution with the magnetometer response. The DAQ program currently does this by transforming to the frequency domain and then algebraically performing the deconvolution. Specifically, if $\xi(\omega) = \chi(\omega)e^{i\phi(\omega)}$, then $B(t)$ is recovered by

$$\tilde{B}(\omega) = \frac{\tilde{V}_m(\omega)}{\xi(\omega)} \quad (7.1)$$

$$B(t) = \text{IFFT} \left(\tilde{B}(\omega) \right), \quad (7.2)$$

where $\tilde{x}(\omega) = \text{FFT} (x(t))$ and the m-subscript indicates the quantity from the originally measured signal.

This initial step is completed on all signals in order to get a sensible measure of the magnetic field during the recording time window. If the goal is to measure a signal of interest, in our case a biomagnetic signal, further signal processing techniques are often available. Any information that allows separation of intended signal and interfering noise is an avenue for signal processing. The techniques we use fall into two categories: those which can be performed independently on a single magnetometer measurement, and those requiring multiple magnetometers.

When we refer to noise, we are dealing with several different sources. Actual magnetic noise adds to the signal of interest and would be detected by any magnetometer. SERF detector noise, either fundamental or technical, also adds to each channel, but with different multichannel results. Table 7.1 gives a sample of the characteristics of the various sources of signal that eventually makes it to each magnetometer channel. Table 7.1 provides insight into how each noise source might be distinguished from the sought signal, because different signal processing techniques are suitable for SNR enhancement in the presence of different types of noise. In what follows, we will assume we are attempting to detect an fMCG signal in the presence of all the noise sources listed in table 7.1.

Table 7.1: Properties of noise sources for our magnetometers. For the spatial characteristics, “near” or “far” indicates effective magnetic source distance compared to the channel spacing. White noise implies the power spectral density is uniform and stationary. A signal localized in both the frequency and time domain has regularly changing frequency content with time. Correlated indicates the technical meaning and does imply equality of response from all channels to the noise source. We use the nonuniform spatial characteristic label to indicate the noise source emanates from the detectors, and is generally different from one detector to another. The detection noise includes electronic noise and noise relating to the probe detection scheme but unrelated to the intensity or frequency of the probe laser itself. An example would be beam deflection on photodiodes due to vibrations.

Source	Type	Frequency/time rep.	Spatial characteristics	Correlated?
MCG/fMCG	Magnetic	Localized (both)	Nearby source	Yes
Coil circuit noise	Magnetic	white	nonuniform	No
HVAC fan	Magnetic	Single frequency	Distant source	Yes
Johnson noise (from MSR)	Magnetic	White	Mostly far, uniform field	Yes
Mother’s MCG	Magnetic	Localized (both)	Further, not far	Yes
Laser fluctuation	Technical	1/f	nonuniform	Yes
Detection noise	Technical	1/f	nonuniform	No
Quantum	Fundamental	white	nonuniform	No

7.2.1 Single-channel processing techniques

Single channel signal processing relies on finding ways to eliminate parts of the signal that cannot originate from fMCG, where signal processing can be applied to each magnetometer channel separately. The lowest hanging fruit, here and in almost any application, is bandwidth limiting. An accurate representation of an fMCG requires a bandwidth of about DC–80 Hz, as can be seen from the sample fMCG in figure 7.1 (real measurements are abundant in the literature, e.g. Rassi and Lewis [1995]). Higher frequencies are only noise and should be eliminated. This is done both by hardware antialiasing filters (2-pole, 300 Hz low-pass for each channel) and by digital filtering after data acquisition.

The next step in sophistication utilizes the joint time-frequency representation of fMCG. In this representation, the frequencies contained in the signal are themselves periodic in time. Infinitely periodic signals, such as the HVAC fan, are immediately identifiable as noise and can be separated by their narrow frequency representation. These non-physiological signals could be removed by notch filtering, however traditional FIR and IIR (types that obey causality) require compromises in phase response leading to ringing and signal distortion as a price for high rejection of narrow frequency. This can be a large problem for biomagnetic applications, where ringing distorts the signal of interest [Leeuwen et al., 2004], and the ringing problem increases with the wavelength selectivity of the filter.

A better approach to remove sinusoidal interference is direct subtraction. We use a LabView VI (Extract single tone information.vi) to estimate the amplitude and phase of the sinusoidal signal and then subtract it from the time domain signal. This technique works best for transform-limited signals, i.e. when the signal bandwidth is limited by the FFT bin-width, rather than its own phase noise. This method is easily implemented, does not introduce edge effects, and is effective at eliminating sinusoidal noise sources without any ringing or overshoot.

The limited time-frequency content of fMCG can be used to further advantage. From figure 7.2, it is clear that higher frequency components of the MCG signal all occur within a narrow time-window around the QRS peak. One way to use this information is through wavelet decomposition.

The basis of the technique can be described by an analog in data compression theory (indeed, noise reduction and data compression are parallel fields).

The key idea is as follows: the Fourier transform is just one way of representing a function in an infinite basis set, where the coefficients of that basis set are the amplitudes in the Fourier space representation. Because the basis functions are sines and cosines, infinitely periodic functions have a compact representation in this basis set, which is the same as saying a periodic function can be well approximated by a few Fourier terms with amplitudes much larger than the others. If we had reason to believe that our signal was composed of constant periodic functions, we could treat terms with low FFT coefficients as noise without losing much information.

As figure 7.1 makes clear, MCG signals are only somewhat compactly represented in the frequency domain. The amplitude of the Fourier terms drops off rather slowly from the fundamental amplitude. This indicates it could be advantageous to choose a different set of basis functions. Wavelet analysis uses limited time, limited frequency wavelets to express a function, and are a common choice for the decomposition and filtering of biomagnetic signals [Khobragade, 1999, Sternickel and Braginski, 2006].

7.2.2 Multiple-channel processing techniques

Methods in the previous section use function-space representations of the recording in which the signal and/or interference have limited and separable representations. Frequency-space representations can provide useful information on real-time or quasi-real-time frequency filters to use, but more advanced techniques require time-intensive and manually tuned signal processing, and currently must be completed offline. This represents a problem for real-time signal optimization, when the signal of interest is comparable to background interference sources.

The spatial signature of a signal can be made to have different characteristics than the interference, such as simply placing the detector as close as possible to the source and as far as possible from interference. Using multiple, spatially separated magnetometers allows spatial filters to be used, which can reject noise with different spatial frequencies than the signal. If the detectors are

close to the source, the spatial frequency will be relatively high, and therefore the noise spatial frequency must be low in order for spatial filtering to increase SNR.

There are two situations to consider. The first is where the interference is primarily common-mode to all magnetometers, as is the case for background magnetic field fluctuations from sources far away from the magnetometers compared to the array spacing. Uniform fields correspond to low spatial frequencies, and these are the signals best separated from fMCG.

Consider a noise source located far enough away that it can be represented as a dipole. Then its field is

$$\mathbf{B}(\mathbf{r}) \propto \frac{3\hat{\mathbf{r}}(\hat{\mathbf{r}} \cdot \mathbf{m}) - \mathbf{m}}{r^3}, \quad (7.3)$$

where \mathbf{r} is the vector from the center to the measurement point and \mathbf{m} is the dipole generating the field. Then we can write the fractional change in the field at two detectors separated by a distance \mathbf{d} as

$$\begin{aligned} \frac{\Delta B}{B} &= 1 - \frac{|\mathbf{B}(\mathbf{r}_0 + \mathbf{d}/2)|}{|\mathbf{B}(\mathbf{r}_0 - \mathbf{d}/2)|} \\ &\approx \frac{(r_0 - d/2)^3}{(r_0 + d/2)^3}, \end{aligned} \quad (7.4)$$

where r_0 is from the source to the center of the array and the approximation in the second line is $r_0 \gg d/2$. For a noise source outside of the MSR case, $r_0 \geq 2$ m away from the array center, and the array spacing 7 cm, the difference in signal between the two detectors is $\Delta B/B \leq 10\%$. This number is further reduced by the shielding factor of the MSR. Roughly the same analysis holds true for Johnson noise from the MSR shielding, as long as the magnetometer array is centered towards the middle of the room.

For the SNR of an MCG to be enhanced, it must have larger relative difference across the magnetometer spacing than the background. An example of a magnetic field map from the heart can be found in Steinhoff et al. [2004]. If the magnetometer array is centered well, two elements should measure oppositely directed fields from the other pair, in which case $\Delta B/B > 1$.

There is one other important source of magnetic interference in the fMCG application: the mother's signal. Figure 2 of [Steinhoff et al., 2004] displays the measured magnetic field map as a function of position in the plane above the Thorax. At 12 cm above the chest and 30 cm away from

the center of the Thorax towards the naval, the magnetic field gradient of the QRS peak appears to be approximately 0.4 pT/cm, so we would expect $\Delta B/B \approx 2/3$ from one magnetometer to another, disregarding changes in the projection of the field vector on the magnetometer detection direction over this region. Though this signal is obviously not strongly suppressed by detecting gradients in the fields, and though the field cannot be described as common mode, it does have a different spatial pattern than a fMCG if the magnetometers are placed in position above the fetal heart. Further signal processing will be required to suppress the maternal interference.

7.2.3 Advanced nonlinear noise reduction

More complicated nonlinear state-space methods have been developed for MCG applications, such as Sternickel et al. [2001], and used previously in atomic magnetometer biomagnetism experiments [Weis and Wynands, 2005]. This algorithm works by using two channels, one as a signal and one as a reference. We assume the signal channel contains the magnetic signal of interest, deterministic magnetic background, and stochastic noise, while the reference channel contains the deterministic magnetic background and uncorrelated stochastic noise. The nonlinear denoising algorithm uses a state-space analysis to compare the signal and reference channels and discard the correlated information to remove background magnetic noise. The filtered signal is then analyzed again using a state-space method to suppress stochastic noise compared to the periodic fluctuations of interest.

This technique still works best when narrow frequency components of the signal have been removed first. The effect of this technique upon fetal signal extraction for clinical application is still unclear, though it has been used for this application [Sternickel and Braginski, 2006]. An example of this analysis on an adult MCG in a configuration where the magnetometers are spaced far enough apart that only one is sensitive to MCG is shown in figure 7.3.

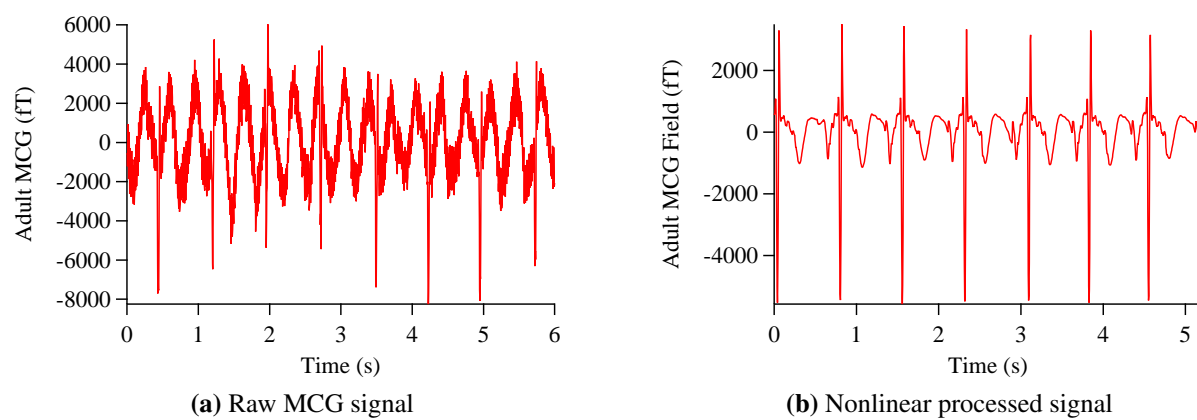


Figure 7.3: Raw adult MCG signal (a) and nonlinear processed signal (b) using another reference channel.

7.2.4 Comparison of SERF and SQUIDs for noise processing

Signal processing biomagnetic signals is an active area of research. The relatively brief overview here has only touched upon the most basic signal processing methods we have used. More advanced techniques can be found in the literature, and there is an open question how the signal processing techniques traditionally developed for ECG or SQUID gradiometer signals should be adapted to SERFs.

SERF magnetometers are capable of fantastic sensitivity. The fundamental noise limits of a vapor cell with similar size to those used here is $\sim 50 \text{ aT}/\sqrt{\text{Hz}}$ [Dang et al., 2010], far below the ambient magnetic noise level of a MSR. To take advantage of this extraordinary sensitivity in a relatively noisy MSR, multiple magnetometers must be used as gradiometers.

SQUIDs have been successful in developing hardware gradiometers for their detection circuits. In the typical configuration, SQUIDs are coupled to magnetic fields through superconducting pickup loops, which can be wrapped as two subtracting loops to make a hardware gradiometer with high precision [Vrba and Robinson, 2001]. The equivalent task is more difficult for SERF magnetometers. The easiest way to make gradiometers from a SERF magnetometer is to use a single cell and detect the difference signal from spatially separate parts of the cell [Johnson et al., 2010, Xia et al., 2006]. The advantage of this method is using one cell ensures the best uniformity in the parameters of (2.24). For best SNR improvement, however, the cell would have to allow a baseline separation of $\sim 5 \text{ cm}$ or more if the signal from the source of interest is not to be suppressed as well. This would require large vapor cells, which are problematic to heat, insulate, and pump effectively.

In this work, we have pursued the goal of using multiple modular magnetometers to perform the measurement. The obstacles to performing a gradiometric measurement are essentially non-common mode noise in the magnetometer signal, either from real magnetic fields which are not correlated from one magnetometer to another, or variations in the non-magnetic terms of (2.38) or the spatial sensitivity profile of the atomic vapor, as in figure 5.5 and figure 6.2.

Uncorrelated magnetic noise can come from imperfectly correlated sources, mostly far away (see previous section) or magnetic fields generated by our apparatus. One source of the latter is

noise in the circuitry of the nulling coils. This applies a (mostly) white noise field to each magnetometer, independent of the others, which looks like a high spatial frequency signal to multichannel processing methods. Another source is from the electrically operated heaters or any residual magnetization in the fiber components. Chapter 5 has more details about these sources.

Uncorrelated non-magnetic noise is especially problematic in the low frequency range from 0–10 Hz, still of interest in the MCG signal in figure 7.1. This noise is mainly the result of probe beam fluctuations, and can be mitigated by modulating the signal and using lock-in detection techniques [Li et al., 2006, Shah and Romalis, 2009a], as well as decreasing the overall probe intensity (see figure 4.4). Another difficulty is that each magnetometer is sensitive to slightly different vector combinations of the ambient magnetic fields (see section 2.2.6), preventing straight-forward subtraction of signals from one another, even after calibration.

Finally, our ability to accurately characterize the magnetometer limits our ability to make a broadband gradiometer. The main problem is uncertainty in the frequency response of the magnetometer, seen in figure 4.1. The suppression of gradients is limited by the accuracy of this characterization. Further, displaying a calibrated magnetic field time series is difficult to do in real time. Feedback helps these issues.

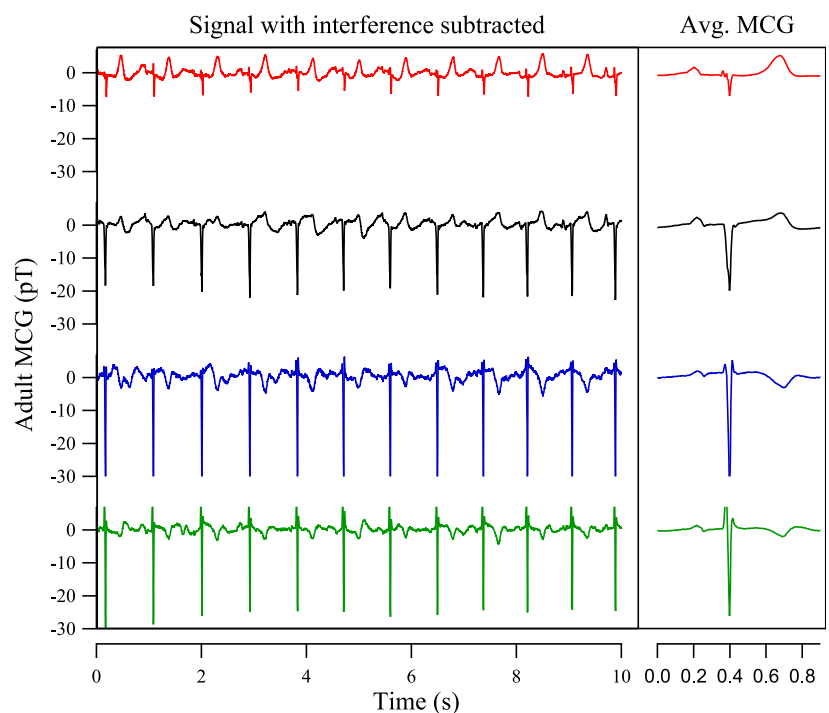
7.3 MCG

To test the performance of our magnetometer and signal processing techniques, we used the four channel array in the MSR to measure adult MCG. The procedure for obtaining these measurements is described in section 4.5. We performed these measurements on 17 healthy adult with informed consent. Adult MCG was easy to see even on top of the omnipresent fan noise.

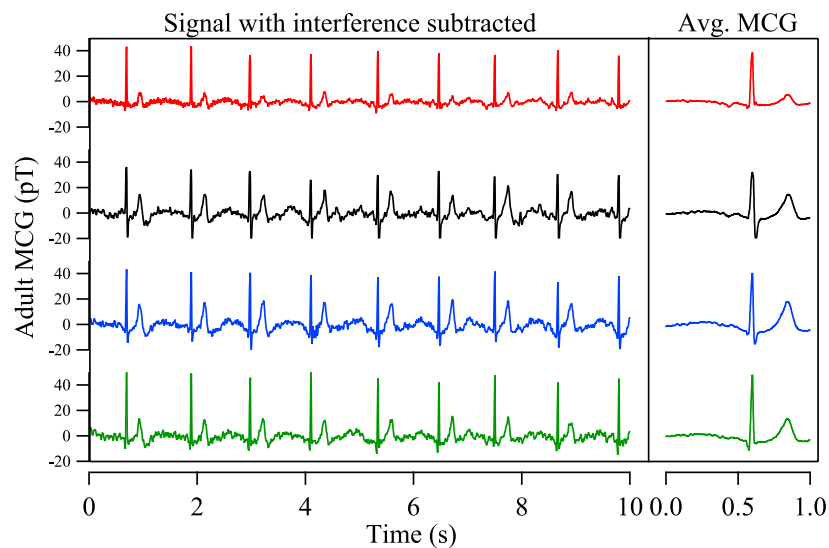
Data representative of the obtained signal quality is shown in figure 7.4, where simultaneous measurements from all four channels operating in DC mode are shown. The data has been filtered to 128 Hz by a high tap-number FIR filter and detrended by a wavelet detrending technique. Also, any sinusoidal interference identifiable in the noise spectrum was removed through the subtraction method described in this chapter. The right-hand side of figure 7.4 shows average of about 30 beats. The data in figure 7.4(a),(b) are from different subjects. In (a), the array was positioned

over the subject's chest where we estimated the signal should be maximized. In (b), the real time MCG signal was used to guide the positioning of the array, which was adjusted until the signal from all four channels was roughly equal. The P, QRS, and T components are well resolved. We emphasize these are magnetometer signals (rather than gradiometer signals), and contain any unfiltered background magnetic noise in the MSR as well as the MCG signal.

The data taken in figure 7.4(b) has an instructive noise spectrum from a signal processing standpoint. Figure 7.5(a) shows the noise spectrum of a reference measurement taken immediately after the measurement in figure 7.4(b), but without a subject in the MSR. The large, equally spaced, and narrow set of frequency components was later identified as arising from the electronics for a permanently installed SQUID system (Tristan Technologies Inc) in the MSR. Since it is composed of narrowly peaked frequency components, we deal with it as described earlier in this chapter. Sinusoidal functions were matched to each frequency component and subtracted from the time series. The results after this process and the usual detrending are shown for both the MCG signal and reference, in figure 7.5(b).



(a) MCG, uncentered array



(b) MCG, centered array

Figure 7.4: MCG acquired from different subjects, representative of the signal quality obtained in all runs. The lefthand side of each figure shows the signal obtained after subtraction of sinusoidal interference and the application of a detrending algorithm. The righthand side shows about 30 averaged beats. In (a), the magnetometers were positioned above the chest by sight. In (b), the real-time signal was used to guide the positioning of the magnetometers to maximize the signal in all channels.

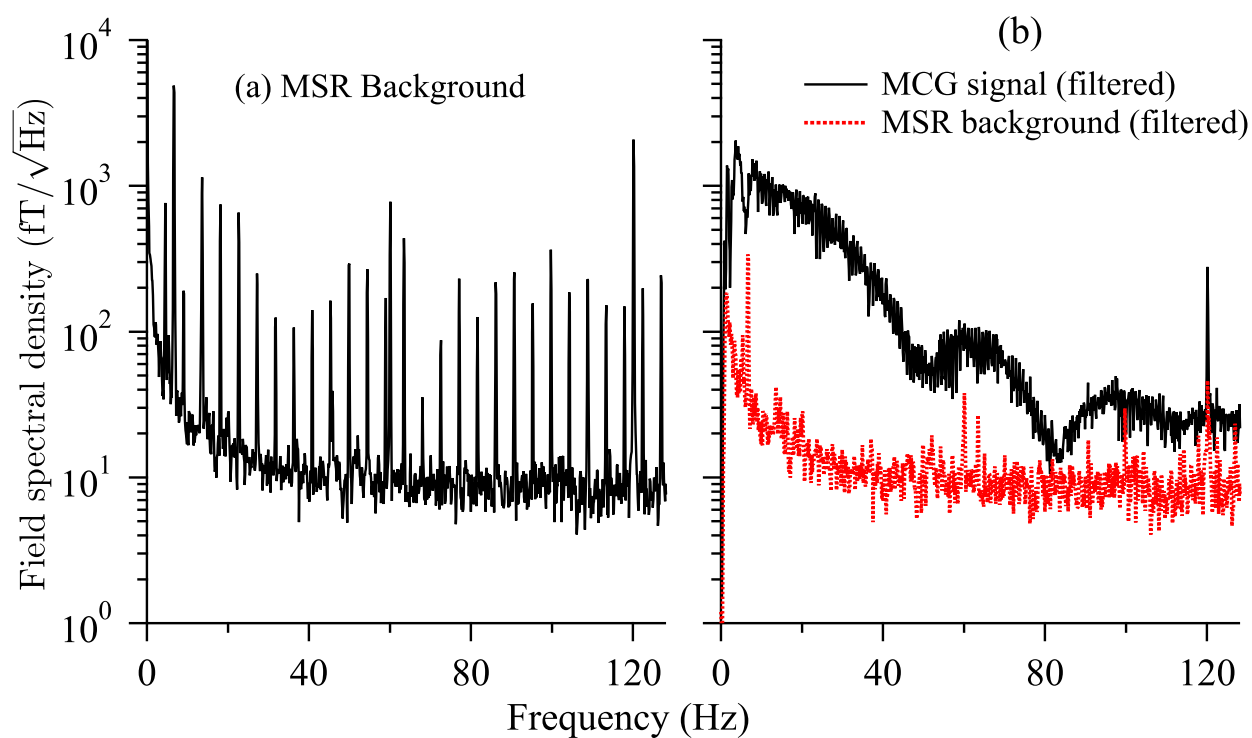


Figure 7.5: (a) Reference noise spectrum taken immediately after the data presented in figure 7.4(b). The equally spaced peaks are from electronics for one of the SQUID systems permanently installed in the MSR. This noise was present during the MCG measurement. (b) power spectral density of the filtered MCG measurement (black) and the filtered reference measurement (red dots). Each frequency component was removed by finding and removing a sinusoidal signal from the time series. The noise was effectively suppressed.

7.4 Phantom measurements

To test the magnetometer measurement capabilities for signals of similar size, bandwidth, and spatial structure to fMCG, we also simulated fMCG using a head phantom (Biomagnetic Technologies), which is a spherical shell filled with saline solution and five different current dipoles that can be driven individually. The head was placed as close as possible to the array center and aligned so that the detected signal from driving a dipole was maximized. We drove the phantom with a test waveform [Goldberger et al., 2000] shown in figure 7.6(b). The amplitude was varied by changing the voltage scaling of the signal applied to the phantom head driver, and the calibrated magnetometers were used to adjust the magnetic field at the detectors to the desired level.

Figure 7.6(a) shows 28-beat averages for all four magnetometer channels, after processing the signals in the same way as the MCGs of the previous section. The detected QRS amplitude is about 2 pT, and the averages for each channel have the correct general shape and representation.

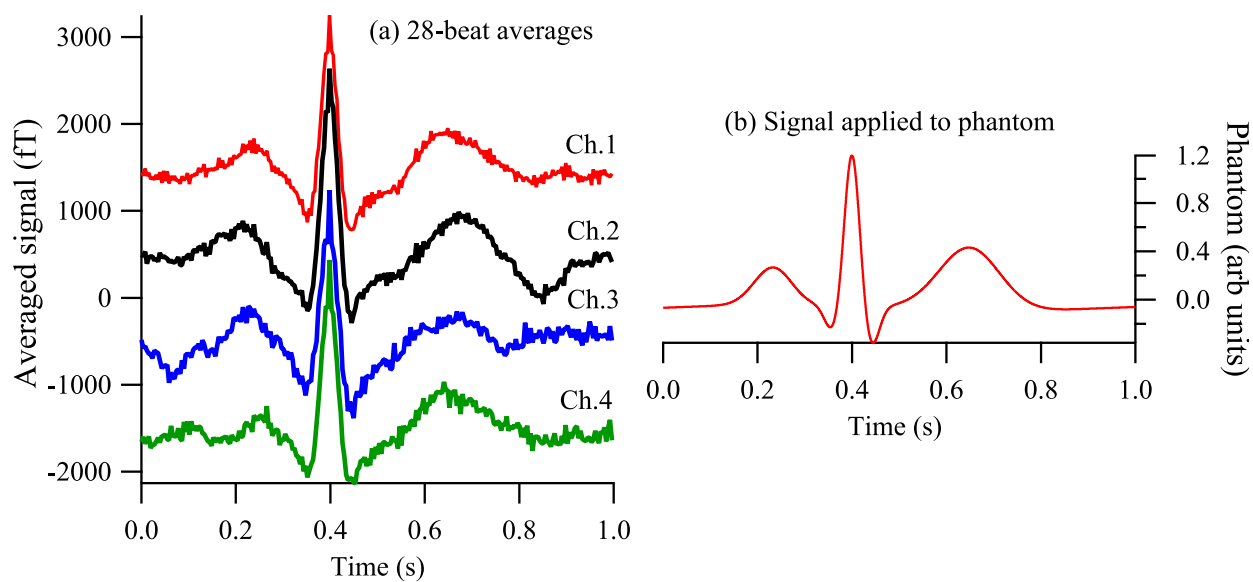


Figure 7.6: (a) 28-beat average response from the phantom driven with the waveform shown in (b), with magnetic field offsets applied to aid visualization. Before averaging, the signals are processed in the same way as the MCG above, by removing only narrow frequency components.

7.5 Fetal MCG

The goal of this work was to make a device capable of fMCG detection and to investigate the suitability of such a device to replace SQUIDS for some biomagnetism applications. We have now tested one healthy fMCG subject, at 31 weeks gestation. For most of the measurements here, the ambient noise sources are minimal. The HVAC fan was shut down and unnecessary SQUID electronics were turned off during our portion of the measurement.

Figure 7.7 shows the raw data as it looks before calibration and more sophisticated signal processing. Figure 7.7(a) shows the large common mode baseline drift that often occurs. The drift amplitude in this figure is actually relatively small. It is mostly unimportant until it saturates the I-V converter for a channel, and then it is catastrophic. For comparison, the I-V maximum output is ± 6 V. The large peaks in every channel are the mother's MCG signal. The right hand side of Figure 7.7(a) displays a blowup portion of channel 2, which seemed to have the largest amplitude fMCG signal. The fMCG QRS-complex is easily seen (highlighted in red) without any signal processing (except for the 300 Hz anti-aliasing filter applied by the I-V converters). The first fMCG QRS-complex in this selection is visible, but is mostly hidden by the mother's MCG, a common challenge for fMCG and illustrative of the need for multichannel techniques, where these features can be isolated by spatial filtering.

Figure 7.7(b) shows the response from the raw signal in (a) bandpass filtered from 3-30 Hz using two single pole filters. These filters are available on demand from the I-V converters. The 3 Hz high-pass is sufficient to remove the large baseline drift, and the left-hand side of (b) emphasizes the largely uniform MCG signal from the mother. A blowup of these signals (right-hand side of (b)), with an offset applied to separate them, shows the portion of the signal that contains the fMCG QRS complex, picked out most easily from channel-2 but present in all channels. This is an important feature if the array position is to be optimized to get the largest signal.

Figure 7.8 shows the same set of signals after calibration, detrending, and removal of of sharply peaked frequency components. Additionally, the signal was down sampled to 200 Hz. A time-segment with different offsets applied for channels 1-2 and channels 3-4 highlights the close QRS

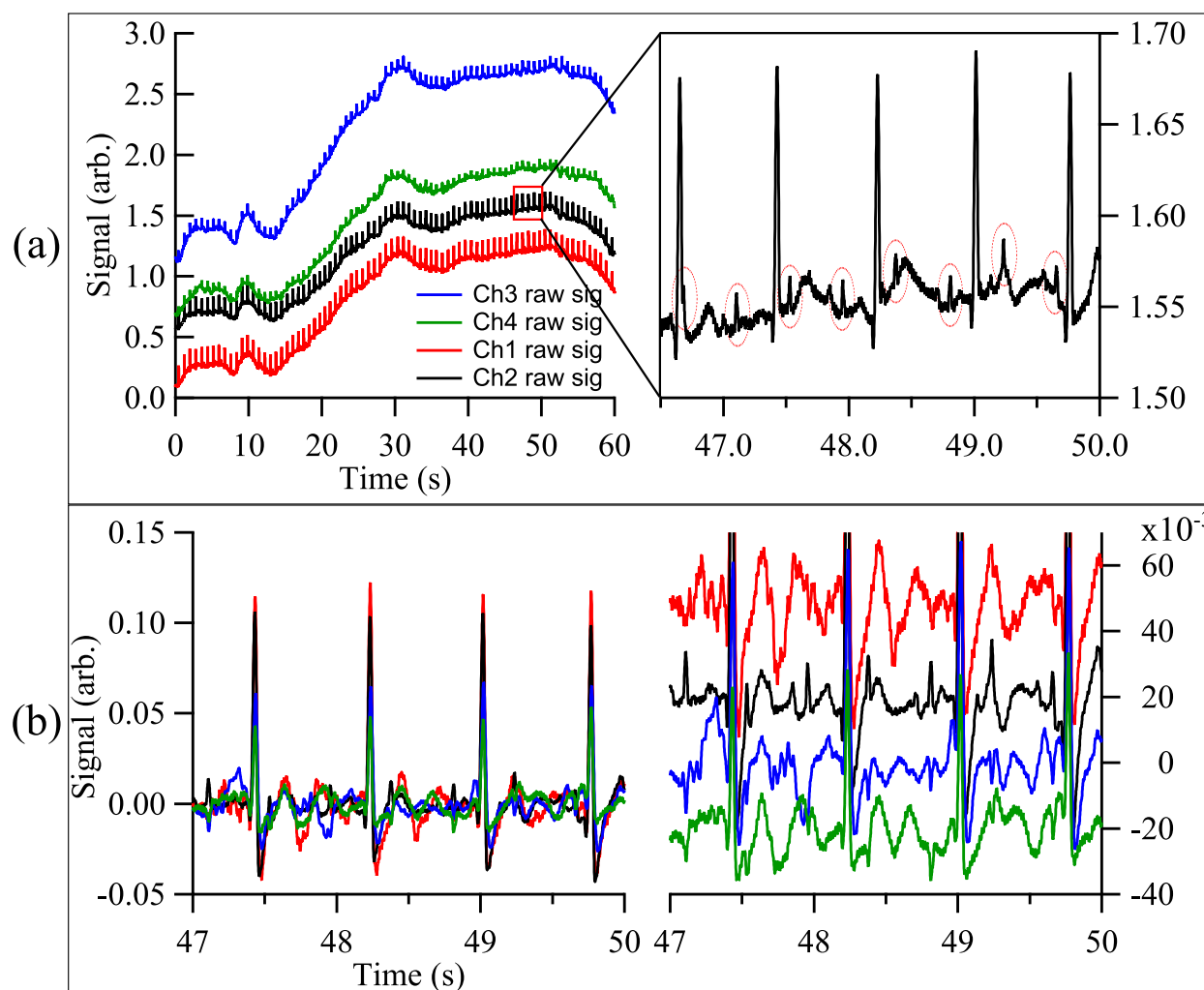


Figure 7.7: (a) Raw, uncalibrated fMCG signals. The inset on the right hand side shows the fMCG is clearly identifiable in the raw signal without any signal processing. Fetal MCG beats are highlighted with red ellipses. (b) Bandpass filtered signals from (a), at 3-30 Hz, chosen to enhance the QRS SNR for real time visualization and optimization. The right hand side shows the signals on a smaller scale with offsets applied. The signal is visible in each channel.

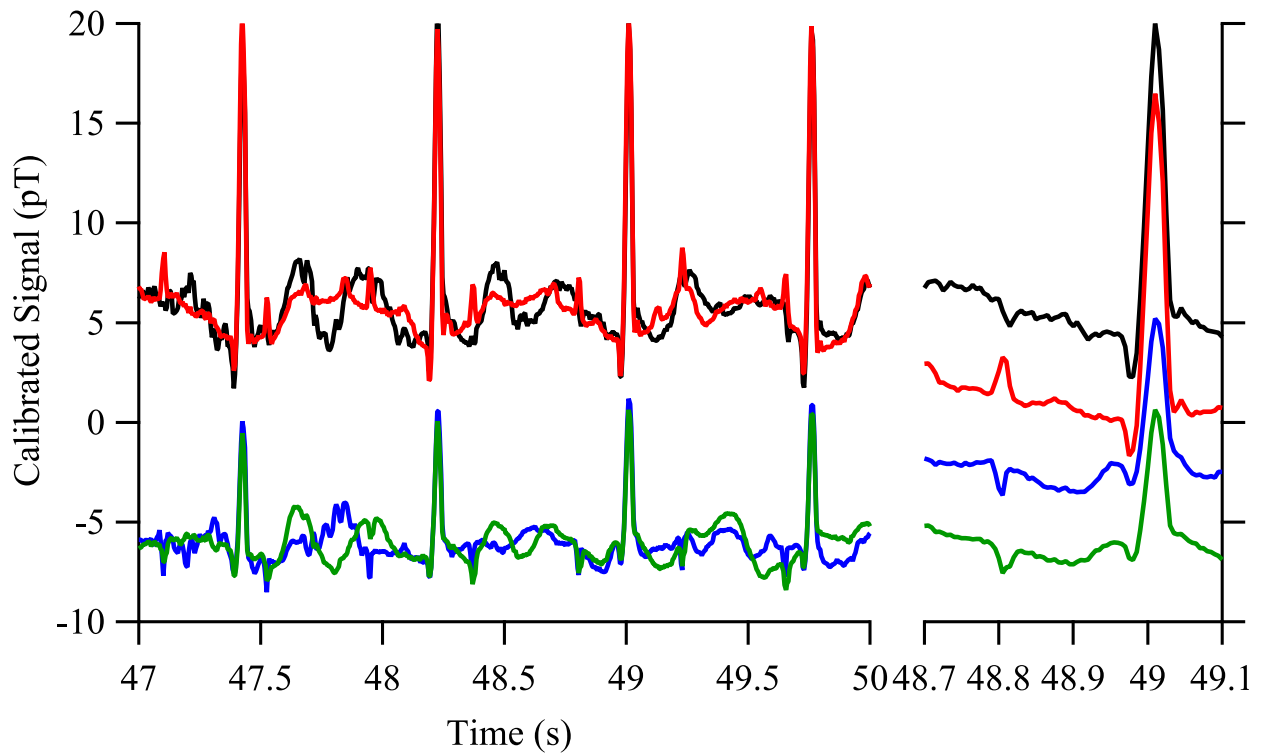


Figure 7.8: The calibrated signal filtered to remove 40 Hz and 60 Hz harmonics, low-passed 200 Hz using a FIR filter, and detrended to remove low-frequency noise. The mother's QRS in Channels 1-2 are well matched, and 3-4 are well matched, the amplitude is not uniform between the two sets. A short a short time segment of this data is shown, where differences in the fMCG QRS complex phase are visible.

peak agreement among those subsets. On the right of figure 7.8 is an even shorter segment from the same dataset, where the phase difference between the fCMG QRS components is apparent. To reiterate, these images show the mother's QRS is the same, only amplitude scaled, while the fetal QRS has an entirely different profile for the different channels.

To remove the mother's signal, we use principal component analysis (PCA), in which the cross-correlation matrix of the signals is calculated and diagonalized to produce the principal components. The first principal component corresponds to the part of all four signals that is most strongly correlated, and simple inspection of figure 7.8 indicates that should be the mother's signal and any remaining common mode background, as well as a small amount of fetal signal. Deleting this component and then reconstructing the signal without it offers a crude way of eliminating common mode signal through correlation, rather than direct subtraction. The results of this procedure performed on the data in figure 7.8 are shown in figure 7.9. The mother's signal has been almost entirely suppressed, and the fetal signal is easily visible.

Appendix F contains a report generated by Ron Wakai's group from the set of measurements obtained with this first subject. The report computes clinically relevant fMCG parameters, such as the QT, PR, and RR intervals, as well as the P and QRS duration. Two different segments of a single data set were analyzed, and the final page contains the same measurements made by a commercial SQUID system that is normally used for such measurements. The SERF array measurements agree reasonably well with the SQUID data, and would obviously benefit from the introduction of 4-more channels by using z-mode. The next step for the biomagnetism portion of this experiment are to use z-mode to measure 8-channel data, and to replicate these exciting results with more subjects.

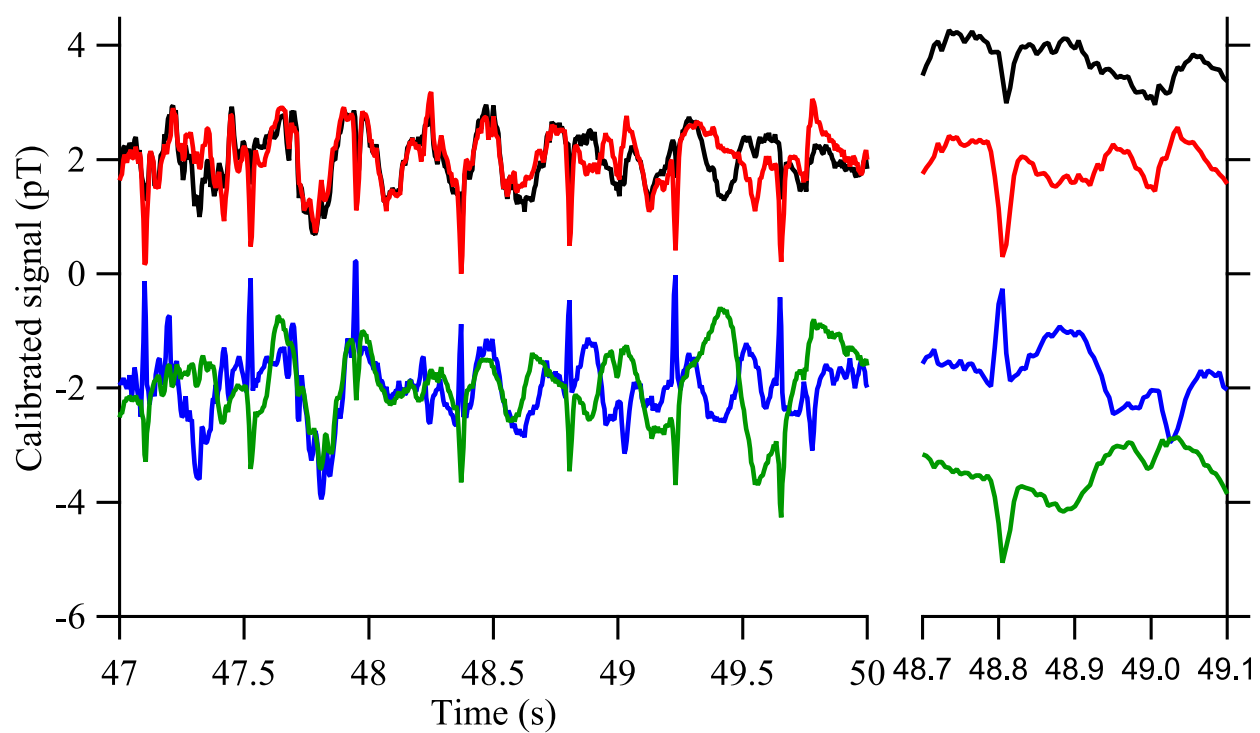


Figure 7.9: Data with the first principal component removed, as discussed in text. The mother's signal has been suppressed, and the fMCG QRS complex is the largest remaining feature.

Chapter 8

Conclusions and future work

In this thesis, we have presented the design and implementation of a four channel magnetometer array. We offered a complete description of the array, its noise sources, and its theory and method of operation. Additionally, we discussed different operating modes designed to overcome shortcomings for SERF, including using feedback to make a gradiometer, utilizing parametric modulation modes to increase the channel count or operate in high DC bias fields, or take advantage of diffusion to make magnetometer measurements in a part of the cell without pump light. Finally, we proved for the first time that an atomic magnetometer array can be used to detect fMCG, a demanding biomagnetic application.

There are two general directions for future work. First, fMCG measurements must be replicated and improved. The gestation age of the fMCG in this work was relatively late, 31-weeks. Judging by the signal quality in this work and the way fMCG signals develop [Golbach et al., 2000], earlier detection should be possible. Additionally, an effort should be made to better match the feedback field to all magnetometers. Finally, z-mode operation needs to be attempted to increase the channel count and see if signal processing algorithms correspondingly benefit.

Longer term, there are several improvements that can be made. The current magnetometer design philosophy pays a space premium in exchange for optical flexibility. In the future, magnetometer size can be reduced further by sacrificing this flexibility in place of permanent optical setups, which would allow increasing the channel count.

A new setup might use diffusion mode pumping and small grin-lens terminated fibers. The optical components could be glued directly to the lenses and attached to the cell or to a thermally insulating spacer. To significantly shrink the magnetometer, a beam cube (rather than a Wollaston) should be investigated, with the detection photodiodes glued directly to the cube faces.

Another improvement is background suppression of the ambient magnetic fields in the MSR. The feedback technique discussed here works well as long as the magnetic fields do not change significantly in the directions orthogonal to the feedback direction. When they do, the DC fields can acquire significant offsets that require re-nulling. During especially noise periods, this can happen often enough that measurement becomes difficult, as the signals become saturated during recording. The only solution to this problem is feedback stabilization of the background fields in all directions. This could be done with a set of semi-permanent coils wrapped around the walls of the MSR and a single reference magnetometer in the middle, operating in the feedback method described in Seltzer and Romalis [2004], whose stabilization levels were more than sufficient for work in our MSR.

Finally, there might be significant benefit using hybrid magnetometer cells, with a dual alkali optical pumping technique. For example, Rubidium could be optically pumped and used to pump Potassium intermixed in the cell via spin-exchange. Several benefits come from the Potassium not interacting with the pump laser, such as reduced light shift and laser absorption at the cell walls.

The comparison fMCG measurement of our SERF magnetometer to the commercial SQUID measurement of an fMCG signal shows both that SERF magnetometers have a long way to go, but also that they have come a long way. We must remember the technology will only be ten years old this year. Considering the results presented in this work, the SERF magnetometer promises continued improvement in biomagnetic applications as more technical advances are made. If successful,

they will provide a cheaper and less maintenance intensive alternative to SQUIDs, and may enable much smaller cylindrical shields rather than expensive magnetically shielded rooms.

Bibliography

- C. Alcock, V. Itkin, and M. Horrigan. Vapor pressure equations for the metallic elements: 298–2500 K. *Canadian Metallurgical Quarterly*, 23(309), 1984.
- E. B. Aleksandrov, M. V. Balabas, and A. E. Ivanov. Laser pumping in the scheme of an Mx-magnetometer. *Optics and Spectroscopy*, 78(2):292–298, 1995.
- E. Alexandrov and V. Bonch-Bruevich. Optically pumped atomic magnetometers after three decades. *Optical Engineering*, 31(4):711–717, 1992. URL <http://adsabs.harvard.edu/abs/1992OptEn..31..711A>.
- J. C. Allred, R. N. Lyman, T. W. Kornack, and M. V. Romalis. High-sensitivity atomic magnetometer unaffected by spin-exchange relaxation. *Physical review letters*, 89(13):130801, 2002.
- L. Anderson, F. Pipkin, and J. Baird Jr. Hyperfine structure of hydrogen, deuterium, and tritium. *Physical Review*, 120(4):1279, 1960.
- S. Appelt, A. B. A. Baranga, A. Young, and W. Happer. Light narrowing of rubidium magnetic-resonance lines in high-pressure optical-pumping cells. *Physical Review A*, 59(3):2078–2084, Mar. 1999. ISSN 1050-2947. doi: 10.1103/PhysRevA.59.2078.
- A. B.-a. Baranga, S. Appelt, M. V. Romalis, C. J. Erickson, A. R. Young, G. D. Cates, and W. Happer. Polarization of ^3He by Spin Exchange with Optically Pumped Rb and K Vapors. *Physical Review Letters*, 80(13):2801–2804, 1998.
- W. E. Bell and A. L. Bloom. Optical Detection of Magnetic Resonance in Alkali Metal Vapor. *Physical Review*, 107(6):1559–1565, July 1957. ISSN 0003-6935. URL <http://www.ncbi.nlm.nih.gov/pubmed/20119180>.
- G. Bison, N. Castagna, A. Hofer, P. Knowles, J. L. Schenker, M. Kasprzak, H. Saudan, and A. Weis. A room temperature 19-channel magnetic field mapping device for cardiac signals. *Applied Physics Letters*, 95(17):173701–173703, June 2009. ISSN 00036951. doi: 10.1063/1.3255041.

- A. L. Bloom. Principles of Operation of the Rubidium Vapor Magnetometer. *Applied Optics*, 1 (1):61, Jan. 1962. ISSN 0003-6935. doi: 10.1364/AO.1.000061.
- K. Bonin and V. Kresin. *Electric-dipole polarizabilities of atoms, molecules, and clusters*. World Scientific Pub Co Inc, 1997. ISBN 9810224931.
- J. Bork, H. Hahlbohm, R. Klein, and A. Schnabel. The 8-layered magnetically shielded room of the PTB: Design and construction. In *Biomag*, pages 970–973, 2000.
- M. Bouchiat and J. Brossel. Relaxation of optically pumped Rb atoms on paraffin-coated walls. *Physical Review*, 147(1):41, 1966. URL http://prola.aps.org/abstract/PR/v147/i1/p41_1.
- D. Budker and M. V. Romalis. Optical magnetometry. *Nature Physics*, 3(4):227–234, Apr. 2007. ISSN 1745-2473. doi: 10.1038/nphys566.
- D. Budker, V. Yashchuk, and M. Zolotarev. Nonlinear Magneto-optic Effects with Ultranarrow Widths. *Physical Review Letters*, 81(26), 1998.
- D. Budker, D. F. Kimball, S. M. Rochester, V. V. Yashchuk, and M. Zolotarev. Sensitive magnetometry based on nonlinear magneto-optical rotation. *Physical Review A*, 62(4):43403, 2000.
- W. Chen, T. Gentile, T. Walker, and E. Babcock. Spin-exchange optical pumping of ^3He with Rb-K mixtures and pure K. *Physical Review A*, 75(1):1–14, Jan. 2007. ISSN 1050-2947. doi: 10.1103/PhysRevA.75.013416. URL <http://link.aps.org/doi/10.1103/PhysRevA.75.013416>.
- D. Cohen, E. A. Edelsack, and J. Zimmerman. Magnetocardiograms taken inside a shielded room with a superconducting point-contact magnetometer. *Applied Physics Letters*, 16(7):278, 1970. ISSN 00036951. doi: 10.1063/1.1653195.
- C. Cohen-Tannoudji, J. DuPont-Roc, S. Haroche, and F. Laloe. Detection of the Static Magnetic Field Produced by the Oriented Nuclei of Optically Pumped ^3He Gas. *Physical Review Letters*, 22(15):758–760, 1969. URL <http://link.aps.org/doi/10.1103/PhysRevLett.22.758>.
- B. F. Cuneo, M. Ovadia, J. F. Strasburger, H. Zhao, T. Petropulos, J. Schneider, and R. T. Wakai. Prenatal diagnosis and in utero treatment of torsades de pointes associated with congenital long QT syndrome. *The American journal of cardiology*, 91(11):1395–8, June 2003. ISSN 0002-9149. doi: 10.1016/S0002-9149(03)00343-6.
- H. B. Dang, A. C. Maloof, and M. V. Romalis. Ultrahigh sensitivity magnetic field and magnetization measurements with an atomic magnetometer. *Applied Physics Letters*, 97(15):151110, 2010. ISSN 00036951. doi: 10.1063/1.3491215.

- H. Dehmelt. Modulation of a light beam by precessing absorbing atoms. *Physical Review*, 105(6): 1924, 1957. URL http://prola.aps.org/abstract/PR/v105/i6/p1924_1.
- C. J. Erickson, D. Levron, W. Happer, S. Kadlecik, B. Chann, L. W. Anderson, and T. G. Walker. Spin relaxation resonances due to the spin-axis interaction in dense rubidium and cesium vapor. *Physical review letters*, 85(20):4237–40, Nov. 2000. ISSN 0031-9007. URL <http://www.ncbi.nlm.nih.gov/pubmed/11060607>.
- M. Fleischhauer, A. Matsko, and M. Scully. Quantum limit of optical magnetometry in the presence of ac Stark shifts. *Physical Review A*, 62(1):013808, 2000. URL <http://pra.aps.org/abstract/PRA/v62/i1/e013808>.
- R. K. Ghosh. *Spin exchange optical pumping of neon and its applications*. Dissertation, Princeton, 2009.
- H. M. Gibbs and R. J. Hull. Spin-Exchange Cross Sections for Rb^{87} - Rb^{87} and Rb^{87} - Cs^{133} Collisions. *Physical Review*, 153(1):132—151, 1967. URL http://prola.aps.org/abstract/PR/v153/i1/p132_1.
- E. Golbach, J. Stinstra, P. Grot, and M. Peters. Reference values for fetal MCG/ECG recordings in uncomplicated pregnancies. In *Proc. 12th International Conference on Biomagnetism*, pages 595–98. Citeseer, 2000. URL <http://citeseerx.ist.psu.edu/viewdoc/download?doi=10.1.1.2.9979&rep=rep1&type=>
- A. Goldberger, L. Amaral, L. Glass, J. Hausdorff, P. Ivanov, R. Mark, J. Mietus, G. Moody, C. Peng, and H. Stanley. PhysioBank, PhysioToolkit, and PhysioNet: Components of a new research resource for complex physiologic signals. *Circulation*, 101(23):e215, 2000.
- W. C. Griffith, S. Knappe, and J. Kitching. Femtotesla atomic magnetometry in a microfabricated vapor cell. *Optics Express*, 18(26), 2010.
- S. Groeger, G. Bison, J. L. Schenker, R. Wynands, and A. Weis. A high-sensitivity laser-pumped Mx magnetometer. *The European Physical Journal D-Atomic, Molecular, Optical and Plasma Physics*, 38(2):239–247, 2006.
- M. Hämmäläinen, R. Hari, R. J. Ilmoniemi, J. Knuutila, and O. V. Lounasmaa. Magnetoencephalography theory, instrumentation, and applications to noninvasive studies of the working human brain. *Reviews of Modern Physics*, 65(2):413–497, Apr. 1993. ISSN 0034-6861. doi: 10.1103/RevModPhys.65.413.
- W. Happer. Optical Pumping. *Reviews of Modern Physics*, 44(2):169–249, 1972.
- W. Happer and B. Mathur. Effective operator formalism in optical pumping. *Physical Review*, 163(1):12, 1967. URL http://prola.aps.org/abstract/PR/v163/i1/p12_1.

- W. Happer and A. C. Tam. Effect of rapid spin exchange on the magnetic-resonance spectrum of alkali vapors. *Physical Review A*, 16(5):1877—1891, 1977. URL http://pra.aps.org/abstract/PRA/v16/i5/p1877_1.
- W. Happer and H. Tang. Spin-exchange shift and narrowing of magnetic resonance lines in optically pumped alkali vapors. *Physical Review Letters*, 31(5):273–276, 1973. ISSN 1079-7114.
- W. Happer and W. a. Wijngaarden. An optical pumping primer. *Hyperfine Interactions*, 38(1-4): 435–470, Dec. 1987. ISSN 0304-3843. doi: 10.1007/BF02394855.
- W. Happer, Y.-Y. Jau, and T. Walker. *Optically Pumped Atoms*. Wiley-VCH Verlag GmbH & Co. KGaA, Weinheim, Germany, 1st edition, Feb. 2010. ISBN 9783527629503. doi: 10.1002/9783527629503. URL <http://doi.wiley.com/10.1002/9783527629503>.
- P. Hobbs. *Building electro-optic systems*. Wiley-Interscience, Hoboken, NJ, 1st edition, 2000. ISBN 978-0471246817.
- P. Horowitz and W. Hill. *The Art of Electronics*. Cambridge University Press, New York, NY, 2nd edition, 1989. ISBN 0521370957.
- C. N. Johnson, P. Schwindt, and M. Weisend. Magnetoencephalography with a two-color pump-probe, fiber-coupled atomic magnetometer. *Applied Physics Letters*, 97(24):243703, 2010. ISSN 00036951. doi: 10.1063/1.3522648.
- S. Kadlecik, T. Walker, D. Walter, C. Erickson, and W. Happer. Spin-axis relaxation in spin-exchange collisions of alkali-metal atoms. *Physical Review A*, 63(5): 1–5, Apr. 2001. ISSN 1050-2947. doi: 10.1103/PhysRevA.63.052717. URL <http://link.aps.org/doi/10.1103/PhysRevA.63.052717>.
- K. Khobragade. ECG analysis using wavelet transforms. *Computer Standards & Interfaces*, 20 (6-7):466, Mar. 1999. ISSN 09205489. doi: 10.1016/S0920-5489(99)91016-4.
- J. Kirschvink. Uniform magnetic fields and double-wrapped coil systems: Improved techniques for the design of bioelectromagnetic experiments. *Bioelectromagnetics*, 13(5):401–411, 1992. ISSN 1521-186X.
- J. Kitching, S. Knappe, and E. Donley. Atomic Sensors—A Review. *Sensors Journal, IEEE*, 11(9):1749–1758, 2011. URL http://ieeexplore.ieee.org/xpls/abs_all.jsp?arnumber=5778937.
- S. Knappe, T. H. Sander, O. Kosch, F. Wiekhorst, J. Kitching, and L. Trahms. Cross-validation of microfabricated atomic magnetometers with superconducting quantum interference devices for biomagnetic applications. *Applied Physics Letters*, 97(13):133703, 2010. ISSN 00036951. doi: 10.1063/1.3491548.

- I. K. Kominis, T. W. Kornack, J. C. Allred, and M. V. Romalis. A subfemtotesla multichannel atomic magnetometer. *Nature*, 422(6932):596–9, May 2003. ISSN 0028-0836. doi: 10.1038/nature01484.
- T. W. Kornack. *A Test of CPT and Lorentz Symmetry Using a K-3 He Co-magnetometer*. Dissertation, Princeton, 2005.
- B. Lancor and T. Walker. Effects of nitrogen quenching gas on spin-exchange optical pumping of ^3He . *Physical Review A*, 82(4):1–7, Oct. 2010. ISSN 1050-2947. doi: 10.1103/PhysRevA.82.043417. URL <http://link.aps.org/doi/10.1103/PhysRevA.82.043417>.
- B. Lancor, E. Babcock, R. Wyllie, and T. Walker. Circular dichroism of RbHe and RbN_2 molecules. *Physical Review A*, 82(4):1–11, Oct. 2010. ISSN 1050-2947. doi: 10.1103/PhysRevA.82.043435.
- M. P. Ledbetter, I. M. Savukov, V. M. Acosta, D. Budker, and M. V. Romalis. Spin-exchange relaxation free magnetometry with Cs vapor. *Physical Review A*, 77(33408):33408, Aug. 2008. doi: 10.1103/PhysRevA.77.033408.
- S.-K. Lee and M. V. Romalis. Calculation of magnetic field noise from high-permeability magnetic shields and conducting objects with simple geometry. *Journal of Applied Physics*, 103(8):084904, 2008. ISSN 00218979. doi: 10.1063/1.2885711. URL <http://link.aip.org/link/JAPIAU/v103/i8/p084904/s1&Agg=doi>.
- P. V. Leeuwen, S. Lange, A. Klein, D. Geue, Y. Zhang, H. Krause, and D. Grönemeyer. Reproducibility and reliability of fetal cardiac time intervals using magnetocardiography. *Physiological Measurement*, 25(2):539–552, Apr. 2004. ISSN 0967-3334. doi: 10.1088/0967-3334/25/2/011.
- Z. Li. *Development of a Parametrically Modulated SERF Magnetometer*. Dissertation, University of Wisconsin-Madison, 2006.
- Z. Li, R. T. Wakai, D. N. Paulson, and B. Schwartz. HTS magnetometers for fetal magnetocardiography. *Neurology & clinical neurophysiology : NCN*, 2004:25, Jan. 2004. ISSN 1526-8748.
- Z. Li, R. T. Wakai, and T. Walker. Parametric modulation of an atomic magnetometer. *Applied Physics Letters*, 89:134105, 2006.
- P. McSharry, G. Clifford, L. Tarassenko, and L. Smith. A Dynamical Model for Generating Synthetic Electrocardiogram Signals. *Biomedical Engineering, IEEE Transactions on*, 50(3):289–294, 2003. URL http://ieeexplore.ieee.org/xpls/abs_all.jsp?arnumber=1186732.
- R. Merritt, C. Purcell, and G. Stroink. Uniform magnetic field produced by three, four, and five square coils. *Review of Scientific Instruments*, 54(7):879–882, 1983. ISSN 0034-6748.

- M. A. Moore, J. H. and Davies, C. C. and Coplan. *Building scientific apparatus: a practical guide to design and construction*. Westview Press, London, 3rd edition, 2003. ISBN 978-0813340067.
- I. Novikova, A. Matsko, V. Velichansky, M. Scully, and G. Welch. Compensation of ac Stark shifts in optical magnetometry. *Physical Review A*, 63(6):6–9, May 2001. ISSN 1050-2947. doi: 10.1103/PhysRevA.63.063802.
- D. Platzek, H. Nowak, F. Giessler, J. Rother, and M. Eiselt. Active shielding to reduce low frequency disturbances in direct current near biomagnetic measurements. *Review of Scientific Instruments*, 70(5):2465, 1999. ISSN 00346748. doi: 10.1063/1.1149779.
- W. H. Press, S. A. Teukolsky, W. T. Vetterling, and B. P. Flannery. *Numerical recipes: the art of scientific computing*. Cambridge University Press, New York, NY, 3rd edition, 2007. ISBN 978-0-521-88068-8.
- D. Rassi and M. J. Lewis. Power spectral analysis of the foetal magnetocardiogram. *Physiological measurement*, 16(2):111–20, May 1995. ISSN 0967-3334. URL <http://www.ncbi.nlm.nih.gov/pubmed/7663366>.
- D. Robbes. Highly sensitive magnetometers—a review. *Sensors and Actuators A: Physical*, 129(1-2):86–93, May 2006. ISSN 09244247. doi: 10.1016/j.sna.2005.11.023.
- M. Romalis, E. Miron, and G. Cates. Pressure broadening of Rb $D_{\{1\}}$ and $D_{\{2\}}$ lines by ^3He , ^4He , $\text{N}_{\{2\}}$, and Xe: Line cores and near wings. *Physical Review A*, 56(6):4569–4578, Dec. 1997. ISSN 1050-2947. doi: 10.1103/PhysRevA.56.4569. URL <http://link.aps.org/doi/10.1103/PhysRevA.56.4569>.
- I. M. Savukov and M. V. Romalis. Effects of spin-exchange collisions in a high-density alkali-metal vapor in low magnetic fields. *Physical Review A*, 71(2):23405, 2005.
- P. D. D. Schwindt, B. Lindseth, S. Knappe, V. Shah, J. Kitching, and L. A. Liew. Chip-scale atomic magnetometer with improved sensitivity by use of the Mx technique. *Applied Physics Letters*, 90(8):081102, 2007. ISSN 00036951. doi: 10.1063/1.2709532. URL <http://link.aip.org/link/APPLAB/v90/i8/p081102/s1&Agg=doi>.
- M. Scully and M. Fleischhauer. High-sensitivity magnetometer based on index-enhanced media. *Physical review letters*, 69(9):1360–1363, 1992. URL <http://link.aps.org/doi/10.1103/PhysRevLett.69.1360>.
- S. Seltzer and M. V. Romalis. Unshielded three-axis vector operation of a spin-exchange-relaxation-free atomic magnetometer. *Applied physics letters*, 85:4804, 2004.
- S. J. Seltzer. *Developments in Alkali-Metal Atomic Magnetometry*. Dissertation, Princeton, 2008.
- V. Shah and M. V. Romalis. Spin-exchange relaxation-free magnetometry using elliptically polarized light. *Physical Review A*, 80(1):13416, July 2009a. ISSN 1050-2947. doi: 10.1103/PhysRevA.80.013416.

- V. Shah and M. V. Romalis. Spin-exchange relaxation-free magnetometry using elliptically polarized light. *Physical Review A*, 80(1):13416, 2009b.
- V. Shah, S. Knappe, P. Schwindt, and J. Kitching. Subpicotesla atomic magnetometry with a microfabricated vapour cell. *Nature Photonics*, 1(11):649–652, 2007. ISSN 1749-4885.
- R. E. Slocum and B. I. Marton. Weak Magnetic Fields Using Zero-Field Parametric Resonance. *IEEE Transactions on Magnetics*, Mag-9(3):221–227, 1973.
- U. Steinhoff, A. Schnabel, M. Burghoff, T. Freibier, F. Thiel, H. Koch, and L. Trahms. Spatial distribution of cardiac magnetic vector fields acquired from 3120 SQUID positions. *Neurology & clinical neurophysiology : NCN*, 2004:59, Jan. 2004. ISSN 1526-8748. URL <http://www.ncbi.nlm.nih.gov/pubmed/16012615>.
- K. Sternickel and A. I. Braginski. Biomagnetism using SQUIDs: status and perspectives. *Superconductor Science and Technology*, 19(3):S160–S171, Mar. 2006. ISSN 0953-2048. doi: 10.1088/0953-2048/19/3/024. URL <http://stacks.iop.org/0953-2048/19/i=3/a=024?key=crossref.7350e09f315dd460545533072cbd>
- K. Sternickel, A. Effern, K. Lehnertz, T. Schreiber, and P. David. Nonlinear noise reduction using reference data. *Physical Review E*, 63(3):1–4, Feb. 2001. ISSN 1063-651X. doi: 10.1103/PhysRevE.63.036209.
- J. Vrba. Magnetoencephalography: the art of finding a needle in a haystack. *Physica C: Superconductivity*, 368(1-4):1–9, Mar. 2002. ISSN 09214534. doi: 10.1016/S0921-4534(01)01131-5.
- J. Vrba and S. E. Robinson. Signal processing in magnetoencephalography. *Methods (San Diego, Calif.)*, 25(2):249–71, Oct. 2001. ISSN 1046-2023. doi: 10.1006/meth.2001.1238.
- M. Wagshul and T. Chupp. Laser optical pumping of high-density Rb in polarized ^3He targets. *Physical Review A*, 49(5):3854–3869, 1994.
- R. T. Wakai, J. M. Lenge, and A. C. Leuthold. Transmission of electric and magnetic foetal cardiac signals in a case of ectopia cordis: the dominant role of the vernix. caseosa. *Physics in medicine and biology*, 45(7):1989–95, July 2000. ISSN 0031-9155.
- R. T. Wakai, J. F. Strasburger, Z. Li, B. J. Deal, and N. L. Gotteiner. Magnetocardiographic rhythm patterns at initiation and termination of fetal supraventricular tachycardia. *Circulation*, 107(2):307–12, Jan. 2003. ISSN 1524-4539. doi: 10.1161/01.CIR.0000043801.92580.79.
- T. Walker and W. Happer. Spin-exchange optical pumping of noble-gas nuclei. *Reviews of Modern Physics*, 69(2):629–642, 1997. ISSN 1539-0756.
- L. Walters. Permeabilities of Helium and Deuterium Through a Borosilicate Glass. *Journal of the American Ceramic Society*, 53(5):288–288, May 1970. ISSN 00027820. doi: 10.1111/j.1151-2916.1970.tb12103.x.

- A. Weis and R. Wynands. Laser-based precision magnetometry in fundamental and applied research. *Optics and Lasers in Engineering*, 43(3-5):387–401, May 2005. ISSN 01438166. doi: 10.1016/j.optlaseng.2004.03.010.
- J. Wikswo. SQUID magnetometers for biomagnetism and nondestructive testing: important questions and initial answers. *IEEE Transactions on Applied Superconductivity*, 5(2):74–120, June 1995. ISSN 10518223. doi: 10.1109/77.402511. URL <http://ieeexplore.ieee.org/lpdocs/epic03/wrapper.htm?arnumber=402511>.
- N. Wolters, D. Lomparski, W. Zander, M. Banzet, H. Krause, and P. van Leeuwen. Recording fetal and adult magnetocardiograms using high-temperature superconducting quantum interference device gradiometers. *IEEE Transactions on Applied Superconductivity*, 13(4):3862–3866, Dec. 2003. ISSN 1051-8223. doi: 10.1109/TASC.2003.820505.
- H. Xia, A. B. A. Baranga, D. Hoffman, and M. V. Romalis. Magnetoencephalography with an atomic magnetometer. *Applied Physics Letters*, 89:211104, 2006.
- H. Zhao, J. F. Strasburger, B. F. Cuneo, and R. T. Wakai. Fetal cardiac repolarization abnormalities. *The American journal of cardiology*, 98(4):491–6, Aug. 2006. ISSN 0002-9149. doi: 10.1016/j.amjcard.2006.03.026.

DISCARD THIS PAGE

Appendix A: Dipole electric polarizability

The dipole polarizability tensor is a quantity that fundamentally describes the interaction between atoms and electric fields, including those created by light. Its usefulness derives from the ability to separate the angular momentum properties of transitions from a characteristic coupling strength that depends upon atomic details, and to compress the atomic details into the oscillator strength. We will follow the framework of [Bonin and Kresin, 1997] to express the atomic polarizability for ^{87}Rb in the fine structure basis assuming unresolved hyperfine.

A.1 Fine structure polarizability

As a polarizable medium, when a laser field propagates through an atomic medium, the first order response is an oscillating dipole, with which the propagating field also interacts. This behavior is characterized by the polarizability tensor operator $\hat{\alpha}$, and in the presence of an oscillating electric field, leads to a density matrix evolution characterized by the Liouville equation

$$i\hbar \frac{d\hat{\rho}}{dt} = [\hat{H}_0, \hat{\rho}] + [\delta\hat{H}, \hat{\rho}]. \quad (\text{A.1})$$

The polarizability can be expressed conveniently in a spherical-tensor basis set [Bonin and Kresin, 1997],

$$\hat{\alpha}_{ij} = \alpha_0 \hat{\delta}_{ij} - \alpha_1 i \epsilon_{ijk} \hat{J}_k + \alpha_2 \frac{\frac{3}{2}(\hat{J}_i \hat{J}_j + \hat{J}_j \hat{J}_i) - J(J+1) \hat{\delta}_{ij}}{J(2J-1)}, \quad (\text{A.2})$$

where $\hat{\delta}_{ij} = \delta_{ij} \hat{I}$, where the right hand side is the usual Kronecker-delta function and the identity operator, respectively. The angular momentum dependence of the polarizability is written explicitly in (A.2). The coefficients are written

$$\alpha_0 = \sum_{l \neq 0} A_{l0} G_+(l, 0, \omega) \phi_0(J, J_l) \quad (\text{A.3})$$

$$\alpha_1 = 2 \sum_{l \neq 0} A_{l0} G_-(l, 0, \omega) \phi_1(J, J_l) \quad (\text{A.4})$$

$$\alpha_2 = \sum_{l \neq 0} A_{l0} G_+(l, 0, \omega) \phi_2(J, J_l). \quad (\text{A.5})$$

The sums are over all atomic levels l not equal to the shifted level k . The various quantities used to calculate these coefficients are

$$G_{\pm}(\omega) = \frac{1}{\omega_{l0} - \omega - i\Delta\Gamma_l/2} \pm \frac{1}{\omega_{l0} + \omega + i\Delta\Gamma_l/2} \quad (\text{A.6})$$

$$\phi_0(J, J_l) = \delta_{J_l, J-1} + \delta_{J_l, J} + \delta_{J_l, J+1} \quad (\text{A.7})$$

$$\phi_0(J, J_l) = -\frac{1}{J}\delta_{J_l, J-1} - \frac{1}{J(J+1)}\delta_{J_l, J} + \frac{1}{J+1}\delta_{J_l, J+1} \quad (\text{A.8})$$

$$\phi_0(J, J_l) = -\delta_{J_l, J-1} + \frac{2J-1}{J+1}\delta_{J_l, J} - \frac{J(2J-1)}{(J+1)(2J+3)}\delta_{J_l, J+1} \quad (\text{A.9})$$

$$A_{l0} = \frac{r_e c^2}{2\omega_{l0}} f_{l0}, \quad (\text{A.10})$$

where ω_{l0} is the transition frequency between the shifted level and the level denoted by quantum numbers l , and the oscillator strength between the two levels is f_{l0} .

A.2 Light Shift

The atomic polarizability has a vector component that gives rise to an effective magnetic field [Bonin and Kresin, 1997, Happer and Mathur, 1967, Kornack, 2005]. Continuing to use the formalism of Bonin and Kresin [1997], for a pump laser with narrow linewidth and near resonant with the D1 line, only one excited state in the sum of (A.3)–(A.5) participates, $J = J_l = 1/2$, and we make the rotating wave approximation to simplify G_{\pm} . Under these assumptions, the tensor polarizability for the fine-structure ground state $5^2S_{1/2}$ coupled only to the $5^2P_{1/2}$ state is

$$\hat{\alpha}_{ij} = A_{D1} G(\omega) (\hat{\delta}_{ij} + 2i\epsilon_{ijk} \hat{J}_k) \quad (\text{A.11})$$

$$G(\omega) = \frac{\Delta\omega + i\Delta\Gamma/2}{\Delta\omega^2 + (\Delta\Gamma/2)^2} \quad (\text{A.12})$$

The perturbing term for an oscillating field is

$$\delta\hat{H} = -\frac{|E|^2}{4} \epsilon^* \cdot \hat{\alpha} \cdot \epsilon \quad (\text{A.13})$$

where ϵ is the polarization vector for the electric field. The real part of $\delta\hat{H}$ corresponds to dispersion, while the imaginary part corresponds to absorption, and the dispersive part will be responsible

for the effective field from the light shift. For our magnetometer, we are after the energy shift

$$\langle \delta E \rangle = \text{Tr}(\hat{\rho} \Re(\delta \hat{H})), \quad (\text{A.14})$$

which will be an effective magnetic field because we will write it in the form

$$\langle \delta E \rangle = g_s \mu_B \mathbf{B}_{\text{LS}} \cdot \mathbf{P}, \quad (\text{A.15})$$

where \mathbf{B}_{LS} will be the effective magnetic field seen because of the light shift.

To evaluate (A.14), we need to choose a laser polarization. For the Cartesian basis, we express the polarization in terms of the circular phase θ ,

$$\epsilon = \begin{pmatrix} \cos(\theta) \\ i \sin(\theta) \\ 0 \end{pmatrix} e^{i\alpha_x}. \quad (\text{A.16})$$

Following the convention of [Shah and Romalis, 2009b], the polarization vector $\mathbf{s} = \frac{\epsilon^* \times \epsilon}{i} = \sin(2\theta) \hat{z}$. Then

$$\Re(\delta \hat{H}) = -\frac{|E|^2}{4} A_{l0} (\hat{I} - 2 \sin(2\theta) \hat{J}_z) \Re(G(\omega)) \quad (\text{A.17})$$

$$\Re(\delta \hat{H}) = -\frac{|E|^2}{4} A_{l0} (\hat{I} - \mathbf{s} \cdot 2\hat{\mathbf{S}}) \Re(G(\omega)). \quad (\text{A.18})$$

Finally, we can use an explicit matrix form to evaluate the trace in (A.14), with

$$\hat{I} = \begin{pmatrix} 1 & 0 \\ 0 & 1 \end{pmatrix}, \quad 2\hat{J}_z = \begin{pmatrix} 1 & 0 \\ 0 & -1 \end{pmatrix}, \quad \hat{\rho} = \begin{pmatrix} 1+P & 0 \\ 0 & 1-P \end{pmatrix}. \quad (\text{A.19})$$

The result for the energy shift is

$$\langle \delta E \rangle = -\hbar r_e f c \Phi_0 \mathcal{D}(\nu) (1 - \mathbf{s} \cdot \mathbf{P}), \quad (\text{A.20})$$

where we have substituted

$$|E|^2 = \frac{I}{n\epsilon_0 c} = \frac{8\pi I}{c}, \quad (\text{A.21})$$

and

$$\mathcal{D}(\nu) = \frac{1}{2\pi} \Re(G(\omega)) = \frac{1}{2\pi} \frac{\Delta\nu}{\Delta\nu^2 + \Delta\Gamma/2^2} \quad (\text{A.22})$$

and $\Phi_0 = I/h\nu_0$ is the photon flux. We can rewrite (A.20) by inspection in the form of (A.15) to get the effective field caused by the light shift (ignoring the constant shift to all levels),

$$\Omega_{\text{LS}} = r_e f c \Phi_0 \mathcal{D}(\nu) \hat{z}, \quad (\text{A.23})$$

which agrees with equation (9) of [Shah and Romalis, 2009b]. In the fine-structure basis, we can treat this field precisely as any other Ω_z , and the plots in chapter 2 remain the same. In reality, the Gaussian spatial dependence of the pump laser causing the light shift, as well as the absorption of the pump laser as it passes through the cell, make the light shift a complicated function of position.

In our experiments, the measured Ω_z is a combination of real fields and the light shift field, and its value is minimized but not zeroed during the nulling procedure.

A.3 Faraday rotation

The measurement of atomic spins in our system utilizes the polarization rotation of a far off resonance probe beam. For the D2 transition with unresolved hyperfine structure and in the rotating wave approximation, the polarizability is

$$\alpha_{ij}|_{\text{D2}} = \frac{A_{\text{D2}}}{2\pi} (\mathcal{L}(\Delta\nu) + i\mathcal{D}(\Delta\nu)) (\hat{\delta}_{ij} - i\epsilon_{ijk}\hat{J}_k). \quad (\text{A.24})$$

where

$$A = \frac{r_e f c^2}{2\omega_0} \quad (\text{A.25})$$

$$\hat{\delta}_{ij} = \delta_{ij} \hat{I} \quad (\text{A.26})$$

$$\mathcal{D}(\Delta\nu) = \frac{\Delta\nu}{\Delta\nu^2 + (\Delta\Gamma/2)^2}. \quad (\text{A.27})$$

Equation (A.24) is written in an irreducible spherical basis set, with scalar and vector components (the tensor component is zero)

$$\begin{aligned} \alpha_{ij} &= \alpha^{sc} \delta_{ij} + \alpha_{ij}^v \\ \alpha^{sc} &= \frac{1}{3} \alpha_{ii} \\ \alpha_{ij}^v &= \frac{1}{2} (\alpha_{ij} - \alpha_{ji}). \end{aligned}$$

If we use the geometry in figure 2.6, the polarization of the probe beam is in the $\hat{y} - \hat{z}$ plane. The vector component of (A.24) that will rotate the probe polarization in this plane is given by

$$\alpha_{yz}^v = -\frac{i}{2} \frac{A}{2\pi} (\mathcal{L}(\Delta\nu) + i\mathcal{D}(\Delta\nu)) \hat{J}_x \quad (\text{A.28})$$

Rotation can be described in terms of the index of refraction n_r , which is related to the polarizability through Kramers-Kronig relations [Bonin and Kresin, 1997],

$$n_r = 1 - 2\pi[\text{Rb}]\mathcal{R}(\alpha). \quad (\text{A.29})$$

We are interested in the phase rotation of the probe beam versus the $P_x = 0$ case. This angle is

$$\phi = \Delta n_r \omega t \quad (\text{A.30})$$

$$\Delta n_r = 2\pi[\text{Rb}]\mathcal{R}(\text{Tr}(\rho\alpha_{yz}^v)), \quad (\text{A.31})$$

with the propagation time $t \approx l/c$ for small changes in the index of refraction. The resulting expression is

$$\phi = -\frac{1}{4}[\text{Rb}]l r_e f_{D2} c \mathcal{D}(\Delta\nu) P_x, \quad (\text{A.32})$$

which agrees with [Ledbetter et al., 2008] eq. 13.

If rotation from the D1 line is important (for example, in high pressure buffer gas cells), it can easily be incorporated. The D1 polarizability has the same form as (A.24), with some different numerical factors,

$$\alpha_{ij}|_{D1} = \frac{A_{D1}}{2\pi} (\mathcal{L}(\Delta\nu) + i\mathcal{D}(\Delta\nu)) (\hat{\delta}_{ij} + 2i\epsilon_{ijk}\hat{J}_k). \quad (\text{A.33})$$

Comparison of (A.33) to (A.24) allows us to write down the rotation from the D1 line as opposite in direction and the same numerical factor aside from the frequency dependence ($f_{D2} = 2f_{D1}$ cancels the extra factor of 2 in rotation), and the total rotation for a given detuning is

$$\phi = \frac{1}{4}[\text{Rb}]l r_e f_{D2} c (-\mathcal{D}(\Delta\nu_{D1}) + \mathcal{D}(\Delta\nu_{D2})). \quad (\text{A.34})$$

Appendix B: Operating mode parameters

This appendix is designed to provide a reference for the parameters used for particular operating modes and in our calculations of derived quantities. Daily readjustment of the magnetometers by response optimization makes these parameters only estimates of common operating conditions for each magnetometer. Further, cell-to-cell variation (appendix C) makes discussions of calculations of derived quantities more qualitative than quantitative.

B.1 Standard parameters for all calculations

Symbol	Value	Units	Description
T_c	145	C	Cell temperature
P_{N_2}	50 (0.066)	Torr (Amm)	N ₂ pressure at 300°C
P_{He}	22 (0.029)	Torr (Amm)	He pressure
l	1	cm	Cell side length (modelled as a cube)

B.2 DC-Mode

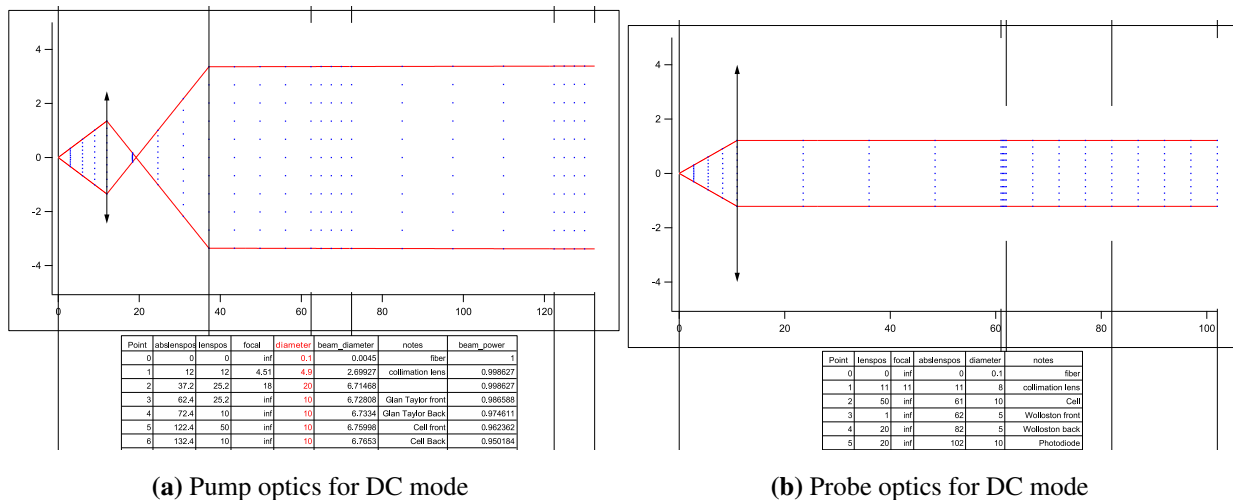


Figure B.1: DC-mode optics

Symbol	Value	Units	Description
\mathcal{P}_{pu}	4	mW	Pump power
w_{pu}	0.256	cm	Pump Waist
$\Delta\nu_1, (x_1)$	20(5.9)	GHz (linewidths)	Pump D1 detuning
\mathcal{P}_{pr}	1.	mW	Probe power
w_{pr}	0.11	cm	Probe Waist
$\Delta\nu_2, (x_2)$	-98.5(-28.9)	GHz (Linewidths)	Probe D2 detuning

B.3 Diffusion pumped mode

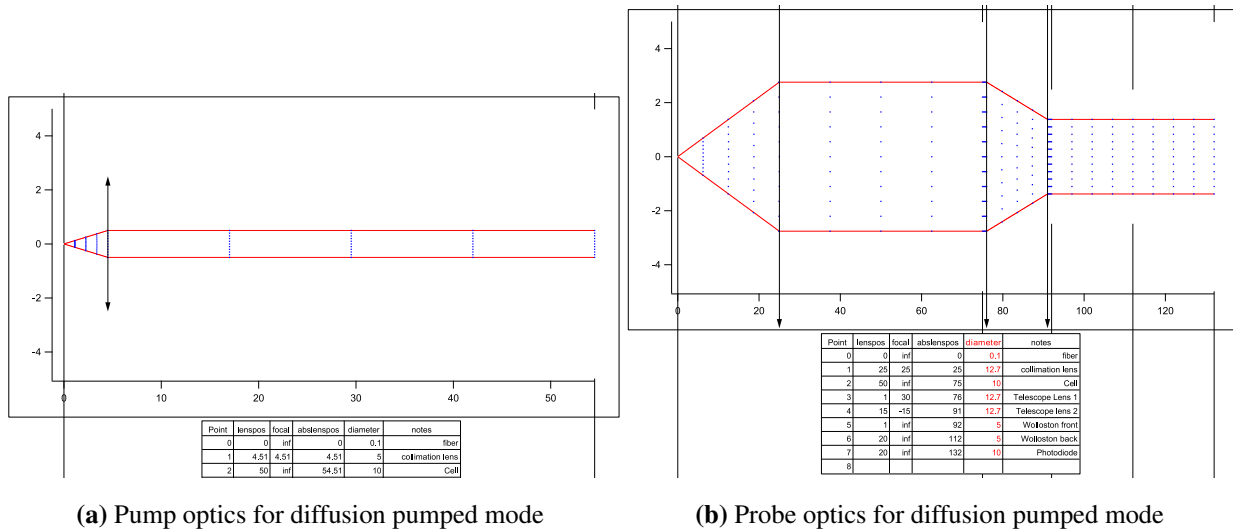


Figure B.2: Diffusion pumped optics

Symbol	Value	Units	Description
\mathcal{P}_{pu}	4	mW	Pump power
w_{pu}	0.051	cm	Pump Waist
$\Delta\nu_1, (x_1)$	20(5.9)	GHz (linewidths)	Pump D1 detuning
\mathcal{P}_{pr}	1.	mW	Probe power
w_{pr}	0.27	cm	Probe Waist
$\Delta\nu_2, (x_2)$	-98.5(-28.9)	GHz (Linewidths)	Probe D2 detuning

Appendix C: Cell characterizations

This appendix has some standard measurements for each of the cells. Though three of the four have the same specifications, they are all different. In this appendix, we try to give a feeling for the individual performance of the four cells used throughout this experiment.

Table C.1 describes the initial nominal properties of the cells. We have some reason for distrusting the cells from Triad Technologies, as cells were initially sent with no N_2 buffer gas, or with incorrect sizing, or mysteriously, seemingly without Rb. Initial measurements confirmed the total buffergas pressure, at any rate, for the cells used.

As mentioned in the text, He diffuses through Pyrex on timescales not insignificant over the course of the measurements presented in this work. We obtained the cells from Triad Technologies in mid-march, 2010. Figure C.1 shows the expected time dependence for diffusion loss of the He through the Pyrex.

Table C.1: The initial nominal properties of each cell. Cells 1–4 are used in all magnetometry experiments described here, while the oscillator cell was used in the transverse pumping experiment. All cells are constructed of Pyrex, and have dimensions $1 \times 1 \times \sim 5 \text{ cm}^3$.

Cell #	Manufacturer	Nominal N_2 (Torr—amg)	Nominal He (Torr—amg)
1	Triad Technologies	50 — 0.066	760 — 1
2		(like cell 1)	
3	Ophos Instruments Inc.	100 — 0.132	—
4		(like cell 1)	
Osc.	Ophos Instruments Inc.	400 — 0.524	—

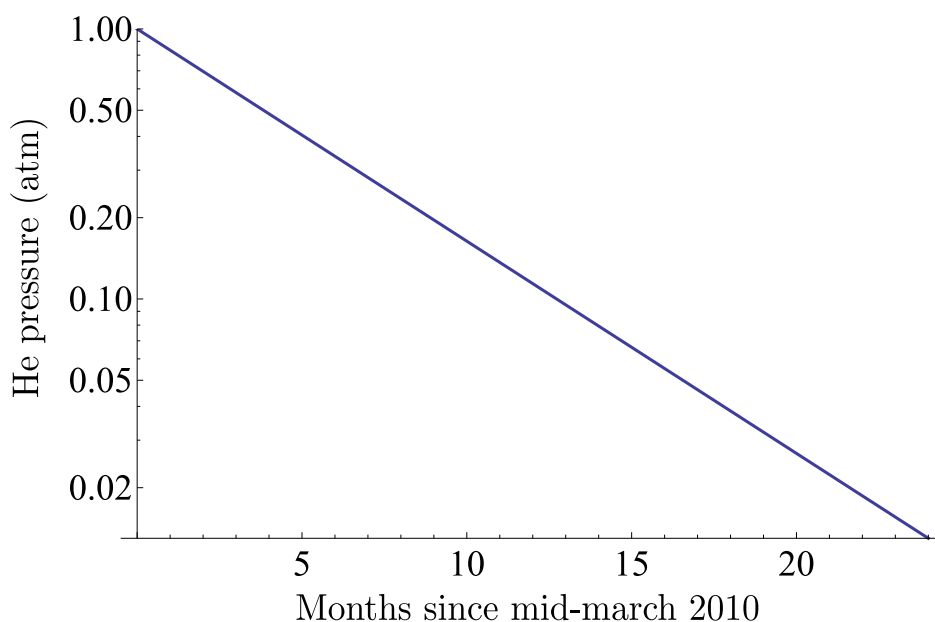


Figure C.1: Expected He diffusion from cells 1,2, and 4. The values roughly agree with measurements extracted from pressure broadened linewidths measured over this time period.

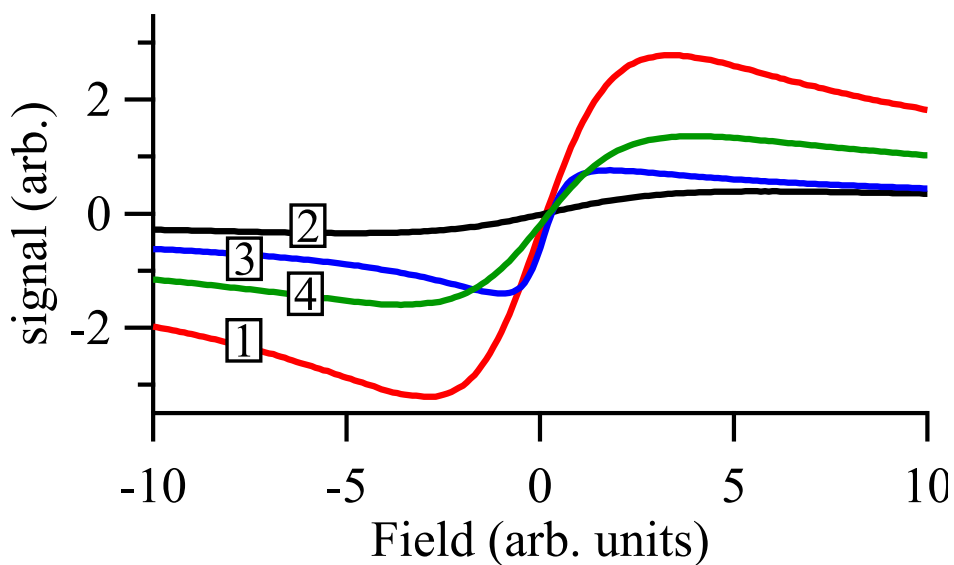


Figure C.2: Uncalibrated sweep of B_y performed simultaneously for each magnetometer. The field is applied with the large coil used for feedback gradiometry, so is nearly the same for each cell. While the details of the sweep shape depends on many individual parameters (section 2.2.5), general features are represented here. For example, cell 2 always has the smallest response, and cells 2-3 always seem to be broader than the others. This may be due to cell birefringence causing probe ellipticity in these cells.

Appendix D: Materials

Many non-traditional materials were researched for this project. The primary requirement for all materials near the magnetometer is that they be non-conducting to eliminate Johnson noise. The thermal parameters are important for the cell, heatsink, and insulation; particularly the thermal conductivity, coefficient of thermal expansion, and maximum use temperature. We have compiled a list of useful materials and their properties in table D.1.

The optics tubes and mirror mounts are made from Delrin. The plastic mount for the magnetometer is made from ABS. The thermal insulation for the heatsink is made from Aerogel. The heat-sinks are made from Boron Nitride, though Shapal-M would have been a better choice. The Boron Nitride heat-sink is clamped together with FEP tape, which is also used to press the Pyrex cell against the heat-sink.

Several of the plastics used in this work are difficult to bond to each other or to other materials. We have had success bonding Delrin to itself and to glass using Permabond Standard Super Glue 105 and 200. These glues are particularly useful for gluing plastic retaining rings to optics or plastic optics adapters. The optic and ring are clamped together, then a small bead of glue is applied on the edge of the optic, against the retaining ring.

Table D.1: Thermal material properties for useful non-magnetic, non-conductive materials. T_{\max} is the maximum use temperature, k is the thermal conductivity and α_L is the linear coefficient of thermal expansion.

Material	T_{\max} (C)	k (W/m K)	α_L (10^{-6} 1/C)	Notes
Macor	800	1.46	0.93	Machinable, low thermal conductivity
Boron Nitride	550	34–66	0.7–1.3	Machinable, higher thermal conductivity
Shapal-M	1000	90	4.4	Machinable, highest thermal conductivity
ABS	88	0.17	50–85	Good all around choice, can chemically weld
Delrin	85	–	123	Good mechanical properties, slippery and difficult to bond
Peek	249	0.25	46.8	Good at high temp., better mechanical properties than PTFE
PTFE	250	0.23	100	Good at high temp., only sticks to itself
Pyrex	230	1	4	Glass for vapor cells, will not hold He gas
Aerogel	200	0.022	–	Good insulation, lower thermal conductivity than air
Polyamide	288	0.035	–	Rigid foam insulation
FEP Adhesive tape	204	–	–	Plastic tape sticks to PTFE, high temp

Appendix E: Electronics

This appendix focuses on the electronics circuits designed and developed as part of the work presented in this thesis.

E.1 Heater H-bridge circuit

The original prototyped magnetometer was driven with a set of heaters operated in the manner of chapter 3, driven with a DC current. In this configuration, with dual heaters aligned to cancel out single-heater magnetic fields, and heater pairs aligned to suppress remaining fields, the 0.5 A DC currents produce fields that are measurable, but smallest in the sensitive direction of the magnetometer due to the heater orientation. Measurements indicate residual fields <1 nT in this direction. No difference was noticed in the noise spectrum between when the heaters were on or off.

Using the 4-channel magnetometer array with a single large set of tri-axial nulling coils, magnetic gradients from the heater fields became noticeable and reduced the magnetometer sensitivity. The magnetic fields could still be nulled at each magnetometer individually, but it became impossible to cancel the fields at every magnetometer simultaneously with four independent sources and only a single control. To address this problem, we developed circuitry to drive the heaters at a high enough frequency that fields caused by the heaters average out on typical biomagnetic timescales.

The circuit is an example of a commonly used technique in stepper-motor control and is called an H-bridge. Functionally, it is simply a set of four digitally controlled MOSFET switches which are controlled to periodically switch the current direction through the load by synchronously switching the sides connected to the DC power supply and ground (see inset to figure E.1). The full circuit schematic is shown in figure E.1. Many ICs exist to facilitate driving the MOSFETs properly. We have chosen a single integrated IC, the ISL83204A, which has many useful features. With inputs of +15 V, it can drive the high-side N-channel MOSFET gates to about $V_{+}+10$ volts. It can also operate in self-oscillatory mode with an oscillation period defined by the value of a few external components.

The circuit can be configured in one of two modes: operation between a positive rail and ground (V_+ mode) or operation between ground and a negative rail (V_- mode), with only a small change in the circuit hardware. Each magnetometer requires one PCB and a dedicated adjustable DC power supply, along with ± 15 V supplies for the ICs. A list of the circuit elements is provided in table E.1.

The simplest setup is V_+ mode, made for switching the heaters with a positive DC source. In this case, R16 should be bypassed, R17, Q1, Q2, and U1 are unnecessary, and the indicated connection should be made across the pins for Q2. Connections for edge connector J1 are $V_+ = V_{\text{control}}$, $V_- = \text{GND}$.

In V_+ mode, a variable DC voltage source provides V_+ . U2 provides a reference voltage at 7.5 V, and the combination of C2, R3, R4, R5, and pots R10 and R11 combine to make a relaxation oscillator with circuitry inside the ISL83204A to determine the gate control switching frequency. The time constant is set by $\tau = R5, R10_{\text{series}} + R11_{\text{series}}$, and C2. Using $C2 = 250$ pF and $1 \text{ k}\Omega \leq R_{5+10+11} \leq 2.11 \text{ M}\Omega$, the oscillation frequency can be adjusted from 1 kHz to 1 MHz.

J5 connects to a ON/OFF/ON DPDT front-panel switch which acts to turn the switching on, high-only, or both sides of the load connected to ground. Resistors R8 and R9 provide dead-time control of the switching circuit to eliminate both switches on a single side of the output load being closed at once, a condition known as shoot-through, which becomes more problematic at higher switching frequencies. D1,2 and C3,4 provide power for the bootstrapping circuit that ensures the high-side gate control voltage is higher than V_+ . D3–6 and R12–15 are to lower pickup noise on the gate control voltages, if necessary. We have not used them, but if noise in the circuit becomes too large they may help. In this case, R12–15 should be 10Ω , and the diodes should be fast recovery types for the highest speed switching.

The actual switching is done by U5,6 which are integrated double MOSFETs arranged with common source-drain connections to facilitate smaller H-bridge component count in situations (such as this) where the switched power is not too high and the chips will not become too hot. J6 is a screw-terminal output connection that goes to the load, while J3 is a set of monitor pins that can be connected to J4 (which leads to a differential amplifier) or can be monitored directly.

Care must be taken when monitoring the output. If coaxial cable is used to connect the circuit output to the load, one must remember the power and grounds are quickly switching, so accidentally grounding a shield for a coaxial cable (by connecting to a scope input, for example) will short the circuit during 1/2 of its cycle.

V_- mode works in essentially the same way as described above, except a virtual ground (V_-) is used, and the H-Bridge controller IC is operated between V_- and $10 V+V_-$ as power supplies. All circuit elements are used (except the optional gate resistors and diodes). U1 is a low-drop 10 V voltage regulator, chosen to ensure it works between the full range of $15 V-V_-$. The extra circuitry is an adaptation of a circuit in [Horowitz and Hill, 1989] to increase the maximum operation current at the regulated voltage. The input connections to J1 are $V_+=GND$, V_- is provided by a variable voltage DC source.

In either operation mode, the output power to the heaters is controlled by adjusting the amplitude of the DC power supply voltage. This circuit will work across the full range $V_+=|V_-| \leq 20 V$ available from the programmable National Instruments PXI-4110 power supplies used in this work.

We have put four of these circuits in an electronics box. The front panel connections are the IC power connections $\pm 15 V$ and GND, as well as two positive and two negative DC voltages which will control each of four magnetometers, and the ground for the DC power supplies. The output is an 8P8C Jack, meant to connect to shielded-Cat6e cabling. Shielding the heater wires is important, as the frequencies and currents are higher and pickup noise exacerbated. Pickup is primarily a problem for the photodiode signals, where the large high frequency pickup is aliased into the detection frequency band.

The higher frequency components of the square wave modulation seem to induce oscillations on other parts of the magnetometer circuitry, most importantly the photodiode cables. There is a ring-down with an oscillation frequency of around 12 MHz, which might correspond to the transmission line behavior of the cables. While this frequency is much higher than those used in magnetometry, they get aliased into the detection band, and for higher modulation frequencies (~ 500 kHz) the aliasing noise becomes noticeable. Lower modulation frequencies induce less ring-down, but perturb the atoms more. While the current setup allows DC heating because there

is individual control over each magnetometer, sine-wave modulation should be considered in the future, perhaps with integral PID control of heater currents.

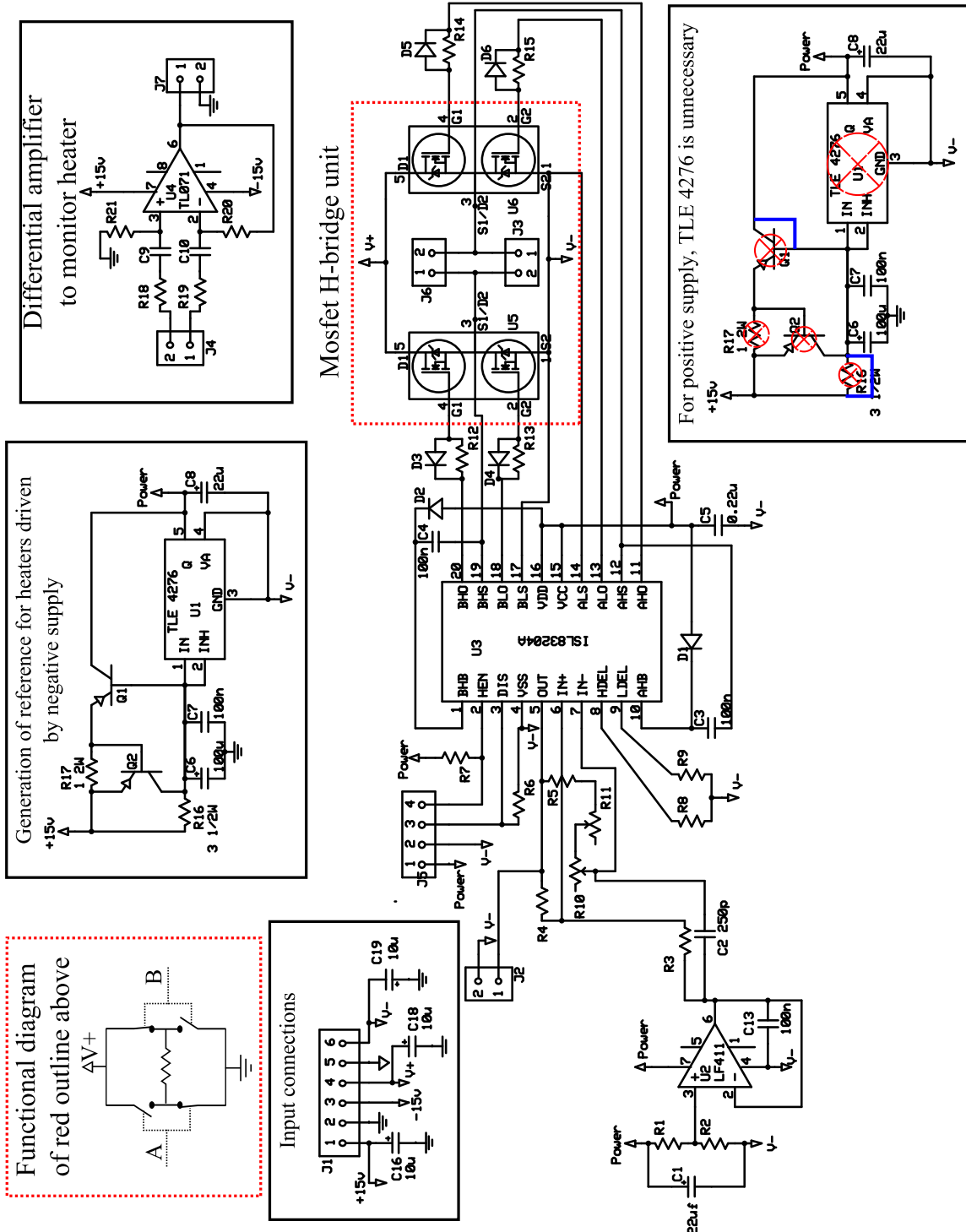


Figure E.1: Heater H-bridge controller

Table E.1: Parts list for the heater controller. D3–D6 and R12–R15 are bypassed unless there’s excessive pickup noise in the switching circuit.

Comp.	Value	Notes	Comp.	Value
C1	22uf		R1	10k
C2	250p		R2	10k
C3	100n	Good leakage/Rf properties	R3	100k
C4	100n	Good leakage/Rf properties	R4	100k
C5	0.22u		R5	2k
C6	100u	Only for V- circuits	R6	10k
C7	100n	Only for V- circuits	R7	10k
C8	22u		R8	100k
C9	1u		R9	100k
C10	1u		R10	2M 1T
C13	100n		R11	100k 10T
C16	10u		R12	
C18	10u		R13	
C19	10u		R14	
D1	1N5817		R15	
D2	1N5817	V- only	R16	3 1/2W
D3	1N4448	V- only	R17	1 2W
D4	1N4448		R18	100k
D5	1N4448		R19	100k
D6	1N4448		R20	10k
J1	6-pin screw terminal	Input power connections	R21	10k
J2	2-pin crimp post	Mon. Comparator (V- only)	U1	TLE 4276
J3	2-pin crimp post	Mon. Bridge	U2	LF411
J4	2-pin crimp post	Mon. Out	U3	ISL83204A
J5	4-pin crimp post	Dis/HEN/On	U4	TL071
J6	2-pin screw terminal	H-Bridge Out	U5	IRFI4019HG-117P
J7	2-pin crimp post	Mon. Out	U6	IRFI4019HG-117P
Q1	2N5194	Only for V- circuits		
Q2	2N5194	Only for V- circuits		

E.2 Thermistors

Many thermistors contain magnetic materials, and many more cannot be used at the high temperatures required for atomic magnetometry. Simply testing the thermistor (including the leads) with a strong magnet is usually sufficient. We have used Honeywell NTC Thermistor 112-103FAJ-B01 in the magnetometers presented in this work. Standard thermistor curves can be used to predict the temperature from the resistance, given $R_0 = 10\text{ k}\Omega$ and $\beta = 3669$. For reference, a plot of the predicted temperature vs thermistor resistance for the thermistor in all channels is shown in figure E.2.

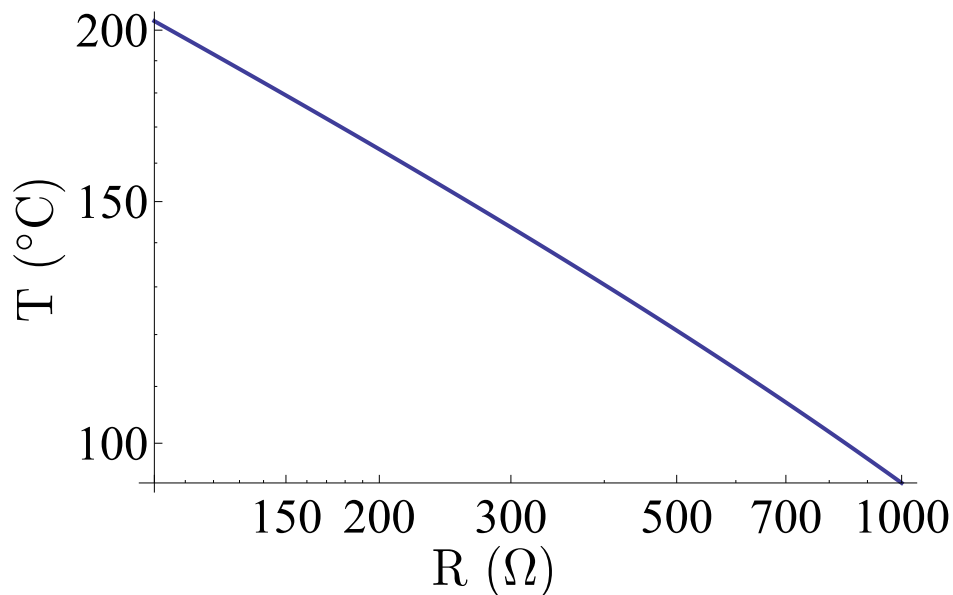


Figure E.2: Nominal thermistor temperature vs. resistance for the thermistors used in all channels.

E.3 Coil driving circuit

An essential component to the magnetometer is the circuitry used to apply offset and calibration fields. The coil control box built for this circuit allows a DC offset and input signal to be coupled and are applied to the coils using a voltage to current converter. There are three characteristic voltages in the box: the DC voltage selected with a front-panel potentiometer (V_{dc}), the input voltage V_i , and the final output voltage V_o . The job of the coil control box is to make $g_i V_i + g_{dc} V_{dc} =$

Table E.2: Coil control box design features

Front panel inputs	BNC for V_i Potentiometer to adjust V_{dc} Switch to adjust $g_i = \{1, 1/10, 1/100\}$ AUX input
DIP Switches inside	Adjust $R = \{50, 500, 1k, 5k\}$ Adjust $g_{dc} = \{1, 1/10, 1/100\}$
Outputs	BNC monitors V_o RJ45 receptacle for an 8P8C Cat. 6 cable
Features	Each enclosure controls 3 boards Using ± 15 V supplies, $V_o(\max) = 12$ V

V_o , and to output V_o across a series resistor R as a current source. Additionally, it must perform this function without adding too much current noise, which is converted to magnetic noise at the coils. With the coil calibration ~ 20 fT/nA, the maximum allowable current noise in the coils is 50 pA/ $\sqrt{\text{Hz}}$. This is on top of a driving current of up to 2 mA for DC cancellation.

The circuit presented here was designed as part of this work and built by Greg Smetana. A list of features of the coil control box are described below:

The circuit diagram for the coil control box is shown in figure E.3. There are three primary subcircuits. In the red-dashed outline, two LM399 Zener reference diodes are used to create a stable reference on either side of ground. The wiper of a front-panel potentiometer selects the DC voltage from $\pm V_{\text{zener}}$ and is buffered by an op-amp to produce V_{dc} . Resistor networks allow division of this voltage in decade steps from 1–100. The blue-dotted line accepts a front panel input voltage V_i using a low-noise differential amplifier, and a resistive voltage divider can step down the voltage in three decade steps from 1–100. The final piece is a balanced line driver using two input op-amps to combine the voltages from previous subcircuits. A third op-amp converts the balanced line driver into a current source by monitoring the output voltage across one of the resistors and feeding back to the input amp. The output resistors can be varied in values of 50, 500, 1k, and 5k. Resistive values much higher are not useful at our voltage ranges (i.e. typical V_o is a few volts across 5k).

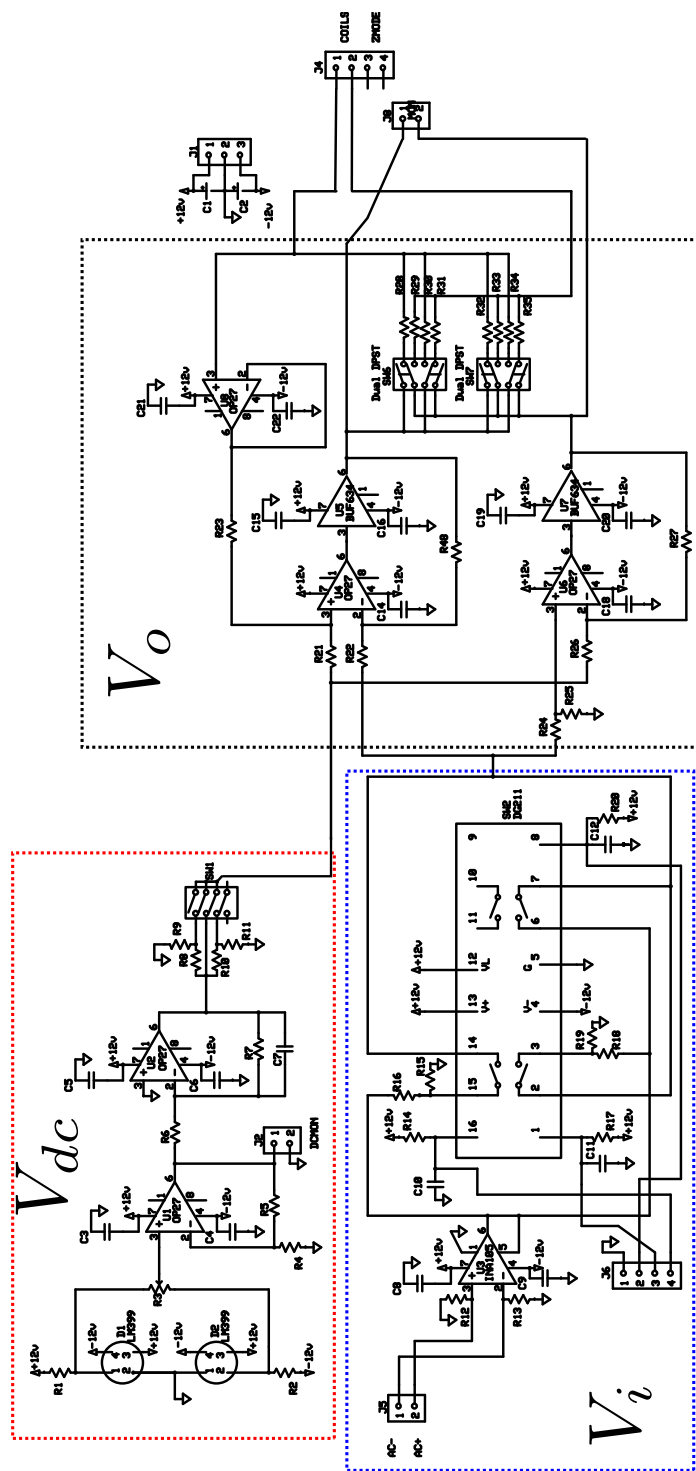


Figure E.3: Coil control box circuit diagram

The transverse oscillator has even more severe demands. The coil calibration is larger by a factor of 100, while the necessary currents are larger by a factor of 100 also. Thus, the maximum current for $1 \text{ fT}/\sqrt{\text{Hz}}$ noise level in the direction of the large field is $500 \text{ fA}/\sqrt{\text{Hz}}$, on top of a 200 mA signal!

We have made measurements of the current noise for zero applied current at every setting of the coil control box. Since increasing R seems to help performance, we conclude that we are still limited by voltage noise from our current source. We generally use $R = 5 \text{ k}\Omega$, where the noise is lowest.

DC Gain	AC Gain	R(out)	current noise (nA)	field noise (fT)
1	1	50	14.000	210.000
1	1	500	1.400	21.000
1	1	1000	0.700	10.500
1	1	5000	0.230	3.450
1	0.1	50	13.000	195.000
1	0.1	500	1.400	21.000
1	0.1	1000	0.700	10.500
1	0.1	5000	0.250	3.750
1	0.01	50	15.000	225.000
1	0.01	500	1.500	22.500
1	0.01	1000	0.700	10.500
1	0.01	5000	0.260	3.900
0.1	1	50	5.000	75.000
0.1	1	500	0.600	9.000
0.1	1	1000	0.380	5.700
0.1	1	5000	0.260	3.900
0.1	0.1	50	3.800	57.000
0.1	0.1	500	0.420	6.300
0.1	0.1	1000	0.220	3.300
0.1	0.1	5000	0.043	0.645
0.1	0.01	50	2.400	36.000
0.1	0.01	500	0.400	6.000
0.1	0.01	1000	0.190	2.850
0.1	0.01	5000	0.060	0.900
0.01	1	50	2.800	42.000
0.01	1	500	0.380	5.700
0.01	1	1000	0.200	3.000
0.01	1	5000	0.062	0.930
0.01	0.1	50	2.100	31.500
0.01	0.1	500	0.360	5.400
0.01	0.1	1000	0.230	3.450
0.01	0.1	5000	0.063	0.945
0.01	0.01	50	3.200	48.000
0.01	0.01	500	0.500	7.500
0.01	0.01	1000	0.230	3.450
0.01	0.01	5000	0.069	1.035

Figure E.4: Noise measurements for coil driving circuit settings, measured using current preamplifier.

Appendix F: Fetal MCG report

This appendix includes a report of the type normally generated for a fMCG study using SQUIDs. The first two attached pages are analysis of fMCG timing intervals for two different portions of our data. The final page is from the reference data taken by a SQUID immediately prior to the SERF measurement. Additional fMCG studies are needed to verify the consistent accuracy of timing measurements made by SERFs vs SQUIDs, but in this initial study the agreement is relatively good.

Table F.1 shows an analysis made by Ron Wakai's biomagnetism group of the average fMCG waveform from figure F.1–figure F.3. The average waveform can be used in certain diagnostic applications, such as long-QT syndrome which is thought to be associated with sudden infant death syndrome [Cuneo et al., 2003, Zhao et al., 2006]. All intervals measured with the SERF and SQUID systems match to within 15%, with most better than 5%. For this application, the relevant measurement would be the QT or QTc interval. While more measurements are necessary, comparison with the data from Zhao et al. [2006, figures 2 and 3] leads us to feel cautiously optimistic that our magnetometer could be suitable for this kind of measurement.

Table F.1: Fetal MCG report generated for the first fMCG measurements made using a SERF magnetometer of a 31-week pregnancy. The two SERF measurements represent different measurement periods during the same visit. The analysis was performed by Ron Wakai's medical physics group.

Method	Interval (ms)					
	RR	PR	P	QRS	QT	QTc
SERF (# 1)	425	95	42	47	264	405
SERF (# 2)	426	95	48	49	282	432
SQUID	415	90	41	48	241	375

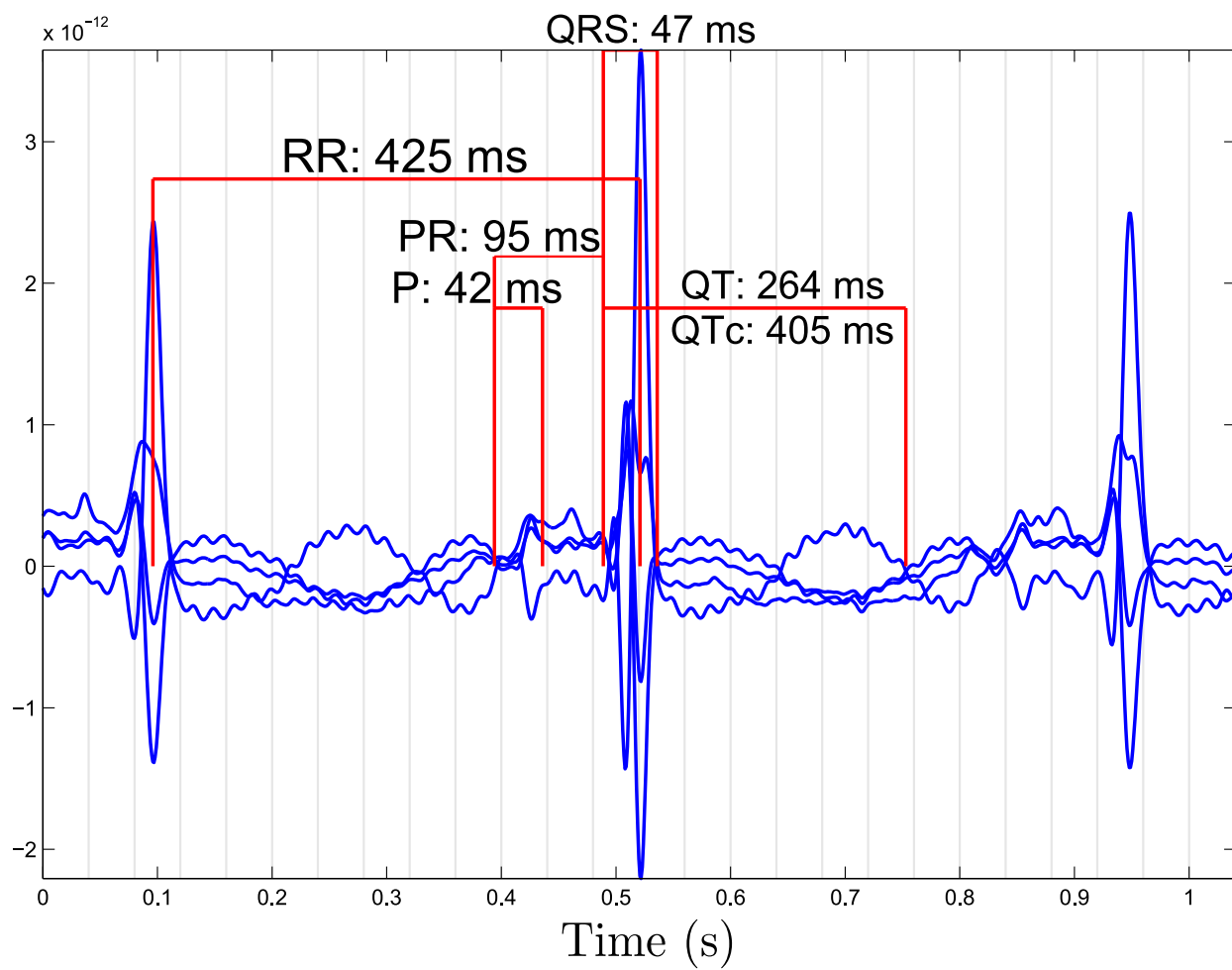


Figure F.1: Average SERF fMCG waveform, showing relevant intervals.

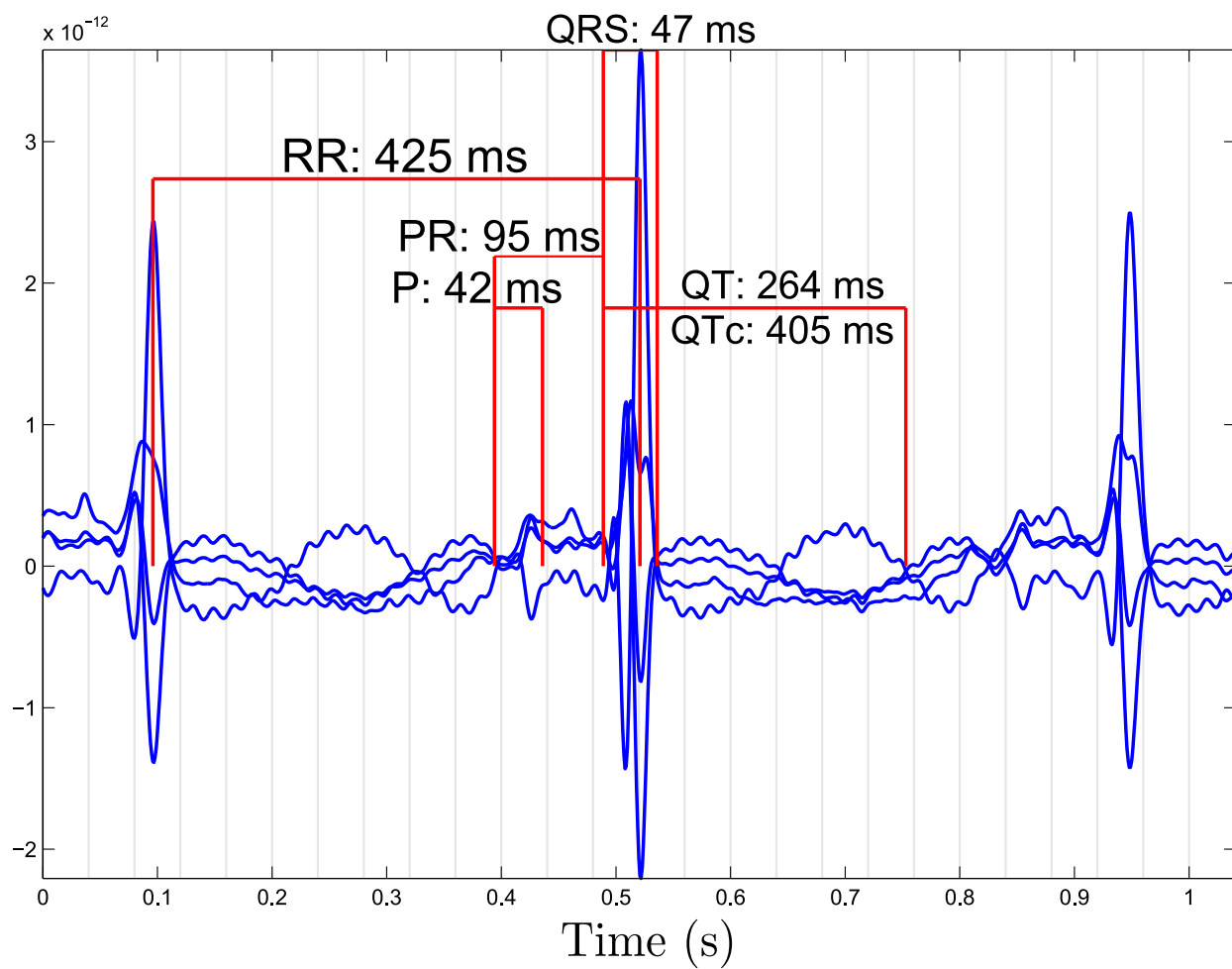


Figure F.2: Average SERF fMCG waveform, showing relevant intervals for a different time segment than in figure F.1.

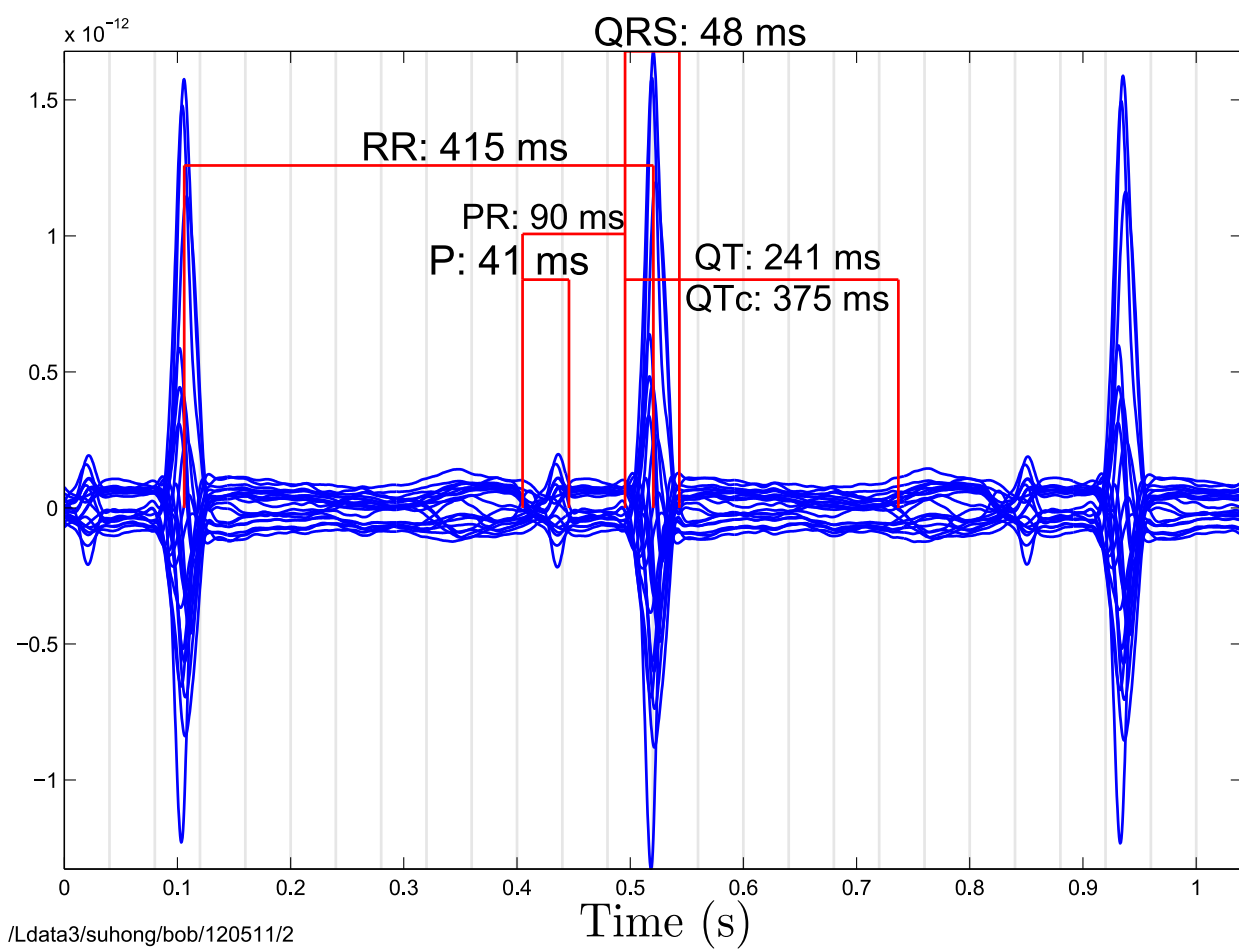


Figure F.3: 21-channel SQUID measurement for the same fMCG subject as in figure F.1 and figure F.2

Appendix G: Magnetic field coils

Several sets of coils were produced and characterized for this work. Where possible, the coils were calibrated with low-frequency (10 Hz) currents applied to the coils, and the resulting response measured by a calibrated fluxgate placed at the center. For the individual set of coils wrapped around each magnetometer, a fluxgate could not be placed in the center, so the coils were calibrated by centering the magnetometer inside a larger Helmholtz set that had been calibrated using the fluxgate method. Perturbations were induced with the Helmholtz set, and the current necessary to cancel those perturbations with the small coils was measured. Below, we describe some of the coils details and calibrations.

G.1 Individual coils for each magnetometer

Each of the four magnetometer channels is wrapped with a single set of tri-axial coils. Each axis is composed of two single turn loops wrapped on either side of the thermal insulation and centered around the cell windows. Square turns were used to maximize field uniformity Kirschvink [1992]. All coils have approximate size $a = 4$ cm and a pairs for an axis are all separated by $d = a$. The coil calibration and expected field uniformity are shown in figure G.1.

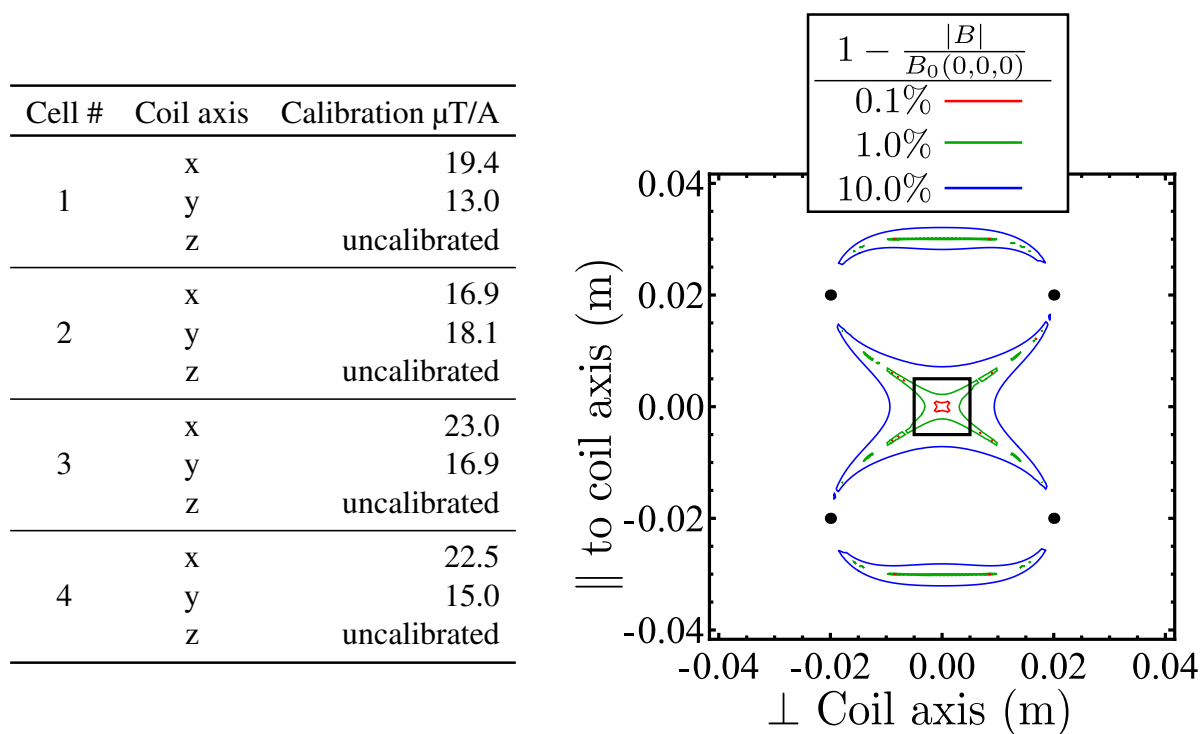


Figure G.1: (Table-left) Calibration factors for the individual coils wrapped around the four magnetometers used throughout this work. The z-coils were not calibrated. (Figure-right) A simulation of 4 cm side, 4 cm separated single-turn coils. The contour lines represent field uniformity levels. The central square is the cell.

G.2 Large single coil

The large single gradiometer coil consists of 1-turn in a rectangular geometry. The coil calibration is $3 \mu\text{T/A}$ in the center. The magnetometers are offset from the center in a square pattern, and with an offset value of 3.5 cm for all the measurements made here. Figure G.2 shows a contour plot of the coils and the field uniformity in the center. The black squares show the dimensions of the four cells.

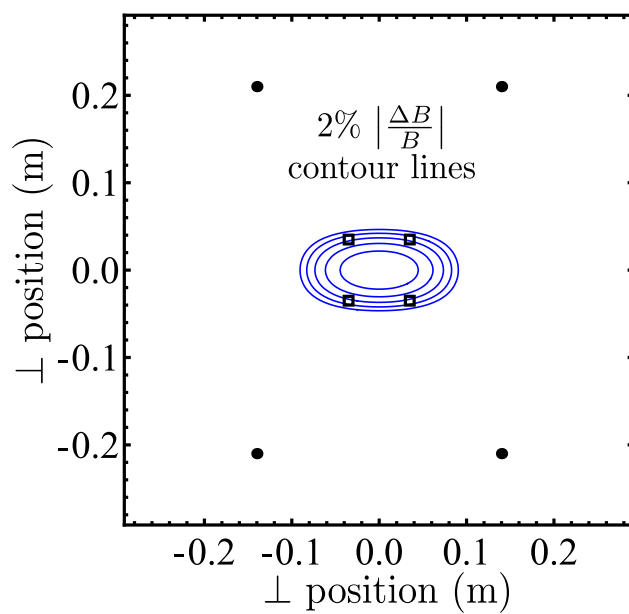


Figure G.2: Gradient coil contour map. A single coil is in the plane of this image. The contour lines represent 2% variation in the field amplitude. If the magnetometers are perfectly centered around the center of the coils, then the fields are the same. However, any offset will impact the average field of the magnetometers at the percent level.

G.3 Transverse pumping magnetometer coils

For technical reasons, it is useful to use separate triaxial DC coils and a pulse coil for the transverse pumping magnetometer. For the directions along the pump and probe laser, we use single-turn square coils wrapped around the thermal insulation. For \hat{z} direction, large DC fields are needed, as well as a very short, high amplitude pulse.

Using the notation in section 6.4, the transverse spin-resonance is not as sensitive to the pulse amplitude Ω_1 , so the field uniformity requirements are not as important for the pulse-coil. We use multi-turn Helmholtz configuration for this set, centered around the center of the cell.

In contrast, Ω_z needs to be very uniform. The resonance condition is that $\Omega_z/q = \omega_1$. If we suppose a magnetic field gradient proportional to the applied field, $\delta\Omega_z/\Omega_z = c$, then atoms in different parts of the cell have different resonance frequencies, and $\delta\Omega_z/\Omega_z = \delta\omega_1/\omega_1$. If the resonance linewidth is not to be affected by the magnetic field gradient, the resonance linewidth must be large compared to the field inhomogeneity, $\delta\omega_1 \ll \Gamma'$. At 125 °C, $\Gamma \approx 180$ 1/s (including Γ_D). Then we require $c\omega_1 \ll 2\Gamma$, or $c \ll 0.01$. In other words, we need the DC field Ω_z to be uniform across the cell volume to much better than 1%. This fact should reinforce the very narrow resonance width of the transverse spin.

Inspection of figure G.1 immediately makes it obvious the single square set of coils will not be adequate. Various symmetric planar geometries are available Merritt et al. [1983]. We use a four coil system with integral turn ratios. The geometry can be seen in figure G.3. Integrating the average deviation from $B_z(0, 0, 0)$ along the probe beam gives a linewidth of less than 2 Hz, and the deviation in the whole cell should be smaller than 0.1%.

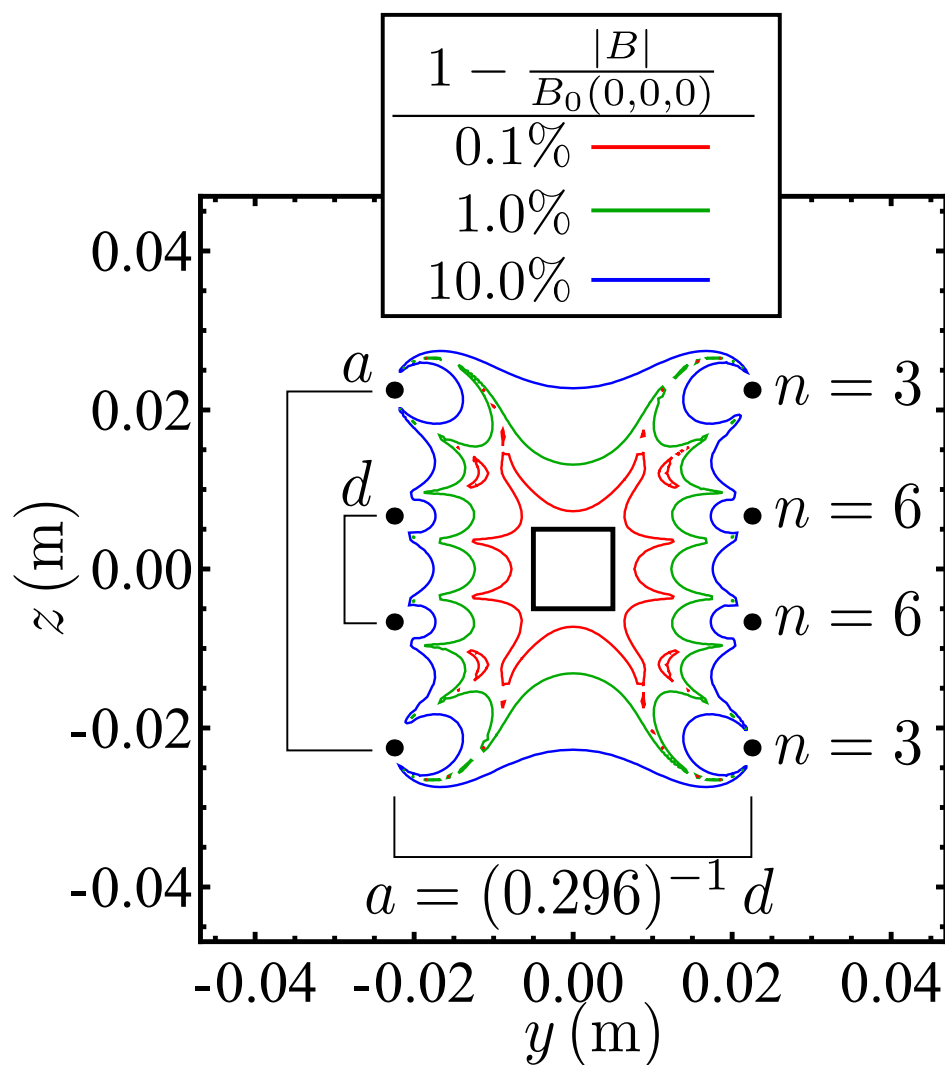


Figure G.3: The coils used in the transversely pumped magnetometer to produce very uniform Ω_z . The uniformity is better than 0.1% in the cell volume from these coils, which should not broaden the transverse spin resonance until the resonance frequency is several MHz.

Table G.1: Calibration for all axis of the transversely pumped magnetometer. The numbers below the coil columns are the calibrations measured in the coil centers by a fluxgate. The matrix represents measurements of how orthogonal coil axis are to one another, and are normalized by the total calibration in the top column.

	B_{pulse}	B_x	B_y	B_z
	242 $\mu\text{T/A}$	30.6 $\mu\text{T/A}$	29.8 $\mu\text{T/A}$	251.7 $\mu\text{T/A}$
B_x	0.03	1	0.04	0.003
B_y	0.03	0.01	1	0.05
B_z	1	0.01	0.03	1

Appendix H: Magnetometer parts list

Table H.1: A list of the custom parts used in the magnetometers, both designed as part of this work and purchased from outside vendors. Custom parts which are adapters for external optics have the optic part # listed.

Description	Vendor (adapted from)
1 in adapter for 18 mm large-diameter aspheric lens	custom (Thorlabs)
SM05 adapter for 11 mm aspheric lens	custom (Thorlabs)
SM05 adapter for 8 mm aspheric lens	custom (Thorlabs)
SM05 adapter for 4.51 mm aspheric lens	custom (Thorlabs)
SM05–SM1 adapter to mount smaller lenses in SM1 tubes	custom (Thorlabs)
SM1 retaining ring	custom (Thorlabs)
SM1 FC-APC fiber connector plate	custom (Thorlabs)
SM05 FC-APC fiber connector plate	custom (Thorlabs)
SM05 retaining ring	custom (Thorlabs)
Two-axis mirror mounts	custom (for prism mirrors)
Tri-bore optics tube	custom
Ceramic heat-sink	custom
Magnetometer plastic scaffold	custom
photodiode adapter piece	custom
Heater-controllers	Custom (see appendix E)
Coil drivers	Custom using circuit in appendix E
1 in Glan-Taylor polarizer, AR-coated 795 nm	United Crystals
1 in 10 cm clear aperture 0-order waveplate at 795 nm	United Crystals
0.5 in Wollaston beam splitter	United Crystals
0.5 in 0-order half-waveplate at 780 nm	United Crystals
0.5 in Glan-Taylor polarizer	United Crystals
Lasers (Pump)	Eagleyard Photonics EYP-DFB-0795-00040-1500-BFY02-0002 (80 mW)
Lasers (Probe for transverse magnetometer)	EYP-DFB-0780-00080-1500-TOC03-0002
Lasers (Probe for array)	Sacher Lion Littman Metcalf ECDL (25 mW)
Lenses (diffusion probe)	f=25 mm Thorlabs #AC127-025-B f=-15 mm Thorlabs #LC2265-B

Table H.1: A list of the custom parts used in the magnetometers, both designed as part of this work and purchased from outside vendors. Custom parts which are adapters for external optics have the optic part # listed.

Description	Vendor (adapted from)
Lenses (DC-probe)	f=30 mm spherical singlet
Lenses (diffusion pump)	f=11 mm aspheric lens
Lenses (DC-pump)	f=4.51 mm aspheric lens
Polarizer (thin)	f=18 mm large aspheric lens Thorlabs #AL2018-B
Mirrors	0.5" Thorlabs #LPVIS050
Fiber mating sleeves	Dielectric prism mirrors Thorlabs #MRA10-E03
Laser controller (current)	Thorlabs #ADAF2-PMN
Laser controller (temp.)	Thorlabs #LDC202C
Fibers	Thorlabs #TED200C
Fiber splitters	Oz-optics 6 m polarization maintaining #PMJ-3A3A-633-4/125-3-6-1
Aerogel insulation	5-way (4-equal power, 1 5%) Oz-optics #FOBS-15P-111111-5/125-PPPPPP-780-95/5,50/50-40-3A3A3A3A3A3A-3-1
Heaters	from McMaster-Carr part no. 9590K8
Thermistors	Minco thermofoil heaters, HR5578R4.6L12A (ordered from distributor, Temflex controls inc.
Data Acquisition equipment	NTC Thermistor 112-103FAJ-B01, from Newark
	National Instruments FPGA DAQ system